SINGLE-COMPONENT OPTOGENETIC TOOLS FOR CYTOSKELETAL REARRANGEMENTS

Erin Berlew

A DISSERTATION

in

Bioengineering

Presented to the Faculties of the University of Pennsylvania

in

Partial Fulfillment of the Requirements for the

Degree of Doctor of Philosophy

2022

Supervisor of Dissertation

_____

Brian Y. Chow, Ph.D., Associate Professor of Bioengineering

Graduate Group Chairperson

_____

Yale Cohen, Ph.D., Professor of Bioengineering

Dissertation Committee

Joel D. Boerckel, Ph.D., Assistant Professor of Bioengineering

Lukasz J. Bugaj, Ph.D., Assistant Professor of Bioengineering

Kevin H. Gardner, Ph.D., Professor of Chemistry

Daniel A. Hammer, Ph.D., Professor of Bioengineering

SINGLE-COMPONENT OPTOGENETIC TOOLS FOR CYTOSKELETAL REARRANGEMENTS

ACKNOWLEDGEMENTS

First, I would like to thank my mentor, Brian Chow. Brian first hired me as a lab technician when I had no engineering experience, and his confidence in me allowed me to adjust to a new scientific field, ask big questions, and explore new techniques for finding answers. Brian often says that the only reasons not to do an experiment are violation of a law of physics or astronomical cost, demonstrating his commitment to thinking outside the box and prioritizing student learning. Brian has enabled me to become a better scientist by giving me the freedom to explore projects and techniques I found interesting and encouraging me to expand my scientific skillset; I am especially grateful for the emphasis he puts on his trainees' interests and career goals. Throughout my Ph.D., Brian has been supportive both professionally and personally, and I am lucky to have had a mentor who cares so much about his students' health and happiness in addition to their research progress.

Over the last five and a half years, the Chow Lab has made the process of completing a Ph.D. during a tumultuous decade and global pandemic bearable and enjoyable. Spencer Glantz was particularly generous in sharing his expertise on BcLOV4 and allowing me to work on the protein he discovered. I am grateful to current lab members Michael Magaraci, Ivan Kuznetsov, and Gabrielle Ho, as well as past members including Keisuke Yamada (who made direct contributions to this thesis), Eleanor Rand, Pimkhuan Hannanta-Anan, Molly Sheehan, Chris Herbst, Amy Chuong, and honorary member Kristina Li. Throughout various iterations of students and post-docs, the lab has remained a constant source of support, scientific guidance, logistical assistance, and general good humor; I cannot imagine a better group of people to work with. I also wish to thank my thesis committee, particularly Joel Boerckel and Lukasz

Bugaj, for their insightful guidance and encouragement. I also thank Lou Charkoudian for her years of mentorship and support.

Finally, I consider myself incredibly lucky to have such a long list of family and friends to thank for getting me to this point. My grandparents, aunts, uncles, and cousins of the Berlew, Brennan, Carroll, Corcoran, Burns, Recupero, and O'Malley families have given me a secure support network from which to try new things. I thank Karina Wiener, Christopher Donnelly, Daniel Fries, and Zoë Lewis for their friendship and support. My cat Oscar has provided me with endless entertainment and companionship through long days of studying and analysis, and I am grateful for his dedication to research. My therapist Melanie Rychok has helped me keep perspective, cope with life's difficulties, and navigate my mental health. and I appreciate the support of Carol and John Newman, Rob Borchert, and Rebecca and Eloise Newman, who have adopted me into their family and provided so much encouragement over the last three years.

My sister Shaylyn Berlew and brother-in-law Aaron Abel have been incredible sounding boards, meal providers, neighbors, cheerleaders, and role models as I navigated grad school. I cannot adequately put into words my gratitude for my parents, Rob and Kathleen Berlew, who encouraged me to pursue my interests in science from a young age, sacrificed comfort and free time to provide for our family, learned about cells and optogenetics with me, and never end a phone call without words of love and encouragement. I want to be just like them. Lastly, I am eternally grateful to my partner, Matt Newman, who has been full of support and encouragement through every step of this process. Matt has supported me through research setbacks and celebrated successes with me, taken care of household responsibilities to allow me to focus more on thesis work, encouraged me to take risks, and generally made my life so much more fun. I am so glad I did not have to do this without him.

ABSTRACT

SINGLE-COMPONENT OPTOGENETIC TOOLS FOR CYTOSKELETAL REARRANGEMENTS

Erin Berlew

Brian Y. Chow

The Rho family of small GTPases coordinate actin cytoskeletal rearrangements underlying crucial cell processes including migration and mechanotransduction. Dysregulation in these signaling pathways has been associated with neurodegenerative disease and cancer. Rho GTPase signaling is tightly controlled in space and time: GTPases are activated by guanine nucleotide exchange factors (GEFs) and inactivated by GTPase accelerating proteins (GAPs) at the plasma membrane. To study Rho GTPase signaling, several optogenetic tools have been developed, most of which use light to induce a protein-protein interaction, recruiting a GTPase-activating GEF to the plasma membrane. Other optogenetic strategies involve the use of single-chain photoswitches sterically occluding a constitutively active GTPase, which can result in undesirable high dark-state activity of the tool. We sought to create single-component optogenetic tools to perturb Rho GTPase signaling at the GTPase, GEF, and GAP level, resulting in lower dark state activity and easier implementation in mammalian systems.

In this work, we used BcLOV4, a fungal photoreceptor which directly binds membrane lipids in response to blue light inputs, to recruit Rho signaling proteins to the membrane, resulting in spatiotemporally precise signaling perturbation. We created BcLOV4 activation tools using the GTPase and GEF from the three best studied Rho

GTPase pathways: RhoA, which induces cell contraction through stress fiber formation; Rac1, which induces sheet-like lamellipodial protrusions; and Cdc42, which induces spiky filopodial protrusions. Notably, we demonstrated that the BcLOV4 system is compatible with wildtype GTPases, resulting in lower unintended pathway activation in the dark state. We also report progress toward the creation of RhoA termination tools using GAP domains and dominant-negative GTPases, allowing for the induction of signaling activation and termination on the same optogenetic platform. Using structural knowledge we gained from Rho GTPase tool development, we created a plasmid set and cloning workflow to simplify BcLOV4 tool engineering for other signaling targets. Together, the BcLOV4 optogenetic toolbox will further the study of Rho GTPase signaling and enable others to use this technology for single-component optogenetic membrane recruitment.

TABLE OF CONTENTS

LIST OF FIGURES

CHAPTER ONE: Background and Motivations

1.1 Rho-family GTPase signaling

1.1.1 GTPases as mediators of cytoskeletal rearrangements

To maintain their shape, adhere to substrates, respond to external mechanical stimuli, and migrate, cells must possess machinery to remodel the actin cytoskeleton with spatiotemporal precision (227). GTPases, or GTP-hydrolyzing proteins, act as molecular switches: in their active, GTP-bound state, they interact with downstream effectors to induce cell signaling events; GTP hydrolysis yields an inactive, GDP-bound state resulting in signaling termination (58). Two main types of GTPases exist in the cell. Gα domains interact with transmembrane G protein-coupled receptors (GPCRs) which associate with membrane receptors to control cyclic AMP (cAMP) and phosphatidylinositol signaling (257). Small GTPases, in contrast, are single-component proteins; while they can associate with membranes, they are not integral membrane proteins like their heterotrimeric counterparts. Five major families exist within the Ras superfamily of small GTPases: Ras, which regulates gene expression; Rab, which coordinates membrane trafficking; Arf, which is involved in vesicular transport; Ran, which plays a role in nuclear protein shuttling and microtubule rearrangements; and Rho, which regulates remodeling of the actin cytoskeleton (230). Rho GTPases play key roles in critical cell processes including morphology maintenance, migration, and proliferation (58). Accordingly, dysfunction or dysregulation in Rho GTPase signaling has been associated with neurodegenerative disease (77) and cancer (57).

Rho GTPases contain three main structural features: the G domain, the helical insert, and the C-terminal hypervariable region (213). The G domain is responsible for

nucleotide (GTP or GDP) binding. It consists of a six-stranded mixed β-sheet surrounded by five α-helices and contains five conserved structural motifs, designated G1 through G5. G1, also referred to as the P-loop, coordinates the β-phosphate of the bound nucleotide and a Mg^{2+} ion, which helps maintain the domain structure. G2 and G3 comprise two switch regions (switch I and switch II, respectively) which sense whether the domain is bound to GDP or GTP. Based on this determination, the switches drive a conformational change of the GTPase using a conserved “load-spring” mechanism, allowing the active GTPase to interact with downstream signaling partners (258). The insert region is located between the G4 and G5 motifs of the G domain and serves as a binding site for associated guanine nucleotide exchange factors (GEFs) and pathway effectors. Importantly, this insert determines which isoform-specific downstream binding interactions can occur, preventing unintended inter-pathway crosstalk from occurring (134). Finally, the variable C-terminus consists of about 10 amino acids which, with the insert region, help determine downstream interactions. This region often contains charged amino acids, allowing the GTPase to associate with charged lipid head groups, and a terminal CAAX box which can be modified with lipids, allowing for membrane association (236).

The best characterized members of the Rho GTPase family are RhoA, Cdc42, and Rac1, due to their roles in diverse cell processes (197) and interactions with over 60 downstream effectors (58). RhoA activates Rho-associated protein kinase (ROCK) and myosin light chain (MLC), leading to actin stress fiber formation and cell contraction (241). Cdc42 and Rac1 both play important roles in cell motility through actin polymerization and cell protrusion formation. Cdc42 activation results in the formation of filopodia, spiky membrane protrusions, through Wiscott-Aldrich Syndrome protein (WASp) and actin-related proteins complex (Arp2/3) (256). Rac1 induces the formation

of larger, veil-like lamellipodia through WASp-family verprolin-homologous (WAVE) and Arp2/3 (192). Together, these three Rho GTPases coordinate cell motility and cytoskeletal remodeling through spatiotemporally precise activation and inactivation. A variety of accessory proteins and mechanisms exist to maintain tight control over Rho GTPase signaling at the plasma membrane.

1.1.2 Spatiotemporal regulation of Rho-family GTPases

1.1.2.1 Guanine nucleotide exchange factors (GEFs)

GTPase activation (**Figure 1.1**) requires dissociation of bound GDP from its binding site so that a GTP molecule can replace it and induce an activity-conferring conformational change (23). Once this dissociation occurs, GTP quickly re-binds the GTPase due to its outnumbering of GDP in the cell by an order of magnitude (242), making GDP dissociation the rate-limiting step. If left to its own devices, GDP dissociation would occur too slowly for the rapid GTPase activation which is necessary for robust responses to speed the GTPase turnover process. The general GEF mechanism involves pulling GTPase switch I away the cellular environment. Thus, accessory proteins called guanine nucleotide exchange factors (GEFs) are necessary to speed the GTPase from the bound nucleotide, allowing it to undock from the protein. Once GDP leaves the binding site, the GTPase is unstable, so the GEF binds the switch II region, preventing the protein from unfolding and providing stability until a GTP molecule can enter and bind (38).

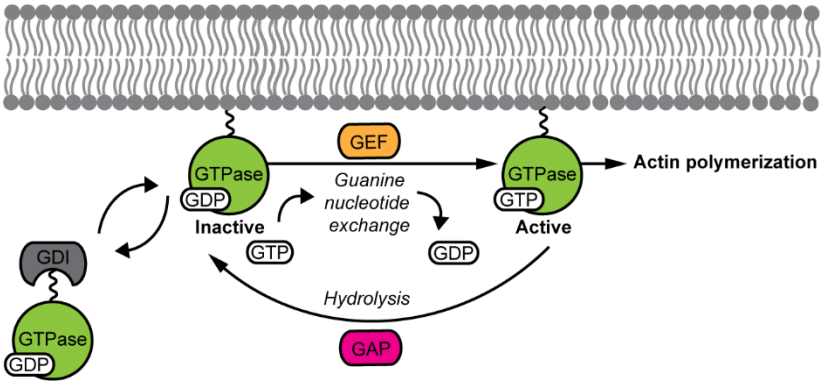

Figure 1.1 Overview of GTPase signaling

GTPases are inactive in their GDP-bound state. Guanine nucleotide exchange factors (GEFs) catalyze GTP loading and GTPase activation. GTPase accelerating proteins (GAPs) catalyze GTPase hydrolysis and inactivation. Guanine dissociation inhibitors (GDIs) bind the GTPase prenylation motif, keeping them in the inactive state.

This mechanism varies slightly between Rho GTPase-associated GEF (RhoGEF) families. For example, the PRONE (plant-specific ROP (Rho of plants) nucleotide exchange factor) GEFs predominate RhoGEF signaling in plants (168) and interact with two GTPases simultaneously. Mammalian GTPase signaling occurs with the help of two GEF families: dedicator of cytokinesis (DOCK) GEFs and Dbl homology/pleckstrin homology (DHPH) GEFs. In the DOCK family, each GEF contains two DOCK homology regions (DHRs). DHR-1 interacts with phospholipids, allowing the GEF to stably localize to the membrane, while DHR-2 acts as a GEF and interacts with the GTPase. DOCK GEFs interact with both Cdc42 and Rac1, differentiating between the two based on the identity of the fifty-sixth amino acid of the GTPases (129).

GEFs in the DHPH family, which is the focus of the GEF work in this thesis, contain a Dbl homology (DH) domain followed by a pleckstrin homology (PH) domain. Like the DOCK family, the DHPH family separates membrane association and GTPase binding responsibilities between two protein domains. DH domains contain 10-15 helices comprising three core (CR) regions. CR1 and CR3 interact with switch I of the

associated GTPase, with switch II residing in the DH hydrophobic cleft. These interactions allow the bound GDP to leave the GTPase core and stabilize the GTPase until GTP binding can occur. PH domains interact with membrane lipids to serve as a membrane anchor (207), keeping the GEF in the two-dimensional plane of the membrane with which the GTPase is associated. For DHPH GEFs interacting with the major Rho GTPases, some GEFs are specific to one GTPase, like Tiam1 (100) and ARHGEF11 (108), which activate Rac1 and RhoA, respectively. Others exhibit broader interactions, activating two or all three major Rho GTPases (170). GEF-GTPase specificity is thought to be mediated by residues on DH domain helices 4 and 5; mutation of these residues has been shown to alter GEF interaction profiles (37).

1.1.2.2 GTPase activating/accelerating proteins (GAPs)

GAPs, or GTPase activating/accelerating proteins, serve as the inactivation counterparts to GEFs, catalyzing GTP hydrolysis resulting in GTPase signaling termination (236). GAP domains function by stabilizing the transition state as GTP is hydrolyzed by water in a nucleophilic attack. Specifically, a conserved arginine finger found in all GAPs interacts with a conserved glutamine residue on switch II of the GTPase, orienting the GTP so that its γ-phosphate can be hydrolyzed (38). Notably, this GTPase glutamine residue can be mutated, resulting in a constitutively active (i.e., permanently GTP-bound) GTPase which is unresponsive to GAP-mediated inactivation. Structurally, GAPs are less evolutionarily conserved than GEFs, with mechanistic specifics varying from family to family (31). Like GEFs, GAPs also often contain additional domains beyond the catalytic GAP domain to regulate protein interactions and subcellular localization. For example, N-terminal BAR (Bin, Amphiphysen, Rvs) (8) and CRAL-TRIO (cellular retinaldehyde-binding protein and TRIO-GEF) (183) domains found

in RhoA-inactivating ARHGAP29 and ARHGAP1, respectively, allow the proteins to bind membranes via lipid binding pockets.

Another similarity between RhoGEFs and Rho GTPase-associated GAPs (RhoGAPs) lies in their specificity: some GAPs only interact with one GTPase, while others can inactivate more than one. GAP specificity is thought to be mediated by their co-localization with GTPases: expression of each GAP is not ubiquitous, with preferential GAP expression varying across tissues, cells, and subcellular zones (235). Thus, RhoGAPs may exhibit in vitro interactions with GTPases with which they do not interact in a physiologically meaningful way. Mechanisms of GAP regulation are varied and not fully understood. Crosstalk between Rho GTPase signaling pathways may allow for persistent GTPase signaling by preventing premature termination by GAP inhibition (266). Interestingly, an example of a mechanotransductive feedback loop was recently discovered in which GAP expression is turned on in response to an increase in RhoA-mediated stress fibers to prevent over-rigidification of the cytoskeleton (157). Recent interactome analysis has also shown evidence for auto-inhibition by GAPs (170). Further investigation into these various potential mechanisms of GAP regulation requires additional methods for GTPase and GAP signaling perturbation within the cell.

1.1.2.3 Guanine dissociation inhibitors (GDIs)

In addition to activating GEFs and inactivating GAPs, GTPases also rely on guanine dissociation inhibitors (GDIs) to keep GTPases in the off state, preventing spurious signaling activation. The structure of GDIs allows them to accomplish this goal through several mechanisms. First, GDIs contain a C-terminal domain with a geranylgeranyl pocket lined with hydrophobic amino acids. The GTPase prenylation motif can be inserted into this pocket, shielding the C-terminus from membrane

incorporation and sequestering the GTPase in the cytosol (38). This process alters GDI folding so that the GDI N-terminal regulatory domain can interact with GTPase switches I and II, preventing the conformational change associated with GTP binding from occurring (145). Thus, this binding event both removes the GTPase from its active location in the cell and prevents re-activation through locking the protein in its off state. In addition, GDIs have also been shown to prevent depletion of available Rho GTPase populations in the cell by stabilizing inactive GTPases and preventing them from being degraded by cytosolic protein complexes (24). When more GTPase is needed at the membrane, GDI removal and GTPase membrane translocation can occur (65).

Several factors may play roles in GDI removal. Ezrin-Radixin-Moeisin (ERM)-family proteins may bind to the GDI and act as GDI dissociation factors, causing the GTPase to be released and insert into the membrane (153), where GEF activation can occur. There is also evidence for cooperativity between membrane lipids and activating GEFs (203) in removing the GDI from the prenylation motif, and of GDI phosphorylation by Pak1 kinase (50), resulting in GTPase release. The Rho family of small GTPases interacts with three RhoGDIs: RhoGDI1, which has high affinity for several Rho GTPases, including RhoA, Rac1, and Cdc42 in most cell types (24); RhoGDI2, which exhibits similar broad activity but is limited to expression in hematopoetic cells (80); and RhoGDI3, predominantly interacts with lesser-studied Rho GTPases RhoB and RhoG (26).

1.2 Optogenetic strategies for membrane recruitment of proteins

1.2.1 The plasma membrane as a signaling hub

Beyond cytoskeletal remodeling, many cellular phenomena are coordinated at least in part at the plasma membrane, including cell-cell communication, vesicular

transport, and cell growth and division (79). At the membrane, signaling events are tightly controlled in space and time; thus, studying these pathways using global approaches without spatial targeting is often sub-optimal. For example, pathway knock-down by drug treatment lacks temporal precision as the experiment relies upon the timelines of cellular drug uptake and washout. Genetic targeting approaches like overexpression of a protein of interest or gene knockout affect the whole cell, in contrast to endogenous signaling events, which often occur asymmetrically (210). To establish better spatiotemporal control over cell signaling, optogenetic tools have been engineered to recruit proteins of interest (POIs) to the membrane in response to light inputs that can be programmed precisely in space and time. Through the engineering of natural photoreceptors which endogenously exhibit light-induced conformational changes, several platforms have been developed to recruit POIs to the membrane to perturb cell physiology and study cell signaling (87). Three well-studied approaches to optogenetic membrane recruitment are single-chain photoswitching, light-induced heterodimerization, and light-induced protein clustering.

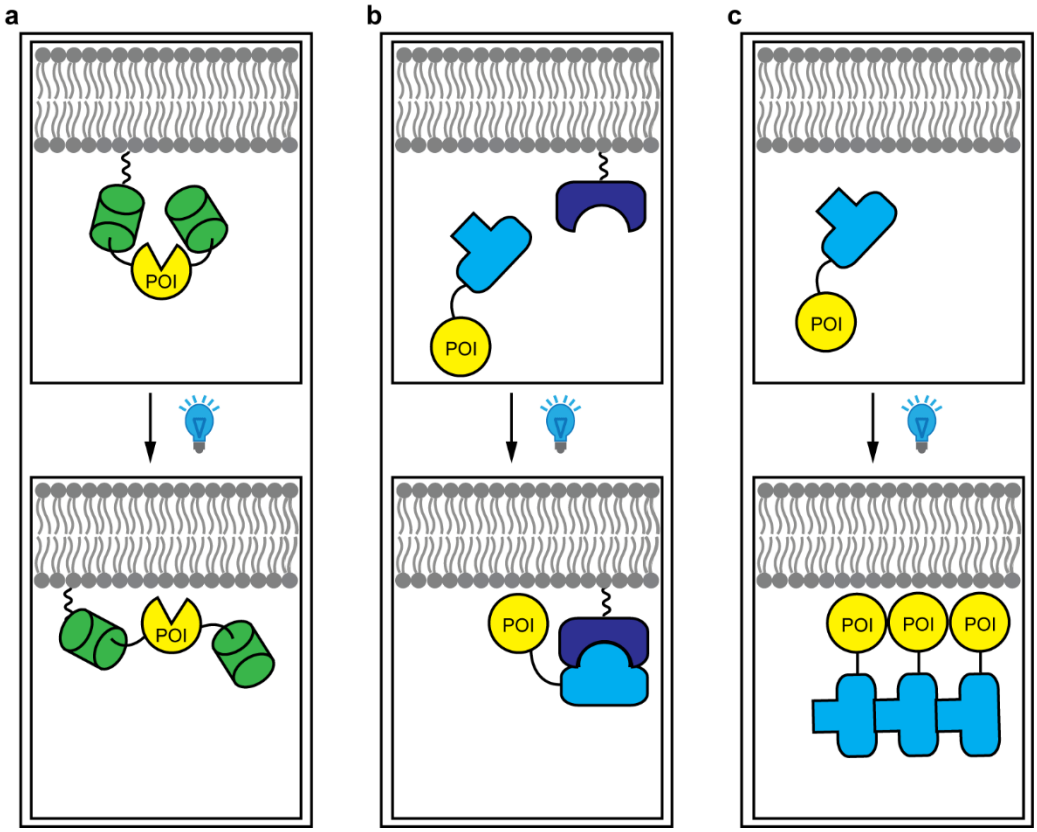

Figure 1.2 Optogenetic tool mechanisms for membrane recruitment

a. Single-chain photoswitching. **b**. Photoinducible heterodimerization. **c**. Light-induced protein clustering.

1.2.2 Single-chain photoswitching

One approach to membrane recruitment of POIs is to fuse the POI to a single-chain photoreceptor and couple the light-induced conformational change to solvent exposure of a POI site which binds a membrane partner. Thus, in the dark state, the POI remains sequestered in the cytosol because its binding site is sterically occluded by the photoreceptor; in the illuminated state, the binding site is exposed and the protein can activate downstream signaling through diffusive contact with the membrane. While this engineering strategy presents the genetic payload advantage of only needing to express a single protein for pathway perturbation, single-component photoswitching tools can be

difficult to engineer as total binding site occlusion is required to ensure no dark state activity occurs, and more extreme measures may be required during experimentation to prevent premature light exposure and pathway turn-on (262).

1.2.2.1 Dronpa

One class of single-chain optogenetic recruitment tools is based on Dronpa, a 29 kDa green fluorescent protein (GFP) with dual light responses: fluorescence turns on in response to UV (390 nm) light and turns off in response to cyan (490 nm) light (5). Mechanistic insight into Dronpa photoswitching suggests that UV light may induce a structural rearrangement promoting multimerization of the protein and fluorescence via endogenous amino acids rather than additional cofactors (274), while cyan light induces monomerization and fluorescence extinction. Dronpa photoswitching is rapid, with association and dissociation of monomers occurring within seconds of light exposure (84). This protein can be engineered as an optogenetic tool by fusing POIs to Dronpa monomers, which then aggregate and disaggregate in response to light cues (275). One early use case involved the creation of a light-inducible protease, in which Dronpa-protease fusions were active in their monomeric, cyan-illuminated state and inactivated upon UV-induced oligomerization. A membrane recruitment system was also engineered by encoding a Cdc42 GEF sandwiched between two Dronpa monomers. Oligomerization resulted in occlusion of the GTPase-interacting site on the GEF, while cyan-triggered monomerization resulted in binding site exposure and Cdc42 activation at the membrane (275).

1.2.2.2 AsLOV2

Another class of single-chain tools was engineered from AsLOV2, the sensor domain from *Avena sativa* phototropin I (209). Like other light-oxygen-voltage (LOV) domains, AsLOV2 undergoes a blue light-induced conformational change in which the interaction between its Jα helix and a β-sheet is disrupted. In LOV-containing proteins, this conformational change is transmitted to a fused C-terminal effector domain, resulting in signaling activation (88, 89). This natural signaling mechanism can be used to create single-component optogenetic tools by fusing POIs to the LOV C-terminal Jα helix. With engineering, the POI active site is occluded by the LOV in the dark state and exposed in the lit state, allowing it to interact with downstream signaling partners. This technology was used to engineer an optogenetic Rac1 tool in which a permanently GTP-bound Rac1 GTPase was fused to AsLOV2; blue light induced membrane contact between Rac1 and downstream effector WAVE, resulting in the formation of sheetlike lamellipodia (261). AsLOV2 was also used to create a light-inducible nuclear export system, in which the POI initially expressed in the cell nucleus due to an exposed nuclear localization signal (NLS) in the photoreceptor dark state. Illumination resulted in exposure of a previously occluded nuclear export signal (NES), resulting in POI export from the nucleus to the cytosol (179). A similar platform was used to engineer an optogenetic protease system using an analogous LOV domain from *Arabidopsis thaliana* (200).

1.2.3 Heterodimer association

As demonstrated with Dronpa and AsLOV2, a powerful strategy for optogenetic membrane recruitment is to pair the light-induced conformational change of a natural photoreceptor to a change in protein binding ability. Heterodimer association uses similar logic: in its illuminated state, the photoreceptor can bind to a partner with much

higher affinity than in its dark state. By fusing POIs to one or both components, one can design a system in which proteins interact only in the presence of light (122). In the context of membrane association and GTPase signaling, this technology can be used to recruit POIs to a subcellular location like the plasma membrane by fusing one of the heterodimerizers to the membrane by prenylation or fusion to a membrane-anchored protein (208). The POI can then be fused to the cytosolic component; light-triggered dimerization then results in membrane recruitment of the POI. As discussed in this section, photoreceptors that heterodimerize can either be found in nature or engineered by screening for protein-peptide interactions with known photoreceptors.

Though widely used, this membrane recruitment strategy presents issues in the areas of genetic and optical bandwidth. Use of a heterodimerization pair requires encoding two proteins for one functional tool system, an increased genetic payload for the cell. Characterization of co-transfection conditions and system component stoichiometry may also be required for optimal signal. In addition, this strategy also requires the use of two optical channels to confirm plasmid transfection, limiting the number of optical channels available to visualize other cellular proteins or structures.

1.2.3.1 Tunable light-induced dimerization tags (TULIPs)

Several heterodimerization systems have been created by engineering AsLOV2 (or another LOV domain) to bind a second protein only in its blue light-illuminated state. In the tunable light-induced dimerization tag (TULIP) system, a peptide called LOVpep is fused C-terminally to the Jα helix of AsLOV2. In the protein dark state, this epitope is sterically caged within the LOV core; blue light triggers its release, allowing it to bind an engineered Erbin PDZ (ePDZ) domain, which clamps onto the LOVpep like a clamshell. This binding brings any proteins fused to AsLOV2 or ePDZ into close proximity (225).

Advantages of this system include its relatively small protein size (AsLOV2 is 17 kDa; ePDZ is 23 kDa) and its rapid kinetics (1.3 s association; 53 s dissociation) (85). As its name suggests, the binding affinities in this system are tunable; LOVpep and ePDZ can be modified to exhibit binding affinities over several orders of magnitude (225).

This system can be modified to target POIs to subcellular localizations by fusing AsLOV2 to the membrane of interest using prenyl moieties and fusing the POI to be recruited to the cytosolic ePDZ domain. Examples of this application include in the recruitment of MAP kinase signaling proteins to the membrane in yeast cells, resulting in inducible cell polarization and budding (225). A TULIP system was also developed to control RhoA signaling by fusing a RhoGEF to the ePDZ domain and the LOVpep to the plasma membrane (34). In addition, TULIPs were used to re-position organelles by fusing system components to mitochondrial or endosomal membranes and motor proteins (250). Though these examples demonstrate the versatility of this optogenetic system, TULIPS are associated with higher dark-state activity ("leakiness") and lower light responsivity than other heterodimerization systems like Phy/PIF (discussed in section 1.2.3.6) (185).

1.2.3.2 Improved light inducible dimerization system (iLID)

Like TULIPs, the improved light inducible dimerization (iLID) system uses an AsLOV2-epitope sensor to bind an accessory protein in response to blue light. The epitope in the iLID system is SsrA, a 7-amino acid peptide from *E. coli* which binds the SsbP protein in the AsLOV2 lit state when it is not sterically occluded by the LOV (81). This system also exhibits rapid association (τ_{on} = 5 s) and dissociation (τ_{off} = 53 s) kinetics (85) and has been used to control cell signaling at the membrane. Some salient examples include GEF domain membrane recruitment to drive cell migration (81, 180)

and calcium signaling (104), induction of receptor tyrosine kinase (RTK) signaling (99), and tracking the plus ends of microtubules (2). Further advancements have been reported to limit the diffusion of iLID along the two-dimensional surface of the membrane with the goal of improving resolution of iLID-based tools (174, 251).

1.2.3.3 FKF1:Gigantea

While TULIPs and iLID consist of a photoreceptor which has been engineered to bind a second protein, the FKF1:Gigantea is comprised of two natural heterodimerizers. FKF1 and Gigantea are dimerizing proteins from *Arabidopsis thaliana* whose interaction plays a role in the plant circadian rhythms and day length measurement (212). The photoreceptor in this system is FKF1, a LOV domain with an FMN cofactor whose blue light-induced conformational change allows it to bind Gigantea. This system has been used to control Rac1 signaling by recruiting a GEF to the membrane using a similar membrane fusion strategy as discussed before (267) and to induce gene expression by forming a transcription factor upon light-induced dimerization (29, 193). The FKF1:Gigantea system has significant downsides. First, the proteins are large—FKF1 is 68 kDa and Gigantea is 129 kDa, which is a high genetic payload for the targeted cells. This system also exhibits slow kinetics, with full association occurring within 30 minutes and dissociation taking over an hour. Thus, the FKF1:Gigantea optogenetic system is unsuitable for applications requiring fast on and off times, like cytoskeletal remodeling.

1.2.3.4 Magnets

Another LOV-based dimerization system uses two engineered isoforms of the LOV photoreceptor Vivid called Magnets which heterodimerize in their blue light-illuminated state via an electrostatic interaction. Association and dissociation in this

system are both rapid (τ_{on} = 1.5 s; τ_{off} = 6.8 seconds) (116), though the speed of Magnet dissociation could require higher light stimulation duty cycles to maintain protein-protein interaction. This system was used to recruit an SH2 domain to the membrane to control phosphoinositide production (116). Additionally, by fusing complementary protein pieces to each Magnet monomer, it is possible to reconstitute a functional protein in response to blue light, as demonstrated in light-inducible Cre recombinase (115) and CRISPR Cas-9 applications (178). While Magnets' small size (17 kDa each) initially appears to be an advantage from a genetic payload perspective, the initial reported system required concatemerization of the encoding DNA sequences, in which the transfected plasmid contained multiple Magnet genes in parallel, increasing the payload. This issue as well as the requirement of a low-temperature incubation step of Magnet-expressing cells prior to experimentation were resolved in a second-generation system, which was used for subcellular POI recruitment to endomembrane organelles for transport and metabolism applications (13).

1.2.3.5 Cryptochrome2

The optogenetic heterodimerization systems discussed up to this point have been based on LOV domains. The Cry2 heterodimerization system capitalizes on a natural light-induced binding interaction exhibited by cryptochrome2. Cryptochromes are flavin adenine dinucleotide (FAD) binding photoreceptor domains from plants and animals which play a physiological role in circadian rhythms (36). One of the cryptochrome blue light-inducible signaling modalities is through protein-protein interaction (277). As demonstrated in *Arabidopsis thaliana* cryptochrome AtCRY2, blue light induces a tertiary structure change, causing AtCRY2 to bind the cryptochrome-interacting basic-helix-loop-helix (CIB1) protein (143). This Cry2-CIB interaction has

been used to engineer optogenetic tools used to control protein dimerization and DNA recombination using Cre (120), gene expression (95), and subcellular localization (102). Advantages of this system include its rapid kinetics, with protein translocation in membrane recruitment systems occurring in under 10 seconds and dissociation within 5 minutes after the light stimulus is removed (120), and, like the LOV-based systems, its compatibility with heterologous expression in mammalian cells without the need for exogenous cofactor supplementation (146). In addition to the protein stoichiometry issue posed by all heterodimerization systems, cryptochromes also cluster in response to blue light, potentially confounding the light-induced dimerization response (27). Further engineering on Cry2 systems has been reported to improve the tool's dynamic range without significantly increasing protein size from the original 60 kDa and 20 kDa for Cry2 and CIB, respectively, as well as the creation of photocycle-tuned mutants for customizable association and dissociation timescales (233).

1.2.3.6 Phytochrome/PIF

Like the Cry2 system, the phytochrome optogenetic system also utilizes a natural light-induced photoreceptor binding interaction for subcellular recruitment of POIs. Phytochromes are plant photoreceptors from *Arabidopsis thaliana* which link environmental light input to physiological outputs including germination and flowering (105). Phytochrome B (PhyB, 108 kDa) exhibits light-dependent binding to phytochrome-interacting factor 6 (PIF6, 12 kDa) (196). Unlike LOV and cryptochromes, which are sensitive to one wavelength range of light for activation and rely on thermal reversion for return to the dark state, Phy/PIF pairs are bistable and exhibit conformational changes in response to two light colors: red (activation and onset of binding) and far-red (inactivation and dissolution of binding) (205). This difference in light response is due to

the phytochrome cofactor; unlike LOV and cryptochromes, phytochromes bind bilin, a linear tetrapyrrole. In response to red light (λ = 680 nm), a cis-trans isomerization event occurs, resulting in a conformational change. This new form of the protein can either thermally revert like LOV and cryptochromes back to its dark-adapted state or absorb far-red (λ = 720 nm) light and rapidly revert on the seconds timescale (119, 177). In the context of an optogenetic tool, this dual-state approach is incredibly powerful: by fusing POIs to PhyB and PIF, protein interactions can be turned on and off with spatiotemporal precision through the delivery of red or far-red light, respectively (139).

The PhyB optogenetic system has been used to control protein subcellular localization to induce cytoskeletal rearrangements (139), PI3K, and MAPK signaling events (238, 240). It has also been applied to the study of intracellular transport by controlling organelle positioning (3), and in an extracellular setting to cross-link substrate fibers and alter substrate stiffness (101). The PhyB system's use of red and far-red light makes it compatible with blue light-sensitive optogenetic tools, presenting the opportunity for multiplexed tool use in the same cell without spectral overlap. However, a downside lies in the system's use of a bilin cofactor: since cells do not produce phycocyanobilin (PCB) naturally, exogenous cofactor must either be added to cells prior to experimentation, or a PCB biosynthetic pathway must be co-expressed with the PhyB system (169, 244).

1.2.4 Clustering-based

As mentioned earlier, Cry2 exhibits two blue light responses: heterodimerization with binding partner CIB and oligomerization with itself, particularly in the absence of CIB (27). This oligomerization occurs rapidly (τ_{on} = 30 s), and clusters dissociate within 5 minutes. This clustering phenotype has been used to create optogenetic signaling tools

in the Wnt/β-catenin and RhoA pathways, the latter of which led to the discovery that GTPase clustering can result in activation (27) (see section 1.3.2). Later, this methodology was used to disrupt clathrin-dependent endocytosis and induce actin polymerization (232).

1.3 Existing optogenetic strategies for GTPase signaling perturbation

1.3.1 Activation by GEF recruitment

Because a major application of heterodimerization-based optogenetic tools is the control of POI subcellular localization, it is unsurprising that this approach has been applied to control GTPase signaling, whose activation relies upon membrane recruitment of GTPases and activating GEFs. The main strategy for optogenetic GEF tool engineering is to anchor one heterodimerizer to the plasma membrane through prenylation and to fuse the pathway-activating GEF to the other, resulting in cytosolic, inactive GEF in the dark state and GEF localized to the membrane in the illuminated state, where it can activate endogenous GTPase. For RhoA, existing GEF tools include LARG recruitment using an AsLOV2-derived heterodimerization system (90), PR_GEF recruitment using TULIPs (254), and ARHGEF11 recruitment using Cry2/CIBN (249). Notably, the ARHGEF11 system recruited only the DH domain of the GEF, demonstrating that the PH domain is not necessary when another membrane association mechanism (i.e., protein heterodimerization-based recruitment) is implemented. For Rac1, the DH and PH domains of GEF Tiam1 were used to create tools using the iLID (81), Magnets (116), and Phy/Pif (139) platforms. For Cdc42, recruitment tools were engineered using the DH and PH domains of Intersectin1 and iLID (81), Phy/Pif (139), another phytochrome-derived system (113), and Cry2 (248).

In addition to demonstration of pathway activation, these GEF-based optogenetic tools also led to the development of Rho GTPase pathway quantification strategies including the use of biosensors to quantify activated GTPase before and after recruitment; the measurement of subcellular structures using actin visualization or membrane markers; the measurement of changes in cell morphology (centroid position, area, dimensions) or polarity; and demonstration of downstream pathway activation by measuring cell migration or effector concentrations using mass spectrometry or pulldown assays. While GEF recruitment is a well-characterized optogenetic strategy that results in GTPase activation, all existing systems are heterodimerization-based, which presents the implementation issues discussed earlier. In addition, recruiting a GEF to the membrane may result in less robust activation compared with other activation methods as it is inherently limited by GTPase concentration at the membrane.

1.3.2 Activation by GTPase clustering

As mentioned in section 1.2.4, the light-induced homo-oligomerization of Cry2 can be used to cluster and activate the GTPase RhoA. In this tool, Cry2 was fused to the wildtype RhoA GTPase. Blue light then induced clustering of Cry2-RhoA, particularly along the stress fibers of the actin cytoskeleton, leading to cell retraction. This clustering was reversible, with dissolution occurring within minutes following light stimulus withdrawal. Pathway activation was also confirmed with an ELISA assay to measure RhoA-GTP levels following photoactivation as well as by stress fiber visualization and intensity measurement (27). This engineering strategy was also used to create Cry2-Rac1, also using a wildtype GTPase; membrane recruitment of this tool resulted in lamellipodia formation and cell spreading. While this tool engineering strategy does not require the stoichiometric tuning or take up two optical channels as discussed with

heterodimerization systems, clusters can diffuse out of the stimulation region (as discussed in Chapter 3), resulting in lower spatial precision of pathway activation.

1.3.3 Activation by GTPase recruitment

Evidence that some GTPases translocate from the cytosol to the plasma membrane when activated or are constitutively localized near the plasma membrane (162) suggests that membrane recruitment of a GTPase should result in its activation by endogenous GEFs. Another strategy is to recruit a constitutively active (i.e., GEF-independent) GTPase whose activation does not rely upon endogenous GEFs. This strategy was first demonstrated with the creation of photoactivatable Rac1 (PA-Rac1) (261), using an engineered AsLOV2 bound to constitutively active Rac1. In the dark state, the WAVE binding site of Rac1 was designed to be occluded by AsLOV2 to prevent dark-state membrane association and downstream signaling activation by PA-Rac1; the blue light-induced conformational change would allow for Rac1 diffusion to the membrane and pathway activation. Light-induced activation of this tool was confirmed by observed membrane extension and pharmacological Rac1 pathway inhibitors as mechanistic controls; a biosensor-measured decrease in RhoA activation, suggesting that Rac1-RhoA push-pull regulation (176) was indeed occurring as a consequence of tool-mediated pathway activation. As discussed earlier, this system is associated with dark-state leakiness and the requirement for stringent pre-experimentation dark conditions to prevent transient pathway activation (262).

A Cry2-based Cdc42 recruitment system was later reported, with signaling activation occurring with both wildtype and constitutively active Cdc42 tool variants. Recruitment of either tool to the yeast membrane resulted in Cdc42-WASp interaction; the system was used to measure the effects of different spatial signaling organization

schemes in yeast (133). Tool function was characterized by measuring localizations and intensities of downstream and interacting proteins, as well as measuring changes in cell dimensions. This successful use of a wildtype GTPase in a membrane recruitment system suggests that endogenous GEFs are sufficient to activate recruited GTPase and that GTPase recruitment tools deserve further exploration and engineering.

1.3.4 Inactivation by GAP recruitment

To fully understand the dynamics of cell signaling, our optogenetic tool suite must contain signaling termination tools in addition to activation tools. Thus, one strategy of terminating GTPase signaling with spatiotemporal precision is the creation of optogenetic GAP recruitment systems to terminate signaling for endogenous GTPases. This strategy was used successfully in heterotrimeric G protein signaling by recruiting the regulator of G protein signaling (RGS, a GAP subtype) domain to the membrane (86). Termination of GPCR signaling was measured by quantifying cellular Ca^{2+} concentrations using a genetically encoded calcium sensor. Recently, a Cry2-based system was reported for the recruitment of RhoGAP71E to the inner leaflet. This tool was used to control actomyosin contractility in *Drosophila* embryogenesis (96), and tool function was confirmed by quantifying the amount and distribution of myosin as a result of downstream signaling, as well as cell morphology metrics like cell area and length. This initial successful GAP tool report bodes well for future engineering efforts to expand the repertoire of optogenetic GTPase termination tools.

1.4 Goal of the thesis

Optogenetic tools for perturbing Rho family GTPase signaling enable the study of crucial cellular phenomena like motility and division, the elucidation of mechanisms

underlying Rho dysfunction-associated disease, and the dissection of complex biological pathways in space and time. Current approaches to Rho tool development rely extensively on the use of heterodimerization pairs, which pose issues in implementation related to the use of two system components and the requirement of more than one optical channel to confirm tool expression; or on the use of constitutively active GTPases, which are often plagued with high dark-state activity and poor resolution. Additionally, there is a lack of focus on light-controlled signaling termination, a key piece of the Rho signaling integration puzzle.

The overarching goal of this thesis is to create a Rho-family optogenetic tool suite using a single-component membrane recruitment system to activate RhoA, Rac1, and Cdc42 using GTPase and GEF tools, as well as terminate RhoA signaling using a GAP or dominant negative GTPase tool. To accomplish this goal, I plan to use BcLOV4, a newly discovered natural fungal photoreceptor which binds directly to membrane lipid headgroups in response to blue light. Biophysical characterization of this protein is presented in Chapter 2 and was published in 2018 in the *Proceedings of the Natural Academy of Sciences* (69). Using BcLOV4, we engineered GTPase activation tools to recruit wildtype GTPase and GEF to the membrane for the three major Rho family GTPases. This work is presented in Chapters 3 and 4 and was published in *Advanced Biology* (RhoA, 2021 (16)) and *Photochemical and Photobiological Sciences* (Rac1, 2020 (17)). Work toward the creation of a RhoA signaling termination tool is presented in Chapter 5. Finally, to provide a workflow for future membrane pathway optogenetic tool engineering work, we elucidated some structural principles underpinning BcLOV4-POI fusion creation and created a plasmid set for facile fusion screening, presented in Chapter 6 and published in *ACS Synthetic Biology* (18). Together, the Rho GTPase toolbox and BcLOV4 characterization reported in this thesis will enable single-

component optogenetic control of important biological circuits and expand the utility of a new optogenetic membrane recruitment platform.

CHAPTER TWO: Biophysical characterization of BcLOV4 and CeRGS

This chapter adapts work from the following publication:

Glantz, S. T.; Berlew, E. E.; Jaber, Z.; Schuster, B. S.; Gardner, K. H.; Chow, B. Y., Directly light-regulated binding of RGS-LOV photoreceptors to anionic membrane phospholipids. *Proceedings of the National Academy of Sciences* 2018, 115 (33), E7720-E7727.

Author contributions: STG, EEB, ZJ, BSS, KHG, and BYC designed research; STG and EEB conducted all experiments; KHG and BYC coordinated all research; ZJ conducted in vitro experiments and bioinformatics; BSS conducted yeast and confocal imaging experiments; STG, EEB, Z.J., BSS, KHG, and BYC analyzed data; and STG, EEB, ZJ, BSS, KHG, and BYC wrote the paper.

2.1 Introduction

2.1.1 LOV proteins

LOV (light-oxygen-voltage-sensitive) protein domains play key roles in the ability of organisms to sense and respond to light and have served as starting points for the engineering of new optogenetic tools to perturb cellular physiology. LOVs are members of the Per-aryl hydrocarbon receptor nuclear translocator (ARNT)-Sim (PAS) superfamily of proteins and allow organisms in multiple kingdoms of life to sense blue light (45, 97, 127, 147, 277). Structurally, LOV proteins consist of a PAS fold made of a five-stranded antiparallel β sheet and several α helices. The core of the protein contains a

hydrophobic binding pocket which binds a flavin cofactor, either flavin mononucleotide (FMN) or flavin adenine dinucleotide (FAD). This binding pocket contains a conserved sequence GX(N/D)C(R/H)(F/I)L(Q/A), whose cysteine residue allows the LOV domain to undergo a light-induced conformational change resulting in signal transmission (71).

In photoreceptor proteins, LOV domains are paired with effectors of a range of functions, placing effector activity under light control. In the dark state, the flavin cofactor is non-covalently bound to the LOV protein and fully oxidized, with an absorption peak at 450 nm with vibronic structure at 425 and 475 nm (277, 278). Blue light absorption by the cofactor triggers the reversible formation of a covalent adduct between flavin and the catalytic cysteine residue of the LOV hydrophobic core, diminishing blue light absorbance and increasing UV absorbance at 390 nm. This photoadduct formation also results in conformational change of the protein, which transmits light input to a change in the biochemical activity of the paired effector (45, 60, 89, 97). Examples of LOV-mediated phenomena include circadian rhythms (103), virulence (228), phototropism (142), and stress responses (9).

In an engineering context, the modularity of LOV photoreceptors presents an opportunity to develop new gain-of-function tools by customizing the LOV-paired effector for light-inducible protein activity (165). Some examples of the utility of LOV proteins in optogenetics include bacterial LOV EL222, which was adapted to control cellular transcription (167); and photoswitchable AsLOV2 from *Avena sativa*, which has been applied to manipulate Rho-family GTPase signaling (225, 261). Uncovering new LOV-effector pairs allows for greater insight into light-sensing mechanisms in living organisms and for the development of new optogenetic tools.

2.1.2 The RGS-LOV protein class

The structural and mechanistic diversity of LOV-effector pairs presents a great opportunity to identify novel signal transmission mechanisms and new platforms for optogenetic tool engineering. One method by which to identify new LOV-effector combinations is through bioinformatic analysis of publicly available genomic sequence data. A 2016 analysis cataloged over 6700 LOV domains with over 100 combinatorial sensor-effector arrangements (69). Among the sensor-effector pairs identified were regulator of G-protein signaling (RGS)-LOV proteins. RGS proteins function as the fast terminators of heterotrimeric G-protein coupled receptor (GPCR) signaling, acting as the GTPase accelerating proteins (GAPs) for membrane-localized Gα protein partners (19, 98, 247). The existence of RGS-LOV proteins had previously been predicted by others (60, 61, 127, 216, 273), and some experimental evidence had been reported: genetic deletion of RGS-LOV proteins did not result in pronounced changes in phenotype or physiology (273), and RGS-LOV gene transcription was not regulated by light (217). Thus, experimental characterization of RGS-LOV light response in cells was required to confirm photosensory activity of the predicted LOV domain and establish its signal transduction mechanism.

Conserved domain analyses and secondary structure prediction (61, 127, 216, 273) of the 66 identified RGS-LOV proteins showed a low-complexity region and RGS domain located N-terminal to a single LOV domain, followed by a C-terminal domain of unknown function (DUF), connected to the LOV by a Jα-helical linker and an amphipathic helix (**Figure 2.1**). The Jα-helix linker and amphipathic helix have been identified as mediators of signal transmission in other LOV proteins (88, 89, 163). Initial screening experiments focused on five putative RGS-LOV proteins chosen for their short length (for ease of cell transfection and transduction) and/or previous research by others

into their hypothesized roles in the cell. Of these screened candidates, BcLOV4 from noble rot fungus *Botrytis cinerea* could be expressed and purified in the highest yield from *E. coli* and was subsequently used for further analysis.

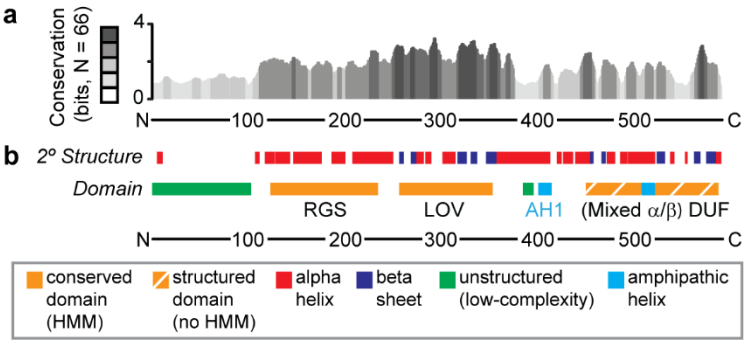

Figure 2.1 Bioinformatics annotation of RGS-LOV proteins

a. Secondary-structure conservation across 66 candidate RGS-LOV-DUF proteins, where height represents information content at a given position, in bits. Grayscale, bit score in fifths. **b**. Consensus secondary-structure prediction and domain architecture of BcLOV4, from JPred, phyre2, PSIPRED, and i-TASSER (secondary structures), IUPRED (disorder), Heliquest (amphipathic helices), and Pfam hidden Markov models database (domains, HMM = match in database).

2.1.3 BcLOV4 membrane translocation

Initial mammalian characterization experiments of BcLOV4 with a C-terminal mCherry visualization tag in HEK293T cells showed an interesting phenomenon. We observed that BcLOV4 was localized to the cytosol in its dark-adapted state and rapidly and reversibly localized to the plasma membrane in response to blue light stimulation. Membrane association and undocking kinetics measured by live-cell imaging were fast, with τ_{on} = 1.11 s and τ_{off} = 89.1 s, suggesting high affinity between BcLOV4 and its membrane target (69) (**Figure 2.2**). This phenomenon was not limited to HEK cells and has since been observed in HeLa, CHO, NIH 3T3, endothelial colony-forming cells, neurons, yeast, and zebrafish cells. It was also observed when the mCherry tag was

replaced with a 3xFLAG C-terminal peptide and protein was visualized by immunostaining.

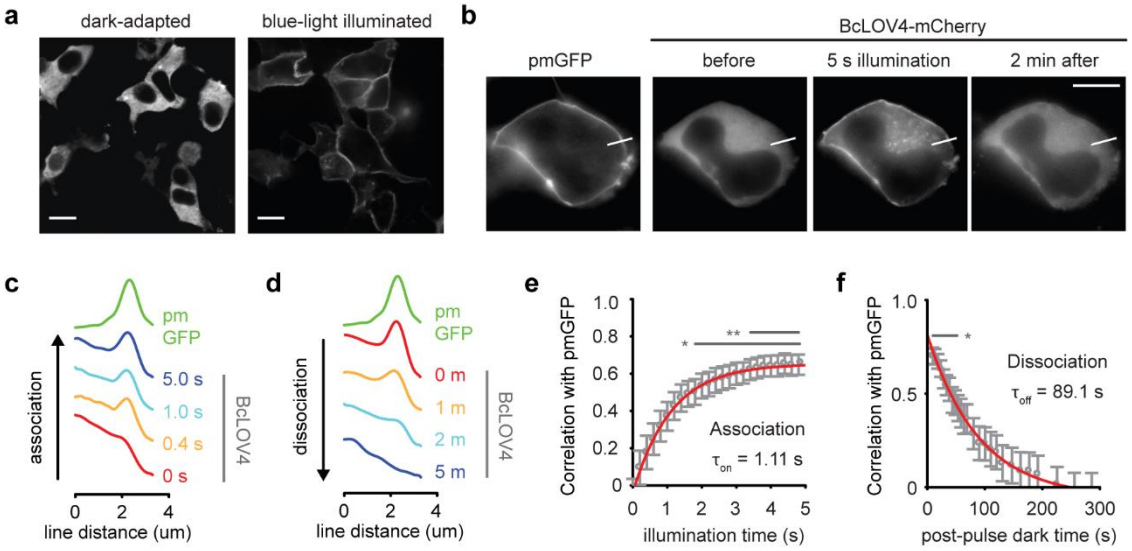

Figure 2.2 Light-activated membrane localization of BcLOV4 in HEK cells

a. Spinning-disk confocal fluorescence micrographs of BcLOV4 show it is cytosolic in the dark and translocates to the plasma membrane in blue light. Cells were fixed with paraformaldehyde in the dark or under blue light, and stained with Alexa Fluor 488-conjugated anti-3×FLAG antibody. Scale = 10 μm. **b**. Example single cell for quantitative membrane localization analysis. pmGFP, isoprenylated GFP marker. Line section for (c). Scale = 10 μm. **c**. Line section profiles of pmGFP and BcLOV4-mCherry from cell in (b). Association, during 5-s illumination. **d**. Same as (c) for dissociation (dissociation, dark after 5-s illumination). **e**. Population analysis of translocation kinetics. Time constants were statistically determined by correlation analysis between the membrane marker and BcLOV4 line section profiles, for similarity (τ_{on} = 1.11 s; 95% CI, 1.05–1.18 s). N = 30 cells, (*) $p < 0.05$, (**) $p < 0.01$. **f**. Same as (e), for membrane dissociation. Time constants were also statistically determined by correlation analysis, for dissimilarity (τ_{off} = 89.1 s; 95% CI, 83.0–96.3 s).

Our hypothesis for why BcLOV4 bound the membrane in its lit state was that BcLOV4 was interacting directly with membrane lipids via a polybasic amphipathic helix (residues 403-416) fused to the signal-transmitting Jα helix. The helix's high concentration of positively charged amino acid residues (sequence TSFFKSFKKYK) could bind the high concentration of negatively charged lipid head groups of the plasma membrane via an electrostatic interaction. Implicating this helix in BcLOV4 membrane

binding involved characterization of BcLOV4's in vitro responses to light and its interactions with membrane-like surfaces of controlled charge composition.

2.1.4 Problem statement

Light-inducible plasma membrane binding has not previously been reported in natural LOV proteins, though engineered LOV-lipid binding was achieved using AsLOV2 and polybasic domains (91, 149). The novelty of this mechanism led us to attempt to understand protein biophysics underlying protein-membrane association and determine which protein substructure interacted with lipid in the lit state. Beyond the photobiological insight this biophysical characterization could provide, there is also great bioengineering potential. Inducible membrane translocation is an attractive property in optogenetic tool development; several tool platforms exist using heterodimerization pairs to recruit proteins of interest to the plasma membrane. Understanding the biophysical basis of BcLOV4's light induced lipid binding may enable us to use its natural light response to engineer a new class of single-component optogenetic tools.

2.2 Results and discussion

2.2.1 BcLOV4 protein purification

Characterization of the biophysical properties of BcLOV4 requires the ability to grow and purify high-yield recombinant protein from bacteria. Early purification efforts demonstrated that BcLOV4 protein production is non-trivial; to maximize yield and prevent protein from crashing out of solution, high salt concentration and glycerol must be present from cell pellet lysis through elution of pure protein. We also found that a second protein species is present in significant yield in the overexpression lysate, ~10 kDa shorter in length than BcLOV4, likely the result of a N-terminal truncation event.

These observations led to the development of an expression and purification regimen for BcLOV4 to maximize the yield of full-length protein from bacterial overexpression.

Full expression and purification conditions can be found in section 2.4.2. Briefly, BL21(DE3) competent cells expressing His_6-BcLOV4 were grown to mid-log phase and protein expression was induced with IPTG. Temperature was reduced form 37°C to 18 °C and cells were grown for ~18 hours at 250 r.p.m. Cells were pelleted, frozen at -20 °C for at least one hour, resuspended in high-salt lysis buffer, and lysed via sonication. Clarified lysate was prepared for FPLC purification by pelleting the insoluble fraction from the sonication mixture. Both wash and elution buffers contained high (0.5 M) NaCl and 10% glycerol. Equilibration and wash steps were performed in 20 mM imidazole. Clarified lysate was loaded onto a 5 mL Ni-NTA column and washed for 15 column volumes. A gradient elution was then performed over 15 column volumes from 20-200 mM imidazole to elute the 10-kDa-truncated protein. Imidazole concentration was then raised stepwise to 500 mM, and full-length protein was collected in 2.0 mL fractions. Purified flavoprotein concentration was calculated using absorbance at 450 nm and the FMN extinction coefficient (εFMN450 = 12,500 M^{-1} cm^{-1}) and buffer-exchanged into phosphate-buffered saline (PBS) for further characterization.

2.2.2 Cofactor identification

Bioinformatics analysis predicts that BcLOV4 contains a LOV domain, meaning it would presumably bind flavin mononucleotide (FMN). Purified BcLOV4 had an optical absorbance peak at λ_{max} = 450 nm with triplet-peak fine structure indicative of a FMN cofactor. To confirm that BcLOV4 binds FMN, we purified BcLOV4 and extracted its cofactor by boiling it in 70% ethanol to precipitate the protein out of solution. The extracted cofactor was then analyzed using thin-layer chromatography (TLC) against

standard solutions of flavin family cofactors FMN, flavine adenine dinucleotide (FAD), and riboflavin. The BcLOV4 cofactor had an R_f value of 0.26 (70, Figure S2), which matched the R_f value for the FMN standard as well as the published FMN R_f value (41). Thus, the LOV domain of BcLOV4 binds FMN.

2.2.3 BcLOV4 responses to blue light

In mammalian cells, we observed that BcLOV4 translocates from the cytosol to the membrane in response to blue light stimulation. We sought to understand this phenomenon by characterizing BcLOV4's in vitro response to blue light. First, the time constants associated with flavin adduct formation in BcLOV4 were measured using UV-vis spectroscopy and exponential fitting. The triplet structure of the BcLOV4 spectrum disappeared within one second of blue light stimulation; thermal reversion kinetics were also rapid, with τ_{off} = 18.5 s (**Figure 2.3a-b**). It should be noted that acquisition of stable photocycle measurements for BcLOV4 required in vitro stabilization by high salinity in the protein buffer (0.5-1.0 M NaCl), with or without 10% glycerol, or the use of solid-phase supports like magnetic Ni-NTA beads to bind BcLOV4's N-terminal His_6 tag. In the absence of these supports, such as in PBS, BcLOV4 quickly aggregated following blue light exposure, forming a turbid solution. Dynamic light scattering (DLS) supported this reversible observed light-induced change in solution particle size, indicating that indicated that these protein aggregates were ~1 μm in diameter, compared to ~10 nm diameter dark-adapted protein. In the presence of stabilizing salt and glycerol, no significant change in particle size was observed by DLS in response to blue light (**Figure 2.3c**).

Mutating the cysteine residue (C292A) in the LOV domain of BcLOV4 canonically responsible for forming the flavin photoadduct (42) resulted in loss of photocycling, with

protein spectra resembling those of dark-adapted BcLOV4 even in the presence of blue light. Similar to other LOV proteins, the C258I mutation (45) in BcLOV4 resulted in a much longer in vitro tau off (586.5 sec), demonstrating that the thermal reversion of BcLOV4 following blue light exposure is kinetically tunable.

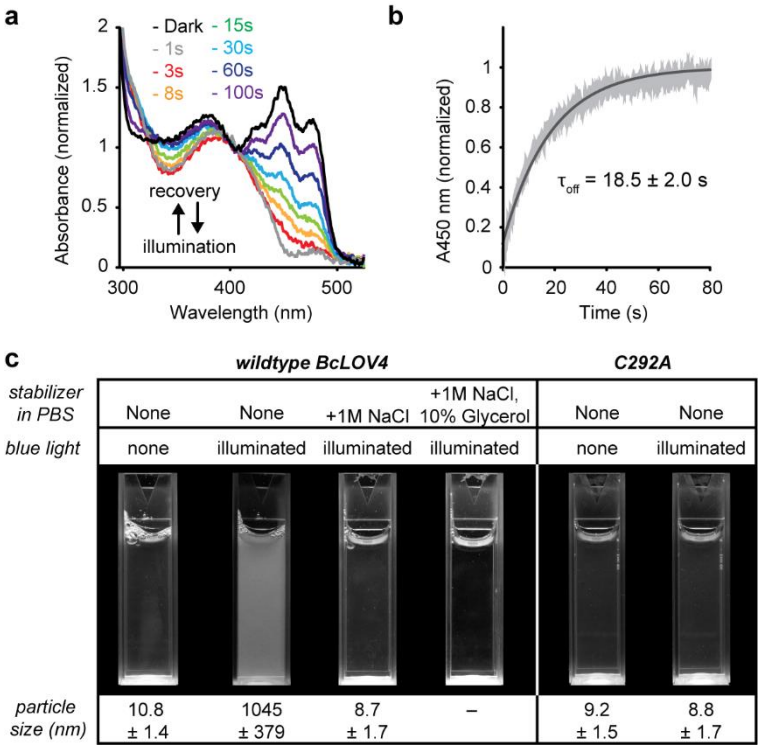

Figure 2.3 Photochemical competence of purified BcLOV4

a. Representative flavin photocycling of BcLOV4 stabilized by 1 M NaCl and 10% glycerol to prevent photoinduced aggregation, measured by absorbance spectroscopy. Illumination, 15 mW/cm^2; λ = 455 nm. Time indicates post-illumination recovery period. **b**. Recovery kinetics monitored at λ = 450-nm absorbance (A450). Black, exponential fit. Gray, mean ± SD (N = 3). **c**. In vitro aggregation of BcLOV4 in direct response to blue light. The C292A mutant is unable to form a covalent cysteinyl-flavin photoadduct and is thus photochemically inactive. Illuminated samples become turbid but can be stabilized by high-salinity and/or molecular crowding agents. Illumination, 15 mW/cm^2; λ = 455 nm. Particle size by DLS (mean ± SD).

2.2.4 BcLOV4 size estimation

SDS-PAGE and anti-His_6 Western blotting confirmed that gradient followed by step elution during FPLC purification resulted in only full-length BcLOV4 protein

(predicted molecular weight 67 kDa) in collected fractions (**Figure 2.4a-b**). To determine the oligomeric state of BcLOV4, size-exclusion chromatography with multi-angle light scattering (SEC-MALS) was performed on purified His_6-BcLOV4 (**Figure 2.4c**). The resulting spectra showed a large peak at 170 kDa, suggesting that BcLOV4 is a dimer/trimer mixture in its dark-adapted state.

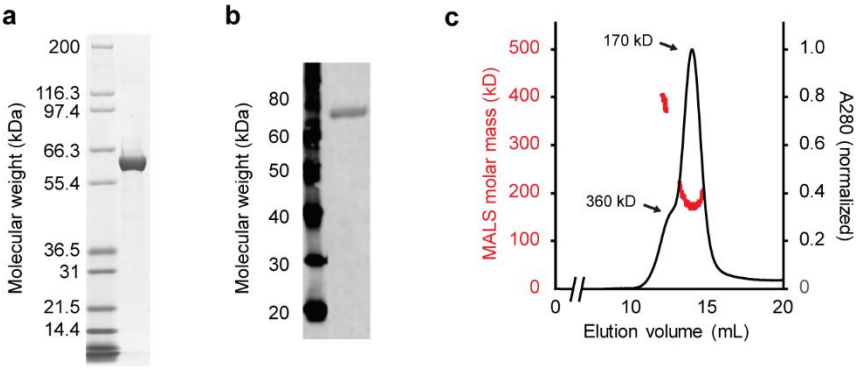

Figure 2.4 Size estimation of purified BcLOV4

a. BcLOV4 purity analysis by SDS-PAGE denaturing gel (left: Mark12 ladder, right: protein). The protein runs fast with respect to the Mark12 ladder. **b**. Molecular weight characterization by Western blot of His6-BcLOV4 (left: Magic Mark ladder, right: protein). Calculated molecular weight = 67 kDa including tag (left: Magic Mark XP ladder, right: protein). **c**. SEC-MALS analysis of FPLC-purified His6-tagged BcLOV4 is a dark-adapted oligomer (dimer/trimer mixture).

2.2.5 Characterization of protein-lipid interaction

To understand the mechanism of BcLOV4's light-induced membrane binding, protein-lipid overlay assays were first conducted to determine the specificity of BcLOV4's lipid binding. Initial screening with commercially available lipid strips showed that BcLOV4 bound anionic but not zwitterionic head groups. However, these strips present only immobilized lipid head groups rather than realistic membrane surfaces. To test for protein-lipid interaction with a more membrane-like target, we created droplets of water-in-oil emulsions to emulate the cytosol and plasma membrane inner leaflet and observed the localization pattern of BcLOV4 in response to blue light stimulation. Droplets

consisted of BcLOV4-mCherry in PBS in the dispersed/aqueous phase and phospholipid monolayers composed of zwitterionic phosphatidylcholine (PC, net charge 0) mixed with anionic phospholipids of varying concentration and headgroup charge density (**Figure 2.5a**).

We observed that in droplets containing 20% phosphatidylserine (PS, net charge -1), illuminated BcLOV4 was primarily localized to the phospholipid interface. This droplet composition mimics the mammalian cell inner leaflet, in which patches of anionic lipid head groups give the membrane a negative charge (121). In contrast, illuminated BcLOV4 droplets with 100% PC membranes aggregated in the aqueous phase, similar to the turbidity imaging of purified, lipid-free BcLOV4 following blue light exposure (**Figure 2.5b-c**). These results suggested that BcLOV4's light-induced membrane binding is the result of electrostatic interactions between the positively charged amphipathic helix and negatively charged membrane lipid head groups. Bolstering this electrostatic hypothesis is the observation that both protein aggregation and protein-lipid association diminished as salinity increased and Na+ and Cl- ions could interact with charged system components.

The photochemically inactive C292A mutant of BcLOV4 did not localize to the lipid monolayer in response to blue light stimulation, while the constitutively active Q355N mutant (63, 72, 173) persistently localizes to the lipid interface even prior to blue light stimulation when anionic phospholipids were present (**Figure 2.5d**). These results confirm that the LOV domain, rather than some unknown blue light-induced mechanism, mediates BcLOV4 lipid binding. Dissociation constants for BcLOV4 binding to immobilized liposomal bilayers were next measured by surface plasmon resonance (SPR). The measurements were made with the photochemically inactive C292A and constitutively active Q355N mutants since controlled illumination within the instrument

was not possible. BcLOV4-mCherry variants were used for SPR assays both to maintain consistency with droplet assays, and for improved solubility and protein yield. The BcLOV4 constitutively active mutant affinity for 20% PS liposomal bilayers was K_{dQ355N} = 130 nM, or > 20-fold enhanced versus the photochemically inactive mutant K_{dC292A} = 3.2 μM (**Figure 2.5d-e**). Thus, consistent with biophysical inferences from cellular kinetics, BcLOV4 indeed possesses a high-affinity light-switched interaction with anionic phospholipids. Binding increased with total anionic content (with PS), but there were minimal differences between phospholipids of different headgroup charge density under conditions of matching total charge (**Figure 2.5f-g**). Thus, BcLOV4 membrane binding is charge dependent but nonspecific to headgroup identity, unlike the well-established preference of pleckstrin homology (PH) domains for certain phosphatidylinositol phosphates (PIPs) (114) or similar lactadherin-C2 domain-specificity for PS's lipid binding (268).

2.2.6 BcLOV4 truncations and mutations

2.2.6.1 Amphipathic helix mutant

Having identified the light-switched interaction partner as an anionic phospholipid, we next sought to determine the protein binding site and focused on the polybasic amphipathic helix in the linker region that is largely conserved among the fungal homologs (AH1) (**Figure 2.6a**). In BcLOV4, this helix possesses a conserved "FKK" motif (residues 412–414) found in membrane-interacting amphipathic helices of Bcl-2–associated death promoter (BAD) (93), kinase suppressor of RAS (KSR) (6), and cecropin anti-microbial peptides (211), and a "FFK" sequence (residues 408–410) found at the membrane interface of the M2 proton channel of influenza A [Protein Data Bank ID code 2rlf]. In such motifs, aromatic side chains putatively insert into the phospholipid

bilayer, while the proximal lysine side chains electrostatically bind anionic lipids enriched in the inner leaflet without great headgroup specificity (54) (**Figure 2.6b**).

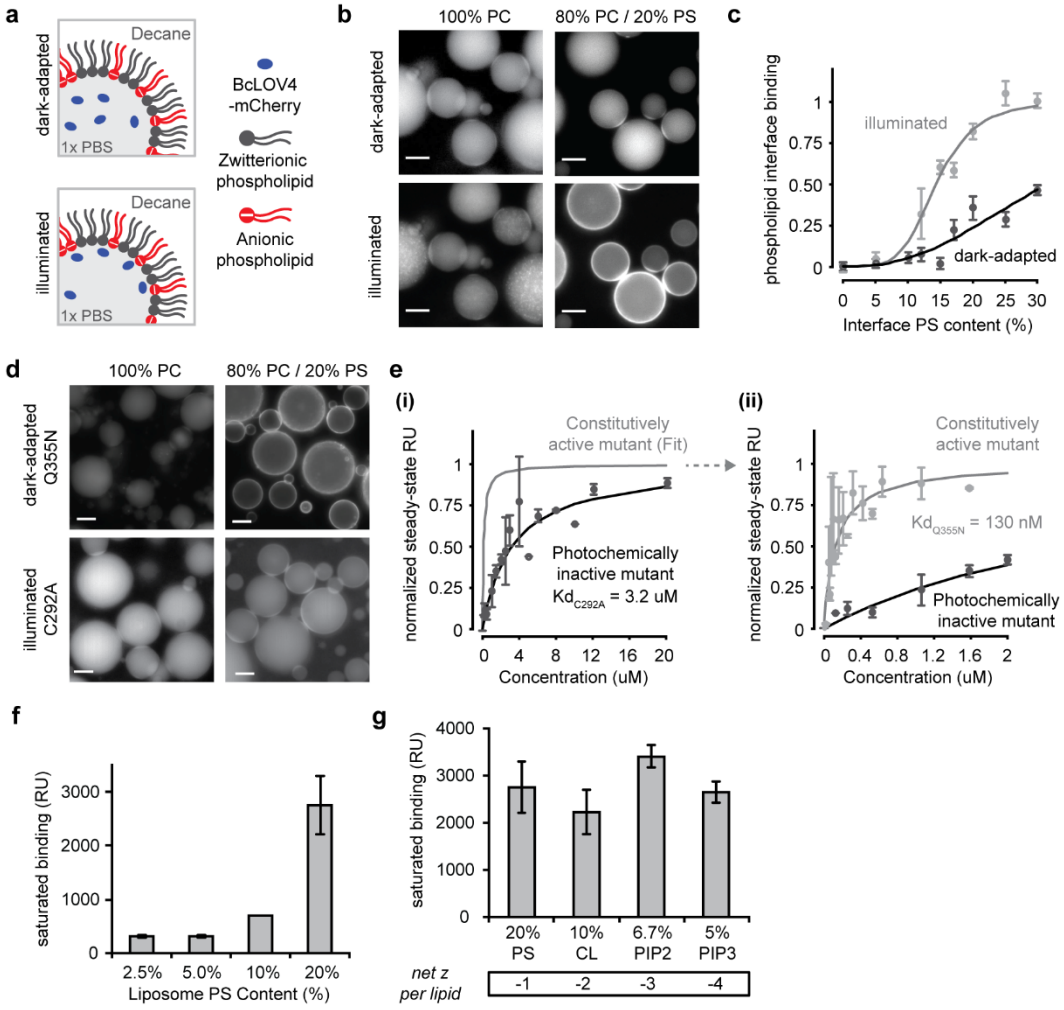

Figure 2.5 In vitro binding of BcLOV4 to anionic membrane lipids

a. Schematic of BcLOV4 in lipid-stabilized w/o emulsions. **b**. Fluorescence micrographs of wild-type BcLOV4 fused to mCherry. Translocation to the inner leaflet-like interface is observed with increasing anionic PS content, but not with purely zwitterionic PC interfaces. Scale = 25 μm. **c**. Phospholipid interface binding curves, calculated as the membrane interface:dispersed phase ratio (normalized) of BcLOV4 in the light and dark. N = 20-75 droplets; error, std err. **d**. Constitutively active BcLOV4 Q355N structurally mimics the photoactivated signaling state, is localized to the interface in the dark, and retains its preference for net anionic phospholipids over zwitterionic ones. The photochemically inactive C292A mutant cannot form a covalent cysteinyl-flavin photoadduct and remains in the aqueous dispersed phase even upon illumination. Scale = 25 μm. **e**. Affinity measures by SPR to 80% PC/20% PS mixed liposomal bilayers. The interaction with constitutively active BcLOV4 is high affinity (K_{dQ355N} = 130 ± 75 nM) and > 20-fold enhanced over the photochemically inactive mutant (K_{dC292A} = 3.2 ± 1.2 μM). (i) The 0–20 μM range, with fit only for constitutively active mutant for clarity, and (ii) 0–2 μM range. N = 2-7; mean ± SEM. **f**.

SPR measures of constitutively active mutant binding to mixed PC/PS liposomes of varying total anionic charge density. N = 3; mean ± SD. **g**. SPR binding assessments of constitutively active mutant to lipids of different headgroup charge density, in liposomes of matching total anionic charge density of 20% (N = 3; mean ± SD). (f) and (g): CL, cardiolipin; PC, phosphatidylcholine; PIP2, phosphatidylinositol-(4,5)-biphosphate; PIP3, phosphatidylinositol-(3,4,5)-triphosphate; PS, phosphatidylserine.

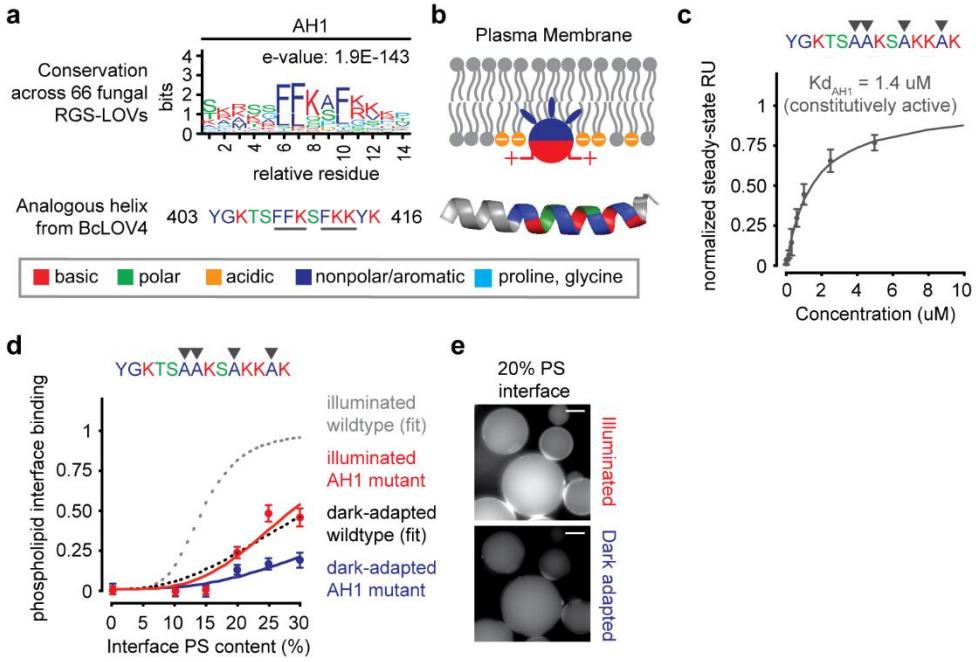

Figure 2.6 Structure-function determinants of BcLOV4-lipid interaction

a. Sequence logo of amphipathic helix (AH1) conserved among 66 RGS-LOV homologs (*top*) and the specific sequence for BcLOV4, which includes known lipid binding motifs (underlined) (*bottom*). **b**. Schematized membrane insertion mechanism of the AH1, where hydrophobic residues embed into the hydrophobic bilayer and basic residues electrostatically bind anionic phospholipids. **c**. SPR-determined affinity of AH1 mutant for 20% PS bilayers, with hydrophobic residues mutated to alanine, is reduced ~10-fold from wild-type BcLOV4. SPR data are of constitutively active Q355N mutant (N = 2; mean ± SD). **d**. Phospholipid interface binding curves, calculated as the membrane interface/dispersed phase ratio (normalized) of the AH1 mutant (no Q355N) when dark-adapted or illuminated with blue light in w/o emulsions, normalized to wild-type saturation level under illumination (N = 20-200 droplets; mean ± SEM). Dotted fits for perspective derived from Fig. 2.5. **e**. Representative fluorescence micrographs showing that the AH1 mutant primarily remains in the aqueous dispersed phase upon illumination. Scale = 25 μm.

Thus, candidate phenylalanine and tyrosine residues within this region were mutated to alanines. The BcLOV4-AH1 mutant (amphipathic helix mutant) photocycled similarly to wild-type protein. In SPR assays, the BcLOV4-AH1 constitutively active

mutant showed a 10-fold reduction in affinity, $K_{dAH1\text{-}Q355N}$ = 1.4 μM, for 20% PS liposomal bilayers (**Figure 2.6c**), providing evidence that light-induced exposure of the specific lipid-binding motifs drives membrane association. BcLOV4-AH1 also showed reduced binding to anionic phospholipids in droplets of w/o emulsions, and largely remained in the aqueous compartment/dispersed phase when illuminated with blue light (**Figure 2.6d-e**). The downward shift in the droplet-based phospholipid interface binding curves of the AH1 mutant from wild-type levels confirmed the direct lipid-binding roles of the aromatic side chains in the FKK and FFK motifs.

2.2.6.2 N-terminal truncations

In vitro truncation analyses were performed to establish the relative contributions of the N-terminal and C-terminal domains in signal transmission from the LOV blue light sensor to the lipid-binding regions (**Figure 2.7a**). mCherry-fused RGS-truncated BcLOV4Δ1–240, or "LOV-DUF," aggregated in the absence of lipids in the dark (particle size 32 ± 43 nm by DLS) and exhibited an upward shift in the phospholipid interface binding curve versus full-length protein, both as photochemically inactive mutants. Deletion of the unstructured N-terminus alone, BcLOV4Δ1–96, had no such effects (**Figure 2.7b**). These data suggest that, first, the RGS domain serves an inhibitory role when dark-adapted and, second, that the LOV-DUF alone is sufficient for membrane association.

2.2.6.3 C-terminal truncations

Removing the C-terminus of BcLOV4 proved more difficult. Several truncation locations were attempted, all of which resulted in low yields of misfolded flavoprotein with a spectral peak at 420 nm rather than the classical LOV λ_{max} at 450 nm and fine

triplet structure. Since attempts at purifying genetically encoded C-terminal truncations were unsuccessful, we next attempted to truncate folded, purified full-length protein. A factor Xa cleavage site (112) was inserted via site directed mutagenesis between the LOV and DUF domains of BcLOV4 (residues 420-423, V420I, I422G) and protein (BcLOV4-IEGR) was expressed, purified, and characterized to verify that the mutation did not affect the normal properties of BcLOV4. Protein was treated with ethylenediamine tetraacetic acid (EDTA) to chelate any nickel eluted from the FPLC column during protein purification, then buffer-exchanged into a lower-salt buffer (50 mM sodium phosphate, 300 mM sodium chloride) without glycerol so as not to interfere with the catalytic activity of Factor Xa. BcLOV4-IEGR was then bound to magnetic nickel beads and treated with Factor Xa to cleave off the C-terminus, leaving the N-terminus stabilized by solid-phase beads to prevent misfolding.

We next wanted to determine whether C-terminally truncated protein was able to photocycle. Since the magnetic nickel beads are incompatible with measuring absorbance, the on-bead fluorescence photocycle was then measured. In response to blue light, LOV fluorescence initially dropped for the cleaved protein, followed by a "runaway" fluorescence trace which continued to increase over several minutes (**Figure 2.7c**). This increase in fluorescence in response to blue light resembled the aggregation response of full-length BcLOV4 in PBS following blue light exposure, suggesting protein instability following removal of the C-terminus. Following the photocycle assay, truncated protein was eluted from the beads with concentrated urea and fragment sizes were analyzed via SDS-PAGE. Multiple bands were present at the expected molecular weight of the truncated protein, which indicated that Factor Xa cleavage was non-specific and incomplete. While no soluble C-terminal truncations of purified BcLOV4 could be

stabilized, these results suggest that the C-terminus of BcLOV4 plays a role in the stability of protein folding and flavin incorporation.

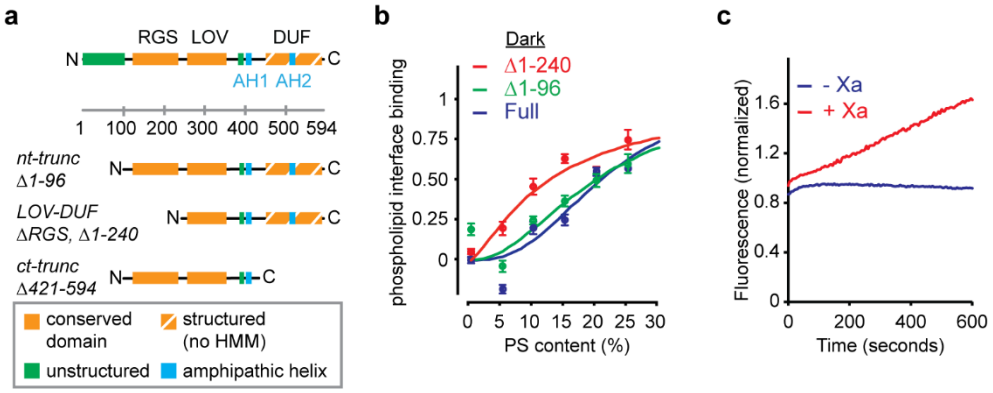

Figure 2.7 BcLOV4 truncation characterization

a. Truncations created to probe domain contributions to light-switched membrane association. HMM, existing hidden Markov model. **b**. Phospholipid interface binding curves, calculated as the membrane interface/dispersed phase ratio (normalized) of BcLOV4, N-terminally truncated protein, and RGS-truncated LOV-DUF, in w/o emulsions and in the absence of illumination. Increased binding by deletion of the RGS suggests that the RGS domain inhibits the membrane interaction in the absence of illumination. Normalized to wild-type saturation level under illumination. N = 30-125 droplets; mean ± SEM. **c**. Recovery kinetics monitored by flavin fluorescence of cleaved and un-cleaved BcLOV4-IEGR bound to magnetic anti-His beads. Illumination, 15 mW/cm^2; λ = 455 nm, 30 seconds prior to monitoring. Fluorescence is normalized to pre-illumination measurement.

2.2.7 CeRGS characterization

To determine whether the light-induced lipid binding properties observed for BcLOV4 were generalizable to the larger RGS-LOV class of proteins, we next performed biophysical and mammalian characterization assays on CeRGS, a homolog from the black yeast *Cyphellophora europaea* (GenBank accession number ETN36999.1). His$_6$-tagged CeRGS was purified using the same protocol as BcLOV4. SDS-PAGE showed a molecular weight of ~70 kDa, consistent with the predicted protein size (**Figure 2.8a**). Purified protein was yellow in color and UV-vis spectroscopy showed the characteristic flavin triplet peak centered at 447 nm, confirming cofactor incorporation (**Figure 2.8b**). In vitro photocycle was measured by recording the protein's absorbance at 450 nm before and after a 5-second pulse of blue light. Exponential fit gave a τ_{off} value of 139.2 ± 19.0 s, much longer than the measured in vitro τ_{off} for BcLOV4 of 18.5 s (**Figure 2.8c**). This

longer observed thermal reversion timescale for purified CeRGS even in the absence of a lipid binding partner suggests structural differences between CeRGS and BcLOV4 resulting in different photocycle kinetics. Dynamic light scattering in dark-adapted and blue light-illuminated states were similar to those observed for BcLOV4: in phosphate-buffered saline, mean particle size for CeRGS in its dark state was 11.8 ± 1.1 nm, which increased to 658 ± 11 nm under blue light. No appreciable increase in protein size was observed when the assay was conducted in 1 M NaCl (**Figure 2.8d**).

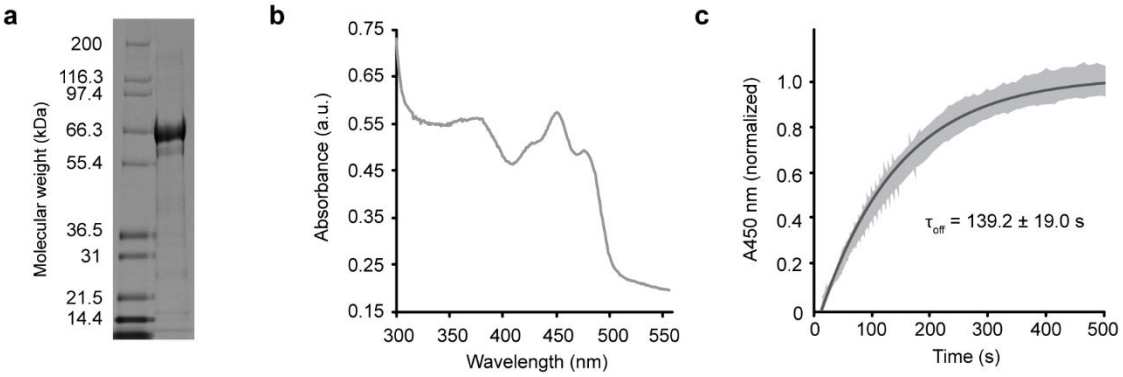

d

condition	mean particle size (nm, ± s.d.) 1x PBS	1000 mM NaCl
dark adapted	11.8 ± 1.1	11.0 ± 1.0
illuminated	656 ± 11	12.2 + 0.4

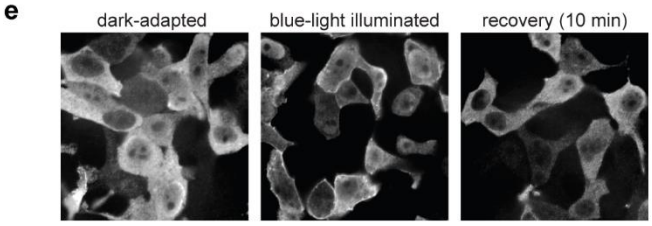

Figure 2.8 Characterization of CeRGS in vitro and in mammalian cells

CeRGS recapitulates the in vitro photo-aggregation and light-dependent membrane localization observed with BcLOV4, confirming the generality of the phenomenon amongst RGS-LOV proteins. **a**. SDS-PAGE denaturing gel of purified CeRGS (left: Mark 12 ladder, right: protein). **b**. UV-Vis spectrum. **c**. Recovery kinetics of protein stabilized by 1M NaCl and 10% glycerol to prevent photo-induced aggregation, monitored at λ = 450 nm absorbance (A450). Black = Exponential fit. Gray = Mean ± SD (N = 3). **d**. Dynamic light scattering data with and without electrostatic stabilization. Illuminated = Immediately after 5 second illumination (15 mW/cm^2, λ = 455 nm) (N = 2-3). **e**. Spinning disk confocal images of HEK cells expressing 3xFLAG-tagged CeRGS, probed with Anti-FLAG M2 monoclonal antibody and stained with Anti-mouse IgG Alexa Fluor 488 conjugated secondary antibody. Scale bar = 10 μm. Images are from separate fixed samples.

CeRGS-3xFLAG was expressed in HEK293T cells, which were fixed in the dark-adapted state, under blue light illumination, and ten minutes after light stimulation. Protein was visualized by anti-FLAG immunostaining with Alexa Fluor 488-conjugated secondary antibodies (**Figure 2.8e**). Similar to BcLOV4, we observed that CeRGS is largely localized to the cytosol in its dark-adapted state, with a small population of cells showing both cytosolic and nuclear protein localization. Under blue light, the protein is membrane-localized, with normal cytosolic expression reappearing following a dark recovery period. This protein localization pattern combined with biophysical data suggests that light-induced lipid binding is not just a feature of BcLOV4 but perhaps a shared feature among RGS-LOV family proteins.

2.3 Conclusions and future directions

The biophysical characterization of BcLOV4-lipid interaction, in combination with data from mammalian cells, suggest a photosensory signal transmission mode by BcLOV4 (and potentially the larger RGS-LOV class) of rapidly blue light-inducible, and reversible, membrane association mediated by electrostatic interactions with anionic phospholipids. While other membrane-binding proteins contain PAS domain sensors (94, 164) related to LOV domains, such as PhoQ, Aer, and LuxQ (39, 175), these are

ligand-regulated transmembrane proteins unlike the cytoplasmic RGS-LOV reported here. De novo secondary-structure and Rosetta (206) structural predictions suggest that the DUF in this region may adopt a PAS-like fold with antiparallel β-sheets (69), and thus it is possible that the LOV–DUF interaction is an evolutionarily conserved PAS/PAS interaction as observed in other systems. It should be noted that other lipid interaction sites may exist beyond the critical amphipathic helix between the LOV and DUF domains. A future high-resolution structure of the lipid-bound state will greatly inform the proposed biophysical model, as well as conclusively determine whether the DUF is indeed a PAS domain.

In an applied context, BcLOV4 also contributes a useful single-component optogenetic system with rapid translocation kinetics for photoinducible membrane localization that is compatible in yeast and mammalian expression systems. Unlike the indirect membrane binding of optogenetic tools that rely on heterodimerization between cytosolic and membrane-bound partners (85, 237), BcLOV4 as a single-component system is insensitive to heterogeneity in relative expression level tuning of two components and is more facile in transgene delivery. As a future direction, finite element modeling will provide a better understanding of the parameters governing BcLOV4 aggregation and translocation.

In summary, biophysical characterization of BcLOV4 and CeRGS demonstrates a signal transmission mechanism of RGS-LOV proteins, linking photosensory cues to changes in protein localization through lipid binding. BcLOV4’s light-inducible protein translocation is an attractive candidate for a new optogenetic platform, allowing the user to fuse protein cargo to BcLOV4 and recruit it to the signaling hub of the plasma membrane in response to spatiotemporally precise blue light inputs.

2.4 Materials and methods

2.4.1 Genetic constructs

Gene fragments encoding BcLOV4 (GenBank ID CCD53251.1) and CeRGS (GenBank ID ETN36999.1) were ordered from Integrated DNA Technologies (IDT) as gBlocks® and assembled by Gibson cloning or PCR assembly. Transgenes were cloned by restriction digest into a pET21/28-derived BamUK bacterial expression vector (a kind gift from Dr. Ranganath Parthasarathy) with the high copy pUC origin of replication, kanamycin resistance, a T7/lacO promoter, and a multiple cloning site for in-frame fusion to an N-terminal His_6 tag. C-terminal mCherry fusions in BamUK were generated by Gibson cloning and feature a short, flexible $(GGGS)_2$ linker. Truncation variants were generated by PCR from the full-length template and subcloned into the mCherry-BamUK vector. All constructs were transformed into competent *E. coli* (New England Biolabs, C2984H).

Mutants were generated by laboratory methods based on QuickChange kits. Overlapping forward and reverse primers encoding the mutation of interest were designed with a melting temperature ≥ 78 ºC. The designed mutation was introduced over 18 cycles of PCR with the high-fidelity Phusion polymerase (New England Biolabs, M0531S), and template plasmid was digested with DpnI for 1 hour at 37 ºC prior to transformation into competent *E. coli* (New England Biolabs, C2984H).

For mammalian expression, CeRGS was cloned into the pcDNA3.1 mammalian expression vector under the CMV promoter (Invitrogen) with a C-terminal 3xFLAG tag.

2.4.2 Protein purification

Bacterial expression plasmids were transformed into BL21(DE3) *E. coli* cells by mixing 10 ng of purified plasmid DNA into 10 µL of chemically competent cells (New

England Biolabs, C2527H), incubating at 4 ºC for 30 minutes, heat-shocking cells in a 42 ºC water bath for 30 seconds, placing heat shocked cells on ice for 2 minutes, and then incubating for 1 hour at 37 ºC in 100 µL S.O.C. media. Transformed cells were grown on Luria Broth (LB) plates with 50 µg/mL kanamycin overnight at 37 ºC, and single colonies were picked and grown overnight to saturation in LB media with 50 µg/mL kanamycin. Cultures for protein production were initiated by diluting saturated overnight cultures 1:200 into fresh LB-kanamycin media in 1-2 L baffled flasks, and subsequently grown at 37 ºC with 250 r.p.m. shaking to a mid-log phase of OD_{600} = 0.5-0.8. Protein production was induced with 0.5 mM isopropyl-beta-D-thiogalactopyranoside (IPTG), and cells were grown for 18-22 hours at 18 ºC with 250 r.p.m. shaking in a refrigerated incubator. Cells were then harvested in 250 mL centrifuge bottles by spinning at 3000 x *g* for 20 minutes, and subsequently frozen at -20 ºC for < 2 weeks prior to cell lysis and purification.

Frozen cells were thawed at room temperature for 5-10 minutes and then resuspended in 50 mL ice-cold lysis buffer (50 mM sodium phosphate, 500 mM NaCl, 0.5% Triton-X-100, pH 6.5) per liter of harvested cell culture. All subsequent steps were carried out on ice or in a 4 ºC cold room. Re-suspended cells were homogenized with 3 passes through a 21-gauge syringe needle. 10 mL aliquots of lysate were each sonicated 5 times with a duty cycle of 15 seconds ON, 30 seconds OFF with a Fisher Scientific Series 60 Sonic Dismembranator at 100% power (60W). Individual aliquots were pooled and transferred to a 50 mL polycarbonate conical tube and clarified by centrifugation at 25,000 x *g* for 30 minutes at 4 ºC to remove insoluble fractions. The supernatant was decanted and kept at 4 ºC prior to further purification.

His_6-tagged proteins were affinity-purified by fast protein liquid chromatogphy (FPLC, AKTA Basic) on Ni-NTA (GE HisTrap FF) columns. All exposed sample-containing FPLC segments were covered with aluminum foil to maintain darkness. After

sample loading onto a 5 mL column at 1mL/min, the column was washed with 20 mM imidazole in buffer (50 mM sodium phosphate, 500 mM NaCl, 10% glycerol, pH 6.5) for 15 column volumes, followed by a linear gradient, from 20 to 200 mM imidazole, over 15 column volumes at 5 mL/minute. Proteins were eluted with 500 mL imidazole and collected in 10 x 2 mL fractions. Samples were pooled based on purity assessed by SDS-PAGE and concentration assessed by absorbance spectroscopy (A280), and then buffer exchanged into 1x PBS using PD-10 desalting columns with Sephadex G-25 resin (GE, 17085101). Buffer exchanged material was centrifuged at 4 ºC at 25,000 x *g* for 30 minutes to pellet insoluble protein debris. Buffer exchange was repeated twice more, and the column was re-equilibrated with 1x PBS prior to each usage. Purified protein was stored for < 2 weeks at 4 ºC.

2.4.3 Thin-layer chromatography

Cofactor identification was performed according to standard flavoprotein cofactor protocol (41). Protein (10 nmol) was boiled in 70% ethanol for 2 minutes, chilled on ice for 2 minutes, and then centrifuged at 16,000 x *g* for 10 minutes. Standards were dissolved in water at 1 µM (all from Millipore-Sigma; FMN, F6750; FAD, F6625; Riboflavin, R4500). Thin-layer chromatography was performed on glass silica gel plates (Millipore-Sigma, Z292974) using standard methods with n-butanol : acetic acid : water (3:1:1 v:v). Plates were dried and imaged on a UV transilluminator. R_f values: BcLOV4 cofactor (0.26), FMN (0.26), FAD (0.14), Riboflavin (0.61).

2.4.4 UV-vis spectroscopy

Absorbance scans were measured on an Ocean Optics USB2000+ spectrophotometer with a deuterium/halogen light source. Full spectrum (λ = 250-700

nm range) absorbance scans were measured in quartz cuvettes (Starna Cells, 16.100F-Q-10/Z15). Photocycle kinetics were measured by monitoring the absorbance at 450 nm (A450). After baseline measurements were made for 15 seconds at room temperature, the samples were stimulated with blue-light (10 s, λ = 455 nm, 15 mW/cm^2) delivered by a collimated LED (Mightex), and then dark-state recovery was monitored every 0.5 seconds for an additional 2 minutes.

To make solid-phase fluorescence-based photocycling measurements, 40 ng of His_6-tagged protein was mixed with 0.5 mg of magnetic Ni-NTA beads (ThermoFisher HIsPur Ni-NTA resin, 88221) in a total reaction volume of 400 µL in 1x PBS and nutated at room temperature for 1 hour. After three x 5-minute-long washes with PBS + 20 mM imidazole, protein-bound bead samples were re-suspended in 200 µL of 1x PBS. Fluorescence scans were measured on a Tecan Infinite M200 plate reader and kinetics were measured by monitoring the fluorescence (excitation 450 nm, emission 505 nm) for 200 µL of protein-bound beads in a 96-well plate. After baseline measurements were made for 15 seconds at room temperature, the samples were stimulated with blue-light (10 s, λ = 455 nm, 15 mW/cm^2) delivered by a collimated LED (Mightex), and then thermal reversion in the dark was monitored continuously for an additional 2 minutes.

2.4.5 Dynamic light scattering

Particle size analysis was performed using a Zetasizer Nano Series (Malvern Instruments, λ = 633 nm) for 5 µM protein in 1x PBS buffer. Three 10 s-long scans were averaged. After establishing baseline values in the dark, samples were illuminated by a collimated LED (Mightex, 5 s, λ = 455 nm, 15 mW/cm^2), and then returned to the dark

DLS chamber for post-illumination measurements for up to 60 minutes. Macroscale turbidity images were taken with a Canon G12 camera.

2.4.6 SDS-PAGE and Western blot

Protein samples in 1x NuPAGE® lithium dodecyl sulfate (LDS) sample buffer (ThermoFisher Scientific, NP0007) were heated to 70 ºC for 10 minutes and loaded on 4-12% Bis-Tris NuPAGE® SDS-PAGE gels, along with Mark12 unstained standard (ThermoFisher Scientific, LC5677). Gels were run in 1x MOPS running buffer for 45 minutes at 200 V. Gels were visualized by staining with InstantBlue Coomassie stain (Expedeon, ISB1L) and imaging on a digital scanner. For Western blotting, proteins were run with MagicMark XP Western Protein Standard (ThermoFisher Scientific, LC5602), transferred to PVDF membranes (ThermoFisher Scientific, LC2005) at 30 V for 1 hour in 1x NuPAGE® transfer buffer (ThermoFisher Scientific, NP0006), probed with mouse monoclonal antibodies to the antigen of interest, and then probed with IRDye 680RD Goat anti-Mouse IgG (Li-Cor Biosciences, 925-68070). Western blots were imaged on an Odyssey CLx Infrared Imaging System (Li-Cor Biosciences, Model 9140).

2.4.7 Size-Exclusion Chromatography with Multi-Angle Light Scattering (SEC-MALS)

FPLC-purified BcLOV4 was buffer-exchanged into a SEC-MALS-compatible buffer (50 mM sodium phosphate, 500 mM sodium chloride) using PD-10 desalting columns with Sephadex G-25 resin (GE, 17085101). The protein was analyzed by SEC-MALS using an in-line HPLC (Agilent Technologies 1200), and MALS system (Wyatt DAWN HELEOS II and OPTILAB T-rEX). SEC-purified protein was loaded onto a Superdex 75 agarose and dextran-based column (GE) in 50 mM sodium phosphate and 500 mM sodium chloride. A 100 µL sample of BcLOV4 at 0.4 mg/mL was injected at a

flowrate of 0.5 mL/min, over a total 53-minute-long profile. Data was collected and analyzed using Astra chromatography software (Wyatt).

2.4.8 Protein-lipid overlay assay

Phospholipids at 3 mM in 1:1 chloroform:methanol (with 0.1% HCl) were spotted (1 µL) onto 0.2 µm pore size nitrocellulose blotting membranes (ThermoFisher Scientific, LC2000). After drying for 1 hour at room temperature, blots were either stored at 4 ºC, or blocked for 1-4 hours in PBS containing 3% BSA (no detergent). 0.5 µM of His_6-tagged BcLOV4 variants were then added to PBS / 3% BSA (GST-tagged positive control at 23.6 nM) and this solution was incubated with a BSA-blocked, lipid-spotted nitrocellulose membrane for 1 hour at room temperature. Membranes were washed 4 times with PBS-T (PBS + 0.1% Tween20) and then probed with mouse anti-His primary antibody at 1:2000 dilution (Cell Signaling Technology, 2366) in PBS + 3% BSA for either 1 hour at room temperature or overnight at 4 °C. After an additional 4 washes with PBS-T, membranes were probed with IRDye 680RD Goat (polyclonal) Anti-Mouse IgG (Licor Biosciences, 925-68070) at 1:15000 dilution in PBS-T + 3% BSA for 1 hour at room temperature. Blots were washed an additional 4 times in PBS-T and then in 1x PBS. Blots were imaged on an Odyssey Infrared Imaging System in the λ = 700 nm channel at Intensity 5.

2.4.9 Water-in-oil emulsion assay (protocells)

Lipids (see section 2.4.10) were resuspended in chloroform in a glass test tube or round-bottom flask. Chloroform was evaporated under a stream of nitrogen and the remaining lipid film was dissolved into decane (Aldrich, D901) at 2.5-25 mg/mL, based on the solubility of each individual phospholipid. To facilitate suspension in decane and

to remove excess chloroform, solutions were heated at 50 ºC for 3 hours and sonicated in a water bath for 30 minutes. Lipids were stored in glass vials with Teflon caps (Thomas Scientific, 1234R80) at -20 ºC. In experiments, 30 µL of 20 mM lipids (total molarity) was mixed vigorously with 1.28 µL of purified mCherry-tagged protein in PBS by pipetting up and down until a cloudy suspension formed. 20 µL of the water-oil emulsion was transferred to microwells and imaged at 20×.

Automated MATLAB scripts were used to identify droplets, segment either just the outer ring interface or the aqueous dispersed phase and to calculate integrated fluorescence intensity and area over these regions. The ratio of membrane inner leaflet-emulating interface fluorescence intensity per unit area to cytoplasm-emulating dispersed phase fluorescence intensity per unit area was considered a measure of membrane-binding and normalized to the max ratio for illuminated wildtype protein. More detail on this protocol can be found in Appendix 1 (67).

2.4.10 Surface plasmon resonance

SPR measurements were performed using a Biacore T200 (GE Healthcare) instrument at 25 °C. Small unilamellar vesicles (SUV) were generated by initially hydrating 1.5 mM phospholipids (phosphatidylcholine, Aldrich, P3556 and Avanti, 840051C; 18:1 (Δ9-Cis) phosphatidylcholine (DOPC), Avanti, 850375; phosphatidylserine, Aldrich, P7769 and Avanti, 840032C; 18:1 phosphatidylserine (DOPS), Avanti, 840035; phosphatidylglycerol, Aldrich, P8318; phosphatidic acid, Aldrich, P9511; cardiolipin, Aldrich, C0563; PIP2, Cell Signals, #902; PIP3, Cell Signals, #908) of a given composition in HBS-N buffer (25 mM HEPES, 150 mM NaCl, pH 7.4), then sonication followed by 8 freeze/thaw cycles in a dry ice/ethanol bath, and finally 15 passes through an Avanti Lipid extruder with a 0.05 µm membrane. SUVs were

immobilized by flowing them over the surface of a carboxymethylated dextran chip with covalently attached lipophilic groups (Sensor chip L1) at 2 µL/min for 30 minutes. Typically, 4000-10000 RU (resonance units) of liposomes were immobilized. His_6-BcLOV4-mCherry variants were buffer exchanged three times into HBS-N and passed over the chip surface at a flow rate of 30 µL/min for 10 minutes. The chip was regenerated after each binding experiment by the injection of 100 mM NaOH at 50 µL/min for 1 minute. SUV coated chips were used for a maximum of ~12 hours before they were stripped with 40 mM octyl-B-glucoside and 0.5% SDS and re-coated. Steady-state equilibrium binding values were fit and analyzed with the curve fitting toolbox in MATLAB.

2.4.11 On-bead cleavage assay

Factor Xa cut sites were introduced to the C-terminus of BcLOV4 by site-directed mutagenesis and His_6-tagged protein was purified as described in 2.4.2. Purified protein was treated with EDTA for a final concentration of 5 mM prior to buffer exchange to remove any nickel eluted from the FPLC column. Protein was buffer exchanged to remove imidazole (50 mM sodium phosphate, 500 mM NaCl, 10% glycerol, pH 6.5 buffer) via a PD-10 column. HisPur™ Ni-NTA magnetic beads (200 µL) were added to a 1.5 mL tube and w mL wash buffer (50 mM sodium phosphate, 500 mM NaCl, 20 mM imidazole, 10% glycerol, pH 6.5 buffer) was added. Beads were vortexed gently for 10 seconds, then collected to the side of the tube with a magnetic rack as wash was aspirated off. This process was repeated for a total of three washes.

Protein was diluted with wash buffer to a final concentration of 1 mL and added to the washed beads. Protein and beads were vortexed to mix, then incubated at room temperature on a rotating tube rack for 30 minutes. Following binding, beads were

separated from solution and supernatant was aspirated and saved. Beads were washed as above with wash buffer for a total of four washes, then washed three times with low-salt buffer (1 mL, 50 mM sodium phosphate, 300 mM sodium chloride). Washes were collected and saved. Following the final wash, Factor Xa (12 µL, 1 mg/mL stock, New England Biolabs, P9010) was added, then the solution was vortexed and incubated wrapped in foil to prevent light exposure on a rocking table overnight.

Following incubation, Factor Xa flowthrough was collected, and beads were washed three times with wash buffer. On-bead fluorescence photocycle was measured as described in section 2.4.4. For SDS-PAGE and Western blot analysis, protein was eluted in two 150 µL fractions (50 mM sodium phosphate, 500 mM sodium chloride, 10% glycerol, 500 mM imidazole, pH 6.5), incubating for 15 minutes with rocking per elution.

2.4.12 Cell culture and transient transfection

HEK293T (ATCC, CRL-3216) cells were cultured in D10 media composed of Dulbecco's Modified Eagle Medium with Glutamax (Invitrogen, 10566016), supplemented with 10% heat-inactivated fetal bovine serum (FBS) and penicillin-streptomycin at 100 U/mL. Cells were maintained in a 5% CO_2 water-jacketed incubator (Thermo/Forma, 3110) at 37°C. Cells were seeded onto poly-D-lysine-treated glass bottom dishes (MatTek, P35GC-1.5-14-C) or into 24-well glass bottom plates (Cellvis, P24-1.5H-N), treated in-house with type I collagen, at 15-20% confluency. Cells were transfected at ~30-40% confluency 24 hours later using the TransIT-293 transfection reagent (Mirus Bio, MIR2700) according to manufacturer instructions and Opti-MEM™ reduced serum media (Thermo Fisher, 3195062). Cells were fixed and imaged 24-48 h post-transfection.

2.4.13 Fluorescence microscopy and hardware

Fluorescence microscopy was performed on an automated Leica DMI6000B fluorescence microscope under Leica MetaMorph control, with a sCMOS camera (pco.edge), an LED illuminator (Lumencor Spectra-X), and a 63× oil immersion objective (for fixed HEK cells) or a 20× air objective (for protocells imaging). Excitation illumination was filtered at the LED source (mCherry imaging λ = 575/25 nm; Alexa Fluor 488 imaging or widefield BcLOV4 stimulation λ = 470/24 nm). Fluorescent proteins were imaged with Chroma filters: mCherry (T585lpxr dichroic, ET630/75 nm emission filter, 0.2-0.5 s exposure), GFP (T495lpxr dichroic, ET 525/50 nm emission filter, 0.2 s exposure)

2.4.14 Cell fixation and immunostaining

Cells were fixed in 4% paraformaldehyde in 1x PBS for 15 minutes at room temperature. Dark-adapted cells were fixed under a dim red light, while illuminated cells were irradiated with strobed illumination (λ = 455 nm, at ≥ 15 mW/cm^2, 5 seconds ON / 25 seconds OFF duty cycle) from a collimated LED (Mightex) for 30 seconds prior to and throughout the fixation. For immunocytochemistry analysis of 3xFLAG-tagged protein, cells were seeded and grown on poly-D-lysine treated #1.5 cover glass (Cellvis, P24-1.5H-N), washed three times with 1x PBS + 0.1M glycine, and then blocked with 1% BSA (Thermo Fisher Blocker BSA 37525), 2% normal goat serum and 0.4% saponin in 1x PBS for 30 minutes at room temperature. Blocked cells were incubated overnight at 4 ºC with mouse Alexa Fluor 488-conjugated anti-3xFLAG monoclonal antibody (Cell Signaling Technology, 5407) at 1:250 dilution in blocking buffer, or with anti-3xFLAG antibody (Cell Signaling Technology, 8146) followed by an Alexa Fluor-488 conjugated

secondary antibody (Cell Signaling Technology, 4408). Cells were washed three times with 1x PBS prior to imaging.

CHAPTER THREE: Optogenetic tools for induction of cell contractility

This chapter adapts work from the following publication:

Berlew, E. E.; Kuznetsov, I. A.; Yamada, K.; Bugaj, L. J.; Boerckel, J. D.; Chow, B. Y., Single-Component Optogenetic Tools for Inducible RhoA GTPase Signaling. Adv Biol (Weinh) 2021, e2100810.

Author contributions: EEB designed genetic constructs, designed all experiments, and conducted all experiments. IAK created the patterned illumination system and assisted with the automated data analysis pipeline development. KY assisted with genetic construct design, engineering, and assays. BYC, JDB, and LJB coordinated all research. All authors contributed to experiment design, data analysis, and manuscript preparation.

3.1 Introduction

3.1.1 The RhoA signaling pathway

The RhoA signaling pathway centrally regulates cellular actin organization and contractility, playing key regulatory roles in cell migration, developmental morphogenesis, and cell cycle maintenance (49, 58). RhoA signaling coordinates cytoskeletal stress fiber formation that determines how cells transmit mechanical forces within the cell, across cell-cell junctions, and to the extracellular matrix (ECM) (43); consequently, activation and inactivation of the RhoA GTPase by GEFs and GAPs, respectively, is tightly controlled in space and time (**Figure 3.1**). New tools for inducible control over RhoA activity may greatly enhance understanding of cytoskeletal dynamics and mechanotransduction (55, 156).

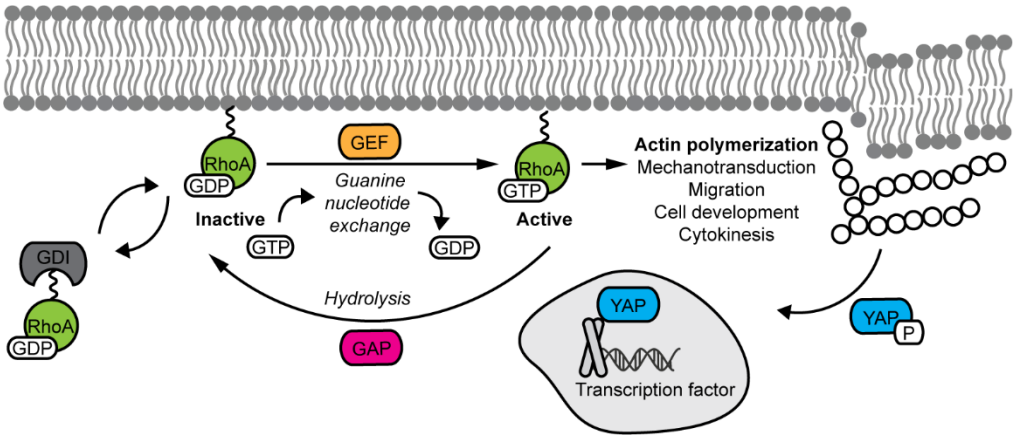

Figure 3.1 The RhoA signaling pathway

RhoA signaling is regulated by guanine nucleotide exchange factors (GEFs), GTPase accelerating proteins (GAPs), and guanosine nucleotide dissociation inhibitors (GDIs). RhoA activation at the membrane induces actin polymerization, contributing to diverse cell processes including mechanotransduction via nuclear recruitment of transcriptional co-activator Yes-associated protein (YAP).

At the plasma membrane, wildtype RhoA is activated by GEFs and subsequently activates Rho-associated kinase (ROCK), a serine-threonine kinase. ROCK regulates both cell contractility and actin filament density. Following activation by RhoA, ROCK phosphorylates myosin light chain (MLC) and simultaneously phosphorylates and inhibits myosin light chain phosphatase (MLCP). Both these activities increase the ATPase activity of myosin II and promote contraction of the cell. Activated ROCK can also phosphorylate LIM kinase (LIMK), which in turn phosphorylates cofilin to stabilize actin filaments, resulting in a denser actin network (241). Thus, activation of RhoA at the plasma membrane and interaction with downstream ROCK has profound consequences for cell motility and morphology.

RhoA-ROCK signaling also drives essential nervous system functions including neuritogenesis, neuron migration, and polarization. In the leading edge of a neurite growth cone, RhoA is activated by membrane receptor signals to regulate the duration of the developing neuron's growth and pause phases (56), likely by promoting the

condensation of actin filaments into an arc which acts as a barrier for microtubule forward projection. In addition, RhoA has been implicated in neurodegenerative diseases and injuries to the central nervous system: elevated levels of active RhoA have been found in injuries to the spinal cord and optic nerve as well as in stroke lesions (62), underscoring the clinical importance of understanding RhoA signaling.

RhoA also plays a role in mechanotransduction, converting external environmental cues to a change in cytoskeletal tension and transcriptional regulation. In response to an increase in ECM stiffness, RhoA signaling increases cytoskeletal tension, driving transcriptional co-activator Yes-associated protein (YAP) from the cytosol to the nucleus (55, 172). YAP, lacking a DNA binding motif, binds TEAD family transcription factors to alter gene expression (140, 141). This conversion of mechanical input to transcriptional activity is crucial in regulating liver (269) and heart (264) organogenesis and regeneration. The centrality of RhoA signaling to cellular programs of growth and migration as well as its roles in the development of multiple organ systems make it an important target for cell signaling interrogation and manipulation.

3.1.2 Existing tools for RhoA signaling perturbation

The main strategies for controlling RhoA signaling are the use of pharmacological pathway activators and inhibitors, the introduction of genetic gain-of-function or loss-of-function mutations, the mechanical manipulation of the cytoskeleton, and the use of optogenetic tools. Drug mechanisms of RhoA signaling inhibition include sterically occluding the GEF-interacting interface on RhoA GTPase molecules as in Rhosin (219, 220), or by impeding downstream interactions with RhoA pathway effectors as in Y-27632, a small-molecule inhibitor of ROCK signaling (246). Activation of RhoA signaling can be achieved by treatment with soluble serum components like

lysophosphatidic acid (199) and calpeptin (215). These pharmacological strategies lack spatial precision; the addition of activators or inhibitors to cell culture media is not compatible with subcellular or even sub-regional targeting of plated cells. In addition, the timescale of drug uptake and washout is incompatible with temporally precise pathway control and has been shown to be too slow to be compatible with cellular differentiation between sustained and pulsatile input (28, 194), a critical need for GTPase signaling dynamics experiments.

RhoA signaling can also be perturbed through genetic mutations or gene knockout. Point mutations to the wildtype RhoA GTPase result in loss or gain of function. The G17V mutation, first identified in T cell lymphoma, results in loss of catalytic GTPase activity, while the dominant negative T19N mutation exhibits RhoA downregulation (66). RhoA can also be locked in its active GTP-bound state by a G14V mutation, which results in increased stress fiber formation and reduced cytokinesis (166). RhoA knockout has also been achieved in a fibroblast tumor model (4), decreasing cell motility and tumor growth. As with pharmacological inhibition, these genetic manipulations lack the spatiotemporal precision necessary to probe RhoA signaling at the subcellular level or to activate RhoA at physiologically relevant timescales. Mechanical approaches focus on altering the cell's microenvironment to induce cytoskeletal and signaling changes, often through the alteration of stiffness of cross-linked substrates (22, 83, 135). These techniques present the advantage of increased temporal precision over pharmacological and genetic techniques for the study of processes like wound healing, but lack the spatial resolution afforded by optogenetic systems (239).

Because small GTPases and their associated GEFs signal at the plasma membrane (10), optogenetic membrane localization techniques are effective for

inducible activation of GTPase signaling: cytosol-sequestered effector proteins are inactive prior to light exposure which dynamically recruits them to the cytosol-facing inner leaflet of the plasma membrane to upregulate effector signaling (87). For Rho-family GTPase signaling, most optogenetic activation tools are two-component heterodimerization systems between a photosensory protein and a binding partner, one of which is membrane-anchored, usually by prenylation. Cryptochrome (110, 126, 249) (Cry2) or light-oxygen-voltage (34, 90, 181, 254) (LOV)-derived systems have been used to recruit the catalytic DHPH domains of RhoA-selective GEFs to the plasma membrane for RhoA signaling activation and increased cytoskeletal tension. Heterodimerization systems require careful tuning of binding partner stoichiometry and the use of two fluorescent channels for imaging in addition to stimulatory blue light, decreasing the optical bandwidth available for other desired visualizations (201). Chemically induced dimerization (CID) approaches have also been reported, but inducer molecule rapamycin has been found to directly regulate RhoA (73, 76, 107). Finally, a Cry2-based system directly controls the GTPase itself through light-induced clustering of RhoA and increasing the binding avidity for activating membrane GEFs, though cytosolic diffusion of clustered protein decreases the system's spatial resolution (27).

3.1.3 Problem statement

Tools capable of inducing spatiotemporally precise, robust RhoA activation in the cell would enable the study of important cell processes like migration and cytokinesis and give insight into how cells translate environmental cues into physiological behaviors. Progress in tool development for RhoA induction shows that optogenetic approaches are currently the best-suited technologies for this problem, but with room for improvement:

most existing technologies require two protein components and focus on GEF recruitment rather than controlling the GTPase itself.

BcLOV4's direct lipid binding presents a promising opportunity to create single-component membrane recruitment tools without the need for a second protein and the associated stoichiometric tuning and genetic payload. We hypothesized that BcLOV4 could be used as a platform to activate RhoA contractile signaling at the plasma membrane (**Figure 3.2**). By engineering tools to activate signaling at both the GTPase and the GEF level, we aim to create a toolbox for shaping cytoskeletal dynamics with light, investigating key questions in mechanobiology, and dissecting activation nodes in RhoA signaling.

3.2 Results and discussion

3.2.1 Design and screening of opto-RhoA and opto-RhoGEF

We conducted initial screening studies in HEK293T cells due to their high protein expression level and simple culturing requirements. For construction of opto-RhoA, we followed the workflow described in Chapter 6 (18). Briefly, six arrangements of wildtype RhoA, BcLOV4, and an mCherry tag for protein visualization were cloned into the pcDNA3.1 backbone, with a flexible $(GGGS)_2$ linker separating each protein pair (**Figure 3.3**). These constructs were transiently transfected into HEK293T cells and visualized 24 hours later to identify domain arrangements with uniform high cytosolic expression in the dark state and intact blue light-induced translocation to the plasma membrane. BcLOV4-RhoA-mCherry expressed preferentially in the nucleus with minimal membrane association. Cells expressing mCherry-BcLOV4-RhoA appeared rounded and unhealthy, suggesting cytotoxicity. Both RhoA-mCherry-BcLOV4 and mCherry-RhoA-BcLOV4 were membrane-localized prior to blue light exposure. Both BcLOV4-mCherry-RhoA and

RhoA-BcLOV4-mCherry exhibited cytosolic expression; the latter was designated “opto-RhoA” based on its higher expression and the similarity of its membrane:cytosol fluorescence ratio before and after blue light exposure to BcLOV4-mCherry.

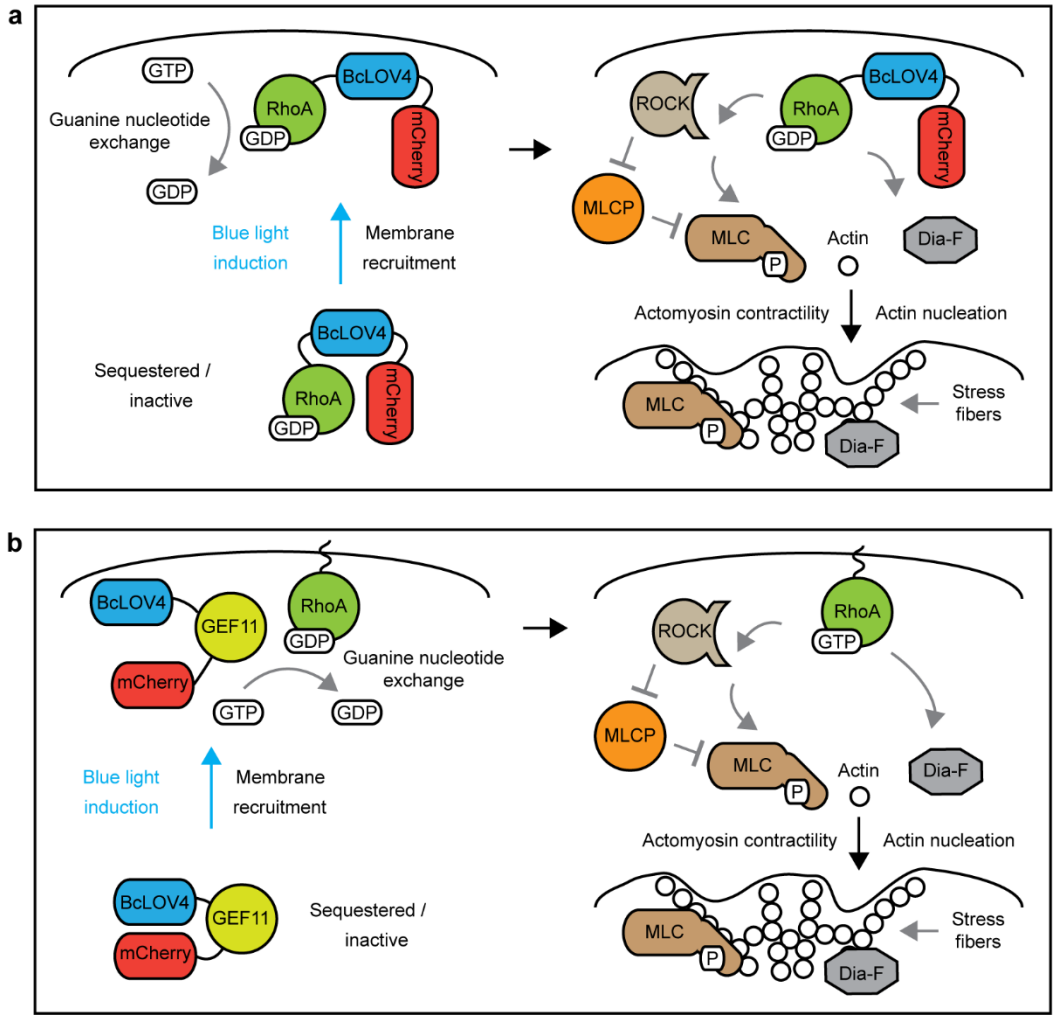

Figure 3.2 Schematic of opto-RhoA and opto-RhoGEF tool function

Schematized induction of cytoskeletal changes and contractile signaling in response to (**a**) opto-RhoA and (**b**) opto-RhoGEF activation by BcLOV4-mediated membrane translocation.

In choosing RhoA-activating GEF proteins for fusion tool development, we focused on identifying GEFs previously used in optogenetic membrane recruitment

systems to induce cell contraction, demonstrating that membrane recruitment of the GEF was sufficient for RhoA signaling activation, with an eye toward GEFs that were smaller in size to preserve membrane translocation efficiency and lower the genetic payload of the system. We screened three candidates: ARHGEF11 (42 kDa), previously used in a cryptochrome fusion tool (249); ARHGEF1 (29 kDa), which was used in a rapamycin activation system to activate RhoA (90); and ARHGEF12 (26 kDa), which caused formation of actin stress fibers in a TULIP tool (254). These GEFs were fused to BcLOV4 and mCherry following the cloning procedure developed for RhoA. Screening of domain arrangements with full-length ARHGEF11 did not result in suitable tool constructs; while three domain arrangements expressed in the cytosol, light-induced membrane association either did not occur or did not result in cell contraction. For further study, we truncated the GEF genes to remove the pleckstrin homology (PH) domain, a membrane lipid-binding region made redundant by BcLOV4's amphipathic helix.

Screening of ARHGEF12 fusions yielded no functional tool constructs, with membrane association failing to induce cell contraction. For ARHGEF1, both BcLOV4-ARHGEF1DH-mCherry and BcLOV4-mCherry-ARHGEF1DH expressed highly and induced modest cell contraction upon blue light stimulation. Because ARHGEF11's successful fusion induced much more rapid and pronounced cell contraction, we proceeded with this GEF for tool development and characterization.

We screened ARHGEF11DH fusions with BcLOV4 and mCherry in HEK293T cells and observed similar pre-illumination membrane binding of ARHGEF11DH-mCherry-BcLOV4 and mCherry-ARHGEF11DH-BcLOV4 as we observed for the analogous RhoA fusions. This phenomenon will be discussed in detail in Chapter 6. ARHGEF11DH-BcLOV4-mCherry's expression was non-uniform, with large bright spots of protein in the lysosome. The remaining three constructs all exhibited uniform cytosolic

expression; BcLOV4-ARHGEF11DH-mCherry was designated as “opto-RhoGEF” based on its robust membrane localization upon blue light stimulation (**Figure 3.4**).

3.2.2 Membrane translocation kinetics of opto-RhoA and opto-RhoGEF

We measured the kinetics of dynamic membrane association for opto-RhoA and opto-RhoGEF (**Figure 3.5**). Briefly, mCherry fluorescence of tool constructs was imaged before, during, and after a 5-second pulse of blue light. To prevent cell contraction which would introduce analytical confounds, we treated cells with RhoGEF inhibitor Rhosin and RhoA-ROCK interaction inhibitor Y-27632 for 24 hours before imaging. Line sections of the plasma membrane were drawn and Pearson’s correlation between mCherry intensity along the line section and a GFP membrane marker was measured at each timepoint. Exponential fits were applied to these association and dissociation measurements for N = 20 cells per construct and 95% confidence intervals were calculated. For opto-RhoA, membrane association τ_{on} was 1.27 s (95% CI 1.14-1.40 s) and membrane dissociation τ_{off} was 114.2 s (95% CI 106.6-121.8 s). For opto-RhoGEF, membrane association τ_{on} was 1.13 s (95% CI 1.01-1.26 s) and membrane dissociation τ_{off} was 108.4 s (95% CI 103.4-113.4 s). These values are similar to those measured for effector-less BcLOV4-mCherry in HEK cells (τ_{on} = 1.15 s, τ_{off} = 89.1 s), in yeast (τ_{on} = 1.20 s, τ_{off} = 84.9 s), and of purified recombinant BcLOV4 with *in vitro* lipid interfaces (τ_{on} ~ 1 s, τ_{off} = 133 s).

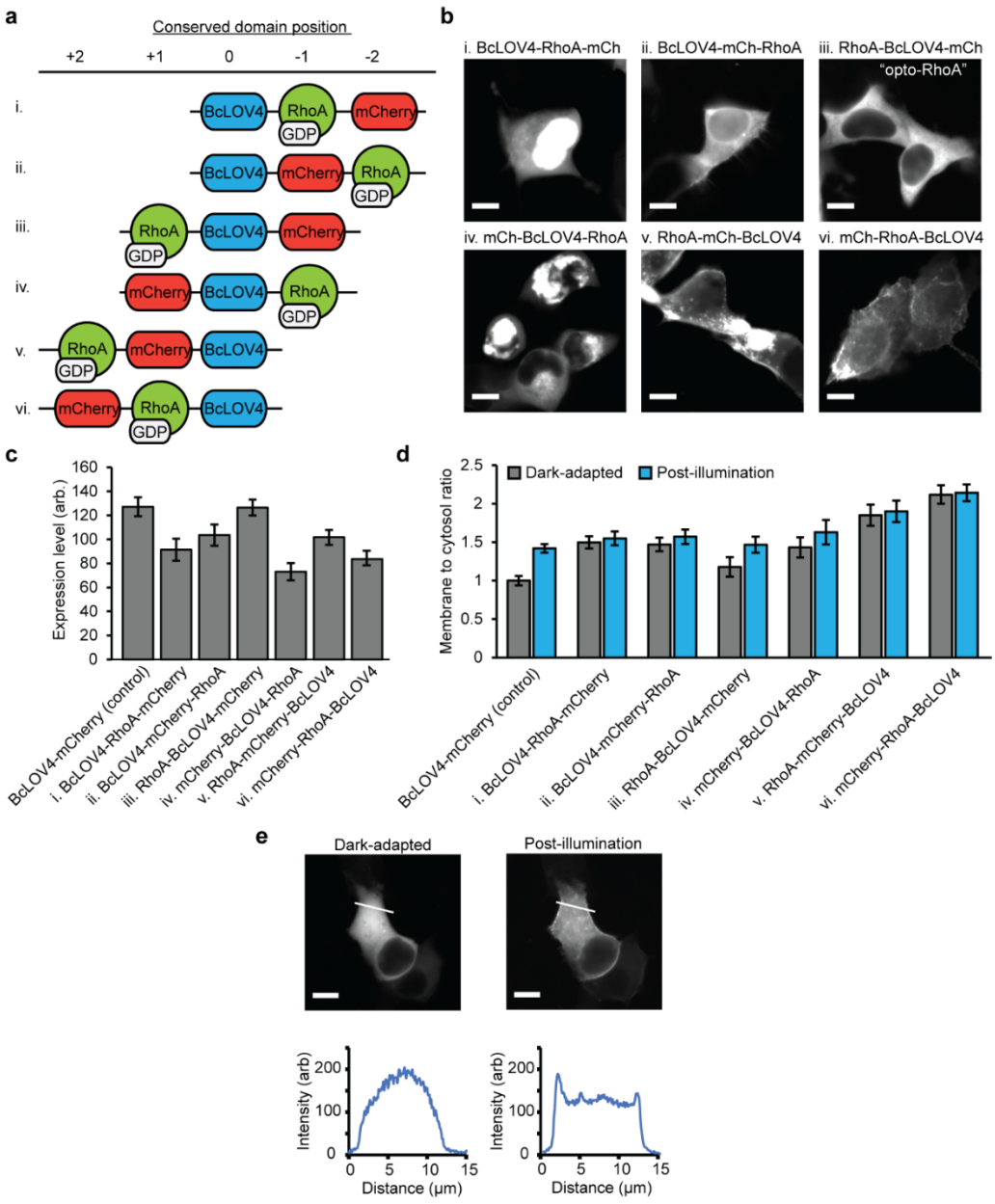

Figure 3.3 Molecular engineering of opto-RhoA

a. Domain arrangement combinations of BcLOV4, wildtype (GDP-bound) RhoA GTPase, and mCherry visualization tag. Domains were separated by flexible $(GGGS)_2$ linkers. **b**. Fluorescence micrographs showing representative expression patterns of the six domain arrangements in the dark-adapted state in HEK293T cells. Scale = 10 μm. **c**. Relative expression level of genetic constructs versus BcLOV4-mCherry control with no effector. N = 25-31 cells per condition. Mean ± SEM. **d**. Ratio of membrane-localized vs. cytosolic protein for each domain arrangement in the dark-adapted and blue light-illuminated states, normalized to BcLOV4-mCherry control. N = 25-31 cells per condition. Mean ± SEM. **e**. Representative membrane localization of opto-RhoA following blue light stimulation. (Top) Fluorescence micrograph; scale = 10 μm. (Bottom) Line section pixel intensity.

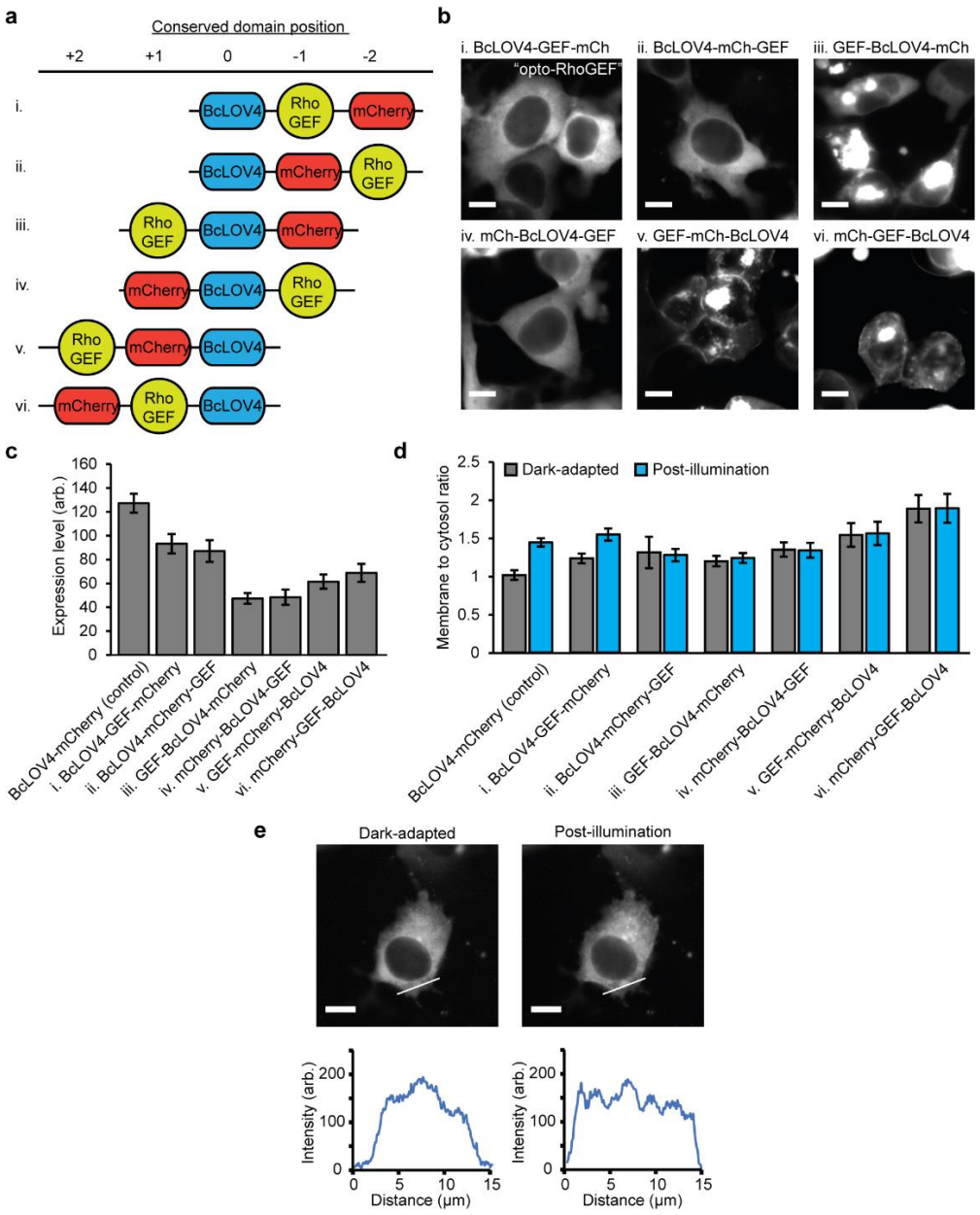

Figure 3.4 Molecular engineering of opto-RhoGEF

a. Domain arrangement combinations of BcLOV4, the DH domain of ARHGEF11, and mCherry visualization tag. Domains were separated by flexible $(GGGS)_2$ linkers. **b**. Fluorescence micrographs showing representative expression patterns of the six domain arrangements in the dark-adapted state in HEK293T cells. Scale = 10 μm. **c**. Relative expression level of genetic constructs versus BcLOV4-mCherry control with no effector. N = 25-31 cells per condition. Mean ± SEM. **d**. Ratio of membrane-localized vs. cytosolic protein for each domain arrangement in the dark-adapted and blue light-illuminated states, normalized to BcLOV4-mCherry control. N = 25-31 cells per condition. Mean ± SEM. **e**. Representative membrane localization of opto-RhoGEF following blue light stimulation. (Top) Fluorescence micrograph; scale = 10 μm. (Bottom) Line section pixel intensity.

3.2.3 Widefield stimulation-induced cell contraction

To our initial surprise, we observed that cells expressing opto-RhoA or opto-RhoGEF contracted following a single pulse of widefield stimulation; spatially confined, asymmetrical illumination is not necessary to induce RhoA activation and observe morphological changes (**Figure 3.6**). This feature of our RhoA tools differs from other GTPase and GEF tools (explored fully in Chapter 4), which required repeated illumination pulses and region-of-interest stimulation to effect cytoskeletal remodeling.

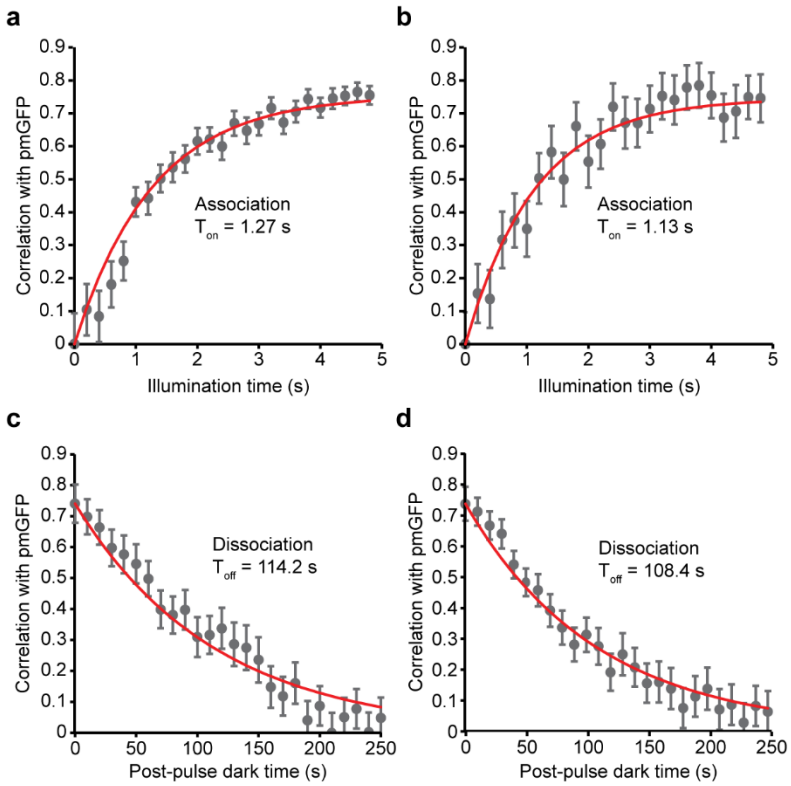

Figure 3.5 Membrane translocation kinetics of opto-RhoA and opto-RhoGEF in HEK cells

Time constants were determined by correlation analysis between the membrane marker (pmGFP) and line section profiles of the mCherry tag. RhoA signaling was pharmacologically inhibited with Rhosin and Y-27632 to isolate the membrane association/dissociation time constants attributable to the protein-lipid interaction. **a**. Membrane association of opto-RhoA: τ_{on} = 1.27 s, 95% CI 1.14-1.40 s. **b**. Membrane association of opto-RhoGEF: τ_{on} = 1.13 s; 95% CI, 1.01-1.26 s. **c**. Membrane dissociation of opto-RhoA: τ_{off} = 114.2 s; 95% CI, 106.6-121.8 s. **d**. Membrane dissociation of opto-RhoGEF: τ_{off} = 108.4 s; 95% CI, 103.4-113.4 s. N = 20 cells per condition. Mean ± SEM. Values are in line with those of effector-less BcLOV4 in HEK and yeast cells, and of purified recombinant BcLOV4 with in vitro lipid interfaces.

To assess the morphological changes induced by activation of opto-RhoA and opto-RhoGEF, we quantified the changes in cell area and cell length along the polarization axis, the direction of cell centroid displacement, and the stress fiber levels visualized by phalloidin staining of filamentous F-actin.

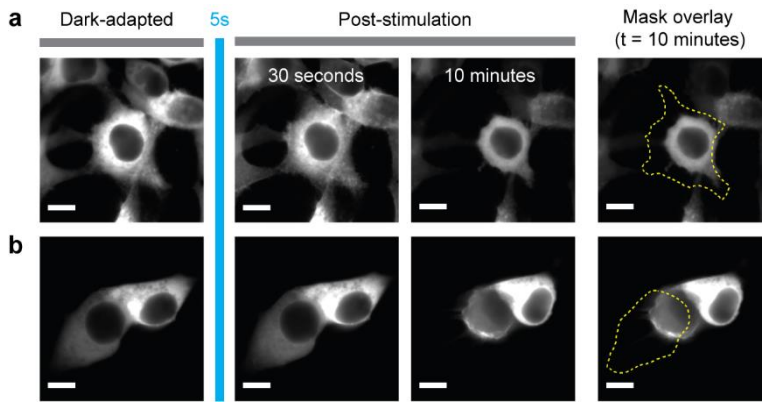

Figure 3.6 Optogenetic induction of contractility by a single pulse of unpatterned stimulation

Representative images of HEK cells expressing (**a**) opto-RhoA and (**b**) opto-RhoGEF, before and after one 5-second pulse of whole-field blue light stimulation. Visualized by mCherry tag. “Mask Overlay” shows the initial cell boundary in yellow. Scale = 10 μm.

3.2.3.1 Automated cell morphology analysis

The ability to use unpatterned stimulation to drive RhoA activation and subsequent morphological changes over a whole field-of-view (FOV) facilitated higher experimental throughput and statistical powering than if spatially confined stimulation were required for characterization of optogenetic pathway induction. We also determined that, for HEK293T cells, the polarization axis aligns with the long axis of the cell (**Figure 3.7**). We imaged cells co-transfected with miRFP703-tagged LifeAct and a BFP-tagged nuclear marker and measured the angle between the long-axis of the cell and the vector connecting the cell centroid and the centroid of the actin arc, the thickest portion of filamentous actin which is indicative of the leading edge of the cell. In the overwhelming majority of cells (93 of 108, 86%), this angle was between 0 and 30 degrees, confirming that the nucleus position along the cell’s long-axis was a viable morphological marker to define the cell’s leading edge during analysis.

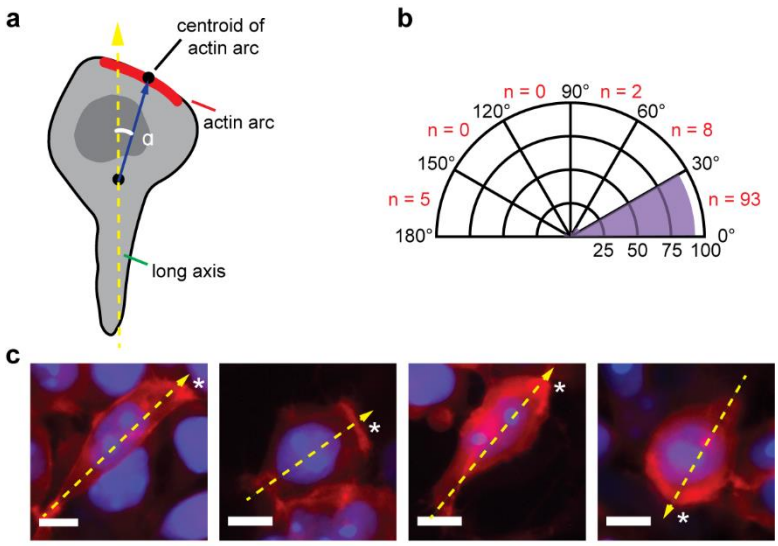

Figure 3.7 Actin imaging of HEK cell polarization axis

a. The angle α is defined as the angle between the long axis of the cell (when the nucleus is positioned toward the top) and the line segment connecting the cell centroid to the centroid of the brightest region of F-actin, imaged by LifeAct-miRFP703. **b**. The angle was overwhelmingly (in 93 of 108 cells, 86%) between 0 and 30 degrees, confirming nucleus position along the long axis as a viable morphological marker to define the leading edge during automated analysis. **c**. Representative images of HEK293T cells expressing LifeAct-miRFP702 (red) and a nuclear marker (mTagBFP-nucleus-7, blue). Yellow dotted line = algorithm-identified polarization axis of the cell. (*) = actin arc. Scale = 10 μm.

For data collection, we imaged mCherry fluorescence of cells transfected with opto-RhoA, opto-RhoGEF, or BcLOV4-mCherry control at 63× magnification before and for 10 minutes following a 5-second pulse of blue light stimulation. We manually cropped these whole-FOV videos into smaller visual fields (10-12 per FOV) focusing on only one cell, then randomly assigned each video a number so the analyst was blinded to experimental condition. Cell and nucleus boundaries at initial and final timepoints were manually drawn, and binary masks of these boundaries were rotated using Python package imutils to align the cell's leading edge (defined by the long axis and nuclear position) with the vertical axis of the image. Python package OpenCV was used to calculate cell area, length and width dimensions, and centroid position (**Figure 3.8a**).

3.2.3.2 Change in stress fiber levels

We quantified changes in cellular stress fiber levels using fluorescent-tagged phalloidin to stain filamentous actin in control and tool-expressing cells fixed in the dark and following blue light stimulation (**Figure 3.8b**). All constructs exhibited similar levels in dark-state phalloidin intensity (indicating basal stress fiber levels), suggesting little leakiness in RhoA and GEF signaling from diffusive tool-membrane contact in the dark-adapted state, even at the level of protein overexpression supported by HEK cells. Untransfected and BcLOV4-mCherry-expressing cells exhibited no significant change in stress fiber levels between dark and illuminated populations. Significant increases in phalloidin intensity were observed for both opto-RhoA and opto-RhoGEF ($p < 0.001$, by Mann-Whitney U test), verifying that optogenetic activation of RhoA signaling results in a downstream increase in actin polymerization.

3.2.3.3 Change in cell area and length

Optogenetic activation by whole-field stimulation of both opto-RhoA and opto-RhoGEF drove extensive morphological changes: most cells rapidly decreased in size in the ten minutes following blue light stimulation (Mean ± SEM; opto-RhoA, -16.3 ± 1.16%; opto-RhoGEF, -14.1 ± 1.28%). In contrast, cells expressing BcLOV4-mCherry largely remained unchanged in size (3.14 ± 1.63%) (**Figure 3.8c**). We assessed the statistical significance of the differences between these cell populations using the non-parametric Mann-Whitney U test uncorrected for multiple comparisons and calculated effect sizes using the Wilcoxon-Mann-Whitney rank sum test. The activation-induced change in cell area for both tools was significant and of large effect compared to the BcLOV4 control (BcLOV4 vs. opto-RhoA, $p < 0.0001$, effect = 0.692; BcLOV4 vs. opto-RhoGEF, $p <$

0.0001, effect = 0.661). No significant difference was measured in the comparison of opto-RhoA and opto-RhoGEF ($p = 0.139$, effect = 0.080).

Following alignment of the cell's polarization axis with the vertical axis of the image, we measured the differences in cell dimensions, calculated as the length and width of the minimum-area rectangle bounding the cell. While dimensions of BcLOV4 control cells remained unchanged (Δlength = 0.57 ± 0.77%; Δwidth = 4.79 ± 1.15%), we observed that tool-expressing cells decreased more in length than in width (opto-RhoA, Δlength = -14.2 ± 1.05%, Δwidth = -9.60 ± 1.22%; opto-RhoGEF, Δlength = -12.7 ± 0.64%, Δwidth = -7.34 ± 1.13%), suggesting that contraction pattern depended upon the cell's underlying polarity (**Figure 3.8d**). For cell length, we again observed significant differences between tools and BcLOV4, and no significant difference between opto-RhoA and opto-RhoGEF (BcLOV4 vs. opto-RhoA, $p < 0.0001$, effect = 0.629; BcLOV4 vs. opto-RhoGEF, $p < 0.0001$, effect = 0.583; opto-RhoA vs. opto-RhoGEF, $p = 0.0575$, effect = 0.117).

3.2.3.4 Angle of cell centroid displacement

Following our observation that change in cell length dominated the dimensional response to optogenetic stimulation, we next examined the movement of the cell centroid during contraction. We computationally identified the centroid of the binary cell masks at initial and final timepoints and measured the angle of the vector connecting them relative to the cell's polarization axis (**Figure 3.8e**). Thus, a displacement angle of 0° corresponds to the cell's trailing edge retracting toward the leading edge; an angle of 180° implies leading edge retraction toward the trailing edge. We tabulated displacement angles for each condition in bins 30° in width. For BcLOV4, no clear trend in direction of centroid displacement was observed. For both opto-RhoA and opto-RhoGEF, the cell

centroid displacement vector was highly preferential toward the 0-30° bin, meaning that the cytoskeletal retraction was predominantly at the trailing edge and along the polarization axis when the whole cell was stimulated (**Figure 3.8f**). This trend suggests that the cell's tensile asymmetry due to its underlying actin organization and polarization drives the morphological changes we observed when RhoA signaling was optogenetically activated. This observation is also consistent with the fact that RhoA signaling complexes are most abundantly active in the cell rear during cytoskeletal retraction (21, 187, 259).

3.2.3.5 Differences in pathway activation between opto-RhoA and opto-RhoGEF

By all observed measures, GTPase-level signaling activation by opto-RhoA was consistently but modestly more effective than GEF-level stimulation by opto-RhoGEF. No differences were observed in initial tensile state or subcellular distribution between the tools, although opto-RhoA expressed at slightly higher levels (**Figure 3.9**). Despite this lack of observable difference, the existence of both tools on the same optogenetic platform is useful in that it enables the nodal dissection of RhoA activation inputs in the cell. For simplicity and experimental throughput, our subsequent characterization focuses on opto-RhoA since it generally induces a more potent cytoskeletal response to activation (including its ability to separate adherens junctions) and fewer tools exist to control RhoA directly than for its activating GEFs.

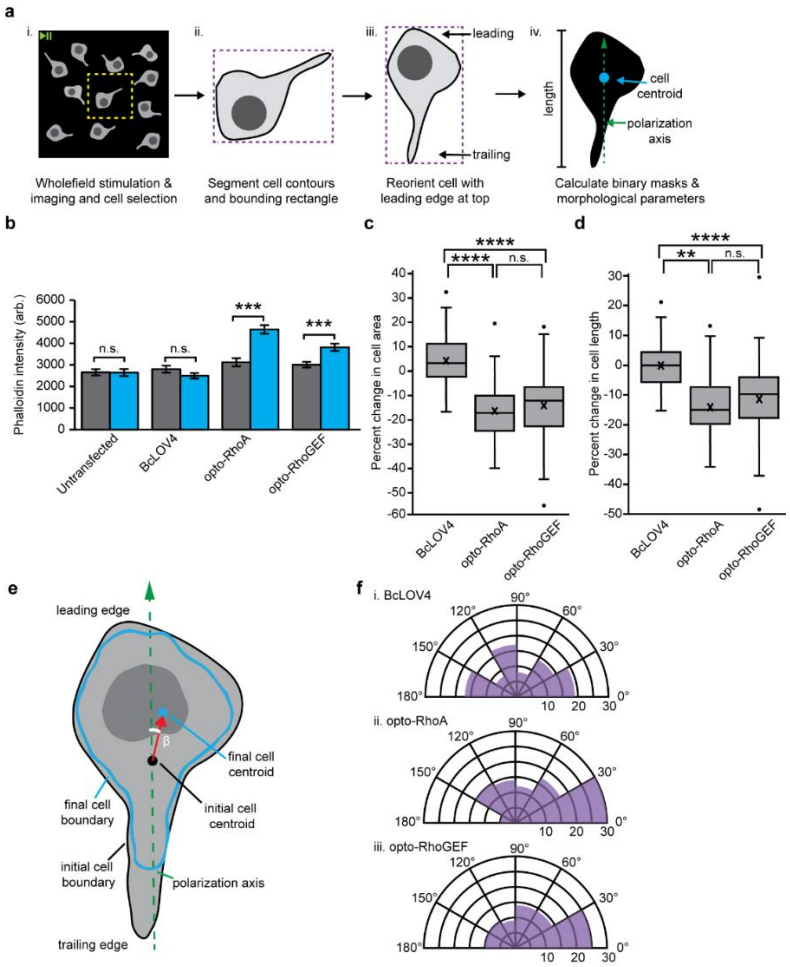

Figure 3.8 Analysis of cell contractility in response to unpatterned wide-field stimulation

a. Image analysis workflow. (i) Whole-FOV video cropping (yellow) to contain one cell. (ii) Cell contour (black) and bounding rectangle (purple) definition from the initial frame in OpenCV (threshold function and imutils). (iii) Iterative cell rotation (5° increments) and calculation of associated bounding rectangle. The angle that maximizes rectangle height and positions the nucleus closer to the top (as a leading-edge marker) is applied to all frames to align the y-axis with the cell polarity. Iv. Binary mask creation for initial and final timepoints for calculating cell areas, centroids, and lengths. **b**. Phalloidin stain intensity in dark-adapted vs. stimulated cells. Mean ± SEM. N = 40 cells per condition. **c**. Box-and-whisker plot of cell area change upon whole-field stimulation. **d**. Box-and-whisker plot of cell length change upon whole-field stimulation. N = 82-93 cells per condition. **e**. Schematized calculation of angle of cell movement. Centroids of the initial (red) and final (blue) cell boundaries are calculated in OpenCV (moments function). The angle of movement between the cell polarization vector (green, dashed) and the centroid movement vector (red) is designated as β. f. Circumplex charts of the angle of movement relative to the polarization vector in cells expressing (i) BcLOV4, (ii) opto-RhoA, and (iii) opto-RhoGEF. N = 82-93 cells per condition. **b-d**. Mann-Whitney U test: (**) $p < 0.01$; (***) $p < 0.001$; (****) $p < 0.0001$; (n.s.) not significant. **c-d**. Center line, median; "X", mean; box limits, upper and lower quartiles; whiskers, 1.5x interquartile range; points, outliers.

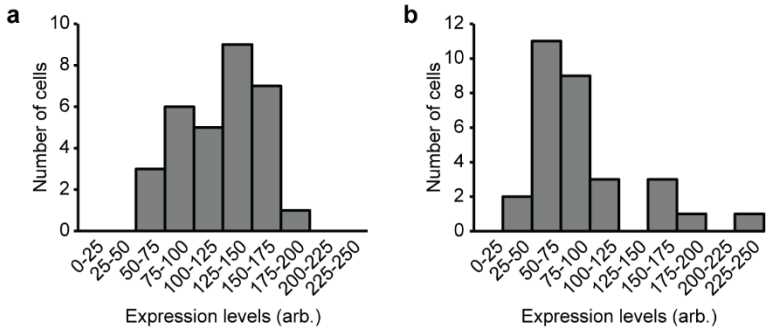

Figure 3.9 Expression level distribution of opto-RhoA and opto-RhoGEF for transfected HEK cells

a. Expression level distribution for opto-RhoA-transfected HEK cells. **b**. Expression level distribution for opto-RhoGEF-transfected HEK cells. N = 30-31 cells per construct.

3.2.4 DMD stimulation-induced cell contraction

Following characterization of the response of opto-RhoA to widefield blue light stimulation, we next sought to examine the effects of digital micromirror device (DMD)-delivered spatially confined blue light stimulation on tool activation and cell morphology. We observed that region-of-interest (ROI) illumination induced localized contraction of the cell and created membrane blebs, presumably from the transient delamination of the membrane from the actomyosin network (**Figure 3.10**). We also observed that selective activation of opto-RhoA at an adherens junction resulted in separation of multiple cell contacts within a 10-minute timecourse. The stimulation of duty ratio (Φ) of 1.6% (i.e., one second of blue light stimulation per minute) was initially chosen to ensure that optogenetic activity was not photochemically limited by providing one flavin photochemistry-saturating pulse per BcLOV4 membrane association-dissociation cycle.

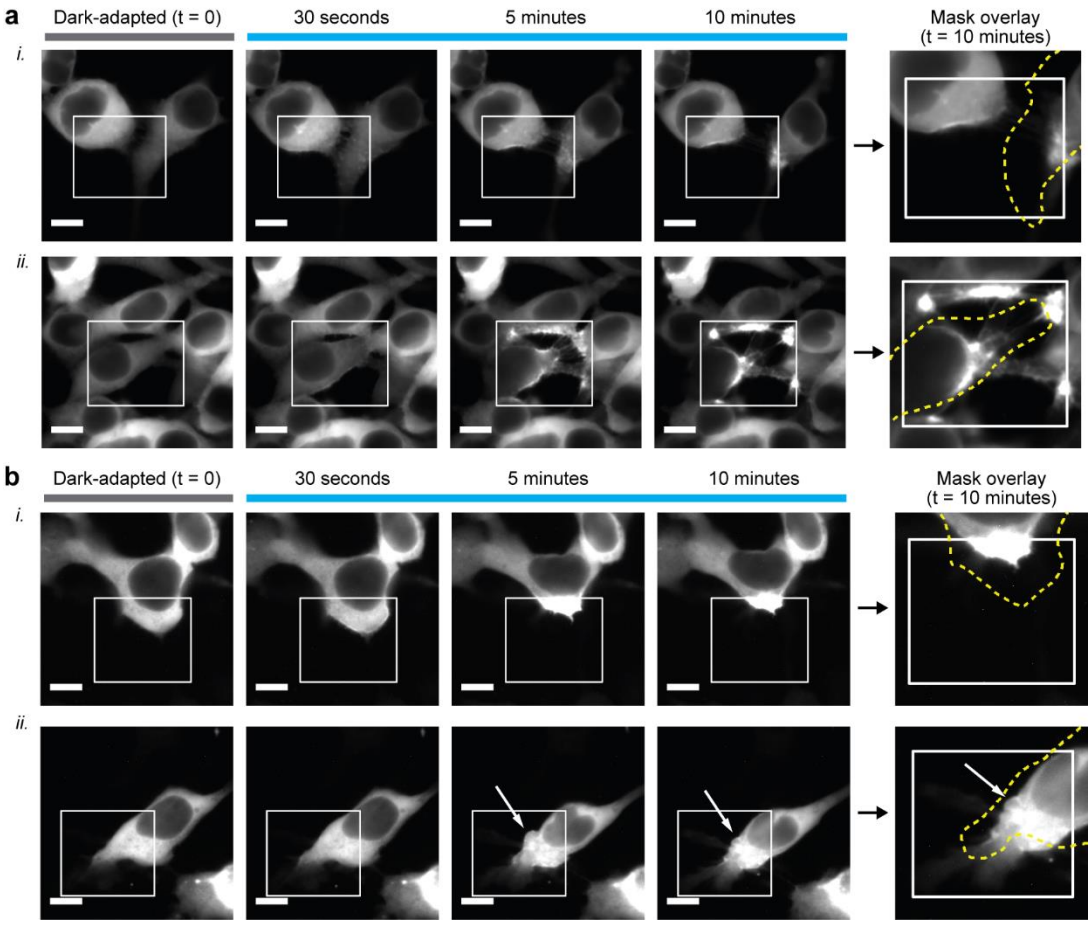

Figure 3.10 Optogenetic induction of contractility by patterned stimulation

a. Epifluorescence micrographs of HEK cells expressing opto-RhoA, visualized by mCherry. i. Trailing edge contraction in two adjacent cells. ii. Four-cell adherens junction separation. **b**. Epifluorescence micrographs of HEK cells expressing opto-RhoA, visualized by mCherry. (i) Leading edge contraction. (ii) Contraction and reversible bleb formation. White arrow = bleb location. White box = spatially patterned blue light illumination field, stimulated at 1.6% duty ratio. Dotted yellow line = cell boundary mask in the dark-adapted state. Scale = 10 μm.

3.2.5 Stimulation angle dependence of opto-RhoA-mediated contraction

Our observations of the direction of cell contraction when opto-RhoA was activated by wholefield stimulation suggested that the cell's underlying polarity spatially determines how the cell contracts. We next wanted to explore the issue of polarity further by measuring whether the extent of morphological changes depend upon the orientation of blue light stimulation with respect to the cell polarization axis. With these

experiments we sought both to gain insight into how RhoA activation intersects with cell polarity in determining morphological outcomes, and to better understand how user-specified optical stimulation paradigms impacts experimental outcomes.

We defined the stimulation angle as the angle between the cell's polarity axis and the vector connecting the centroid of the whole cell to the centroid of the stimulated region; thus, an angle of 0° implies stimulation of the leading edge, while an angle of 180° implies the trailing edge (**Figure 3.11a**). For each datapoint, one cell was stimulated with DMD-guided blue light (Φ = 1.6%) in a ~25 μm square overlaying about 25% of the cell area. We varied the stimulation angle and measured the percent changes in cell area and cell length as a function of stimulation angle bin (angles spanning 0-180°, 30° bin width).

We observed that the magnitude of induced morphological changed with stimulation angle alignment to the polarization axis: stimulation at the leading and trailing edges led to the largest constrictions, which was again consistent with the organization of the cell's original stress fiber network and the endogenous subcellular distribution of RhoA signaling complexes (**Figure 3.11b-d**). Statistical differences between bins were measured using the Mann-Whitney U test. Interestingly, *any* stimulation angle we tested, even those orthogonal to the polarization axis, still caused the contraction resulting in decrease in cell area and length. Thus, while alignment of optical excitation to the polarization enhances morphological changes induced by RhoA activation, it is not required to observe dramatic morphological change. These experimentally determined spatial relationships, between the input of optogenetic RhoA signaling induction and the downstream output of cytoskeletal contractility, will be useful for guiding experimental design and data interpretation across optical stimulation paradigms.

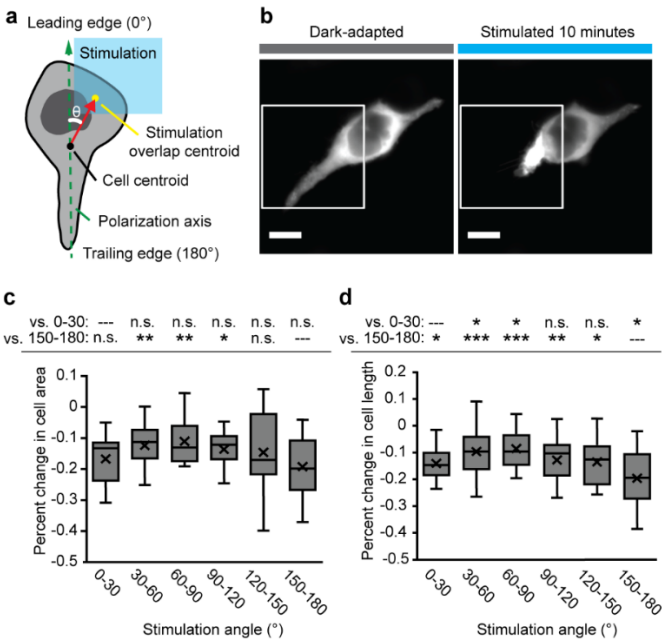

Figure 3.11 Stimulation angle dependence of opto-RhoA driven contraction

a. Schematic of stimulation angle (θ) calculation from the polarization axis, cell centroid, and centroid of the overlap region of the cell with the patterned stimulation field. **b**. Exemplar images of focal contraction of the trailing edge of a HEK cell after 10 minutes of pulsatile patterned stimulation (1.6% duty ratio). White box = illumination field. Scale = 10 μm. **c**. Box-and-whisker plot of change in cell area (relative to initial area) for binned stimulation angles. **d**. Box-and-whisker plot of change in cell length (relative to initial length) for binned stimulation angles. **c-d**. N = 10-35 independent videos per bin. Mann-Whitney U test: (*) $p < 0.05$; (**) $p < 0.01$; (***) $p < 0.001$; (n.s.) not significant. Top row = vs. 0-30° leading edge bin; bottom row = vs. 150-180° trailing edge bin. Center line, median; "X", mean; box limits, upper and lower quartiles; whiskers, 1.5x interquartile range.

3.2.6 Characterization of constitutively active opto-RhoA

For nodal dissection of RhoA signaling, opto-RhoA and opto-RhoGEF allow for GTPase- and GEF-level pathway activation. We next modified opto-RhoA to create a version in which the RhoA GTPase was constitutively active, or locked in the GTP bound state, via a G17V mutation. In theory, opto-RhoA-G17V activity is not regulated by GEF or GAP interaction. We initially hypothesized that, resulting from its lack of reliance on GEFs for activation, opto-RhoA-G17V would result in more potent cell contraction than opto-RhoA. In response to whole-field stimulation, however, the area and length

changes (**Figure 3.12a-b**) we observed were less pronounced than those generated with opto-RhoA and opto-RhoGEF (area, -8.79 ± 0.94%; length, -10.6 ± 0.72%), but still statistically significant compared to BcLOV4 (area, $p < 0.0001$, effect = 0.570; length, $p < 0.0001$, effect = 0.629).

Phalloidin stain data of dark-adapted cells expressing opto-RhoA-G17V revealed a significantly higher stress fiber level compared to BcLOV4 ($p < 0.01$ by Mann-Whitney U test) (**Figure 3.12c**). This increased basal tensile state suggests some leakiness in the constitutively active tool; its lack of reliance on GEF activation increases the probability of RhoA signal transduction in the dark by diffusive membrane contact alone. Thus, the diminished morphological changes observed relative to wildtype opto-RhoA are likely due to a decreased dynamic range. We observed a similar outcome with constitutively active Rac1, which will be discussed in Chapter 4. This finding underscores the utility of wildtype GTPase tool fusions as potent actuators of cell signaling without perturbing basal cytoskeletal states.

3.2.7 Inhibition of RhoA:RhoGEF interaction and ROCK:RhoA interaction

To confirm the dependence of observed morphological changes on RhoA signaling, we treated cells with ROCK interaction inhibitor Y-27632. For both opto-RhoA and opto-RhoGEF, cytoskeletal changes were largely abrogated, demonstrating that membrane recruitment of both tools induces downstream signaling through RhoA-ROCK interaction. Contraction was also diminished in cells treated with Rhosin, an inhibitor of RhoA-activating GEFs including ARHGEF11, the effector in opto-RhoGEF (220). Rhosin's inhibition of opto-RhoA-mediated contraction further establishes that opto-RhoA is GDP-bound in its cytosolic dark state (**Figure 3.13**).

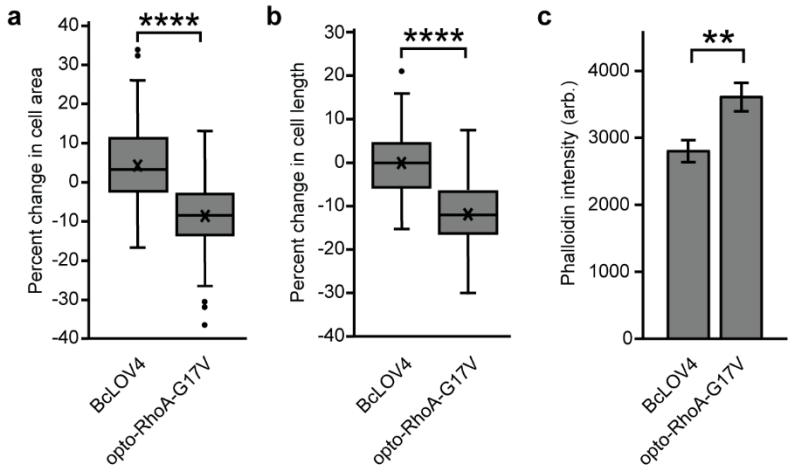

Figure 3.12 Basal and induced activity of constitutively active opto-RhoA-G17V mutant

Box-and-whisker plots of (**a**) change in cell area normalized to initial area, and (**b**) change in cell length, normalized to initial length, vs. BcLOV4-mCherry control. N = 82-90 cells each. **c**. Quantification of basal actin stress fibers in transfected cells in the dark. Mean ± SEM. N = 40 cells per condition. a-c. Mann-Whitney U test: (**) $p < 0.01$; (****); $p < 0.0001$; (n.s.) not significant.

3.2.8 Opto-RhoA-induced YAP nuclear recruitment and mechanotransduction

Having characterized opto-RhoA as a driver of RhoA-ROCK signaling and cytoskeletal tension, we next explored its role in mechanotransduction. RhoA-controlled stress fibers relay mechanical cues from the extracellular matrix to the transcriptional co-activator Yes-associated protein (YAP) and its paralog, TAZ. YAP/TAZ nuclear translocation is followed by their regulation of TEAD-family transcription factors (140, 141), linking an increase in cytoskeletal tension to a change in gene expression (**Figure 3.14a**). Beyond expanding our optogenetic toolbox to include control of downstream gene expression, controlling YAP activation with opto-RhoA could also prove useful in the study of cell migration and tissue development, in which the RhoA-YAP relay is particularly important (118, 157, 264).

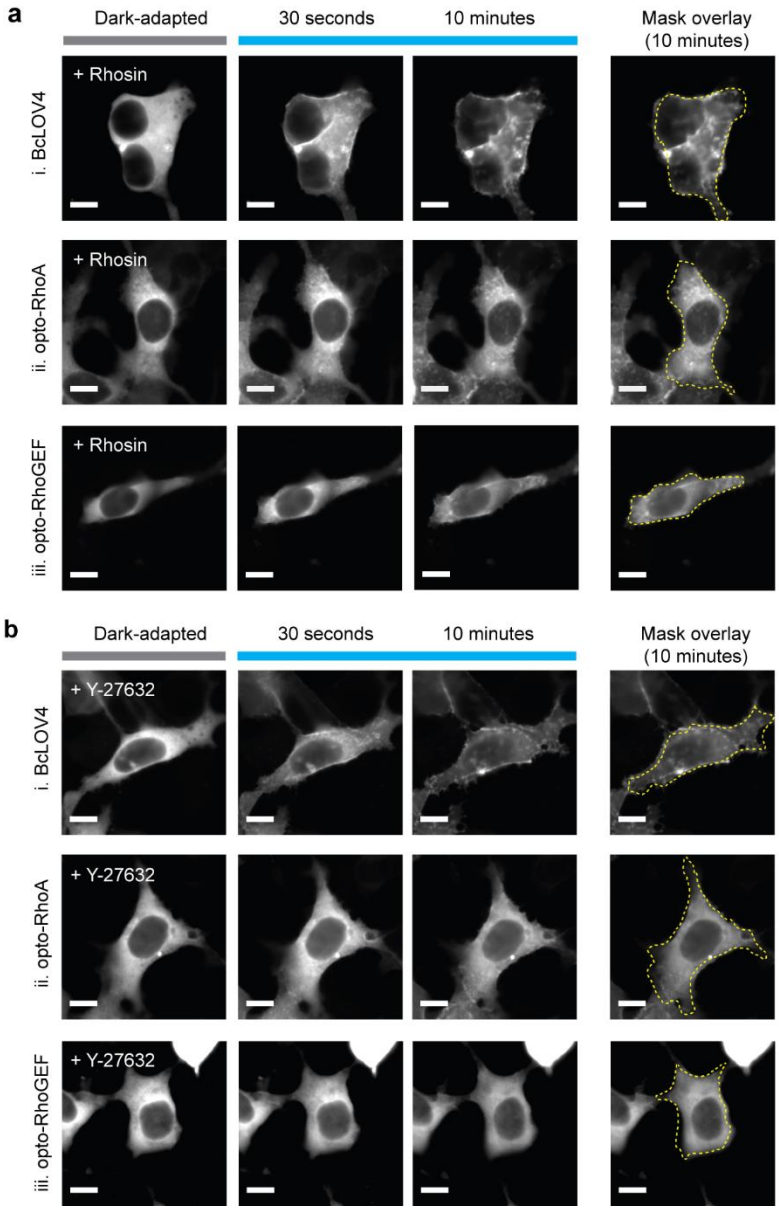

Figure 3.13 Pharmacological suppression of optogenetic RhoA pathway signaling

a. Inhibition of RhoA-GEF interaction with Rhosin in representative cells expressing (i) BcLOV4 control, (ii) opto-RhoA, (iii) opto-RhoGEF. Mask overlay shows the initial cell boundary (dotted yellow line). Optogenetic induction of contractility is largely abrogated. **b**. Inhibition of ROCK signaling by Y-27632 results in similar suppression. 1.6% stimulation duty ratio. Scale = 10 μm.

We stimulated serum-starved opto-RhoA-expressing cells co-transfected with EGFP-tagged YAP with widefield blue light (Φ = 1.6%) and monitored YAP localization over a time course of 10 minutes. We observed an influx of YAP to the nucleus (**Figure**

3.14b-c) within ~3 minutes of tool activation, in line with previous work by others showing that optogenetic activation of ARHGEF11 could drive rapid nuclear import of YAP within ~5 minutes of increased cytoskeletal tension (249). In contrast, photoactivation of effector-less BcLOV4-mCherry did not result in a change in nuclear YAP. Differences in endpoint cytosolic YAP, nuclear YAP, and nuclear:cytosol YAP ratio between opto-RhoA and BcLOV4 cells were statistically significant ($p < 0.0001$, assessed by Mann-Whitney U test) (**Figure 3.14d**).

Beyond nuclear localization, we next sought to determine whether opto-RhoA stimulation resulted in a change in transcriptional activity. Using a previously described luciferase reporter system (55) in serum-starved cells of low initial cytoskeletal tension, we measured transcriptional activity of a YAP-dependent promoter, 8XGTIIC (**Figure 3.14e**). For luciferase-only and BcLOV4 controls, no significant difference was observed between dark and photoactivated cells; for opto-RhoA, photoactivation resulted in a significant ($p < 0.05$) increase in YAP-TEAD transcriptional reporter output. Thus, we demonstrated that opto-RhoA drives an increase in cytoskeletal tension sufficient to induce YAP nuclear import and alter transcriptional activity, making it a valuable addition to the recently reported optogenetic YAP toolbox (52, 255).

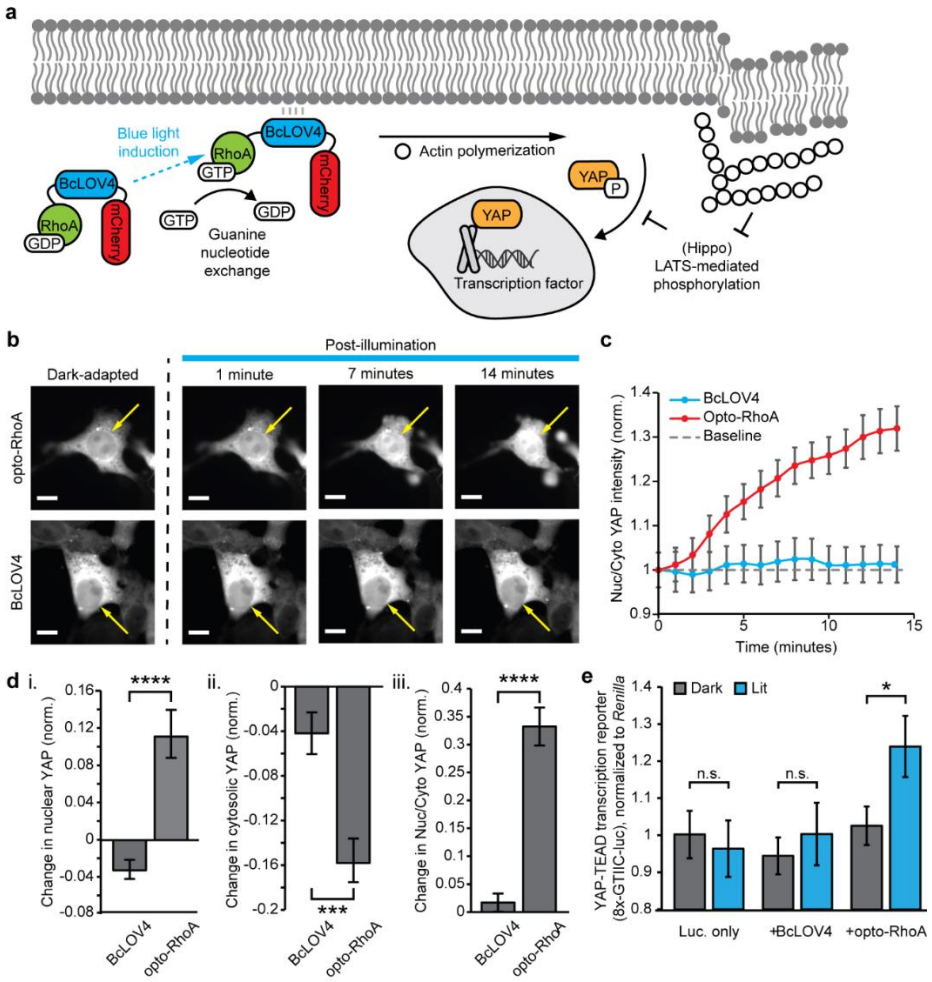

Figure 3.14 Opto-RhoA induction of YAP-dependent mechanotransduction

a. Photoactivated opto-RhoA increases cytoskeletal tension to drive YAP nuclear import and transcriptional co-activation. **b**. Exemplar images of YAP-GFP nuclear import following blue-light photoactivation of opto-RhoA and effector-less BcLOV4 control. Scale bar = 10 μm. Arrows indicate nucleus position. **c**. Nuclear:cytosolic YAP in response to 1.6% duty ratio stimulation of opto-RhoA and BcLOV4 control. N = 30 cells each. **d**. Change in (i) nuclear YAP, (ii) cytosolic YAP, and (iii) nuclear:cytosolic YAP, normalized to region area. N = 30 cells each. **e**. Dual luciferase reporter assay showing increased YAP-coactivated TEAD-dependent transcription driven by opto-RhoA but not BcLOV4-only control. Luminescence was measured from firefly luciferase under a YAP-sensitive synthetic promoter ("8xGTIIC"), normalized to co-expressed Renilla luciferase. N = 8 wells per condition. c-e. Mean ± SEM. Mann-Whitney U test: (*) $p < 0.05$; (***) $p < 0.001$; (****) $p < 0.0001$; n.s. not significant.

3.2.9 Demonstration of opto-RhoA functionality in CHO, HeLa, and 3T3 cells

We tested opto-RhoA in other cell lines to better understand its potential for use in cell migration and tissue morphogenesis studies (**Figure 3.15**). Photoactivation of

opto-RhoA was sufficient to induce cell contraction in Chinese hamster ovary (CHO), HeLa and 3T3 (mouse embryonic fibroblast) cells. In CHO and HeLa cells, a 20-40% reduction in the mass of DNA transfected (versus HEK293T cells) was required to reduce cytotoxicity. Preliminary studies in endothelial colony-forming cells (ECFCs) have resulted in significant protein aggregation in the dark-state cytosol and poor cell health, despite good tolerance of BcLOV4-mCherry expression; further optimization is required to determine viability in this line.

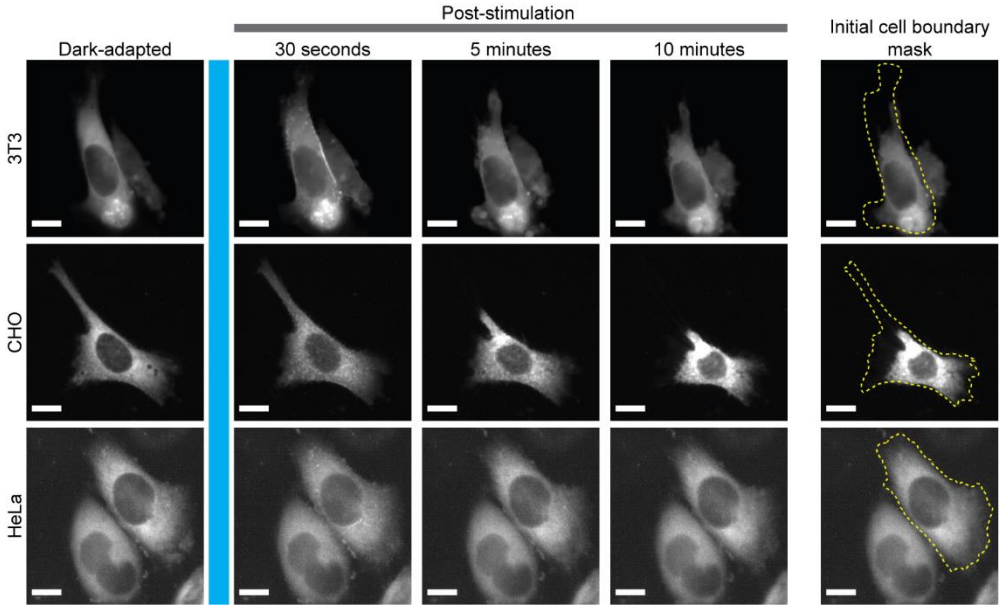

Figure 3.15 Demonstration of opto-RhoA function in other cell lines

Epifluorescence micrographs of other cell lines expressing opto-RhoA, visualized by mCherry, before and after a 5-second pulse of blue light stimulation. Dotted yellow line = cell boundary mask in the dark-adapted state. Scale = 10 μm.

3.3 Conclusions and future directions

Here, we report the engineering of single-component optogenetic RhoA GTPase and ARHGEF11 to potently drive actomyosin contractility, stress fiber formation, and rapid activation of transcriptional mechanotransduction. Opto-RhoA demonstrates that membrane recruitment of a wildtype GTPase is sufficient for pathway activation following

nucleotide exchange catalyzed by endogenous GEFs. Because the GTPase in opto-RhoA lacks a ("CAAX") prenylation site (24, 65), it is less likely to be activated by the external stimuli that activate the endogenous cellular RhoA residing at the membrane; thus, the occlusion of the RhoA C-terminus in opto-RhoA also enhances its orthogonality to the endogenous GTPase. In addition, opto-RhoA lacks a GDI (guanosine nucleotide dissociation inhibitor) binding site because of the disrupted prenlyation, which we hypothesize prevents the overexpressed opto-RhoA from destabilizing the endogenous pool of Rho-family GTPases by otherwise outcompeting it for regulatory interactions with the chaperone GDI. These features are useful for leaving the basal cytoskeletal physiology intact when opto-RhoA is inactive in its dark-adapted state.

Opto-RhoA and opto-RhoGEF exhibit similar membrane association kinetics to BcLOV4, which are favorable for manipulating cytoskeletal dynamics with high spatiotemporal precision. Throughout the data herein, opto-RhoA accumulation is observable in DMD-patterned illumination fields, even well after the induction period is complete. Such gradual accumulation of activated Rho-family GTPase is also observed with a heterodimerizing optogenetic Cdc42 created by others (12, 132). However, this accumulation is not as readily observed in control cells treated with GEF- and ROCK inhibitors, or in effector-less BcLOV4-mCherry controls, all of which exhibit similar membrane dissociation kinetics to one another. Together, these photoactivated distribution profiles and kinetics data suggest that the puncta originate de novo and persist from interactions amongst activated RhoA/actomyosin signaling complexes (10, 11), as opposed to homo-oligomerization into large photobodies, which is the clustering mechanism of Cry2-RhoA (27) (**Figure 3.16**).

In summary, we have created high-performance single-component tools for optogenetic activation of RhoA GTPase and ARHGEF11 to control cell contractility and

RhoA-driven transcriptional mechanotransduction. The accompanying characterization of how cytoskeletal changes depend on spatial patterning of the optical stimulation informs how tool performance should vary across different experimental setups and designs, and will also advance the study of diverse cell behaviors by connecting spatiotemporal patterns of focal RhoA signaling induction to the consequent cell-wide cytoskeletal responses. These tools demonstrate the versatility of BcLOV4 technology for single-component optogenetic control over peripheral membrane proteins.

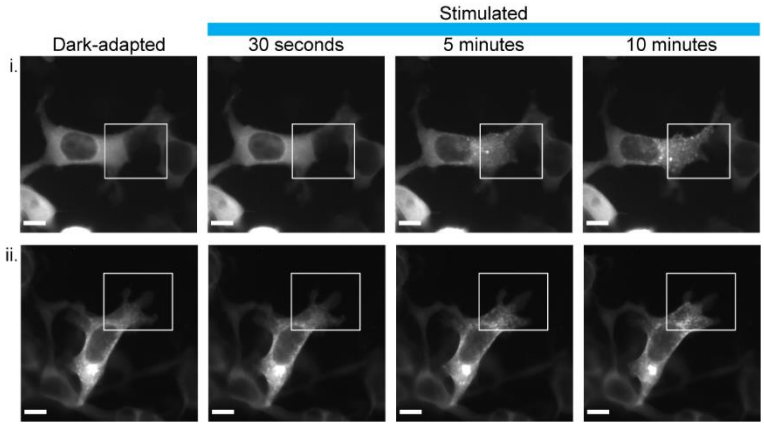

Figure 3.16 Expression of Cry2-RhoA activation by photoinduced clustering

Epifluorescence micrographs of HEK cells expressing Cry2-RhoA, visualized by mCherry. White box = spatially patterned blue light illumination field, stimulated at 1.6% duty ratio; two fields of view (i and ii). Scale = 10 μm.

3.4 Materials and methods

3.4.1 Genetic constructs

Domain arrangement combinations of BcLOV4, mCherry, and the RhoA or ARHGEF11 effector (with a flexible $(GGGS)_2$ linker between each pair) were assembled into the pcDNA3.1 mammalian expression vector under a CMV promoter by Gibson cloning with HiFi DNA Assembly Master Mix (New England Biolabs, E2621). BcLOV4 and mCherry were amplified from their previously reported mammalian codon-optimized fusion (Addgene plasmid 114595) (69). Wildtype RhoA GTPase was amplified from

CLPIT Cry2PHR-mCherry-RhoA (Addgene plasmid 42959, a kind gift from Dr. Lukasz Bugaj) without the C-terminal “CAAX” motif to prevent prenylation (27). The DNA sequence of ARHGEF11 (Genbank ID XP_011508491.1) was human codon-optimized using the Integrated DNA Technologies (IDT) Codon Optimization Tool and ordered as a gBlock®. The DH domain of this GEF was identified using the PROSITE ExPASy database and amplified from the full-length gene. The DH domain of ARHGEF12 was amplified from PR_GEF (Addgene plasmid 80407). The DH domain of ARHGEF1 was amplified from pCAG-mCherry-FKBP-GEF (Addgene plasmid 85152). All genetic constructs were transformed into competent *E. coli* (New England Biolabs, C2984H). All sequences were verified by Sanger sequencing.

The RhoA constitutively active G14V mutant was generated by QuikChange site-directed mutagenesis according to manufacturer’s instructions. Briefly, overlapping primers encoding the mutation with melting temperatures ≥ 78°C were designed using Agilent’s online primer design tool (https://www.agilent.com/store/primerDesignProgram.jsp). The mutation was introduced over 18 PCR cycles with 8-minute elongation time using the Phusion® high-fidelity DNA polymerase master mix (New England Biolabs, M0531). The opto-RhoA template plasmid was digested with DpnI for one hour at 37°C before transformation into Turbo competent cells.

The following plasmids were acquired from Addgene:

Table 3.1: Plasmids acquired from Addgene

Plasmid	Assay	Addgene #
pCIBN(deltaNLS)-pmGFP	Membrane localization kinetics	26867
mTagBFP-Nucleus-7	Actin imaging	55265
pLifeAct-miRFP703	Actin imaging	79993
pEGFP-C3-hYAP1	YAP translocation	17843
8XGTIIC-luciferase	YAP mechanotransduction	34615

Renilla luciferase plasmid was a kind gift from Dr. Lukasz Bugaj.

For bacterial overexpression and purification, non-codon-optimized BcLOV4 and mCherry were amplified from their previously reported fusion (Addgene plasmid 114596) and Gibson assembled with RhoA into the BamUK backbone with HiFi DNA Assembly Master Mix (New England Biolabs, E2621) and transformed into Turbo competent cells.

3.4.2 Cell culture and transient transfection

All mammalian cells were maintained in a 5% CO_2 water-jacketed incubator (Thermo/Forma, 3110) at 37°C. For imaging experiments, cells were seeded onto poly-D-lysine-treated glass bottom dishes (MatTek, P35GC-1.5-14-C) or into 24-well glass bottom plates (Cellvis, P24-1.5H-N), treated in-house with type I collagen, at 15-20% confluency. Cells were transfected 24 hours after seeding at ~30-40% confluency, then imaged 24-48 hours after transfection. All transfections were performed with Opti-MEM™ reduced serum media (Thermo Fisher, 3195062).

HEK293T (ATCC, CRL-3216) were cultured in D10 media composed of Dulbecco's Modified Eagle Medium with GlutaMAX (Invitrogen, 10566016), supplemented with 10% heat-inactivated fetal bovine serum (FBS) and penicillin-streptomycin at 100 U/mL. HEK cells were transfected using the TransIT-293 transfection reagent (Mirus Bio, MIR2700) according to manufacturer instructions.

Chinese Hamster Ovary (CHO) cells (cDNA Resource Center, CEM3000000) cells were cultured in Ham's F-12 Nutrient Mixture with GlutaMAX (Invitrogen, 31765035) supplemented with 10% heat-inactivated fetal bovine serum (FBS) and penicillin-streptomycin at 100 U/mL. CHO cells were transfected using TransIT-CHO transfection reagent (Mirus Bio, MIR2170) according to manufacturer instructions. For opto-RhoA, DNA transfection mass was reduced from 2.5 µg to 0.5-1.0 µg per 35 mm cell culture dish.

HeLa cells (provided by the Arjun Raj Lab, UPenn) and 3T3 cells (provided by the Lukasz Bugaj Lab, UPenn) were cultured in D10 medium as described above. Both cell lines were transfected with Lipofectamine™ 3000 transfection reagent (Thermo Fisher, L3000008) according to manufacturer instructions. For opto-RhoA in HeLa cells, DNA transfection mass was reduced from 2.5 µg to 0.5-1.0 µg per 35 mm cell culture dish.

Endothelial colony forming cells (ECFCs) (provided by the Joel Boerckel Lab, UPenn) were maintained in Endothelial Cell Growth Medium (Lonza, CC-3162) supplemented with 10% defined FBS (HyClone, SH30070.03) and penicillin-streptomycin-amphotericin B at 100 U/mL. Cells were seeded for imaging experiments between passages 4 and 6 in antibiotic-free media. ECFCs were transfected with X-TremeGENE HP (Millipore-Sigma, 6366244001) according to manufacturer instructions, using 0.2-2.0 µg DNA per 35 mm dish.

3.4.3 Fluorescence microscopy and hardware

Fluorescence microscopy was performed on an automated Leica DMI6000B fluorescence microscope under Leica MetaMorph control, with a sCMOS camera (pco.edge), an LED illuminator (Lumencor Spectra-X), and a 63× oil immersion

objective. Excitation source illumination was filtered at the LED source (mCherry imaging λ = 575/25 nm; GFP or Alexa Fluor 488 imaging or widefield BcLOV4 stimulation λ = 470/24 nm; miRFP imaging λ = 632/32 nm; BFP imaging λ = 395/25 nm). Fluorescent proteins were imaged with Chroma filters: mCherry (T585lpxr dichroic, ET630/75 nm emission filter, 0.2-0.5 s exposure), GFP (T495lpxr dichroic, ET 525/50 nm emission filter, 0.2 s exposure), miRFP703 (AT655dc dichroic, ET655 nm emission, 0.5 s exposure), BFP (455 dichroic, 480/40 nm emission, 0.2 s exposure).

Cells were imaged at room temperature in CO_2-independent media (phenol-free HBSS supplemented with 1% l-glutamine, 1% penicillin-streptomycin, 2% essential amino acids, 1% nonessential amino acids, 2.5% HEPES pH 7.0, and 10% serum).

The custom spatially patterned illuminator was (DMD) digital micromirror device-based and constructed from a digital light processor (DLP, Digital Light Innovations, CEL5500), based on a design by Trojanowski, *et al*. (243). All optics and optomechanics were from ThorLabs unless stated otherwise. A liquid light guide-coupled source (Mightex, LCS-0455-3-22) was collimated into the DLP. The DLP output was infinity corrected with an additional lens, and the coupled through a side auxiliary port window of the microscope to gain direct access to the back of the objective, by using a custom K Type laser cube (Nuhsbaum, Inc.) with a shortpass dichroic mirror (λ < 900 nm). Digital masks were drawn in the DLP Light Commander software (**Figure 3.17**).

3.4.4 Expression level and membrane:cytosol ratio measurement

HEK293T cells were co-transfected with a GFP membrane marker and mCherry-tagged tool construct in a 1:10 ratio. Cells were imaged at 63× magnification for 3-5 fields of view per construct. mCherry fluorescence was imaged with a 0.5 s exposure

time, followed by GFP fluorescence imaging (0.2 s exposure). mCherry fluorescence was the imaged again after 5 seconds of blue light stimulation.

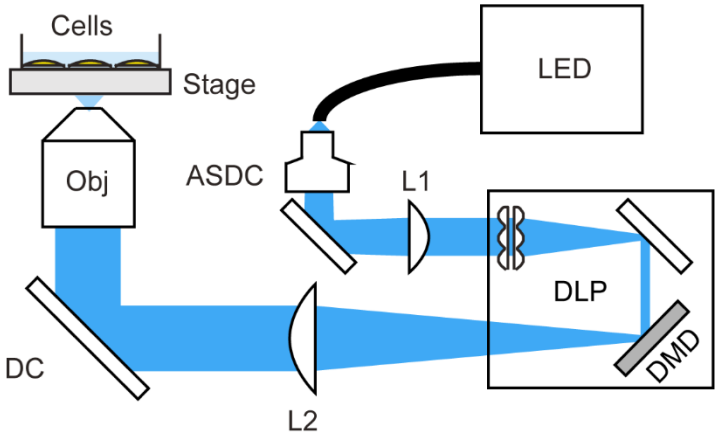

Figure 3.17 Structured illumination schematic

Light from a liquid light guide-coupled λ = 455 nm LED was collimated into the (DMD) digital micromirror device-based DLP (digital light processor, Digital Light Innovations CEL5500) via an air-spaced doublet collimator (ASDC, Thorlabs F810APC-405) and a plano-convex lens (L1, f = 200 mm). After the DLP the projected illumination pattern was infinity-corrected using another plano-convex lens (L2, f = 150 mm). The light was then redirected to the objective (Obj, 63× / 1.40 NA, Leica #506187) using a shortpass dichroic (DC, λ < 900 nm, Thorlabs DMLP900R) mounted in a custom K type laser cube (Nuhsbaum). The LED was from Mightex (LCS-0455-3-22).

To assess expression level, cells were manually segmented using the pmGFP micrograph to identify cell boundaries, and background-subtracted fluorescence was recorded for N = 25-31 cells per condition. Cell fluorescence was normalized to BcLOV4-mCherry mean fluorescence. To measure membrane:cytosol fluorescence ratio, the plasma membrane and cytosol were manually segmented using pmGFP localization as a guide. The ratio of mean membrane to cytosol fluorescence was calculated for dark-adapted and post-illumination states for N = 25-31 cells per condition.

3.4.5 Membrane localization kinetics

For membrane recruitment quantification, pmGFP was co-transfected with tool fusions as described in section 3.4.4. To prevent cell contraction, transfected cells were incubated with RhoGEF inhibitor Rhosin (Millipore-Sigma 555460, 25 μM) and ROCK inhibitor Y-27632 (Millipore-Sigma Y0503, 10 μM) for 24 hours prior to imaging, and inhibitors were also added to CO_2-independent media. A dark-state mCherry image was captured (500 ms exposure), followed by a 5-second blue light pulse with simultaneous mCherry imaging every 200 ms to monitor protein localization. The GFP membrane marker was imaged immediately after blue light stimulation for correlation analysis (200 ms exposure). mCherry was then visualized every 5 seconds for 10-15 minutes in the absence of blue light stimulation. Membrane localization and dissociation were measured by line section analysis and correlation with pmGFP in ImageJ and MATLAB. Briefly, line sections approximately 30 μm in length bisecting the plasma membrane were drawn for N = 20 cells per condition. The Pearson's correlation coefficient was measured between the mCherry and pmGFP fluorescence intensity across this line section for each frame. An exponential fit was applied to calculate τ_{on} and τ_{off} values and 95% confidence intervals for each construct.

3.4.6 Widefield and DMD stimulation assays

For widefield stimulation assays, mCherry fluorescence was imaged before a 5-second pulse of blue light. mCherry fluorescence was then imaged every 15-30 seconds for 10 minutes following stimulation. For data analysis, each cell was treated as a separate data point, with N = 82-93 cells from 10-12 field-of-view videos per condition, 6-8 cells per video.

For DMD stimulation assays, mCherry fluorescence was imaged every 15 seconds for 10 minutes. During this time, cells were stimulated for one second per minute (1.6% duty cycle) patterned illumination (25 μm-wide square encompassing ~25% of cell area). The stimulation angle was defined as the angle defined by the polarization axis and the line segment between the cell centroid and the centroid of the stimulated cell area. Each data point was derived from one cell in an independent video, and cells were binned by angle of stimulation, with bin widths of 30 degrees spanning 0-180 degrees, N = 10-35 videos per bin.

For widefield and DMD stimulation assays, statistical significance was assessed by the two-sided non-parametric Mann-Whitney U test, uncorrected for multiple comparisons.

3.4.7 Cell morphology analysis pipeline

Change in cell area, cell length, and centroid movement were computed via a custom analysis Python script (**Figure 3.8a**). For whole-field stimulation assays, videos of an entire field-of-view were cropped so that each contained only one cell. Contours of the cell membrane and nucleus were identified using the threshold function in OpenCV. Each video was rotated by increments of 5 degrees until the long polarization axis of the cell aligned with the y-axis, and then a cell-bounding rectangle was calculated using the Imutils package with the short edge aligned with the x-axis; the angle of rotation was chosen such that the cell nucleus was closer to the top of the rectangle as a morphological marker for the cell leading edge, as confirmed by LifeAct imaging. Binary masks of the cell at initial (t = 0 min) and final (t = 10 min) timepoints were created for each cell. The change in cell area was calculated by finding the percent change in the area bounded by the cell contours at the final timepoint relative to its area at the initial

timepoint. Change in cell length was calculated using the height of the bounding rectangle at the final and initial timepoints.

For experiments with spatially patterned illumination, a similar imaging processing workflow was followed. The angle of rotation was calculated as above, and binary masks of the cell at the initial and final timepoints and the stimulation zone were created and rotated such that the leading edge of the cell was positioned at the top of the image. Masks of the cell regions inside (the overlap) and outside (the non-overlap) the stimulation zone were created using the OpenCV bitwise operation functions “and” and “xor”, respectively. The centroids of the whole cell and the overlap region were computed at the initial and final timepoints. The angle of stimulation was defined as the angle between (i) the vector connecting the initial cell centroid and overlap region centroid and (ii) the vertical vector between the initial cell centroid and the leading edge of the cell.

For analysis of morphological markers of cell polarization, HEK293T cells were co-transfected with a nuclear marker (mTagBFP-Nucleus-7) and miRFP703-tagged LifeAct. The data analysis pipeline was applied to align the long axis of the cell with the y-axis, and to position the nucleus closer to the top of the cell as a putative marker of the leading edge. The actin arc was then located by identifying the brightest LifeAct-miRFP703 region of at least 5 μm^2 in area. The angle between the long axis and the vector connecting the cell centroid to the actin arc centroid was then calculated to verify that the actin arc occurs at the computationally identified leading edge of the cell.

3.4.8 Phalloidin staining

Cells were plated in 24-well tissue culture treated plates (CytoOne, CC7682-75240) and transfected as described in section 3.4.2. 24 hours after transfection, cells

were washed with PBS and the media was replaced with DMEM supplemented with penicillin-streptomycin and without FBS. Light-exposed 24-well tissue culture-treated plates were incubated under Arduino-controlled blue strip LEDs (light intensity 15 mW/cm^2) strobing at a 1.6% stimulation duty cycle in a 5% CO_2 water-jacketed incubator for two hours. Cells were fixed with 4% paraformaldehyde in PBS at room temperature for 10 minutes, washed twice with PBS (5 min per wash), and then permeabilized with 0.1% Triton-x-100 in PBS for 15 minutes. Cells were blocked with 1% BSA in PBS for 30 minutes, then stained with Alexa Fluor 488 Phalloidin (Invitrogen, A12379) diluted 1:400 in PBS for 20 minutes at room temperature, protected from light. Plates were washed twice prior to imaging. Total filamentous actin was quantified by normalizing total cell Alexa Fluor 488 fluorescence to cell area, with N = 40 cells per condition.

3.4.9 Pharmacological inhibition assays

The GEF inhibitor Rhosin (Millipore-Sigma, 555460) was added to cells at 25 µM final concentration upon transfection, 24 hours before imaging. ROCK inhibitor Y-27632 (Millipore-Sigma, Y0503) was similarly added to cells at 10 µM final concentration. Inhibitors were also added at the same final concentration to the CO_2-independent media in which the cells were imaged.

3.4.10 YAP nuclear localization assay

HEK293T cells were initially plated at 75% confluency in 10 cm dishes to drive YAP to the cytosol. Cells were then passaged one day later and seeded at 25% confluency in 35 mm poly-D-lysine-treated glass bottom dishes. The next day, dishes were washed with PBS (5 min per wash) and media was replaced with DMEM supplemented with 2% heat-inactivated FBS and penicillin-streptomycin. Cells were

then transfected with a 4:1 ratio of opto-RhoA-mCherry or BcLOV4-mCherry to EGFP-YAP. EGFP-YAP was imaged every 15 seconds using a 250 msec excitation pulse that also stimulated BcLOV4, and mCherry fluorescence was imaged every minute. Nuclear and cytosolic fluorescence normalized to the area of each region was calculated every minute by manual segmentation in ImageJ, with N = 20 cells per condition.

3.4.11 YAP-mediated mechanotransduction assay

YAP-TEAD-dependent transcriptional activity was quantified using a dual luciferase reporter system (Promega, E1910). HEK293T cells were co-transfected with plasmids encoding 8XGTIIC-luciferase, a YAP-sensitive promoter driving firefly luciferase expression (500 ng); *Renilla* luciferase (500 ng); and BcLOV4-mCherry or opto-RhoA-mCherry (1500 ng). At transfection, full media was replaced with DMEM supplemented with 2% heat-inactivated FBS and penicillin-streptomycin. Half the cells were incubated under pulsing blue light with a 1.6% stimulation duty cycle for 12 hours. Cells were lysed according to manufacturer instructions. Luminescence was measured in white 96-well plates (Corning, 3917) on a Tecan M200 spectrophotometer with a 10 second integration time. The firefly luminescence value for each sample was normalized to its Renilla luciferase readout. N = 8 lysate samples per condition.

CHAPTER FOUR: Optogenetic tools for induction of cell protrusion

This chapter adapts work from the following publications:

(1) Berlew, E. E.; Kuznetsov, I. A.; Yamada, K.; Bugaj, L. J.; Chow, B. Y., Optogenetic Rac1 engineered from membrane lipid-binding RGS-LOV for inducible lamellipodia formation. *Photochem Photobiol Sci* 2020.

Author contributions: EEB designed genetic constructs, designed experiments, and conducted all experiments. IAK designed experiments, contributed to all experiments, constructed the patterned illumination system, and performed the blinded data analysis. KY assisted with molecular cloning and cellular assays. LJB and BYC coordinated all research. All authors contributed to data analysis and manuscript preparation.

(2) Berlew, E. E.; Yamada, K.; Kuznetsov, I. A.; Rand, E. A.; Ochs, C. C.; Jaber, Z.; Gardner, K. H.; Chow, B. Y., Designing single-component optogenetic membrane recruitment systems: the Rho-family GTPase signaling toolbox. *ACS Syn Biol* 2022.

Author contributions: EEB and KY designed genetic constructs, designed experiments, conducted experiments, and analyzed data. IAK constructed the patterned illumination system, conducted the FRAP measurement, and contributed to automated data analysis development. EAR and CO assisted with genetic construct design, engineering, and assays. BYC coordinated all research. All authors contributed to data analysis and manuscript preparation.

4.1 Introduction

4.1.1 Cell protrusions

The ability of cells to grow, change shape, and migrate depends on their ability to generate a pushing force from actin polymerization (189, 227). In addition to the contractile force-inducing RhoA, the Rho family of small GTPases also contains protrusion-forming Rac1 and Cdc42; together with RhoA, these proteins are tightly controlled in space and time to coordinate cytoskeletal changes enabling cell motility (117), wound healing (1), and cytokinesis (131). Rac1 and Cdc42 signaling is essential in the formation of tissues and organs; its dysregulation can result in tumorigenesis (152). The precise spatiotemporal requirements of these signaling pathways make them appealing candidates for optogenetic manipulation.

4.1.1.1 The Rac1 signaling pathway

The Rho-family GTPase Rac1 drives the formation of sheet-like cellular protrusions called lamellipodia and plays an essential regulatory role in cell growth and migration (46) (**Figure 4.1a**). Like other GTPases, Rac1 is GDP-bound in its inactive state; activation occurs following membrane translocation by interaction with GEFs, the best studied of which include Tiam1, P-Rex1, and Trio (154, 155). Active, GTP-bound Rac1 initiates downstream actin polymerization through WAVE (WASp-family verprolin-homologous) protein-scaffolded interaction with the Arp2/3 (actin-regulated proteins) regulatory complex (190, 191, 224). Overactivation of Rac1 can result in the formation of solid tumors (48, 125), making it a promising therapeutic target (32). Beyond its translational potential of new biological insights, the creation of new optogenetic tools for Rac1 signaling perturbation will enable investigation of the many open questions remain

in understanding Rac1 signaling, including how Rac1 and RhoA activation is temporally controlled at the leading edge of the cell to coordinate directional migration (176).

4.1.1.2 The Cdc42 signaling pathway

Cdc42 signals through a mechanism similar to that of Rac1. Following membrane recruitment and GEF-mediated activation, it also activates Arp2/3-mediated cytoskeletal rearrangement, but Cdc42 interacts with WASp (Wiscott-Aldrich Syndrome protein) instead of WAVE, resulting in a different actin polymerization paradigm that produces shorter, spiky filopodia (47) (**Figure 4.1b**). Cdc42 plays a role in chemokine-driven tumor cell invasion through its crosstalk with RhoA (226), with which it shares several interacting GEFs and GAPs (170).

4.1.2 Existing tools for Rac1 and Cdc42 signaling perturbation

Like RhoA, Rac1 and Cdc42 signal at the plasma membrane, making light-induced membrane recruitment a viable strategy for spatiotemporally precise pathway initiation. For Rac1, most tools (81, 116, 139, 248) sequester RacGEF Tiam1 in the cytosol in the off state by fusing it to a half of an optogenetic heterodimerizing protein pair, with the other half anchored to the membrane. Light-induced conformational change drives heterodimerization and membrane recruitment of Tiam1, where it can activate endogenous membrane-localized Rac1 GTPase. Another approach involves fusing the Rac1 GTPase to AsLOV2 (261, 262), with its downstream protein-interacting surface sterically occluded by AsLOV2 in the protein's dark, as in PA-Rac1. Blue light stimulation induces AsLOV2 conformational change and uncaging of Rac1, allowing it to initiate the lamellipodia formation pathway. However, tool function relies upon point mutations to Rac1 to lock it in its active, GTP-bound state by Inhibiting interaction with guanine

nucleotide dissociation inhibitors (Q61L) and GTPase accelerating proteins (E91H and N92H), relieving the GTPase of the need for GEF activation. This feature results in a propensity for spurious pathway activation following transient contact between PA-Rac1 and the plasma membrane, decreasing its spatiotemporal resolution and requiring stringent experimental setups to prevent unintended illumination (262) which are not feasible in all lab settings.

Existing systems for optogenetic perturbation of Cdc42 signaling are all two-component, using heterodimerization pairs to recruit either catalytic domains of the Cdc42 GEF Intersectin1 (81, 113, 139, 225) or the GTPase itself (132). As discussed earlier, two-protein systems occupy an increased genetic payload in the cell and require the use of two optical channels for visualization of each protein component in addition to the stimulation channel, significantly decreasing the available bandwidth for imaging other wavelengths in the assay. The available tools for inducing the spatiotemporally precise formation of cell protrusions are limited to GEF-level activation, two-component systems, and/or low-resolution of using a constitutively active GTPase, leaving room for improvement with the BcLOV4 system.

4.1.3 Problem statement

Optogenetic tools for the induction of Rac1 and Cdc42 signaling at the GTPase and GEF level are needed to probe the spatiotemporal nuances of cell protrusion formation and to study cell migration and morphogenesis. Given the limitations of existing two-component or constitutively active systems, we sought to create BcLOV4 fusions of wildtype GTPases Rac1 and Cdc42 and two of their respective GEFs, Tiam1 and Intersectin1. For GTPase tools, blue light induces membrane localization of the

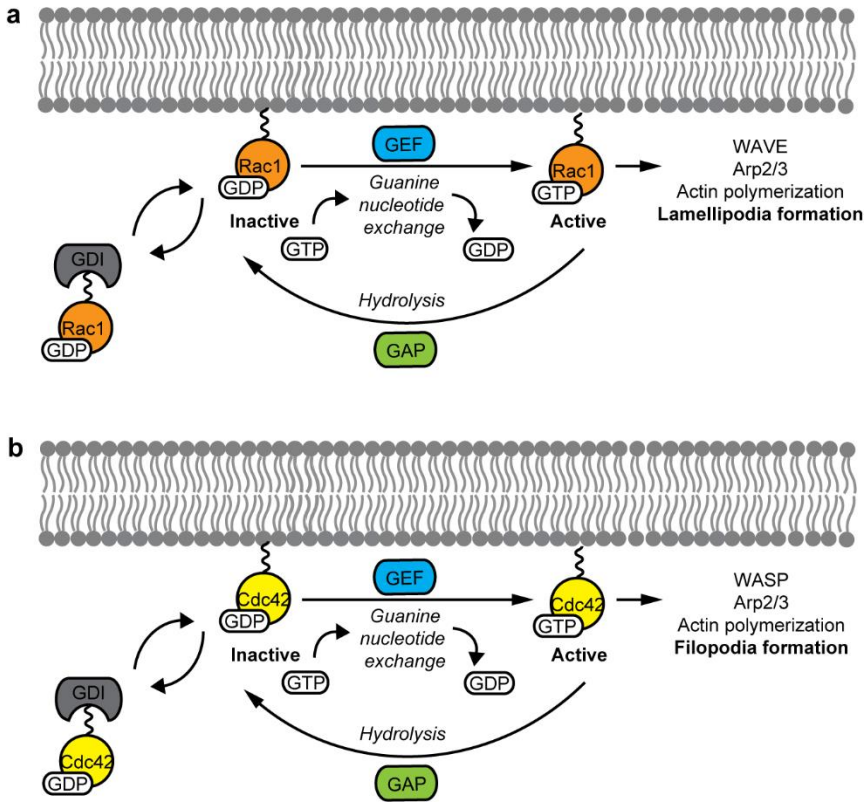

Figure 4.1 The Rac1 and Cdc42 signaling pathways

Rac1 and Cdc42 signaling are regulated by guanine nucleotide exchange factors (GEFs), GTPase accelerating proteins (GAPs), and guanosine nucleotide dissociation inhibitors (GDIs). **a**. Following nucleotide exchange, Rac1 initiates actin polymerization and lamellipodia formation through WAVE (WASP-family verprolin-homologous) and the Arp2/3 (actin regulatory protein) complex. **b**. Cdc42 initiates actin polymerization and filopodia formation through WASP (Wiscott-Aldrich Syndrome Protein) and Arp2/3.

wildtype GTPase fused to BcLOV4, where it undergoes nucleotide exchange and GTP loading by endogenous pathway GEFs. In its active form, the GTPase can then interact with downstream effectors for initiation of actin polymerization. At the membrane, GEF tools catalyze activation of endogenous membrane-bound GTPases, which similarly initiate downstream signaling (**Figures 4.2-4.3**). Development of these tools will also complete the Rho-family BcLOV4 activation toolbox, allowing for the disentanglement of RhoA-Rac1-Cdc42 interactions on the same optogenetic platform.

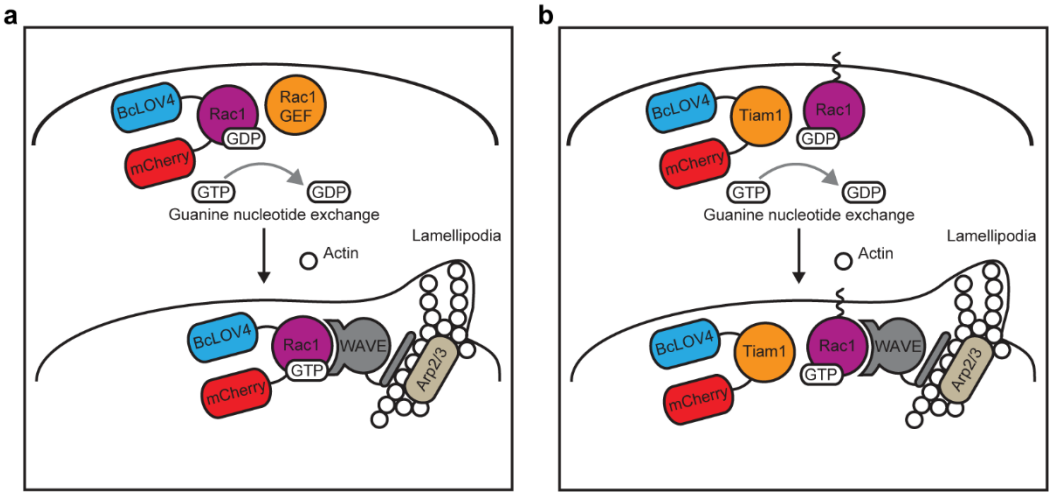

Figure 4.2 Schematic of opto-Rac1 and opto-Tiam1 tool function

Schematized induction of cytoskeletal changes and contractile signaling in response to (**a**) opto-Rac1 and (**b**) opto-Tiam1 activation by BcLOV4-mediated membrane translocation.

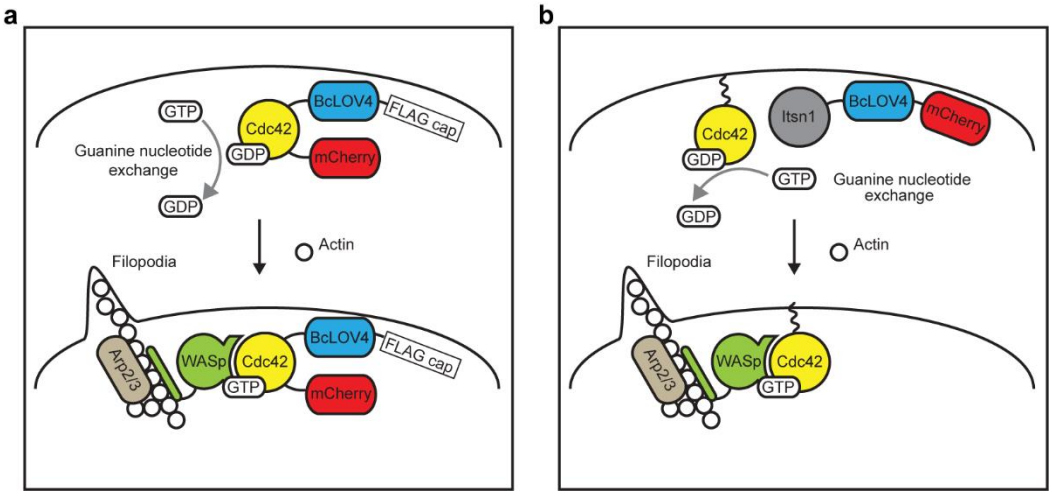

Figure 4.3 Schematic of opto-Cdc42 and opto-Intersectin1 tool function

Schematized induction of cytoskeletal changes and contractile signaling in response to (**a**) opto-Cdc42 and (**b**) opto-Intersectin1 activation by BcLOV4-mediated membrane translocation.

4.2 Results and discussion

4.2.1 Design and screening of opto-Rac1

To engineer opto-Rac1, we screened domain arrangement orderings of mammalian codon-optimized BcLOV4, human Rac1, and a mCherry visualization tag, with a glycine/serine-rich flexible linker, $(GGGS)_2$, between the respective domain pairs. To enable cytosolic sequestration of the Rac1 effector and limit membrane localization of BcLOV4-fusion proteins in the dark-adapted state, a single leucine residue was truncated from the Rac1 C-terminal prenylation site ("CLLL," or more generally "CAAX") (204). These domain combinations were then screened in transfected HEK cells for protein expression uniformity, relative expression level, and light-activated translocation efficiency in response to whole-field illumination with blue light (**Figure 4.4**).

BcLOV4-Rac1-mCherry was chosen as opto-Rac1. This particular domain arrangement was uniformly distributed throughout the cytosol in the dark-adapted state, retained its ability to be reversibly recruited to the membrane upon illumination with similar efficiency to the BcLOV4-mCherry reference protein. Other domain arrangements were not considered viable because their inducible membrane recruitment capabilities were reduced and they displayed undesirable expression profiles, evidenced by poor cell health (e.g. round morphology in domain arrangement mCherry-BcLOV4-Rac1), permanent localization to membrane or trans-Golgi network in the dark, or nuclear sequestration, the latter potentially from exposure of the Rac1 nuclear shuttling sequence (136) that is possible with disrupted prenylation (161). The observed nuclear sequestration was unlikely to depend on cell cycle phase (160), since it is the dominant phenotype observed in an unsynchronized population for domain arrangements BcLOV4-mCherry-Rac1 and Rac1-BcLOV4-mCherry (**Figure 4.5**).

The membrane localization in the dark-adapted state observed when BcLOV4 is at the C-terminus of the chimera (domain arrangements Rac1-mCherry-BcLOV4 and mCherry-Rac1-BcLOV4) suggests that such configurations are disfavored when engineering fusion proteins. This phenomenon will be further explored in Chapter 6.

4.2.2 DMD stimulation-induced lamellipodia formation with opto-Rac1

To test optogenetic function for spatially precise induction of lamellipodia formation, cells expressing opto-Rac1 were stimulated with spatially patterned blue light using a digital micromirror device to emulate a sensory activation gradient. Because BcLOV4 undocks from the membrane within approximately one minute in the dark (68, 70), cells were provided a brief stimulation pulse every 30-60 seconds. Sprawling sheet-like lamellipodial protrusions were rapidly and selectively initiated in the blue light-illuminated field and remained largely confined to the spatial field upon reaching the boundary (**Figure 4.6**). Thus, opto-Rac1 induction of lamellipodia formation is spatially restricted.

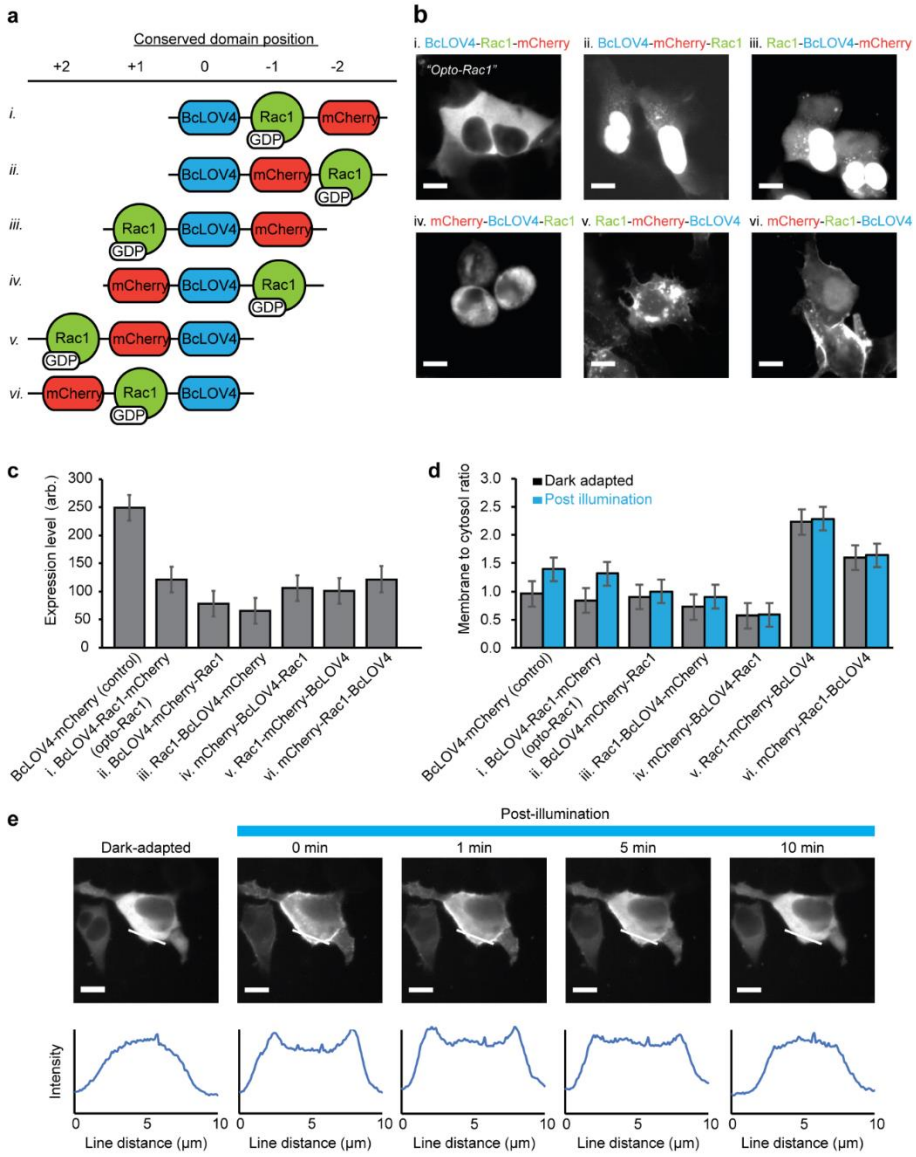

Figure 4.4 Molecular engineering of opto-Rac1

a. Domain arrangement combinations of BcLOV4, wildtype human Rac1, and mCherry visualization tag that were tested. Domains were separated by flexible $(GGGS)_2$ linkers. Candidates were tested for relative expression level and translocation efficiency vs. BcLOV4-mCherry in transfected HEK cells. BcLOV4-Rac1-mCherry was ultimately selected as opto-Rac1 based on its uniform localization profile in the dark-adapted state and similar translocation efficiency to BcLOV4-mCherry. **b**. Fluorescence micrographs showing representative expression patterns of the six arrangements in the dark-adapted state. **c**. Relative expression level vs. BcLOV4-mCherry control with no effector. **d**. Ratio of membrane-localized vs. cytosolic protein for the engineered arrangements (normalized vs. BcLOV4-mCherry control) in the dark-adapted and blue light-illuminated state. N = 25-35 each. Mean ± SEM. **e**. Dynamic membrane localization of opto-Rac1 is reversible under whole-field illumination. Top = Fluorescence micrograph, Scale = 10 µm. Bottom = Line section pixel intensity.

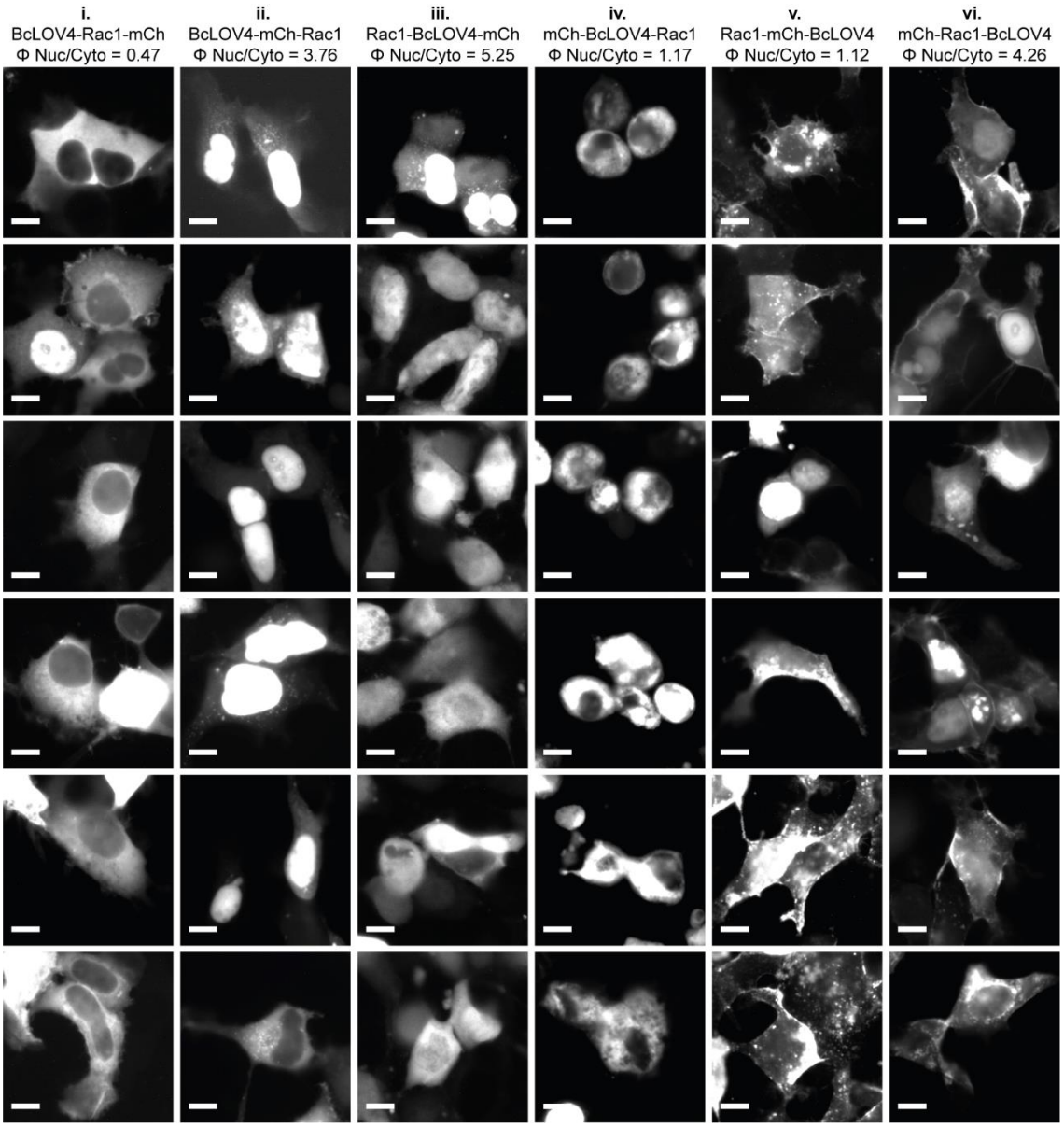

Figure 4.5 Representative distribution of Rac1 construct expression profile in HEK cells

Fluorescence micrographs of transfected HEK cells in the dark-adapted state. (Φ Nuc/Cyto) = ratio of observed average fluorescence intensity in the nucleus vs. cytoplasm (N = 25-35 each). The dominant preference for nuclear localization of genetic constructs ii. and iii., plus their lack of plasma membrane localization, indicates that their nuclear localization is not a consequence of cell cycle phase or sequestration by the plasma membrane. Scale = 10 µm.

We assessed the phenotypic response to different stimulation duty ratios to gauge the functional efficiency of opto-Rac1 and guide experimental parameters for future use. Duty ratio (Φ) was chosen as the “sensitivity” parameter because it is easier to precisely control optical stimulation timing than intensity over time. The 15 mW/cm^2 irradiance was chosen as it is sufficient to saturate flavin photocycling, but this photochemical threshold at the protein-level was not exceeded to avoid photobleaching or compensating for inefficient optogenetic function at the cell signaling level. We quantified the extent of induced lamellipodia formation as the average movement of the stimulated cell boundary over the first two minutes, since protrusions were clearly observable during this initial post-induction period and the spatial confinement of lamellipodia induction to the illumination field decreases the average movement over longer periods. Opto-Rac1 performed consistently at Φ = 1.6% duty ratio, which for context is in the low end of the duty ratio range of Φ ~ 2.5 – 20% that has been reported for related tools for small GTPase signaling with blue light photoreceptors (47, 180, 198, 252, 253). Cell border change for each opto-Rac1 duty cycle was statistically significant compared to BcLOV4-mCherry expressing cells stimulated with a 5.0% duty cycle ($p < 0.01$) (**Figure 4.7**). Thus, the optogenetic efficiency of opto-Rac1 is sufficient to perform reliably on commonplace microscopy setups without major photobleaching risks.

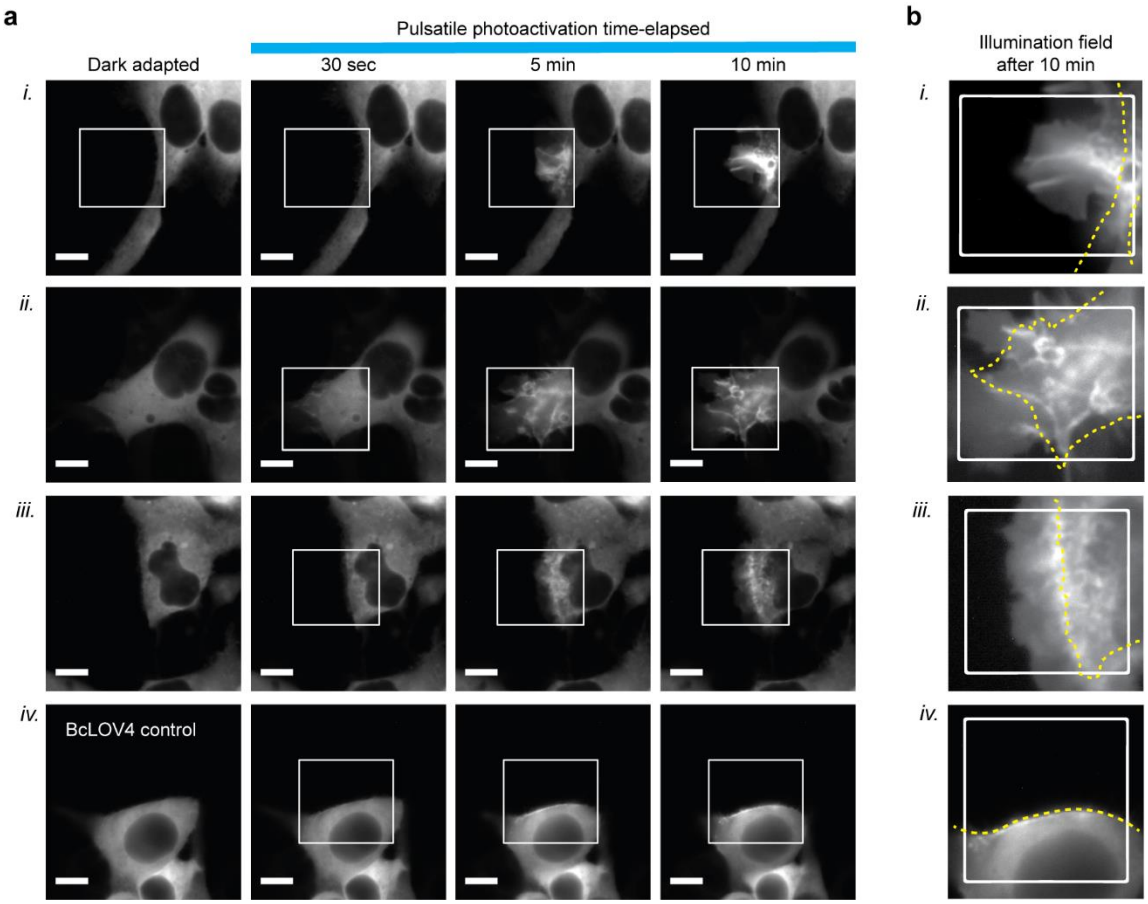

Figure 4.6 Spatially precise induction of lamellipodia formation by opto-Rac1

a. Fluorescence micrographs of three different transfected HEK cells and a BcLOV4 control. Protrusions are rapidly formed in the patterned illumination field for opto-Rac1, and remain largely restricted to the field even many minutes after reaching the edge. Opto-Rac1 also accumulates selectively within the field in an actin network-dependent manner. No protrusions are observed for the effector-less control. Scale = 10 µm. **b**. Region of interest (ROI) selection around the illumination field of view after 10 minutes of pulsatile stimulation show sheet-like protrusions. Indices i-iv correspond to those in panel a, with auto-adjusted levels for the ROI. White box = illumination field. Dotted yellow line = mask of original cell boundary. (**a-b**) λ = 455 nm at 15 mW/cm^2, 1.6 – 5.0% duty ratio.

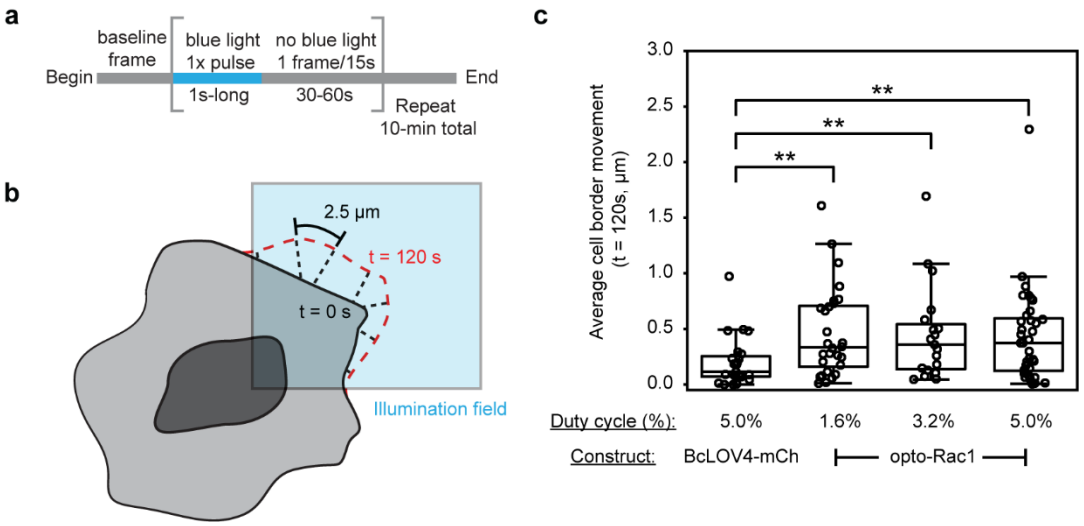

Figure 4.7 Quantification of opto-Rac1 induction of lamellipodia formation

a. Stimulation epochs using a digital micromirror device to spatially pattern illumination fields. **b**. Analysis methodology to determine distance moved by cell. The cell border was manually segmented at 0 seconds post-illumination (black solid border) and at 120 seconds post-illumination (red dashed line). The distance moved by the cell was defined as the mean length of line segments (black dashed line) that were normal to the cell border at 120 seconds, with one endpoint at the t = 0 border and the other endpoint at the t = 120 s border. Line segments were spaced at 2.5 µm intervals along the t = 120 s border. **c**. Lamellipodia formation in response to stimulation duty cycles, with irradiance fixed at the saturation threshold for flavin photocycling. Phenotypic response was quantified by average distance of cell border movement in the illumination field after two minutes. N = 19-37 independent videos each. Mann-Whitney U test: (*) $p < 0.05$, (**) $p < 0.01$ vs. BcLOV4-mCherry control (no Rac1 effector). $\lambda = 455$ nm at 15 mW/cm^2.

4.2.3 Inhibition of Rac1:RacGEF interaction and actin polymerization

To confirm that the wildtype Rac1 domain can be recruited to the membrane in its inactive GDP-bound form as proposed, we performed the spatially patterned induction experiments in the presence of a Rac1-GEF inhibitor NSC 23766 (25, 64), with a high Φ = 5% to ensure robust photochemical activation. NSC 23766 inhibits the interaction between Rac1 and two of its GEFs, Trio and Tiam1. Opto-Rac1 still selectively bound the membrane in illumination field, but lamellipodia formation was suppressed by this pharmacological inhibition monomers ($p < 0.05$ versus untreated, DMD-stimulated opto-Rac1 cells). This finding confirms that its membrane recruitment is GEF-independent and indicates that the wildtype effector domain is in its inactive or

GDP-bound when opto-Rac1 is initially recruited to the membrane. This signaling mode is consistent with single-molecule tracking studies showing that membrane localization of Rac-GDP precedes GEF-activation in natural Rac1 signaling, and is sufficient for actin polymerization (46) (**Figure 4.8a**).

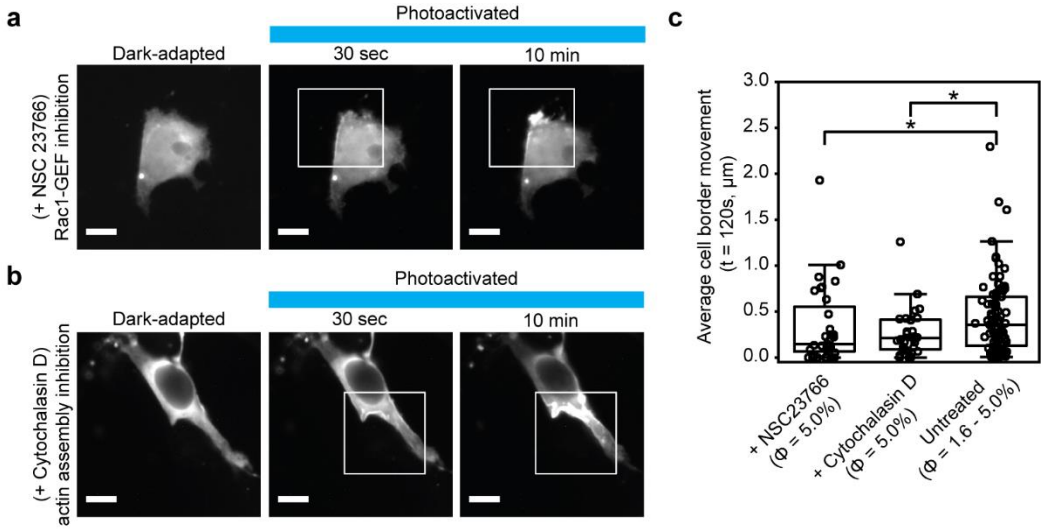

Figure 4.8 Pharmacological inhibition of opto-Rac1 activity

Optogenetic signaling proceeds by GEF-activation of GDP-bound wildtype Rac1 upon membrane localization, followed by downstream actin polymerization. **a**-**b**. Fluorescence micrographs of transfected HEK cells expressing opto-Rac1, treated with the (**a**) Rac1- GEF inhibitor NSC 23766 and (**b**) the actin polymerization inhibitor cytochalasin D. Opto-Rac1 accumulates at the membrane within the patterned illumination field (box) but does not induce lamellipodia formation. λ = 455 nm at 15 mW/cm^2, 5% duty ratio. Scale = 10 µm. **c**. Population level data to quantify pharmacological suppression of opto-Rac1 activity. Mann Whitney U test (*) $p < 0.05$. N = 31 (+ NSC 23766), N = 30 (+ cytochalasin D) independent videos each.

Lamellipodia formation was also inhibited in the presence of the actin polymerization inhibitor cytochalasin D (214), which binds the barbed end of growing actin filaments to block the addition of new actin monomers ($p < 0.05$ versus untreated, DMD-stimulated opto-Rac1 cells). This finding confirms that the cytoskeletal rearrangements were actin-mediated and not a spurious byproduct of other Rac1 signaling pathways or protein accumulation at the inner leaflet. Opto-Rac1 did not

accumulate strongly in the illumination field in the presence of either inhibitor, unlike when actin polymerization is possible, and thus the latter observed accumulation stems from opto-Rac1 binding to a polymerized actin network (**Figure 4.8b**).

4.2.4 Comparison of opto-Rac1 to PA-Rac1

The opto-Rac1 signaling mechanism is distinct from previously reported genetically encoded approaches for inducible Rac1 activity, which have used Rac1-activating GEFs or constitutively active (CA) proteins mutated to eliminate inhibitory interactions with GDI (guanosine nucleotide dissociation inhibitor) and GAPs (GTPase-activating protein) (33, 78, 106, 198, 260, 263). While membrane recruitment systems have not yet been reported using wildtype Rac1 effector (vs. CA-Rac1 or indirect Rac1-GEFs), its use clearly permits effective opto-Rac1 signaling and suggests that basal GEF levels are sufficient to support signaling in response to rapid increases in membrane concentration of GDP-bound Rac1. It should be noted that mutation of the Rac1 domain in opto-Rac1 to CA-Rac1 (260) (corresponding to the GDI-interaction site, Q61L, and the GAP-interaction sites, E91H and N92H) was toxic with evidence of basal activity (**Figure 4.9**). Thus, the use of wildtype Rac1 effector contributes to the optogenetic efficacy, possibly by reducing basal activity of opto-Rac1, which was negligible under normal laboratory conditions (without precautions for blue light-exposure other than brief assay dark-adaptation period) that were less stringent than reported precautions needed to limit basal activity of PA-Rac1, where all cell handling and assays are conducted in darkness (including baffling electronic displays) (263).

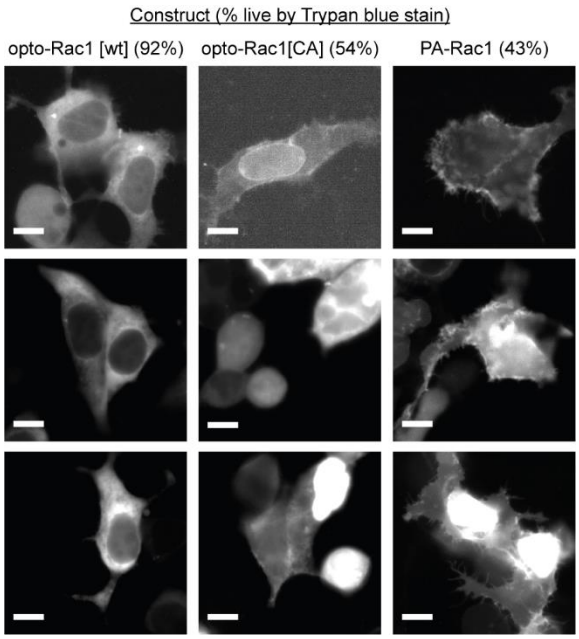

Figure 4.9 Expression of constitutively active Rac1 constructs in HEK cells

Multiple representative cells were imaged in the dark-adapted state. Constitutively active [CA] Rac1 fused to BcLOV4 reduced cell health based on Trypan Blue live/dead cell count, and compromised morphology with evidence of spurious activity in the dark-adapted state. The top-center image, chosen to demonstrate permanent membrane localization in non-rounded cells, shows high background after auto-contrast because of dimmer raw fluorescence. For reference, photoactivatable Rac1 (PA-Rac1), a fusion of AsLOV2 and constitutively active Rac1, shows spurious sheet-like protrusions in the dark-adapted state under similar laboratory conditions. Scale bar = 10 µm.

4.2.5 Design and screening of opto-Tiam1

To engineer an optogenetic tool for induction of Rac1 signaling at the GEF level, we chose to work with the 28 kDa DH domain of Tiam1 based on its previous use in heterodimerization-based activation tools (47, 245). We followed a similar screening workflow as for opto-Rac1, with the addition of two C-terminal FLAG-tagged domain arrangements following our observation that domain arrangements with BcLOV4 at its C-terminus are generally unsuitable for tool engineering (see Chapter 6). With the exception of Tiam1-mCherry-BcLOV4 and mCherry-Tiam1-BcLOV4, all screened

constructs exhibited uniform cytosolic fluorescence in HEK293T cells and an increase in membrane-localized protein following blue light stimulation (**Figure 4.10a-c**).

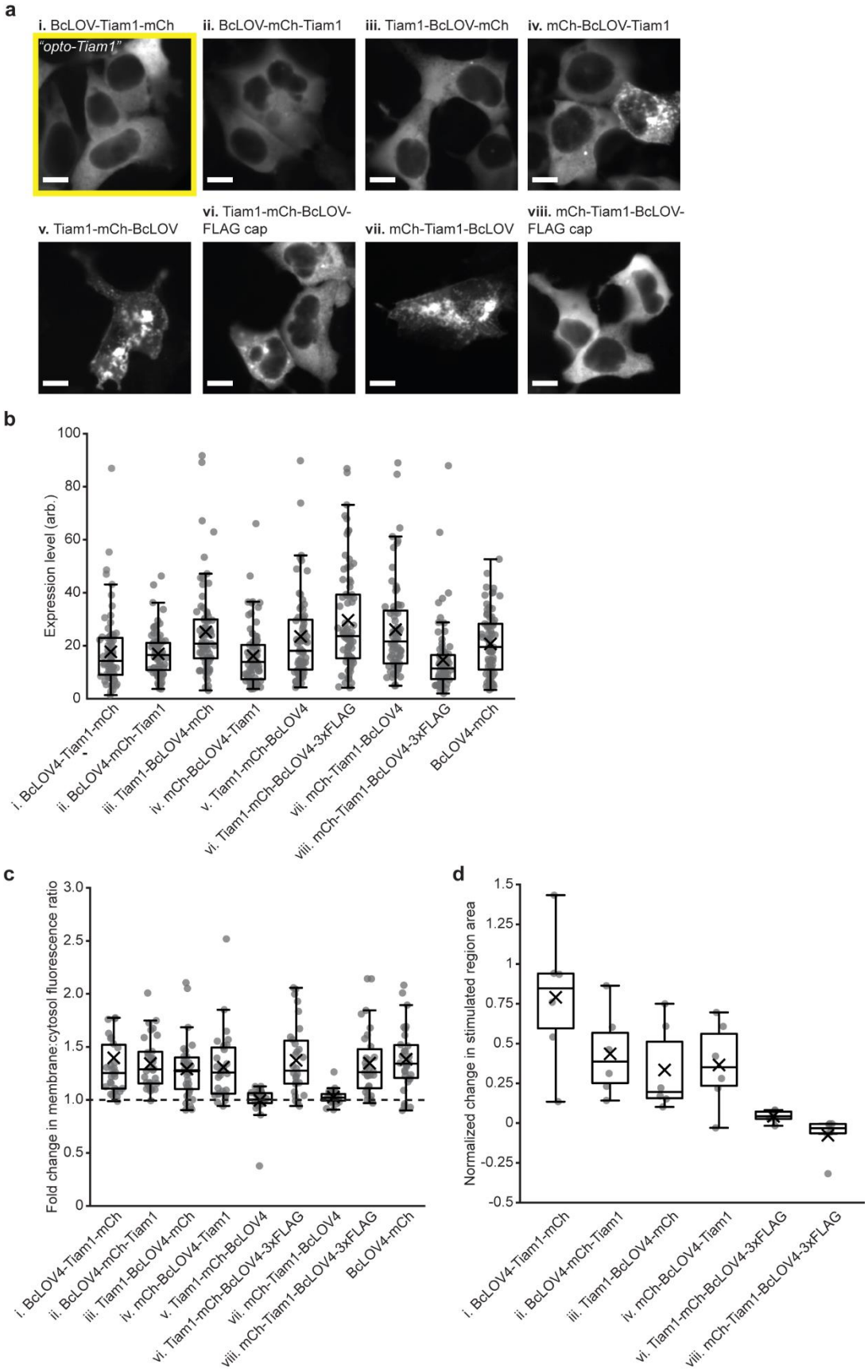
a
i. BcLOV-Tiam1-mCh
"opto-Tiam1"
ii. BcLOV-mCh-Tiam1
iii. Tiam1-BcLOV-mCh
iv. mCh-BcLOV-Tiam1
v. Tiam1-mCh-BcLOV
vi. Tiam1-mCh-BcLOV-FLAG cap
vii. mCh-Tiam1-BcLOV
viii. mCh-Tiam1-BcLOV-FLAG cap
b
Expression level (arb.)
100
80
60
40
20
0
i. BcLOV4-Tiam1-mCh
ii. BcLOV4-mCh-Tiam1
iii. Tiam1-BcLOV4-mCh
iv. mCh-BcLOV4-Tiam1
v. Tiam1-mCh-BcLOV4
vi. Tiam1-mCh-BcLOV4-3xFLAG
vii. mCh-Tiam1-BcLOV4
viii. mCh-Tiam1-BcLOV4-3xFLAG
BcLOV4-mCh
c
Fold change in membrane:cytosol fluorescence ratio
3.0
2.5
2.0
1.5
1.0
0.5
0
i. BcLOV4-Tiam1-mCh
ii. BcLOV4-mCh-Tiam1
iii. Tiam1-BcLOV4-mCh
iv. mCh-BcLOV4-Tiam1
v. Tiam1-mCh-BcLOV4
vi. Tiam1-mCh-BcLOV4-3xFLAG
vii. mCh-Tiam1-BcLOV4
viii. mCh-Tiam1-BcLOV4-3xFLAG
BcLOV4-mCh
d
Normalized change in stimulated region area
1.5
1.25
1
0.75
0.5
0.25
0
-0.25
-0.5
i. BcLOV4-Tiam1-mCh
ii. BcLOV4-mCh-Tiam1
iii. Tiam1-BcLOV4-mCh
iv. mCh-BcLOV4-Tiam1
vi. Tiam1-mCh-BcLOV4-3xFLAG
viii. mCh-Tiam1-BcLOV4-3xFLAG

Figure 4.10 Molecular engineering of opto-Tiam1

a. Representative images of Tiam1 domain arrangements. Scale = 10 µm. **b**. Expression levels of domain arrangements measured by mCherry fluorescence. N = 75 cells per condition. **c**. Fold change in membrane:cytosol mCherry fluorescence ratio between dark-adapted and post-blue light illumination states. N = 30 cells pre condition. **d**. Box-and-whisker plot of percent change in cell area within the stimulated region for viable domain arrangements. N = 6 independent videos per condition.

To identify constructs capable of inducing cell protrusions when recruited to the plasma membrane, all six candidate constructs were subjected to spatially confined blue light stimulation, and the change in cell area within the stimulated region was measured over a 10-minute time course. The greatest area change was observed for BcLOV4-Tiam1-mCherry, which we designated as opto-Tiam1 (**Figure 4.10d**).

4.2.6 DMD stimulation- and serum starvation-induced lamellipodia formation with opto-Tiam1

Upon screening opto-Tiam1 activity in serum-fed cells, we observed that protrusion formation was inconsistent, with hybrid filopodia/lamellipodia forming within the stimulated region. However, serum starvation of tool-expressing cells for 24 hours prior to imaging resulted in consistent formation of sheetlike lamellipodia. We attribute this difference in phenotype to the decreased cytoskeletal tension and focal adhesion strength in serum-starved cells (199, 202), resulting in easier cytoskeletal remodeling (**Figure 4.11**). We quantified lamellipodia formation by measuring the change in cell area within the stimulated region and observed a statistically significant increase ($p < 0.05$ by Mann-Whitney U test) in opto-Tiam1 area compared to BcLOV4-mCherry (**Figure 4.12**). We also used inhibitors of Tiam1:Rac1 interaction (NSC 23766), Arp2/3 signaling (CK 666), and actin polymerization (cytochalasin D) to confirm the tool activation mechanism (**Figure 4.13**). Thus, opto-Tiam1 can be used for reliable induction of Rac1 signaling and

lamellipodia production, complementing opto-Rac1 two nodes of Rac1 signaling pathway activation.

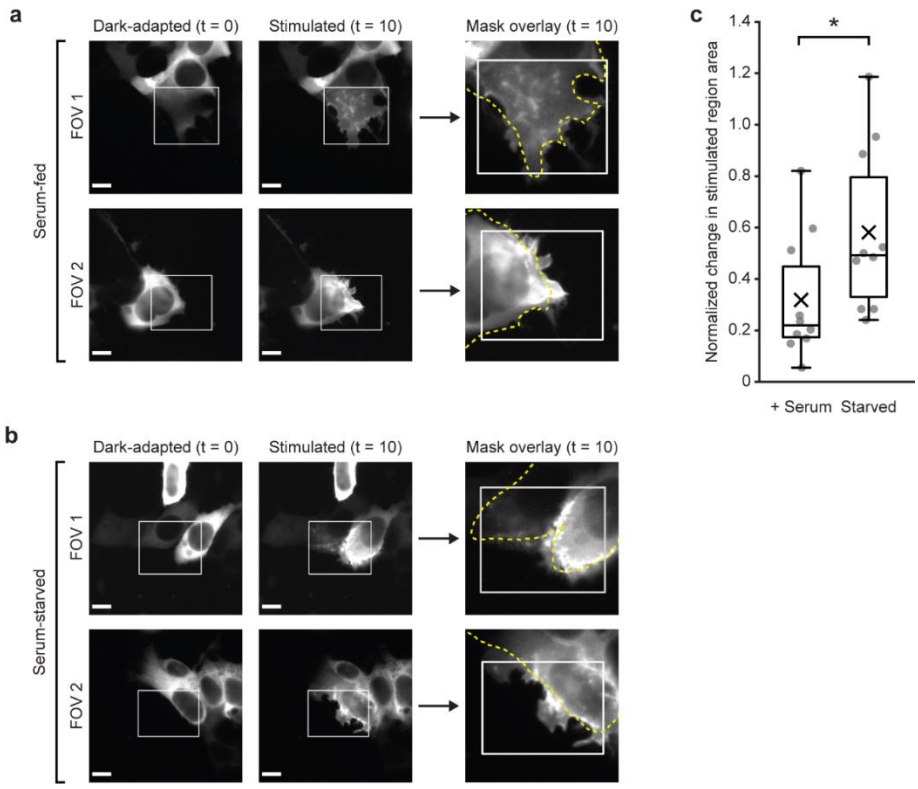

Figure 4.11 Differences in opto-Tiam1 phenotype for serum-fed vs. serum-starved cells

a-b. Exemplar images of opto-Tiam1-induced filopodia formation in serum-fed cells (**a**) and lamellipodia formation in serum starved cells (**b**) with pulsatile patterned stimulation (1.6% duty ratio). White box = illumination field. Dotted yellow line = cell boundary mask in the dark-adapted state. Scale = 10 µm. **c**. Box-and-whisker plot showing change in cell area within the stimulated region for serum-starved vs. fed cells expressing opto-Tiam1. Mann-Whitney U test, uncorrected for multiple comparisons. (*) = $p < 0.05$. N = 12 independent videos per condition.

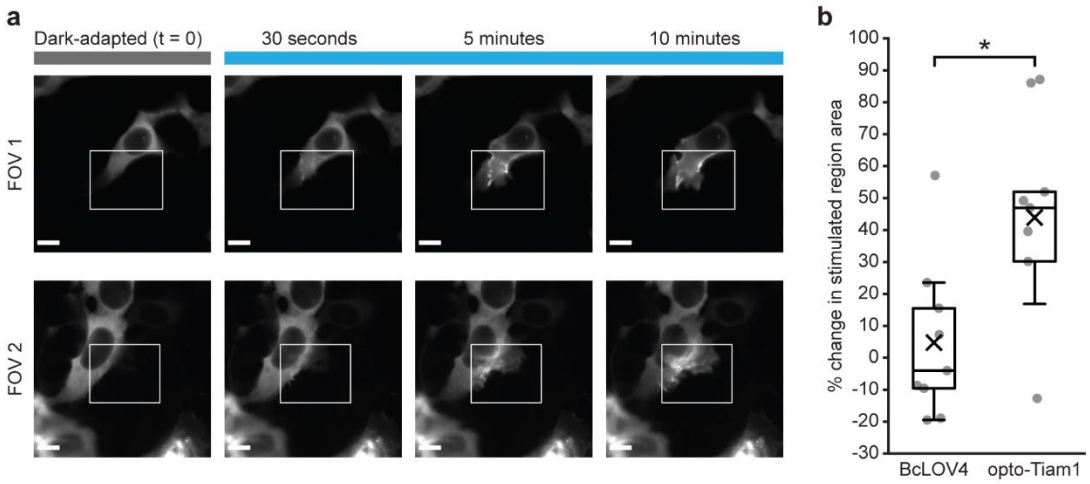

Figure 4.12 Optogenetic induction of lamellipodia formation with opto-Tiam1

a. Exemplar images of opto-Tiam1-induced lamellipodia formation with pulsatile patterned stimulation (1.6% duty ratio). White box = illumination field. Scale = 10 µm.

b. Box-and-whisker plot showing percent change cell area within the stimulated region, compared to effector-less BcLOV4 control. Mann-Whitney U test, uncorrected for multiple comparisons. (*) = $p < 0.05$. N = 9 independent videos per condition.

4.2.7 Design and screening of opto-Cdc42

Domain arrangement combinations of BcLOV4, mCherry, and wildtype Cdc42 GTPase were screened following the same procedure as Tiam1 fusions. All constructs except Cdc42-mCherry-BcLOV4 and mCherry-Cdc42-BcLOV4 expressed uniformly throughout the cytosol and translocated to the plasma membrane in response to blue light stimulation. We next tested whether any of these six candidate tool constructs could activate Cdc42 signaling at the membrane. Because filopodia formation can be subjective and difficult to discern with a membrane-associating protein, we instead imaged actin polymerization with miRFP703-tagged LifeAct before and after pulsatile, spatially confined blue light stimulation. We measured the percent change in LifeAct intensity in the stimulated region of the cell (normalized to the non-stimulated region) after five minutes of stimulation with a duty cycle of $\Phi = 1.6\%$; an increase in stimulated region LifeAct intensity would suggest increased filamentous actin polymerization and

filopodia formation. The best performing construct, mCherry-Cdc42-BcLOV4-3xFLAG, was designated as opto-Cdc42 (**Figure 4.14**).

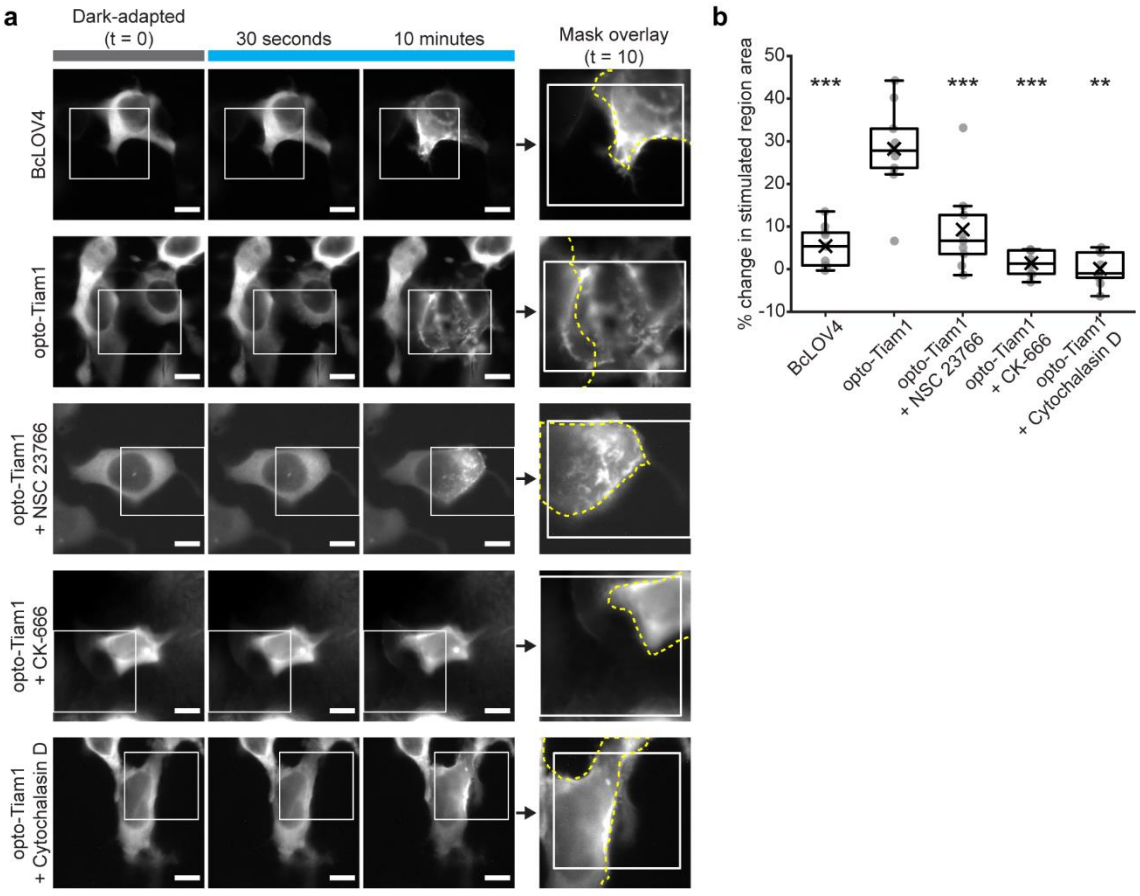

Figure 4.13 Pharmacological inhibition of opto-Tiam1

a. Representative images of BcLOV4 control, wildtype opto-Tiam1, and opto-Tiam1 inhibited with Rac1 inhibitor NSC 23766, Arp2/3 inhibitor CK 666, and actin polymerization inhibitor cytochalasin D. mCherry tag was imaged during pulsatile patterned stimulation (1.6% duty ratio). White box = illumination field. Dotted yellow line = cell boundary mask in the dark-adapted state. Scale = 10 µm. **b**. Quantification of percent change in cellular area within stimulated region. Center line, median; "X", mean; box limits, upper and lower quartiles; whiskers, 1.5x interquartile ranges. N = 9 independent videos per condition. Mann-Whitney U test, uncorrected for multiple comparisons. (*) = $p < 0.05$, (**) = $p < 0.01$, (n.s.) = not significant.

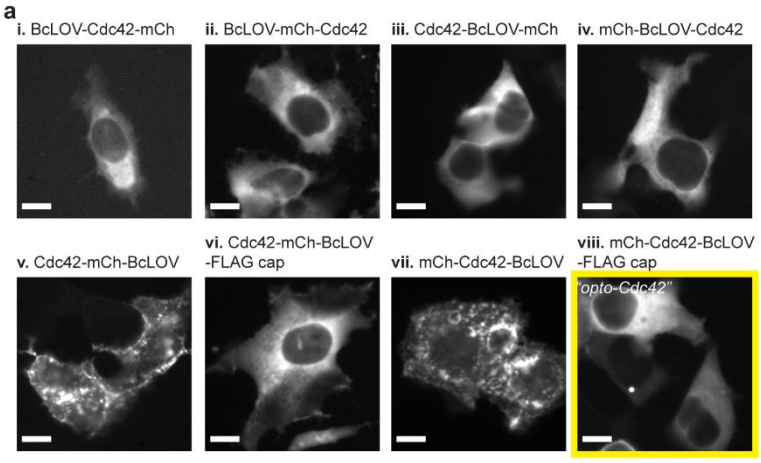
a
i. BcLOV-Cdc42-mCh
ii. BcLOV-mCh-Cdc42
iii. Cdc42-BcLOV-mCh
iv. mCh-BcLOV-Cdc42
v. Cdc42-mCh-BcLOV
vi. Cdc42-mCh-BcLOV -FLAG cap
vii. mCh-Cdc42-BcLOV
viii. mCh-Cdc42-BcLOV -FLAG cap
"opto-Cdc42"

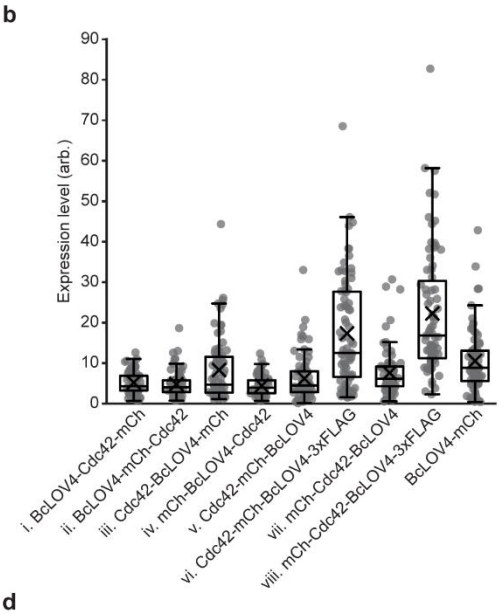
b
Expression level (arb.)
0
10
20
30
40
50
60
70
80
90
i. BcLOV4-Cdc42-mCh
ii. BcLOV4-mCh-Cdc42
iii. Cdc42-BcLOV4-mCh
iv. mCh-BcLOV4-Cdc42
v. Cdc42-mCh-BcLOV4
vi. Cdc42-mCh-BcLOV4-3xFLAG
vii. mCh-Cdc42-BcLOV4
viii. mCh-Cdc42-BcLOV4-3xFLAG
BcLOV4-mCh

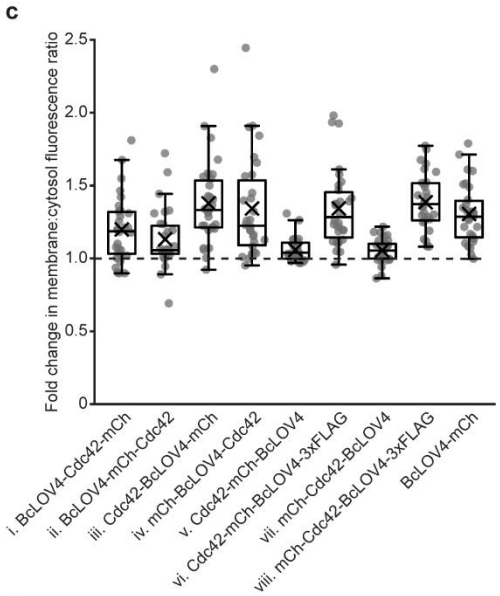
c
Fold change in membrane:cytosol fluorescence ratio
0
0.5
1.0
1.5
2.0
2.5
i. BcLOV4-Cdc42-mCh
ii. BcLOV4-mCh-Cdc42
iii. Cdc42-BcLOV4-mCh
iv. mCh-BcLOV4-Cdc42
v. Cdc42-mCh-BcLOV4
vi. Cdc42-mCh-BcLOV4-3xFLAG
vii. mCh-Cdc42-BcLOV4
viii. mCh-Cdc42-BcLOV4-3xFLAG
BcLOV4-mCh

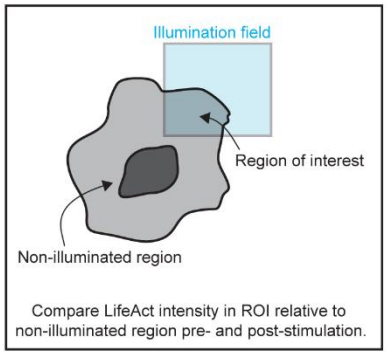
d
Illumination field
Region of interest
Non-illuminated region
Compare LifeAct intensity in ROI relative to non-illuminated region pre- and post-stimulation.

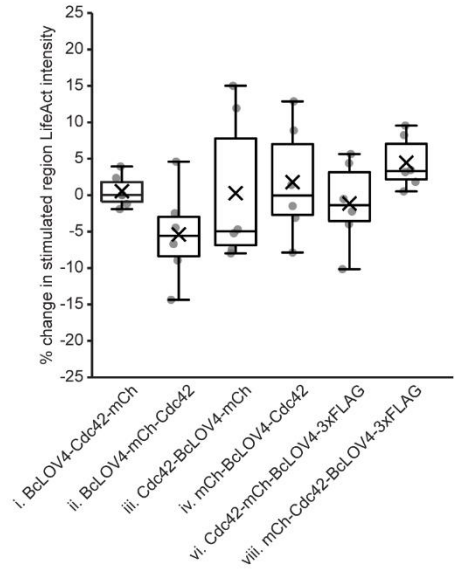
e
% change in stimulated region LifeAct intensity
-25
-20
-15
-10
-5
0
5
10
15
20
25
i. BcLOV4-Cdc42-mCh
ii. BcLOV4-mCh-Cdc42
iii. Cdc42-BcLOV4-mCh
iv. mCh-BcLOV4-Cdc42
vi. Cdc42-mCh-BcLOV4-3xFLAG
viii. mCh-Cdc42-BcLOV4-3xFLAG

Figure 4.14 Molecular engineering of opto-Cdc42

a. Representative images of Cdc42 domain arrangements. Scale = 10 µm. **b**. Expression levels of domain arrangements measured by mCherry fluorescence. N = 75 cells per condition. **c**. Fold change in membrane:cytosol mCherry fluorescence ratio between dark-adapted and post-blue light illumination states. N = 30 cells pre condition. **d**. Schematic of opto-Cdc42 quantification assay using miRFP703-LifeAct. **e**. Box-and-whisker plot of percent change in LifeAct fluorescence within the stimulated region for viable domain arrangements. N = 6 independent videos per condition.

4.2.8 DMD stimulation-induced filopodia formation and actin quantification with opto-Cdc42

Opto-Cdc42 membrane recruitment via spatially confined stimulation induces actin polymerization and filopodia formation. We measured the change in LifeAct fluorescence intensity within the stimulated region and observed a statistically significant increase in opto-Cdc42 cells compared to negative control BcLOV4-mCherry ($p < 0.05$ by Mann-Whitney U test) (**Figure 4.15**). We also used inhibitors of Cdc42:GEF interaction (ZCL 278), Arp2/3 signaling (CK 666), and actin polymerization (cytochalasin D) to confirm the opto-Cdc42 tool signaling mechanism (**Figure 4.16**). Because cytochalasin D affects actin polymerization, we did not quantify LifeAct fluorescence for this inhibition condition. For all inhibitors, we measured the change in cell boundary length within the stimulated region, with an increase in boundary length corresponding to the presence of small membrane protrusions.

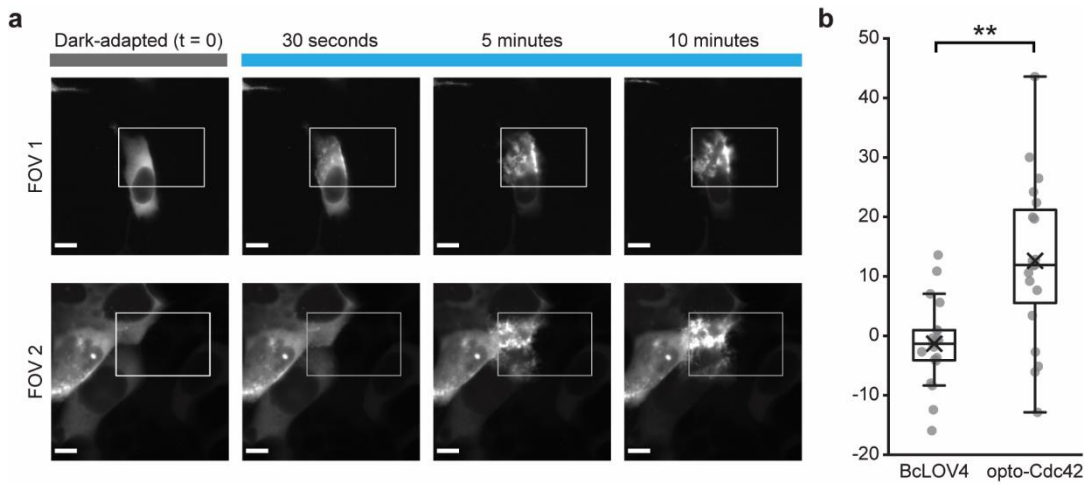

Figure 4.15 Optogenetic induction of filopodia formation with opto-Cdc42

a. Exemplar images of opto-Cdc42-induced filopodia formation with pulsatile patterned stimulation (1.6% duty ratio). White box = illumination field. Scale = 10 µm. **b**. Box-and-whisker plot showing percent change in miRFP703-LifeAct fluorescence intensity within the stimulated region, compared to effector-less BcLOV4 control. Mann-Whitney U test, uncorrected for multiple comparisons. (**) = $p < 0.01$. N = 18 independent videos per condition.

4.2.9 Design, screening, and characterization of opto-Intersectin1

To activate Cdc42 signaling at the GEF level, we used the 51 kDa Dbl-homology, Pleckstrin-homology (DHPH) domain of the Intersectin1 GEF, which has previously been used in other optogenetic heterodimerization systems (47, 113, 180). All screened domain arrangements, except those with BcLOV4 at the C-terminus of the protein which were previously shown to be disfavored, exhibited cytosolic expression in the dark state. Intersectin1-BcLOV4-mCherry was chosen as opto-Intersectin1 based on its robust filopodia formation upon blue light stimulation (**Figure 4.17**).

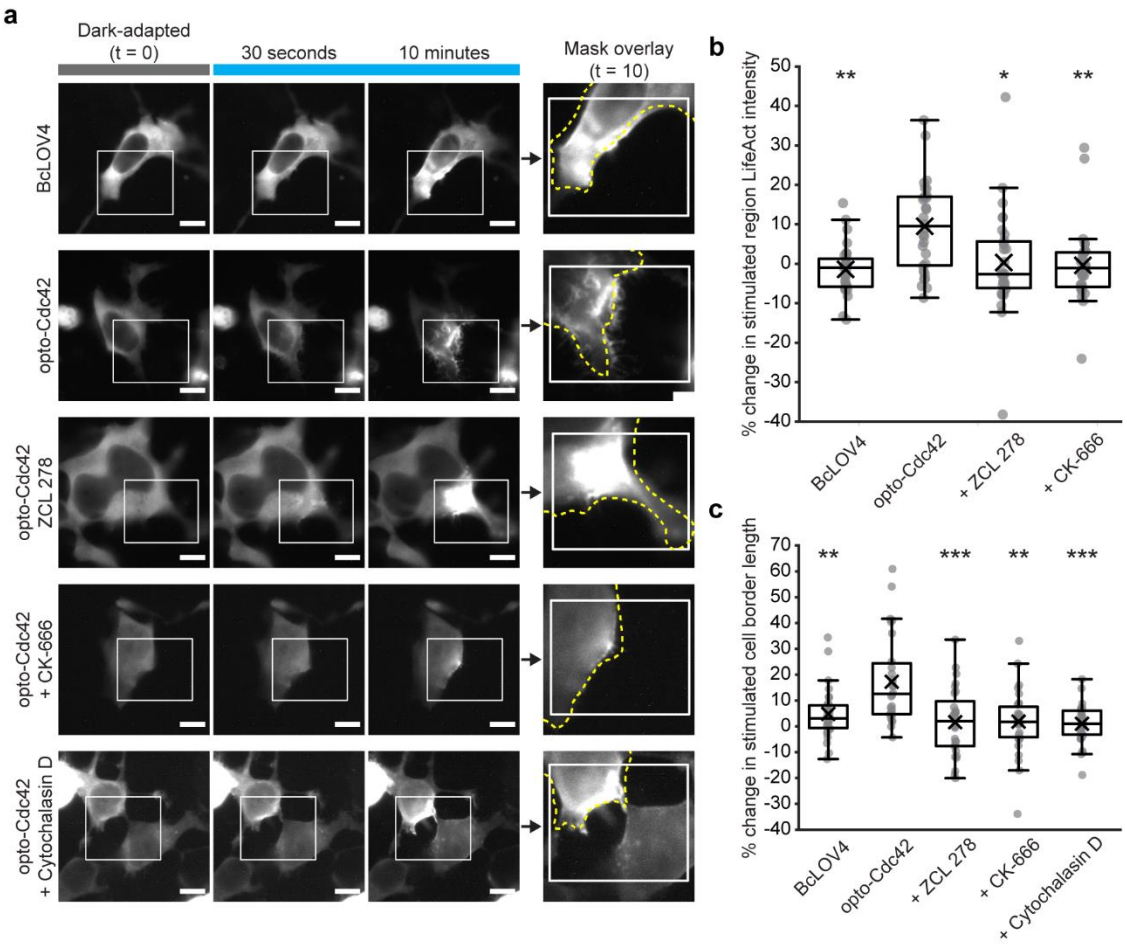

Figure 4.16 Pharmacological inhibition of opto-Cdc42

a. Representative images of BcLOV4 control, wildtype opto-Cdc42, and opto-Cdc42 inhibited with Cdc42 inhibitor ZCL 278, Arp2/3 inhibitor CK 666, and actin polymerization inhibitor cytochalasin D. mCherry tag was imaged during pulsatile patterned stimulation (1.6% duty ratio). White box = illumination field. Dotted yellow line = cell boundary mask in the dark-adapted state. Scale = 10 µm. **b**. Quantification of change in cellular LifeAct-miRFP fluorescence observed within stimulated region, corrected for photobleaching. LifeAct fluorescence was not calculated for cytochalasin D condition due to disruption of LifeAct-actin binding by the inhibitor. **c**. Quantification of change in cell border length observed within stimulated region, normalized to initial border length. (b-c) Center line, median; "X", mean; box limits, upper and lower quartiles; whiskers, 1.5x interquartile ranges. N = 12 independent videos per condition. Mann-Whitney U test, uncorrected for multiple comparisons. (*) = $p < 0.05$, (**) = $p < 0.01$, (***) = $p < 0.001$.

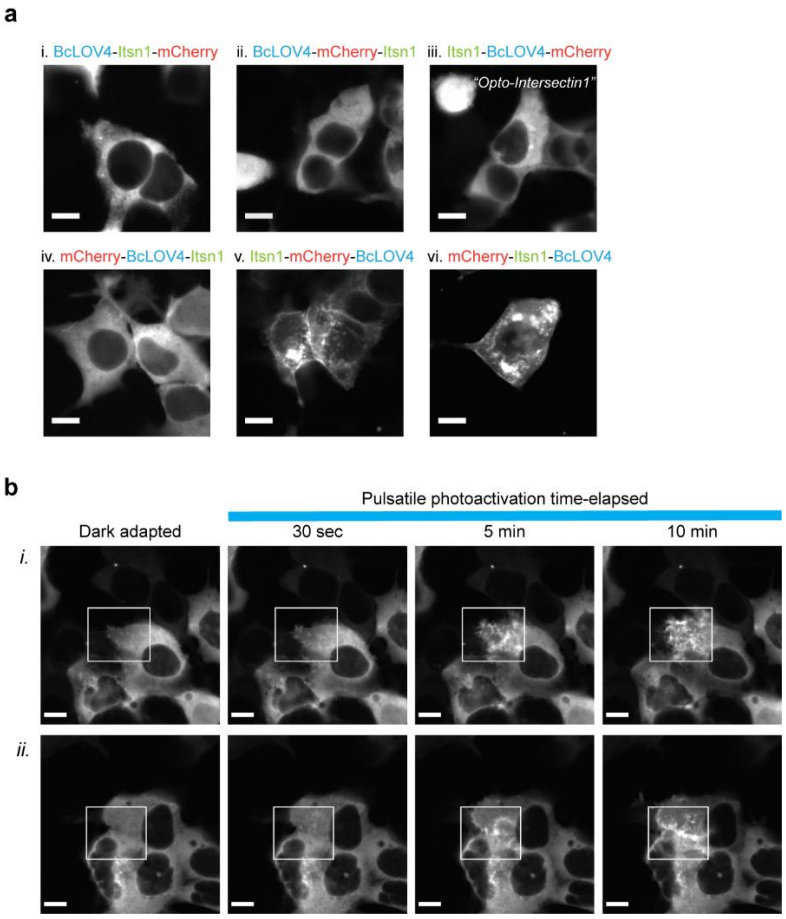

Figure 4.17 Molecular engineering and tool function of opto-Intersectin1

a. Representative images of Tiam1 domain arrangements. Scale = 10 µm. **b**. Exemplar images of opto-Intersectin1-induced filopodia formation with pulsatile patterned stimulation (1.6% duty ratio). White box = illumination field. Scale = 10 µm.

4.2.10 Membrane translocation kinetics of protrusion tools

We measured the kinetics of dynamic membrane association for opto-Tiam1 and opto-Cdc42 (**Figure 4.18**). Briefly, mCherry fluorescence of tool constructs was imaged before, during, and after a 5-second pulse of blue light. Line sections of the plasma membrane were drawn and Pearson's correlation between mCherry intensity along the line section and a GFP membrane marker was measured at each timepoint. Exponential fits were applied to these association and dissociation measurements for N = 20 cells

per construct and 95% confidence intervals were calculated. For opto-Tiam1, membrane association τ_{on} was 1.34 s (95% CI 1.27-1.42 s) and membrane dissociation τ_{off} was 155.1 s (95% CI 136.9-173.2 s). For opto-Cdc42, membrane association τ_{on} was 0.984 s (95% CI 0.936-1.03 s) and membrane dissociation τ_{off} was 98.7 s (95% CI 93.7-103.8 s). The τ_{on} values are similar to those measured for effector-less BcLOV4-mCherry in HEK cells. Opto-Tiam1's τ_{off} value is about a minute longer than that of BcLOV4-mCherry; this longer membrane residence time may be due to Tiam1:Rac1 interactions at the membrane.

4.3 Conclusions and future directions

Here, we present a set of optogenetic tools for the induction of filopodia and lamellipodia formation at the GTPase and GEF level. Opto-Rac1 and opto-Cdc42 serve as further examples that membrane recruitment of a wildtype GTPase is sufficient for pathway activation. In the BcLOV4 system, mutations to lock the GTPase into its active state are unnecessary; the use of a wildtype GTPase adds a requirement for GEF interaction following membrane recruitment for signaling activation to occur, decreasing the tool's dark-state activity and reducing the chances of spurious pathway activation. Like opto-RhoA, our opto-GTPase protrusion tools feature disrupted prenylation, making them less likely to be activated by the cell signals that turn on endogenous GTPase signaling and preventing their interaction with guanosine dissociation inhibitors, increasing their orthogonality to cell GTPase populations (24, 65). Thus, opto-Cdc42 and opto-Rac1 exhibit lower risk for disturbing basal cell physiology or outcompeting endogenous GTPases than other systems.

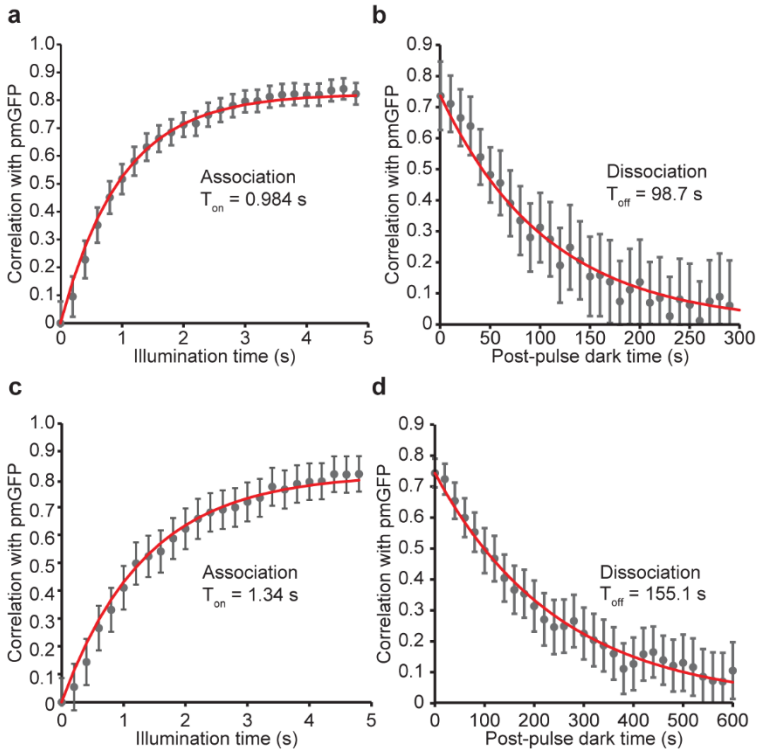

Figure 4.18 Membrane translocation kinetics of opto-Cdc42 and opto-Tiam1

Time constants were determined by correlation analysis between a membrane marker (pmGFP) and line section profiles of the mCherry tag. N = 30 cells per construct. **a**. Membrane association of opto-Cdc42: τ_{on} = 0.984 s, 95% CI 0.936-1.03 s. **b**. Membrane dissociation of opto-Cdc42: τ_{off} = 98.7 s, 95% CI, 93.7-103.8 s. **c**. Membrane association of opto-Tiam1: τ_{on} = 1.34 s, 95% CI 1.27-1.42 s. **d**. Membrane dissociation of opto-Tiam1: τ_{off} = 155.1 s, 95% CI, 136.9-173.2 s.

The GTPase and GEF tools we engineered for Rac1 and Cdc42 allow for two levels of activation from a signal integration standpoint. The level of pathway activation by an opto-GEF tool is limited by the endogenous cellular GTPase concentration, while rapid turnover cycles by endogenous GEFs result in a more robust response by overexpression of an opto-GTPase tool (78, 154, 155). Our characterization of the effects of stimulation duty cycle can be used to guide use of opto-Rac1; similarly, the finding that serum starvation is essential for robust lamellipodia formation with opto-Tiam1 may be useful to lower initial cytoskeletal tension for more effective pathway induction using other tools. With the optogenetic tools presented in this chapter, we hope

to explore their function in more migratory cell types and examine the connections between the signaling pathways of Rho-family GTPases.

4.4 Materials and methods

4.4.1 Genetic constructs

Domain arrangement combinations of BcLOV4, mCherry, and its effector (Rac1, Tiam1-DH, Cdc42, or Intersectin1-DH), with a flexible $(GGGS)_2$ linker between each protein pair were assembled into the pcDNA3.1 mammalian expression vector under a CMV promoter by Gibson cloning with NEB HiFi DNA Assembly Master Mix (E2621). BcLOV4 and mCherry were amplified from their previously reported mammalian codon-optimized fusion (Addgene plasmid 114595) (69). The DNA sequence of Rac1 (Genbank ID AAH04247.1) was human codon-optimized using the Integrated DNA Technologies (IDT) Codon Optimization Tool and ordered as a gBlock®, with a single C-terminal leucine residue (of the “CAAX”-motif) removed to prevent prenylation and membrane localization in dark-adapted fusions. The DH domain of Tiam1 was identified using the PROSITE ExPASy database and amplified from pMXs3-TIAM1 (Addgene plasmid 86143). Wildtype Cdc42 GTPase was amplified from CLPIT Cry2PHR-mCherry-Cdc42 without the ‘CAAX’ motif to prevent prenylation, a kind gift from Lukasz Bugaj. The DH domain of Intersectin1 was also identified using ExPASy and amplified from RpBphP1-mCherry-Intersectin1-DHPH (Addgene plasmid 79839). For Tiam1 and Cdc42 tool screening, mCherry-effector-BcLOV4 and effector-mCherry-BcLOV4 constructs were also cloned with a C-terminal 3xFLAG tag following a GGGS linker.

The Rac1 constitutively active mutant was generated by QuikChange site-directed mutagenesis (Q665L, E695H, and N696H) based on previously reported mutations(260). Briefly, overlapping primers encoding the mutation with melting

temperatures ≥ 78°C were designed using Agilent's online primer design tool (https://www.agilent.com/store/primerDesignProgram.jsp). The mutation was introduced over 18 PCR cycles with 8-minute elongation time using the Phusion® high-fidelity DNA polymerase master mix (M0531). The opto-RhoA template plasmid was digested with DpnI for one hour at 37°C before transformation. All genetic constructs were transformed into competent *E. coli* (New England Biolabs, C2984H).

For filopodia quantification, the miRFP703-tagged LifeAct plasmid was acquired from Addgene (plasmid 79993). For membrane localization kinetics, pCIBN(deltaNLS)-pmGFP was acquired from Addgene (plasmid 26867). Photoactivatable Rac1 (pTriEx-mCherry-PA-Rac1) was acquired from Addgene (plasmid 22027).

4.4.2 Cell culture and transient transfection

HEK293T (ATCC, CRL-3216) cells were cultured in D10 media composed of Dulbecco's Modified Eagle Medium with Glutamax (Invitrogen, 10566016), supplemented with 10% heat-inactivated fetal bovine serum (FBS) and penicillin-streptomycin at 100 U/mL. Cells were maintained in a 5% CO_2 water-jacketed incubator (Thermo/Forma, 3110) at 37°C. Cells were seeded onto poly-D-lysine-treated glass bottom dishes (MatTek, P35GC-1.5-14-C) or into 24-well glass bottom plates (Cellvis, P24-1.5H-N), treated in-house with type I collagen, at 15-20% confluency. Cells were transfected at ~30-40% confluency 24 hours later using the TransIT-293 transfection reagent (Mirus Bio, MIR2700) according to manufacturer instructions and Opti-MEM™ reduced serum media (Thermo Fisher, 3195062). Cells were imaged 24-48 h post-transfection. For experiments imaging actin polymerization, full media was replaced with serum starvation media (2% heat-inactivated FBS) at transfection.

For normal handling, cells were passage, transfected, incubated, and transported under standard laboratory lighting conditions, and then microscopy-based assays were conducted with room lights off after an initial 10-minute dark-adaptation period. All data reported were acquired under the normal handling conditions. Under “stringent” conditions for Rac1 comparison studies, the cells were handled during all steps as prescribed by others for PA-Rac1 to reduce basal optogenetic activity (263). Cell culture was performed under red safe-light conditions. Cells were transferred in completely opaque carriers. Assays were performed in dark rooms with all light-sources tuned off or baffled, including electronic displays and monitors (263).

Cell viability for opto-Rac1 versus PA-Rac was determined by Trypan blue staining. 24 hours after transfection, cells were washed with PBS and incubated with 0.2% Trypan Blue solution (diluted 1:1 with PBS from 0.4% stock solution) for one minute. Trypan Blue solution was then aspirated, and cells were fixed with 4% paraformaldehyde for 10 minutes at room temperature. After fixation, plates were rinsed three times with PBS with agitation for five minutes per wash. Cells were then imaged at 20× magnification with brightfield illumination for three FOV per plate, two plates per condition, to count the number of stained vs. unstained cells for each construct.

4.4.3 Fluorescence microscopy and hardware

Fluorescence microscopy was performed on an automated Leica DMI6000B fluorescence microscope under Leica MetaMorph control, with a sCMOS camera (pco.edge), an LED illuminator (Lumencor Spectra-X), and a 63× oil immersion objective. Excitation illumination was filtered at the LED source (mCherry imaging λ = 575/25 nm; GFP imaging or widefield BcLOV4 stimulation λ = 470/24 nm; miRFP imaging λ = 632/22 nm). Fluorescent proteins were imaged with Chroma filters: mCherry

(T585lpxr dichroic, ET630/75 nm emission filter, 0.2–0.5 s exposure), GFP (T495lpxr dichroic, ET 525/50 nm emission filter, 0.2 s exposure), miRFP703 (AT655dc dichroic, ET655 nm emission, 0.5 s exposure). Cells were imaged at room temperature in CO_2-independent media (phenol-free HBSS supplemented with 1% l-glutamine, 1% penicillin-streptomycin, 2% essential amino acids, 1% nonessential amino acids, 2.5% HEPES pH 7.0, and 10% serum); LifeAct and lamellipodia imaging were performed in CO_2-independent media without serum. The spatially patterned illuminator was custom-constructed from a digital light processor (DLP, Digital Light Innovations CEL5500), as described in section 3.4.3.

4.4.4 Expression level and membrane:cytosol ratio measurement

HEK293T cells were co-transfected with a GFP membrane marker and mCherry-tagged tool construct in a 1:10 ratio. Cells were imaged at 63× magnification for 3-5 fields of view per construct. mCherry fluorescence was imaged with a 0.5 s exposure time, followed by GFP fluorescence imaging (0.2 s exposure). mCherry fluorescence was the imaged again after 5 seconds of blue light stimulation.

To assess expression level, cells were manually segmented using the pmGFP micrograph to identify cell boundaries, and background-subtracted fluorescence was recorded for N = 25-31 cells per condition. Cell fluorescence was normalized to BcLOV4-mCherry mean fluorescence. To measure membrane:cytosol fluorescence ratio, the plasma membrane and cytosol were manually segmented using pmGFP localization as a guide. The ratio of mean membrane to cytosol fluorescence was calculated for dark-adapted and post-illumination states for N = 25-75 cells per condition.

4.4.5 DMD stimulation assays

For assays using spatially patterned illumination, mCherry fluorescence was imaged every 15 seconds for up to 10 minutes. During this time, cells were periodically stimulated with DLP-patterned illumination (typically 25 μm-wide squares, ~25% cell area illuminated) with a 0.8 – 5% duty ratio range (or 0.25-1.5 s-long pulses once every 15-30 s). For actin polymerization visualization, miRFP fluorescence was imaged every 1 minute for up to 10 minutes. In the cases of mechanistic controls: for actin polymerization inhibition, cytochalasin D (Cayman Chemical, 11330) was added to cell media for a final concentration of 10 μM, 1 hour prior to imaging. For Rac1-GEF inhibition, NSC 23766 (Cayman Chemical, 13196) was added to cell media for a final concentration of 50 μM, 24 hours prior to imaging. For Cdc42-GEF inhibition, ZCL 278 (Cayman Chemical, 14849), was added to cell media for a final concentration 7.5 μM, 2 hours prior to imaging. For Arp2/3 inhibition, CK 666 (Millipore-Sigma, SML0006), was added to cell media for a final concentration of 500 μM, 6 hours prior to imaging. Equimolar concentrations of inhibitors were also added to CO_2 independent media for imaging.

4.4.6 Tool function quantification

For all tools, each data point was derived from an independent video. The researcher was blinded during cell segmentation to experimental condition to prevent bias. Statistical significance was assessed by the non-parametric Mann-Whitney U test, uncorrected for multiple comparisons.

4.4.6.1 opto-Rac1

For each video (N = 19-37), a cell within the DMD-illuminated region was selected and segmented in ImageJ from the frame imaged at 0 seconds post-illumination and 120 seconds post-illumination. To compute the distance the cell had moved between the two timepoints, the average distance between segmented cell borders was calculated via a custom analysis Python script.

4.4.6.2 opto-Tiam1

Contours of cell boundaries at initial (pre-illumination) and final timepoints of the DMD-stimulation region were manually drawn, and binary masks of the cell region inside (the overlap) and outside (the non-overlap) the stimulation region were created using the Python OpenCV bitwise operation functions “and” and “xor”, respectively. Percent change in cellular area within the overlap region between initial and final timepoints was calculated. For identification of a viable fusion tool construct, N = 6 independent videos per condition. For comparison between serum-starved and serum-fed cells, N = 12 independent videos per condition. For comparison to BcLOV4, N = 9 independent videos per condition.

4.4.6.3 opto-Cdc42

Contours of cell boundaries were drawn and masks were created as described in (4.4.6.2). For opto-Cdc42 experiments, LifeAct fluorescence intensity was calculated within the overlap region, normalized to the non-overlap region, for each timepoint. The change in this normalized LifeAct fluorescence between initial and final timepoints was calculated for each video. For screening, N = 6 independent videos per condition. For

comparison to BcLOV4, N = 18 independent videos per condition. For inhibitor characterization, N = 30 independent videos per condition.

4.4.7 Membrane localization kinetics

For membrane recruitment quantification, prenylated GFP was co-transfected as a membrane marker with the BcLOV4 fusions as previously described in (4.4.4). Briefly, an mCherry fluorescence image (500 ms exposure) was captured to assess protein expression level and subcellular distribution. Cells were then illuminated with a 5 s-long blue light pulse to stimulate BcLOV4, during which time mCherry fluorescence images were also captured every 200 ms to monitor subcellular localization changes. The GFP membrane marker was imaged immediately after blue light stimulation for correlation analysis. For membrane dissociation via thermal reversion of the photoactivated protein in the dark, mCherry was visualized every 5 seconds for 10-15 minutes in the absence of blue light stimulation. Membrane localization and dissociation were measured by line section analysis and correlation with prenylated GFP in ImageJ and MATLAB as previously described (69).

CHAPTER FIVE: Optogenetic tools for termination of GTPase signaling

5.1 Introduction

Much of our work to this point has revolved around engineering optogenetic tools for spatiotemporally precise activation of signaling using GTPases and GEFs. True bidirectional control of cytoskeletal signaling requires the ability to activate as well as terminate pathways of interest. We sought to engineer a new class of optogenetic tools to terminate RhoA signaling by antagonism (using dominant negative RhoA GTPase) and enzymatic hydrolysis (using RhoA GAP domains). Development of these optogenetic termination tools will complete the RhoA optogenetic toolbox and greatly enhance our ability to study processes like cell migration and mechanotransduction.

5.1.1 Rho GTPase biosensors

In creating optogenetic tools to control GTPase signaling termination, quantification of tool function may not be as simple as observing changes in cell shape or actin polymerization. Induced termination of GTPase signaling events which exist at a low basal level in the cell may not result in pronounced morphological changes; thus, the ability to differentiate between inactive, GDP-bound GTPase and active, GTP-bound GTPase is useful in determining tool efficacy. Biosensors are proteins allowing for the quantification of intracellular concentrations and localizations of molecules or proteins using fluorescence readout (123). For optogenetic signaling termination tools, we are interested in using a GTPase biosensor to measure whether recruitment of a terminating protein results in less GTP-loaded GTPase at the membrane.

For Rho GTPase signaling, two main classes of biosensors exist: FRET-based and localization-based (186). FRET-based biosensors can be bimolecular or unimolecular. For bimolecular sensors (**Figure 5.1a**), two constructs are expressed in the cell: the GTPase fused to a FRET acceptor (e.g., YFP) and a downstream effector-binding protein domain (EBD) is fused to a FRET donor (e.g., CFP). In the off state, the GTPase is GDP-bound and does not interact with its downstream effector. In the on state, activated GTPase interacts with the effector and the EBD binds the active effector. This brings the FRET pair in close proximity and FRET is observed (128).

An obvious downside of the bimolecular biosensor is the requirement that two plasmids be expressed, in addition to the optogenetic tool of interest, requiring stoichiometric tuning of the system components and a higher genetic payload for the cell. In contrast, unimolecular FRET biosensors (**Figure 5.1b**) consist of one protein component: GTPase and FRET donor are fused to FRET acceptor and a GTPase binding domain (GBD) by a long linker. The GBD preferentially binds the GTPase only in its active GTP-bound state. Thus, in the off state, no FRET is observed. GTPase activation induces GBD-GTPase binding, resulting in FRET between the fluorescent proteins (109, 270). Variations on the unimolecular FRET-based biosensor also exist: fluorophores can be positioned inside the clamshell fold created by activation (187), or endogenous GTPase activation can be visualized by fusing the GTPase binding domain between FRET donor and acceptor. In this configuration, FRET is observed in the inactive state and disrupted when the GBD binds activated GTPase. This variation alleviates the need to express multiple proteins in the cell and allows for visualization of endogenous rather than overexpressed GTPase activity (270).

However, issues with FRET-based biosensors still exist, particularly when used in conjunction with optogenetic tools. For example, the commonly used CFP-YFP FRET

pair is incompatible with spatially confined illumination of a blue light-excited LOV-based optogenetic tool as visualizing the FRET pair would result in activation of the LOV. Also,

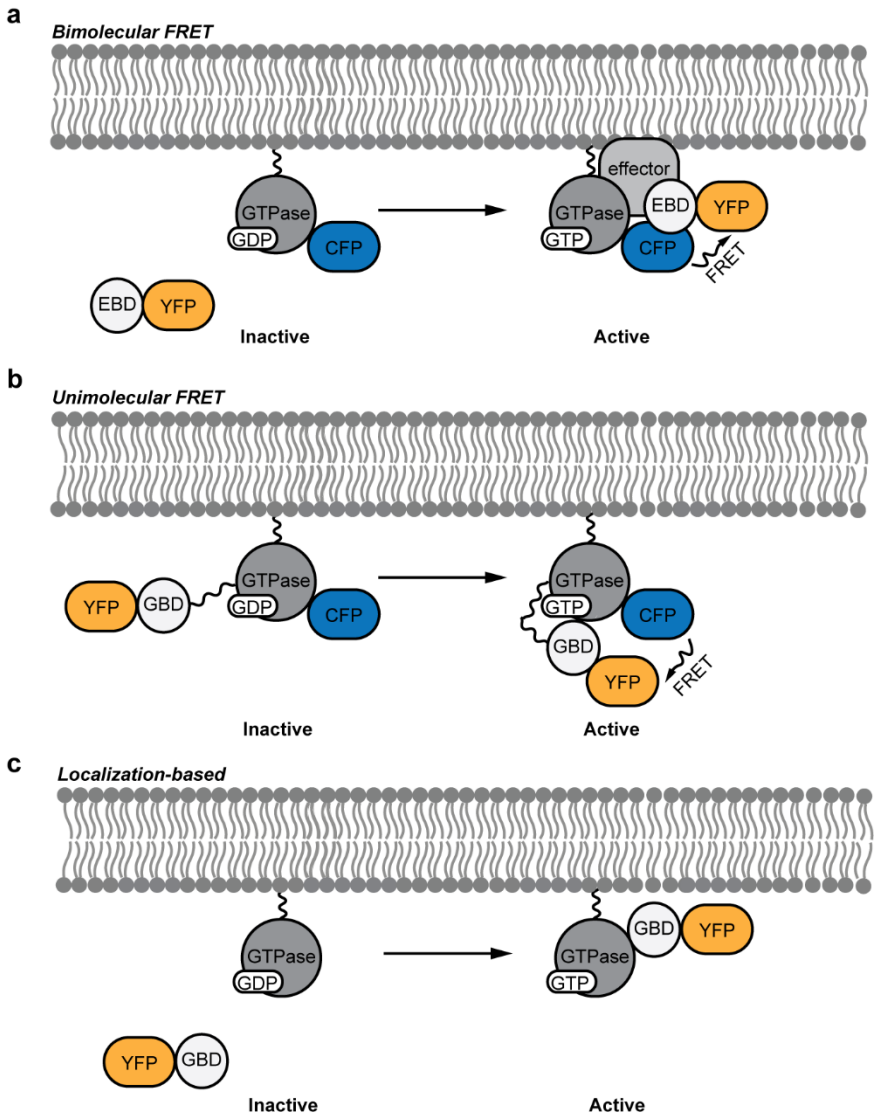

Figure 5.1 Types of biosensors for GTPase signaling interrogation

a. In bimolecular FRET systems, the GTPase is fused to a FRET donor, while an effector binding domain (EBD) are fused to a FRET acceptor. GTPase activation results in EBD-effector binding, bringing the fluorescent proteins together and resulting in FRET. **b**. In unimolecular FRET systems, the FRET donor and acceptor are separated by the GTPase, a GTPase binding domain (GBD) and a long linker. GTP loading results in GBD binding the activated GTPase and co-localization of the FRET pair. **c**. Localization-based biosensors fuse a GBD to a fluorescent protein. Changes in fluorescence localization and intensity reflect changes in GTPase activation.

more generally, FRET systems take up valuable visualization channel bandwidth, limiting the number of fluorescent proteins available for observing other cellular phenomena. This bandwidth issue is compounded with optogenetic tools, which also limit the number of available optical channels.

A solution to the FRET biosensor issue is the use of localization-based biosensors. In these systems, a GBD with preference for the GTP-bound GTPase is fused to a fluorescent protein; when the GTPase is activated, a change in fluorescence intensity and localization is observed (14). For example, for a GTPase signaling at the membrane, we expect high cytosolic fluorescence when GTPase signaling is in the off state, and high membrane fluorescence in the on state. This system uses one protein and one optical channel to visualize endogenous GTPase activation. While this system is associated with high background signal because the fluorescent protein does not “turn on” in response to signaling, it is more compatible with optogenetic tools than FRET-based systems. Notably, a major addition to the localization-based biosensor class was recently reported (151). From a starting point of GFP-bound Rhotekin GBD (14), a second GBD was added each sensor to increase signal, and monomeric GFP or mNeonGreen was replaced with a dimeric fluorescent protein (dTomato) to improve tool resolution. This biosensor is also specific to RhoA, unlike other biosensors which can bind multiple GTPases (199).

5.1.2 Strategies for terminating Rho GTPase signaling

As discussed in Chapter 1, GAPs inactivate GTPases by catalyzing hydrolysis of GTP to form GDP. Similar to optogenetic recruitment of GEF proteins to activate endogenous GTPase at the membrane, we hypothesize that spatiotemporally precise GAP recruitment will result in GTPase inactivation. This strategy was successfully implemented in a *Drosophila* tool, recruiting the RhoA-specific GAP RhoGAP71E to alter embryogenesis (132). To our knowledge, this approach has not been applied in mammalian cell systems. Activating GEFs can also be sequestered to the mitochondria, resulting in a decrease in pathway activation, as described with a cryptochrome heterodimerization tool (249). Another strategy for inactivation of GTPase signaling in the cell is through the use of dominant negative GTPase mutants (**Figure 5.2**). These mutants bind and sequester GTPase-activating GEFs, resulting in inactivation of the GTPase (59) and have long been used to inhibit signaling and identify cell processes that are affected. A dominant negative RhoA mutant (T19N) has been used to implicate RhoA in stem cell differentiation and proliferation (66). However, this strategy for signaling perturbation has only been used in an overexpression context rather than as a POI in optogenetic tool development. We hypothesize that by recruiting a dominant negative GTPase to the membrane, we can inhibit GTPase signaling through GEF sequestration and engineer a new class of optogenetic inactivation tools.

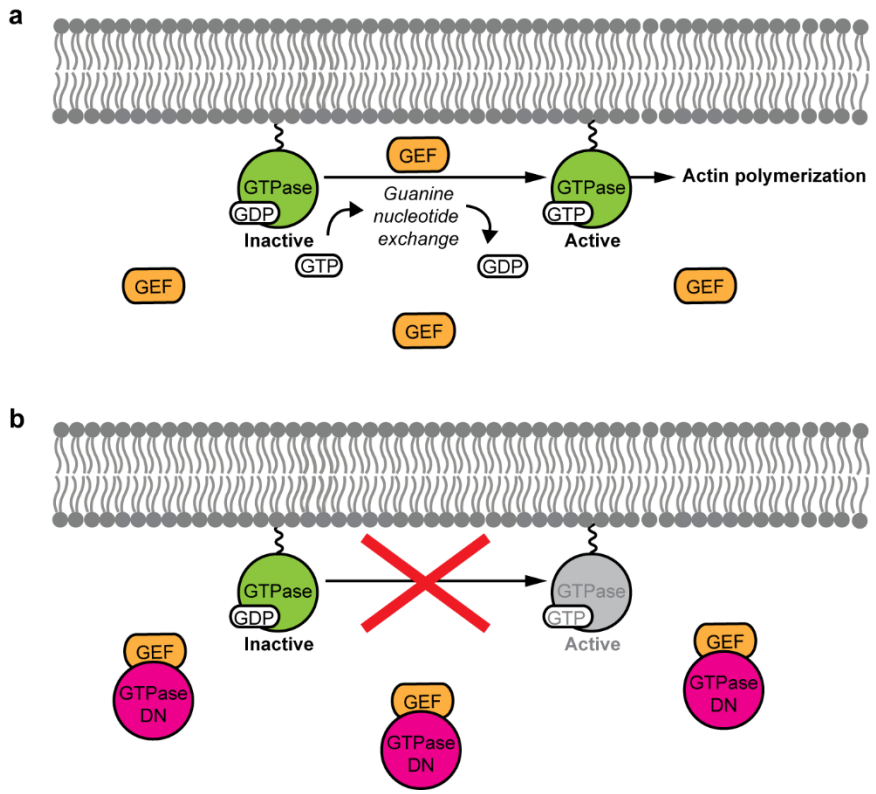

Figure 5.2 Mechanism of dominant negative GTPase inhibition

a. For wildtype GTPases, activation is catalyzed by GEF proteins, which exchange the bound GDP for GTP. The GTP-bound GTPase can then interact with downstream effectors and catalyze signaling events. **b**. Dominant negative GTPase mutants bind and sequester GEFs, preventing them from activating their partner GTPases. As a result, GTPase signaling remains in the inactive state.

5.1.3 Problem statement

To understand complex cell signaling feedback loops and processes involved in migration, we need to be able to perturb both signaling activation and termination. To accomplish this larger goal, a new class of optogenetic tools is needed which use light to recruit proteins to the membrane for inhibition of GTPase signaling. To accomplish this goal, we will use two parallel strategies: recruiting GAPs to catalyze GTP hydrolysis and GTPase inactivation, and recruiting dominant negative GTPase mutants to sequester activating GEFs and prevent activation from occurring. In addition to measuring changes

in cell morphology, we will use the new dTomato-2xrGBD biosensor to quantify RhoA-GTP levels before and after membrane recruitment as a means of assessing tool function.

5.2 Results and discussion

5.2.1 Selection of candidate GAP domains

We decided to focus our initial GAP engineering work on the RhoA pathway because of the availability of a single-chain GBD-based biosensor for RhoA-GTP (dTomato-2xrGBD). To our knowledge, comparable sensors for Rac1- and Cdc42- GTP do not yet exist. Twenty-seven GAP domains are known to inactivate RhoA (170); in choosing GAPs to fuse to BcLOV4, we focused on RhoA GAPs known to localize to the plasma membrane which showed evidence of controlling RhoA-mediated cell contractility and stress fiber formation. Using these criteria, we selected two initial candidates: ARHGAP1 and ARHGAP29. ARHGAP1, also known as p50RhoGAP, has been shown to translocate between the cytosol and the inner leaflet when it is activated (44, 223). ARHGAP29 is implicated in a RhoA-YAP mechanotransductive feedback loop. Activation of RhoA drives YAP nuclear import, where it activates transcription factors to increase ARHGAP29 transcription. ARHGAP29 is thought to turn off RhoA signaling and prevent cytoskeletal over-maturation, which would otherwise inhibit persistent cell motility (157).

5.2.2 Screening method for GAP tool functionality

Observing light-induced signaling with BcLOV4-GAP constructs requires a different experimental and analysis workflow than those used for GTPase or GEF tools. With activation tools, the cell is starting from a “resting state” in which signaling occurs at

a low basal level. Membrane recruitment of the GTPase or GEF results in an increase in signaling above the baseline, which is readily observable in the case of cytoskeletal signaling pathways. In contrast, membrane recruitment of a GAP tool would theoretically result in a decrease in signaling events below the already low baseline, resulting in lower contrast between on- and off-states than observed with activation tools. For example, in the case of RhoA signaling, we observed that the resting state cell does not show extensive stress fibers or cytoskeletal tension. Membrane recruitment of a RhoA GAP, then, may not result in appreciable change in stress fiber formation from the basal state.

Thus, for initial characterization of GAP tools, our strategy was to first pharmacologically activate RhoA signaling with lysophosphatidic acid (LPA), which binds to cell receptors LPA1 and LPA2. The C-termini of these receptors interact with the PDZ domains of RhoA-activating ARHGEF11 and ARHGEF12, resulting in increased stress fiber formation (265). Then, from a state of elevated RhoA signaling, we will then recruit the GAP tool to the membrane with blue light, ideally allowing for more contrast between on and off tool state.

5.2.3 Initial screening of GAP tool constructs

Our first RhoA GAP tool engineering attempt used the full ARHGAP1 gene in the standard BcLOV4 screening workflow. In addition to its GTPase-interacting GAP domain, ARHGAP1 also contains a CRAL-TRIO (183) (cellular retinaldehyde-binding protein and TRIO-GEF) domain, which allows the protein to bind lipids of the plasma membrane. Because of previous successful engineering by us and others using both the catalytic and the lipid-binding domains (i.e., DH and PH domains) in GEF tool engineering, we did not initially remove the non-catalytic domain from ARHGAP1 for BcLOV4 fusion screening.

From the initial six-construct screening workflow, only one construct (ARHGAP1-BcLOV4-mCherry) expressed in HEK293T cells. Interestingly, rather than localizing to the membrane, this construct formed a multi-micron aggregate in the cytosol in response to blue light stimulation, suggesting localization to an organelle. We analyzed illuminated ARHGAP1 localization by co-transfecting organelle markers and saw good alignment of lit-state protein with the Golgi apparatus (**Figure 5.3**). This result suggests that the full-length ARHGAP1-BcLOV4 fusion exhibits lipid binding with some specificity to the Golgi membrane, either due to specific lipid head group composition or larger membrane characteristics like curvature or disorder.

For subsequent engineering attempts with both ARHGAP1 and ARHGAP29, we truncated the fused protein to contain only the GAP domains as predicted by the PROSITE ExPASy database. For ARHGAP1, we saw no viable, healthy cells for mCherry-BcLOV4-ARHGAP1, and cells for BcLOV4-ARHGAP1-mCherry were very dim. The remaining constructs exhibited high expression; two of these (ARHGAP1-mCherry-BcLOV4-3xFLAG and mCherry-ARHGAP1-BcLOV4-3xFLAG) bound the membrane in response to blue light stimulation. For ARHGAP29, only BcLOV4-ARHGAP29-mCherry, BcLOV4-mCherry-ARHGAP29, and ARHGAP29-BcLOV4-mCherry expressed in HEK cells; BcLOV4-mCherry-ARHGAP29 did not associate with the membrane but the other two constructs did. These ARHGAP1 and ARHGAP29 fusion constructs will be starting points for further characterization to determine if light-induced GAP signaling occurs at the membrane.

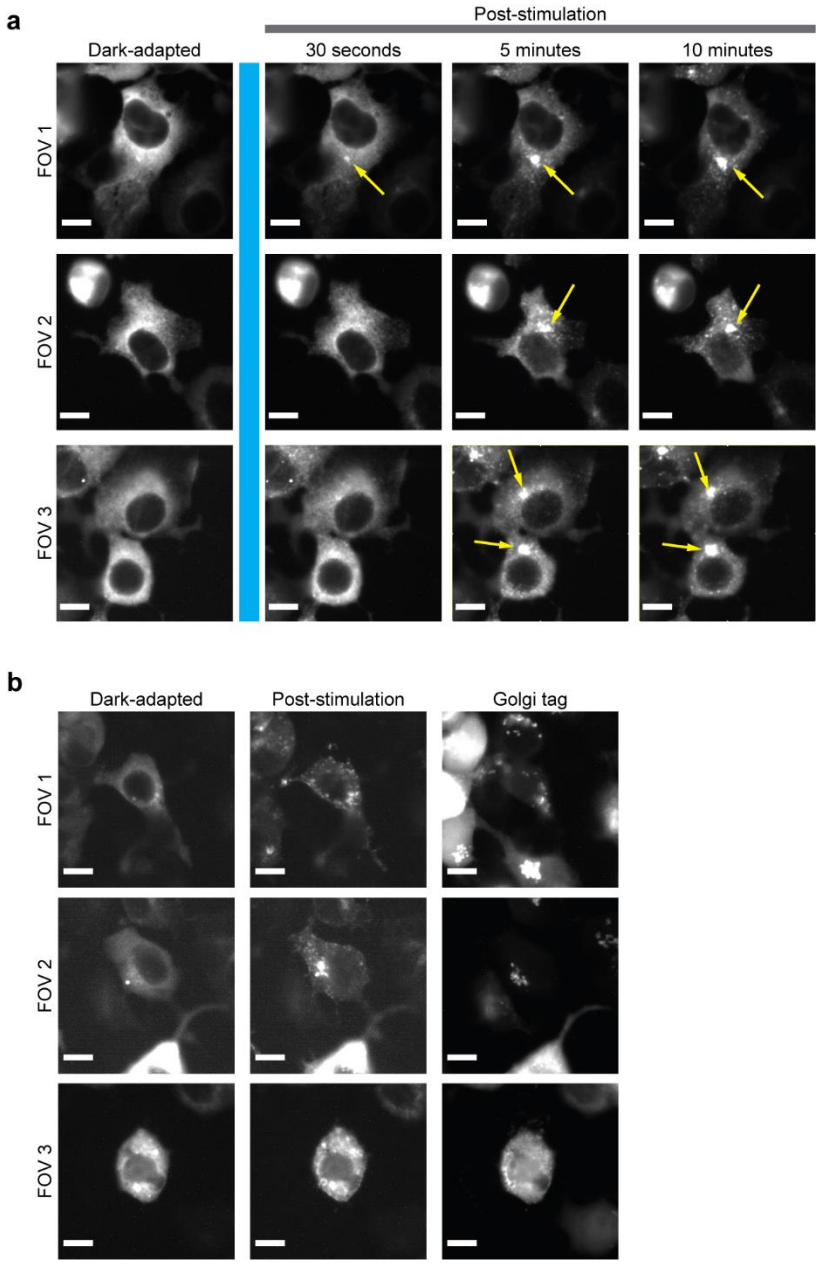

Figure 5.3 Light-induced Golgi association of full-length ARHGAP1-BcLOV4

a. Following a 5 second pulse of blue light, a large protein aggregate gradually appeared in the cytosol. **b**. This protein aggregate overlaps with an mCitrine-tagged Golgi tag. Scale = 10 µm. Yellow arrows = aggregated protein.

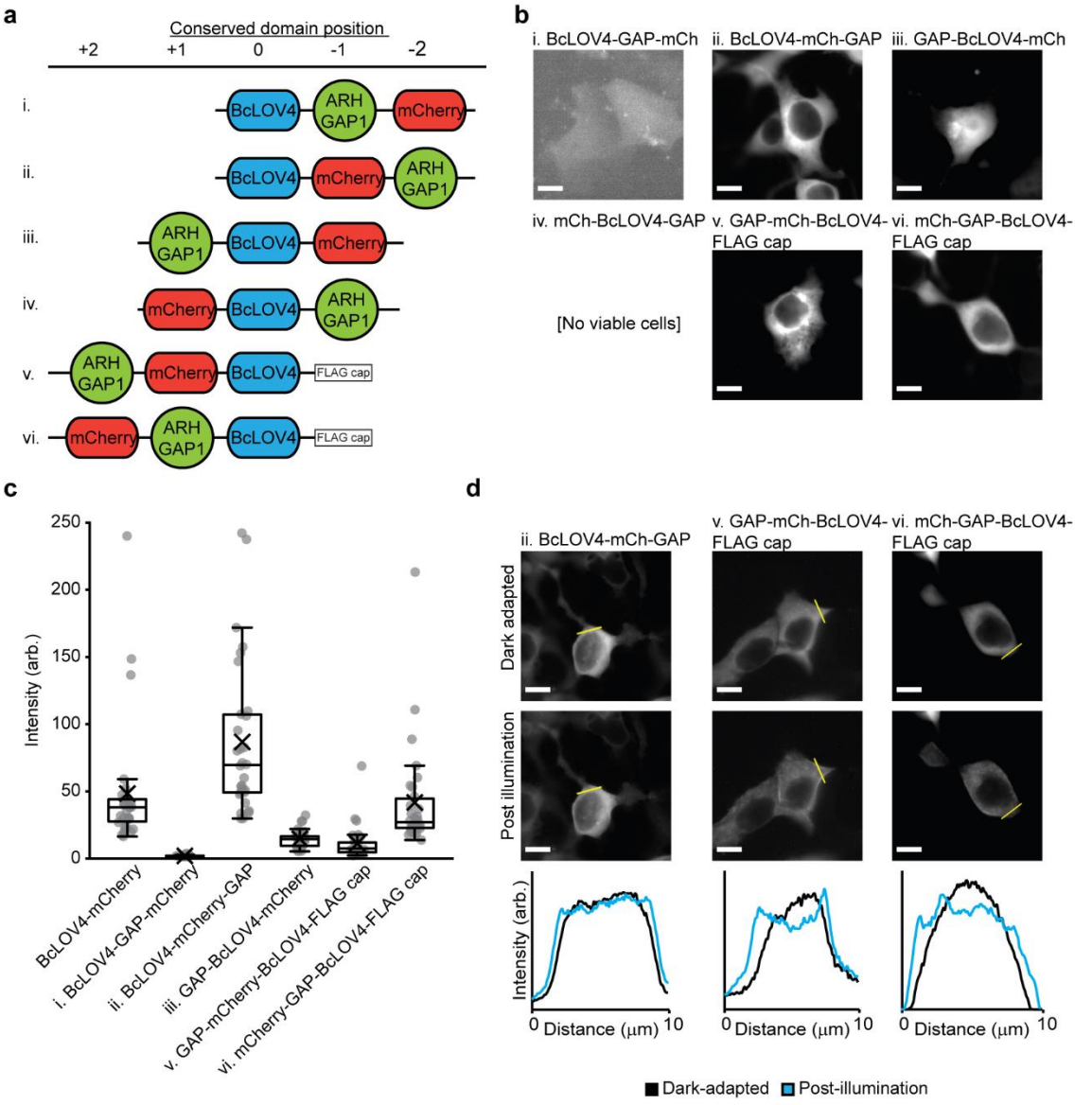

Figure 5.4 Molecular engineering of ARHGAP1-BcLOV4 fusions

a. Domain arrangement combinations of BcLOV4, ARHGAP1, and mCherry visualization tag. Domains were separated by flexible $(GGGS)_2$ linkers. **b**. Fluorescence micrographs showing representative expression patterns of the soluble domain arrangements in the dark-adapted state in HEK293T cells. Scale = 10 μm. **c**. Relative expression level of genetic constructs versus BcLOV4-mCherry control with no effector. N = 30 cells per condition. Center line, median; "X", mean; box limits, upper and lower quartiles; whiskers, 1.5x interquartile ranges **d**. Representative membrane localization of cytosolic-expressing constructs following blue light stimulation. (Top) Fluorescence micrograph; scale = 10 μm. (Bottom) Line section pixel intensity.

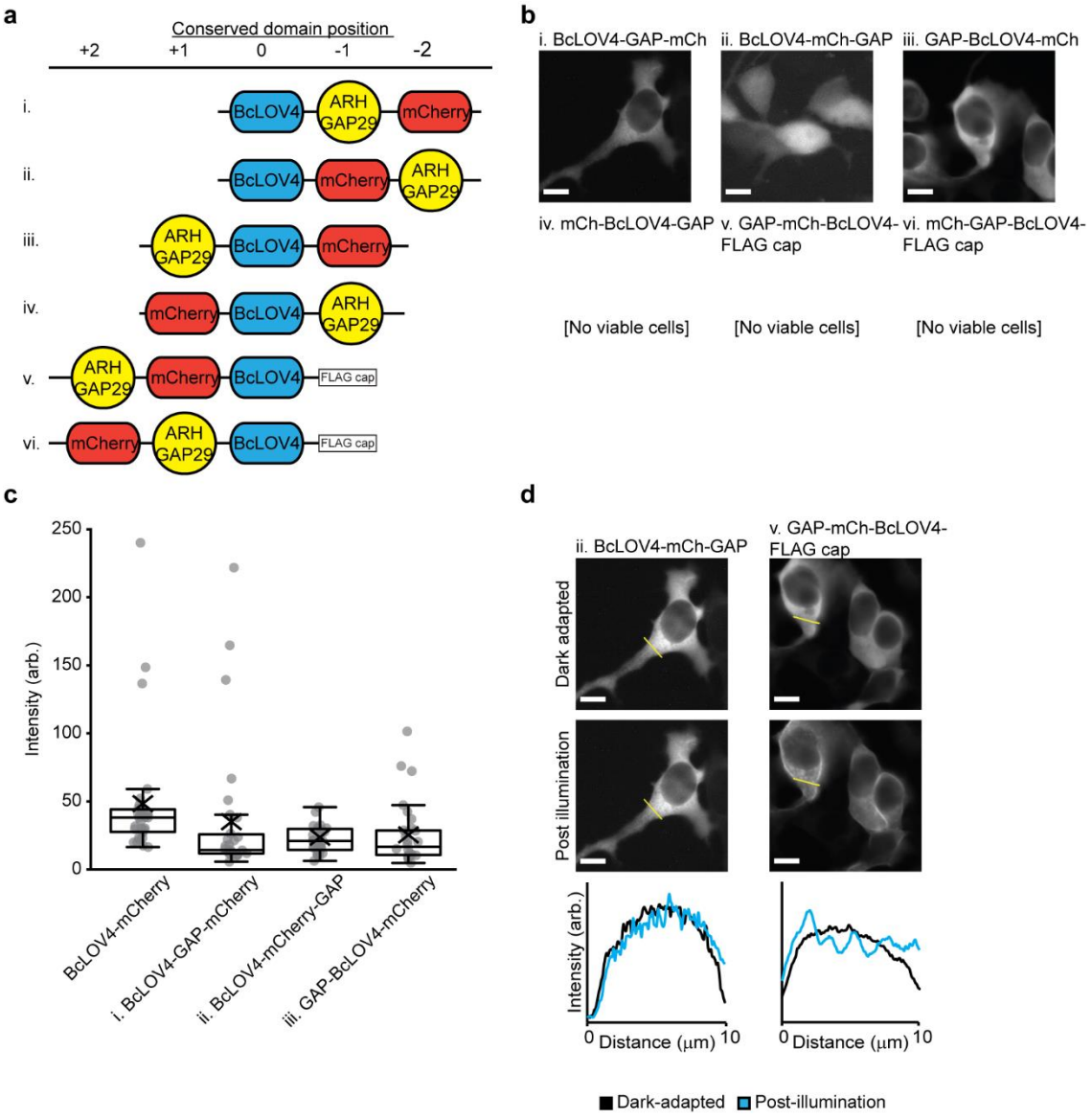

Figure 5.5 Molecular engineering of ARHGAP29-BcLOV4 fusions

a. Domain arrangement combinations of BcLOV4, ARHGAP29, and mCherry visualization tag. Domains were separated by flexible $(GGGS)_2$ linkers. **b**. Fluorescence micrographs showing representative expression patterns of the soluble domain arrangements in the dark-adapted state in HEK293T cells. Scale = 10 μm. **c**. Relative expression level of genetic constructs versus BcLOV4-mCherry control with no effector. N = 30 cells per condition. Center line, median; "X", mean; box limits, upper and lower quartiles; whiskers, 1.5x interquartile ranges. **d**. Representative membrane localization of cytosolic-expressing constructs following blue light stimulation. (Top) Fluorescence micrograph; scale = 10 μm. (Bottom) Line section pixel intensity.

5.2.4 RhoA-GTP biosensor characterization

The most straightforward method for basic functional characterization of GAP tool constructs is through the use of a GTPase biosensor. This approach gives quantitative readout indicating whether the tool in its activated state is altering the amount of active GTPase with subcellular spatial precision. For our tool engineering, we used the dTomato-2xrGBD RhoA-GTP biosensor, which binds GTP-bound RhoA with higher affinity than RhoA-GDP. Thus, RhoA signaling activation at the membrane will correspond with a decrease in cytosolic biosensor fluorescence and an increase in fluorescence in the periphery of the membrane. As previously described (130), measuring membrane fluorescence intensity from widefield micrographs can lead to numerical confounds due to convolution and imaging artifacts, so we will use cytosolic fluorescence intensity to quantify changes in biosensor localization

In the basal state, the biosensor expresses in the cytosol of HEK293T cells. Following the addition of LPA at a final concentration 10 μM, we observed a decrease in cytosolic biosensor and an increase in biosensor localized to the membrane. The extent of the cytosolic intensity decrease ranges between 30 and 50 percent of the pre-stimulation baseline with variance from cell to cell; the decrease stops about three minutes after LPA addition (**Figure 5.6**). Notably, in our hands, significant photobleaching of the dTomato fluor occurred throughout the imaging time course, underscoring the importance of using sparse biosensor imaging paradigms when possible and correcting for bleaching by calculating fluorescence decrease in non-treated cells subjected to the same excitation pulse sequence.

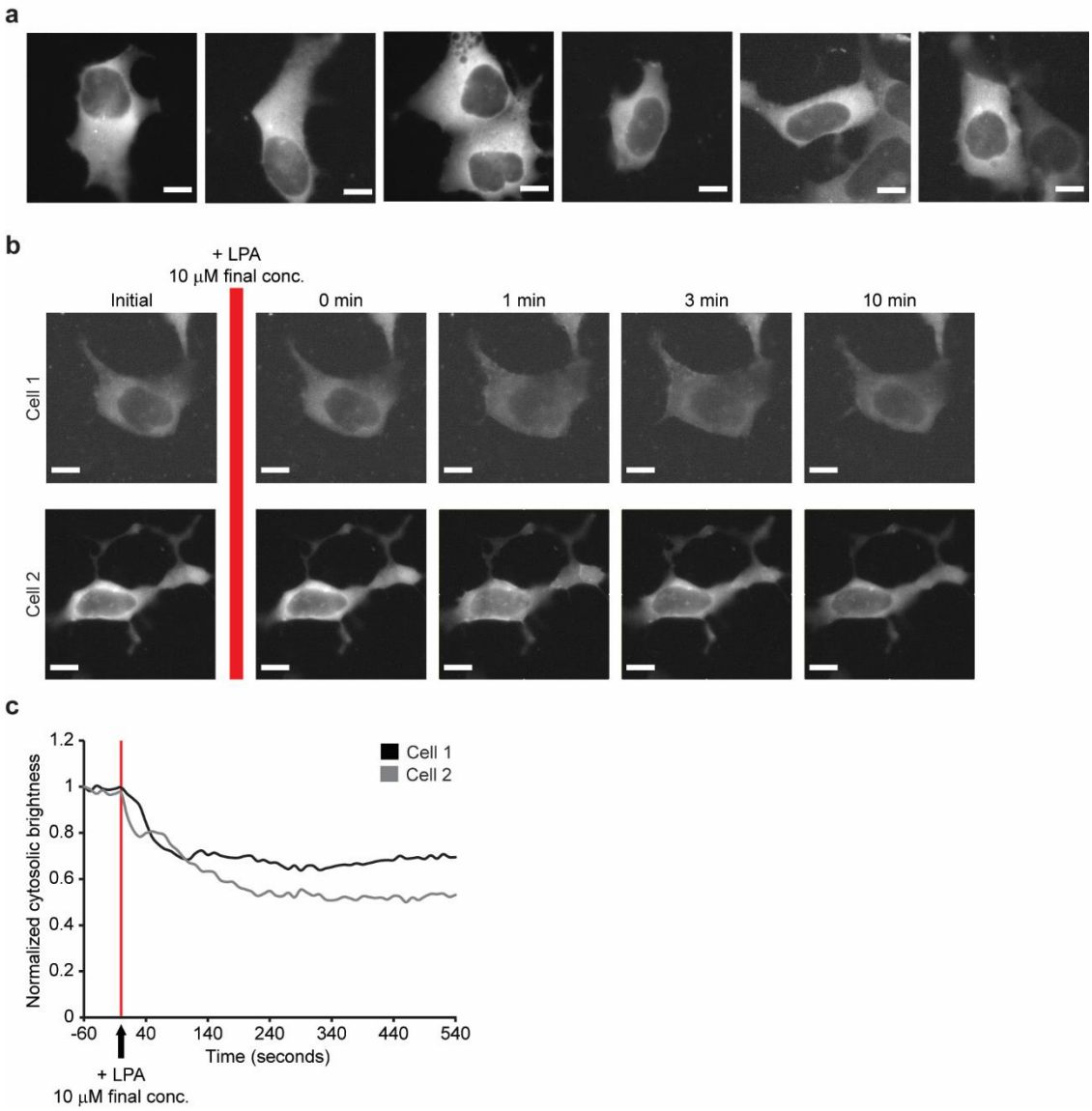

Figure 5.6 RhoA biosensor and LPA stimulation

a. Representative images of dTomato-2xrGBD in HEK293T cells. **b**. Fluorescence micrographs of biosensor-expressing cells before and after LPA stimulation. **c**. Quantification of cytosolic biosensor intensity for cells shown in (**b**), normalized to initial fluorescence readout prior to LPA stimulation. Scale = 10 μm.

Next, we sought to test the RhoA biosensor compatibility with BcLOV4-based tools. We co-expressed a Clover-tagged opto-RhoA with the dTomato-tagged biosensor and observed decrease in cytosolic biosensor similar to that caused by LPA stimulation

(**Figure 5.7a-b**). This result demonstrates that RhoA-GTP readout is compatible with the BcLOV4 system. The increased biosensor intensity at the membrane following blue light stimulation also provides further evidence that opto-RhoA is GDP-bound prior to recruitment to the membrane, where it is activated by endogenous RhoGEFs. For spatially confined illumination, biosensor localization remained the same in the cytosol outside of the stimulated region and increased at the membrane within the illumination boundary (**Figure 5.7c**). We also tested the biosensor with the co-expression of either 3xFLAG-tagged BcLOV4 or 3xFLAG-tagged opto-RhoA (**Figure 5.8**). Over a 10-minute time course, we observed a ~15% drop in cytosolic biosensor signal for BcLOV4, compared to ~40% for opto-RhoA, underscoring the need for photobleaching correction in these assays.

5.2.5 Preliminary characterization of ARHGAP tool activity

We used the biosensor transfection and imaging conditions determined above to test the viability of BcLOV4-RhoA GAP fusions. In this assay, FLAG-tagged ARHGAP1-BcLOV4 or ARHGAP29-BcLOV4 were co-transfected with the biosensor. BcLOV4-3xFLAG was used as a negative control. Cells were treated cells with LPA for three minutes, then subjected to blue light stimulation with a 1.6% duty cycle for ten minutes. LPA treatment resulted in an initial decrease in cytosolic biosensor signal and an increase in biosensor at the membrane. However, for the ARHGAP1-BcLOV4-3xFLAG condition, recovery of the cytosolic fluorescence intensity was observed within 30 seconds of blue light stimulation, eventually plateauing above the baseline observed prior to LPA addition. In contrast, BcLOV4-3xFLAG trace remained flat following the initial decrease caused by LPA treatment (**Figure 5.9**). These data suggest that

ARHGAP1-BcLOV4 may be a functional starting point for light-inducible GTPase signaling termination.

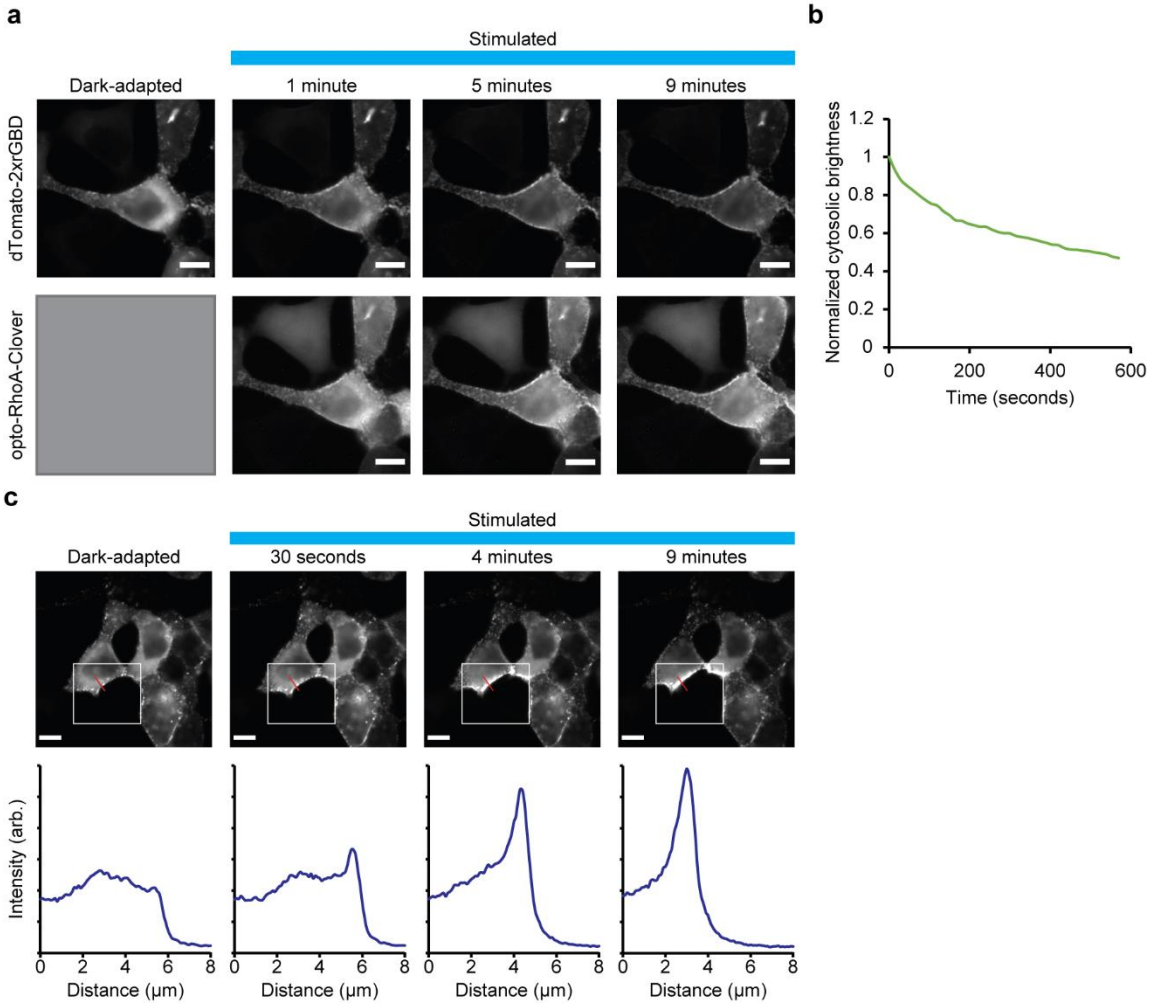

Figure 5.7 RhoA biosensor with opto-RhoA-Clover

a. RhoA biosensor (dTomato-2xrGBD) and opto-RhoA-Clover expressing cells stimulated with whole-field blue light with a 1.6% stimulation duty cycle. Dark state opto-RhoA image via Clover visualization tag could not be captured without stimulating the LOV. **b**. Quantification of cytosolic biosensor fluorescence with whole-field stimulation, normalized to fluorescence at time 0. **c**. RhoA biosensor and opto-RhoA-Clover expressing cells stimulated with spatially confined blue light with a 1.6% stimulation duty cycle. Top, micrographs visualized on dTomato (biosensor) channel. Bottom, line section profile intensity plots. White box = stimulated region. Scale = 10 µm. Red line = line section.

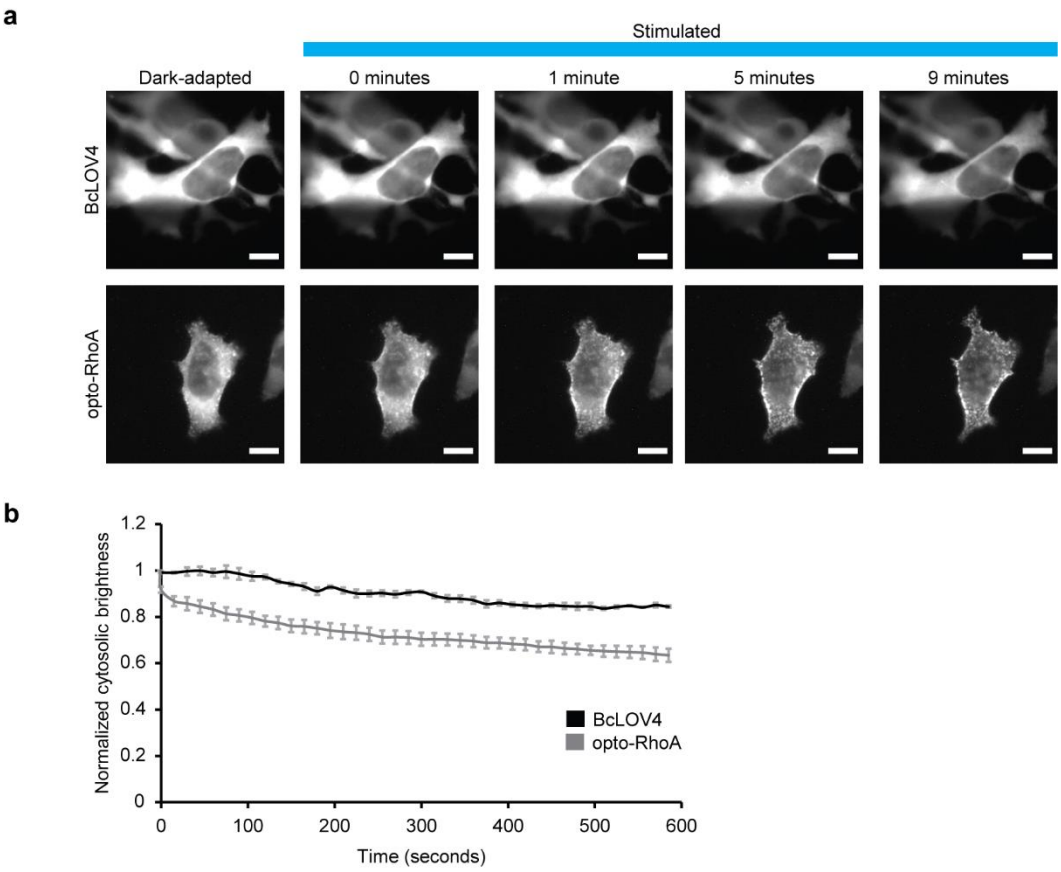

Figure 5.8 Biosensor visualization of widefield opto-RhoA stimulation

BcLOV4-3xFLAG and opto-RhoA-3xFLAG were co-expressed with dTomato-2xrGBD. **a**. Fluorescence micrographs of cells stimulated with widefield blue light with a 1.6% stimulation duty cycle. Scale = 10 µm. **b**. Cytosolic biosensor intensity over 10 minutes of stimulation, normalized to initial fluorescence at time 0. Mean ± SEM.

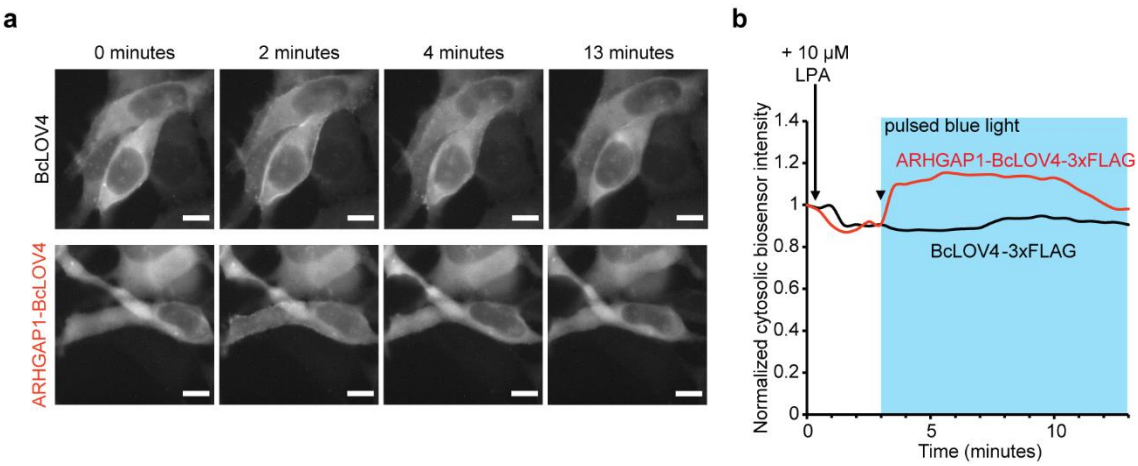

Figure 5.9 Characterization of opto-GAP tool function

BcLOV4-3xFLAG and ARHGAP1-3xFLAG were co-expressed with dTomato-2xrGBD. LPA stimulation (10 µM) was applied at time 0; whole-field blue light was applied with a 1.6% stimulation duty cycle beginning at 3 minutes. **a**. Representative images of biosensor in cells over the course of the experiment. Scale = 10 µm. **b**. Quantification of cytosolic biosensor, normalized to initial value at time 0.

5.2.6 Characterization of opto-RhoA-DN activity

In addition to GAP tool engineering, we also made some progress in the use of the BcLOV4-fused dominant negative RhoA GTPase as a new optogenetic tool. We expected recruitment of this protein to bind endogenous RhoA GEFs and prevent RhoA activation at the membrane. Early data shows that spatially confined illumination of opto-RhoA-T19N-mCherry-expressing HEK293T cells results in membrane protrusion formation within the stimulated zone (**Figure 5.10a**). Whole-field stimulation also showed some membrane ruffling and the appearance of an increase in cell area (**Figure 5.10b**). These results may suggest that RhoA signaling inhibition by the dominant negative tool results in disinhibition and apparent activation of the Rac1 GTPase. Further experiments are necessary to understand these protrusions better: a first step lies in determining whether the observed protrusions are a result of actin disassembly or concerted Rac1 activation. Interestingly, Rac1 and RhoA are typically active at different poles of the cell;

that we are observing possible Rac1 activation in the same region as RhoA inactivation may reveal new insight into RhoA-Rac1 feedback and spatial signal integration (35).

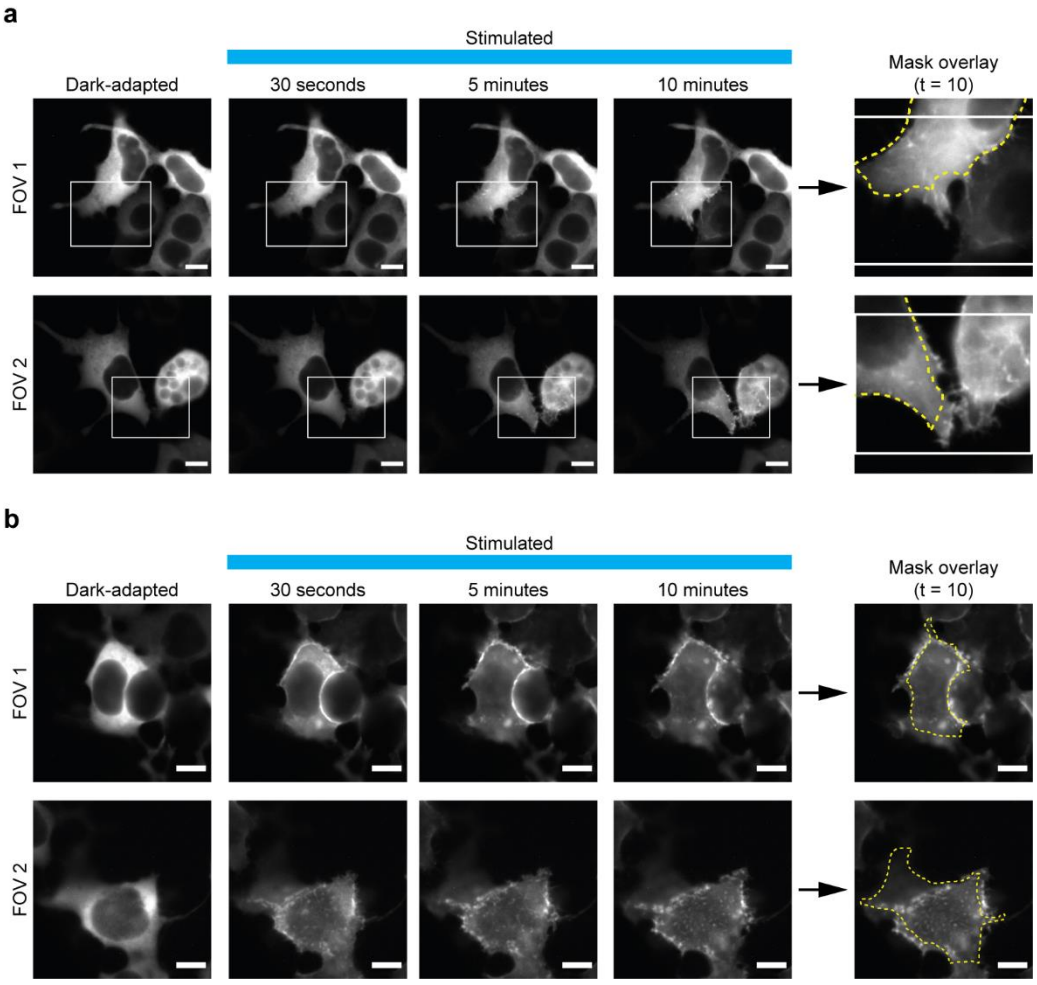

Figure 5.10 Characterization of opto-RhoA-DN

HEK293T cells expressing opto-RhoA-DN were visualized by mCherry tag with (**a**) spatially confined stimulation and (**b**) widefield stimulation at a 1.6% duty cycle. White box = stimulated region. Yellow dotted line = initial cell boundary at time 0. Scale = 10 µm.

5.3 Conclusions and future directions

5.3.1 Conclusions

Here, we report initial progress in the creation of RhoA GAP and RhoA dominant negative tools. For GAP perturbation, we observed a decrease in pharmacologically

elevated RhoA-GTP levels following light-induced activation of an ARHGAP1-BcLOV4 fusion in HEK293T cells. For dominant negative RhoA, we observe protrusion formation following tool stimulation, suggesting either disassembly of RhoA-polymerized actin or the disinhibition of Rac1, resulting in lamellipodia formation. We plan to carry out more extensive characterization and application of these tools as described below.

5.3.2 Further characterization of GAP and DN tools

Several experiments are necessary to characterize the RhoA GAP tools. First, we will repeat the biosensor assay in which RhoA signaling is initially stimulated with LPA and then terminated by BcLOV4-GAP membrane recruitment. In addition to increasing sample size allowing for statistical comparison to dark-state controls, we also seek to understand the timescale and extent of GAP inactivation that can be achieved in this setup. Of particular interest is whether the increase in cytosolic biosensor above pre-LPA treatment baseline observed in the pilot GAP study is reproducible; if so, it may suggest that pharmacological RhoA stimulation is not necessary to observe GAP activation with the RhoA biosensor. In addition, we will conduct the same experiment with DMD stimulation to determine how cell polarization and angle of blue light stimulation affect GAP tool activity, as well as morphological changes which may occur to the rest of the cell following increased local concentration of RhoA GAP.

We also plan to characterize the effect of the GAP tools on cell polarization and investigate whether they can be used to delay or inhibit cell polarization and actin cap formation. We will compare the proportion of GAP tool-expressing cells exhibiting well-formed actin caps (visualized by phalloidin staining) following trypsinization and plating in lit versus dark state conditions compared to BcLOV4 control cells. We hypothesize that membrane recruitment of the GAP will prevent cell polarization, resulting in more

rounded cells without actin caps in the lit state. Finally, we plan to use opto-GAP tools to characterize the timescales of RhoA activation and inactivation. Specifically, we will use genetically encoded biosensors and fluorescently tagged proteins to compare how long it takes to observe changes in downstream proteins like ROCK and myosin light chain, as well as cytoskeletal changes like actin organization and focal adhesions following signaling activation or termination.

For dominant negative GTPase tools, the most pressing question is to determine what is underlying the light-induced protrusion formation we have observed. To determine whether the phenomenon is due to Rac1 activation or simply actin disassembly, we will visualize polymerized actin in either live cells using LifeAct or fixed cells using phalloidin. A decrease in polymerized actin in the lit state suggests disassembly, while an increase suggests a GTPase-mediated event. We can also use pharmacological inhibitors of Rac1 signaling like GEF inhibitor NSC 23766 and Arp2/3 inhibitor CK 666 to confirm that Rac1 mediates the protrusions we observe. Identification of a suitable Rac1 biosensor would provide further confirmation that membrane recruitment of dominant negative RhoA results in disinhibition of Rac1. Identification of the mechanism of protrusion formation will enable us to use the dominant negative tool to investigate RhoA-Rac1 feedback.

5.3.3 Investigating RhoA-YAP mechanotransduction

A major motivation of the creation of the BcLOV4 Rho GTPase optogenetic toolbox was the ability to answer interesting biological questions which previously could not be explored in such depth. An example of this kind of question is the RhoA-YAP mechanotransductive feedback loop (157) which drives persistent cell migration. Creation of opto-RhoA, including wildtype, dominant negative, and constitutively active

mutants, as well as opto-RhoGAP and opto-RhoGEF will allow us to systematically perturb each node in the feedback loop and measure the changes they effect on YAP nuclear localization through visualization of fluorescently tagged or immunolabeled YAP, on transcription through qPCR, and cell migration through long-timescale microscopy assays.

Specifically, we can compare the effects of RhoA activation using opto-RhoA and opto-RhoGEF and measure the effects of local GAP:GEF balance on downstream YAP signaling. Because RhoA signaling leads to RhoGAP transcriptional upregulation, an interesting question is whether the constitutively active opto-RhoA leads to a similar increase in RhoGAP expression. The G17V mutation in the constitutively active RhoA mutant renders it insensitive to GAP-mediated hydrolysis, leading us to question whether its GAP insensitivity would change the nature of the GAP upregulation feedback loop. Finally, we will compare signaling turn-off mechanisms using opto-RhoGAP and opto-RhoA-DN to determine their effects on cytoskeletal tension and the timescale of GTPase inactivation. Characterizing this feedback loop using the tools described in this thesis would allow us to uncover new biological insights into persistent cell migration and deepen our understanding of how cells integrate transcription, signaling, and mechanics.

5.3.4 Investigating RhoA-Rac1 feedback

An important aspect of Rho GTPase signaling which is not fully understood is the ability of GTPases to regulate each other. An example of this inter-pathway crosstalk is the RhoA-Rac1 feedback loop. RhoA and Rac1 activation events are often localized to opposite ends of the migrating cell, with RhoA initiating contraction at the trailing edge while Rac1 induces protrusions to drive the leading edge forward(35). RhoA and Rac1 have been demonstrated to inhibit each other, though many questions remain. Adding

the RhoA dominant negative tool to our signaling toolbox will allow us to investigate the mechanism of RhoA-Rac1 crosstalk by selectively inhibiting RhoA signaling and comparing subsequent Rac1 signaling to direct pathway activation using opto-Rac1 or opto-Tiam1. We will also use pharmacological inhibitors of Rac1 signaling to learn about the mechanism through which RhoA inhibition activates Rac1.

In parallel, we will also create a dominant negative form of opto-Rac1 through the T17N mutant (40) and determine whether parallel inhibition and activation can be observed, i.e., cell contraction following Rac1 inhibition implying disinhibition of RhoA. Using biosensors in conjunction with dominant negative tools, we will investigate how local concentrations of GTPases and GEFs as well as underlying cell polarity affects crosstalk. Specifically, we will co-express wildtype GTPase (i.e., opto-RhoA and opto-Rac1) or dominant negative GTPase (i.e., opto-RhoA-DN and opto-Rac1-DN) tools and recruit both tools simultaneously to the membrane using DMD-patterned illumination, thus activating or inhibiting both players in the feedback loop. We will measure the effects of this dual inhibition using a RhoA or Rac1 biosensor and observed changes in cell morphology to uncover the relative magnitudes of RhoA and Rac1 inhibition and uncover the spatial integration dynamics of the feedback loop.

GEF and GAP tools can also be used to inform mechanism of RhoA-Rac1 feedback, as some proposed mechanisms of inhibition include RhoA activating a Rac1-inhibiting GAP (182) and Rac1 inhibiting a RhoA-activating GEF (176). Using the expanded BcLOV4 toolbox, we can test these proposed mechanisms: for example, we can locally activate a Rac1 GAP to determine whether RhoA activity increases, or inactivate RhoA GEFs using dominant negative Rac1. In conjunction with experiments with pharmacological GEF and GAP inhibitors, we can gain new mechanistic insight into RhoA-Rac1 interaction. Overall, expanding the BcLOV4 toolbox to include dominant

negative GTPases will allow for more thorough investigation of the mechanisms behind Rho GTPase crosstalk and regulation.

5.4 Materials and methods

5.4.1 Genetic constructs

Domain arrangement combinations of BcLOV4, mCherry, and the ARHGAP1 or ARHGAP29 effector (with a flexible $(GGGS)_2$ linker between each pair) were assembled into the pcDNA3.1 mammalian expression vector under a CMV promoter by Gibson cloning with NEB HiFi DNA Assembly Master Mix (E2621). BcLOV4 and mCherry were amplified from their previously reported mammalian codon-optimized fusion (Addgene plasmid 114595) (69). The DNA sequences of ARHGAP1 (Genbank ID NP_004299.1) and ARHGAP29 (Genbank ID AAH93741.1) were human codon-optimized using the Integrated DNA Technologies (IDT) Codon Optimization Tool and ordered as a gBlock® from IDT or as a synthesized gene without adapters from Twist Biosciences. The GAP domain of each protein was identified using the PROSITE ExPASy database and amplified from the full-length gene. All genetic constructs were transformed into competent *E. coli* (New England Biolabs, C2984H). All sequences were verified by Sanger sequencing.

The RhoA dominant negative (T19N) mutant was generated by QuikChange site-directed mutagenesis according to manufacturer's instructions. Briefly, overlapping primers encoding the mutation with melting temperatures ≥ 78°C were designed using Agilent's online primer design tool (https://www.agilent.com/store/primerDesignProgram.jsp). The mutation was introduced over 18 PCR cycles with 8-minute elongation time using the Phusion® high-fidelity DNA polymerase master mix (New England Biolabs, M0531). The opto-RhoA-mCherry

template plasmid was digested with DpnI for one hour at 37°C before transformation into Turbo competent cells.

For co-localization experiments, GFP membrane marker (pCIBN(deltaNLS)-pmGFP, #26867) and Golgi marker (mCitrine-SiT-N-15, # 56318) were acquired from Addgene. The RhoA-GTP biosensor was acquired from Addgene (dTomato-2xrGBD, #129625).

5.4.2 Cell culture and transient transfection

All mammalian cells were maintained in a 5% CO_2 water-jacketed incubator (Thermo/Forma ,3110) at 37°C. For imaging experiments, cells were seeded onto poly-D-lysine-treated glass bottom dishes (MatTek, P35GC-1.5-14-C) or into 24-well glass bottom plates (Cellvis, P24-1.5H-N), treated in-house with type I collagen, at 15-20% confluency. Cells were transfected 24 hours after seeding at ~30-40% confluency, then imaged 24-48 hours after transfection. All transfections were performed with Opti-MEM™ reduced serum media (Thermo Fisher, 3195062).

HEK293T (ATCC, CRL-3216) were cultured in D10 media composed of Dulbecco's Modified Eagle Medium with GlutaMAX (Invitrogen, 10566016), supplemented with 10% heat-inactivated fetal bovine serum (FBS) and penicillin-streptomycin at 100 U/mL. HEK cells were transfected using the TransIT-293 transfection reagent (Mirus Bio, MIR2700) according to manufacturer instructions.

5.4.3 Fluorescence microscopy and hardware

Fluorescence microscopy was performed on an automated Leica DMI6000B fluorescence microscope under Leica MetaMorph control, with a sCMOS camera (pco.edge), an LED illuminator (Lumencor Spectra-X), and a 63× oil immersion

objective. Excitation source illumination was filtered at the LED source (mCherry imaging λ = 575/25 nm; GFP or Alexa Fluor 488 imaging or widefield BcLOV4 stimulation λ = 470/24 nm; mCitrine imaging λ = 513/17 nm). Fluorescent proteins were imaged with Chroma filters: mCherry (T585lpxr dichroic, ET 630/75 nm emission filter, 0.2-0.5 s exposure), GFP (T495lpxr dichroic, ET 525/50 nm emission filter, 0.2 s exposure), mCitrine (T520lpxr dichroic, ET 535/30 nm emission filter, 0.5 s exposure). Digital micromirror device (DMD) was constructed as described in Chapter 3.

Cells were imaged at room temperature in CO_2-independent media (phenol-free HBSS supplemented with 1% l-glutamine, 1% penicillin-streptomycin, 2% essential amino acids, 1% nonessential amino acids, 2.5% HEPES pH 7.0, and 10% serum).

5.4.4 Expression level measurement

HEK293T cells were co-transfected with a GFP membrane marker and mCherry-tagged tool construct in a 1:10 ratio. Cells were imaged at 63× magnification for 3-5 fields of view per construct. mCherry fluorescence was imaged with a 0.5 s exposure time, followed by GFP fluorescence imaging (0.2 s exposure). mCherry fluorescence was the imaged again after 5 seconds of blue light stimulation. N = 30 cells per condition.

5.4.5 Widefield and DMD stimulation assays

For widefield stimulation assays, mCherry fluorescence was imaged before a 5-second pulse of blue light. mCherry fluorescence was then imaged every 15-30s for 10 min following stimulation. For data analysis, each cell was treated as a separate data point, with N = 30 cells per condition. For DMD stimulation assays, mCherry fluorescence was imaged every 15 seconds for 10 minutes. During this time, cells were

stimulated for one second per minute (1.6% duty cycle) patterned illumination (25 μm-wide square encompassing ~25% of cell area). For widefield and DMD stimulation assays, statistical significance was assessed by the two-sided non-parametric Mann-Whitney U test, uncorrected for multiple comparisons.

5.4.6 Biosensor and stimulation experiments

The RhoA-GTP biosensor was co-transfected with the tool plasmid of interest at a 1:1 ratio. The biosensor was imaged using mCherry settings (FIM 100, 0.5 s exposure). Biosensor localization changes were measured by defining a cytosolic region of interest and measuring fluorescence intensity in that region over time. For RhoA activation, lysophosphatidic acid (18:1 LPA, Avanti Polar Lipids, 857130P) was prepared as a 1 mM stock in a 1:1 mixture of ethanol and water. Aliquots were stored at -20 °C in glass vials with Teflon caps. Prior to use, aliquots were warmed on a 50 °C heat block for 10 minutes, then homogenized in a water bath sonicator for 2-5 minutes. For stimulation, cells were treated with LPA for a final concentration of 10 mM, either by adding the lipid mixture directly to cells using a Hamilton syringe or by perfusing serum-free CO_2 independent media pre-mixed with LPA over cells using a syringe pump at a rate of 0.5 mL/min.

CHAPTER SIX: Design principles governing BcLOV4 tool engineering

This chapter adapts work from the following publication:

Berlew, E. E.; Yamada, K.; Kuznetsov, I. A.; Rand, E. A.; Ochs, C. C.; Jaber, Z.; Gardner, K. H.; Chow, B. Y., Designing single-component optogenetic membrane recruitment systems: the Rho-family GTPase signaling toolbox. *ACS Syn Biol* 2022.

Author contributions: EEB and KY designed genetic constructs, designed experiments, conducted experiments, and analyzed data. IAK constructed the patterned illumination system, conducted the FRAP measurement, and contributed to automated data analysis development. EAR and CO assisted with genetic construct design, engineering, and assays. BYC coordinated all research. All authors contributed to data analysis and manuscript preparation.

6.1 Introduction

6.1.1 BcLOV4 structure-function

Optogenetic tools made from different photosensory proteins differ in signal transduction mechanism from sensor to effector. In membrane recruitment systems, the structural basis of this mechanism determines the design rules for how the tool platform can be engineered to bring proteins of interest to the plasma membrane. To our knowledge, BcLOV4 is the first characterized RGS-LOV protein; while its individual protein domains bear sequence homology to known RGS and LOV proteins and its photocycle kinetics are in line with previously reported LOVs, structural insight into

BcLOV4 and other RGS-LOVs is still emerging. Elucidation of the structure-function underlying BcLOV4's light-induced conformational change and lipid binding will support its use as an optogenetic tool platform.

As discussed in chapter 2, BcLOV4 is a multi-domain protein: RGS, LOV, and PAS-like domain of unknown function (DUF) domains are preceded by a 98-residue disordered N-terminus. Attempts to remove non-LOV domains have yielded mixed results, suggesting that the protein may be sensitive to the placement and size of effector proteins when engineering optogenetic fusion tools. The disordered N-terminus can be removed without issue in bacterial overexpression systems, though yield was significantly decreased for the same truncation in mammalian cells. Removal of the N-terminus preceding the LOV domain (i.e., the first 242 residues of the protein) results in lipid binding in the dark state, suggesting that the RGS domain is important for shielding the amphipathic helix prior to blue light exposure. C-terminal truncation after the helix abolished lipid binding in mammalian cells. The sensitivity of BcLOV4 to removal or alteration of its termini suggests that addition of additional protein domains may alter BcLOV4 expression and signal transduction in cells. In light of these results, we wanted to explore the design rules governing BcLOV4 tool fusions to gain insight into RGS-LOV structure-function and guide future engineering of BcLOV4 optogenetic fusion tools.

6.1.2 Problem statement

In screening the expression of domain arrangements during the construction of GEF and GTPase fusion tools, we observed that arrangements with mCherry and the effector at the N-terminus of BcLOV4 were consistently disfavored (**Figure 6.1**). Instead of expressing in the cytosol and translocating to the membrane in response to blue light exposure, these constructs exhibited a permanently lit-like phenotype, with protein

bound to the membrane and/or aggregated in puncta throughout the cytosol even prior to light stimulation. These disfavored domain arrangements share two features: increased steric bulk of both mCherry and the effector protein at the BcLOV4's N-terminus and a solvent-exposed BcLOV4 C-terminus. We sought to uncover the BcLOV4 structure-function underlying this phenotype and engineer the protein to make viable these previously disfavored arrangements.

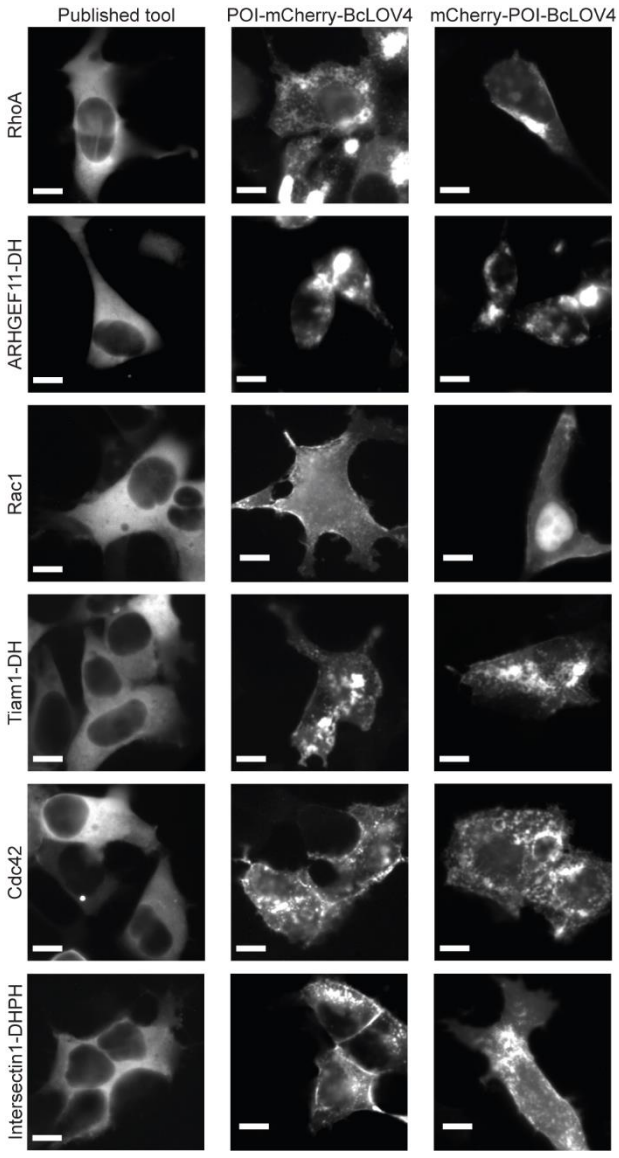

Figure 6.1 Disfavored BcLOV4 domain arrangements

Published tools for Rho-family GTPases and GEFs compared to the same effectors' disfavored domain arrangements. Scale = 10 μm.

6.2 Results and discussion

6.2.1 The effects of terminal fluorescent protein bulk on BcLOV4 localization

To determine whether the phenotype of the disfavored BcLOV4 tool domain arrangements was the result of BcLOV4 folding, we expressed constructs with effector bulk replaced with additional fluorescent protein (FP) tags in cells and observed their localization (**Figure 6.2**). Interestingly, we found that BcLOV4 constructs were permanently membrane-localized if one, two, or three FPs were fused to its N-terminus without any tag on the C-terminus. Unlike the lit-like $(FP)_n$-BcLOV4 fusions, constructs with at least one FP fused to the C-terminus of BcLOV4 were cytosolic in the dark state and reversibly bound the plasma membrane in response to blue light stimulation, regardless of N-terminal bulk. These expression patterns suggested that the pre-stimulation membrane binding observed in disfavored tool constructs was due to interactions between BcLOV4's amphipathic helix and inner leaflet phospholipid head groups, rather than an interaction between the fused effector and its membrane-localized interaction partner.

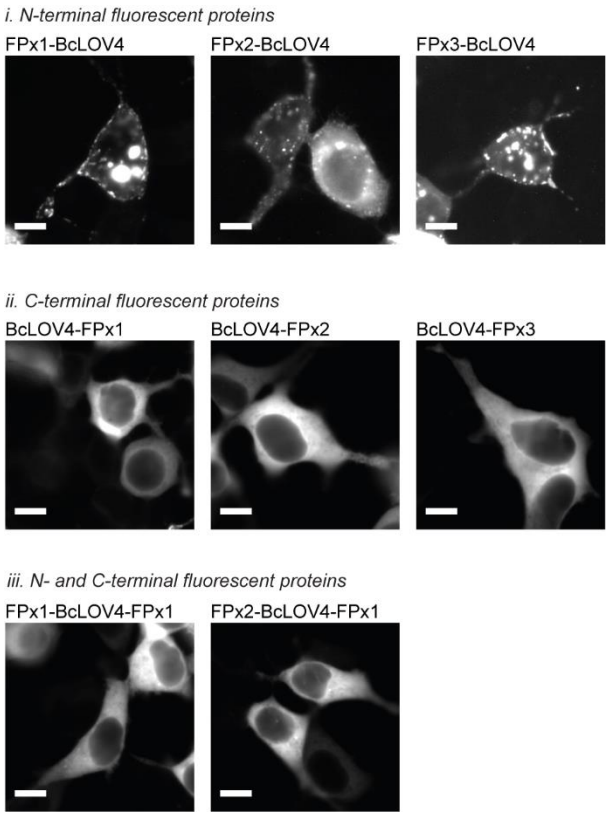

Figure 6.2 The effect of fluorescent protein bulk on BcLOV4 protein localization

mCherry fluorescence was visualized for dark-adapted HEK293T cells. Scale = 10 µm.

6.2.2 Immunochemical investigations into the BcLOV4 C-terminus

Across pathways, effectors, and FPs, the lit-like constructs shared two characteristics: an exposed BcLOV4 C-terminus and at least one protein domain at its N-terminus. We next sought to determine whether the exposed C-terminus alone was responsible for this phenotype and the N-terminal bulk was merely a confound of our experimental need to visualize the proteins in the cell, or whether the combination of bulk and terminus exposure caused pre-stimulation membrane binding. To differentiate between these possibilities, we replaced FP-based visualization with immunostaining fixed cells expressing epitope-tagged BcLOV4. This substitution allowed us to reduce

drastically the steric bulk required to image BcLOV4 in cells and better explore the role of the uncapped C-terminus.

We first imaged BcLOV4 tagged with 3xFLAG at its N-terminus, reducing the N-terminal bulk from several hundred amino acids to 24, and observed that 3xFLAG-BcLOV4 was membrane-localized even in its dark state (**Figure 6.3a**). Previous experiments showed that BcLOV4-3xFLAG (i.e., tagged at its C-terminus) was cytosolic in its dark state and membrane-localized under blue light. We tested a smaller epitope, His_6, and observed similar lit-like expression for His_6-BcLOV4 (**Figure 6.3b**). These results suggest that exposure of BcLOV4's C-terminus is responsible for the lit-like phenotype we observed in these disfavored constructs, though it should be noted that without an antibody to immunostain and image BcLOV4 itself, we cannot rule out that *any* N-terminal bulk, even a few amino acids, is disruptive to BcLOV4 folding without a C-terminal protein domain.

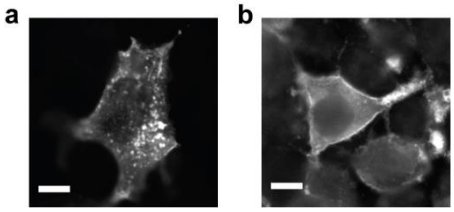

Figure 6.3 Visualization of BcLOV4 localization with N-terminal epitope tags

HEK293T cells expressing (**a**) 3xFLAG-BcLOV4 and (**b**) His_6-BcLOV4 were fixed in the dark and protein localization was visualized by anti-FLAG (**a**) or anti-His (**b**) immunostaining.

6.2.3 Partial rescue of light-induced membrane association with C-terminal mutagenesis

Based on the consistently lit-like expression pattern of two domain arrangements in our tool screening workflow, these arrangements were not suitable for dynamic

signaling induction and the possible constructs for each tool were reduced from six to four. For most effectors, one of these four remaining effectors was found to be a functional membrane recruitment tool, but Cdc42 proved to be an exception: we observed leakiness and some off-target filopodia formation with the potentially viable constructs identified in the screening workflow. To accommodate the diverse structures of proteins of interest for membrane recruitment, we sought to engineer BcLOV4 to tolerate being at the C-terminus of the fusion protein and make viable these previously disfavored arrangements.

The final residue of untagged BcLOV4 is phenylalanine; due to its bulk and aromaticity, we hypothesized that solvent exposure of this amino acid could disrupt protein folding and result in dark-state exposure of the lipid-binding amphipathic helix. We created several mutants of the F594 residue spanning the chemical diversity of amino acids and imaged HEK cells expressing these mutants fused to an N-terminal mCherry tag (**Figure 6.4a-b**). None of the point mutants screened (F594del, F594A, F594E, F594G, F594K, F594S) fully rescued the dark-state cytosolic expression observed for BcLOV4-mCherry, though the F594A mutant exhibited higher cytosolic fluorescence and some enhanced blue light-driven membrane association (**Figure 6.4c**). All screened constructs exhibited a dark-state membrane:cytosol fluorescence ratio greater than one, meaning more protein was localized to the membrane than for BcLOV4-mCherry (ratio ~ 0.8). Thus, point mutations of the C-terminus of BcLOV4 were not sufficient to inhibit dark-state membrane binding and operationalize previously disfavored domain arrangements.

6.2.4 FLAG capping of BcLOV4's C-terminus

In some tool characterization studies, we replaced the mCherry visualization tag with a 3xFLAG peptide tag to increase the number of optical channels available to us in the experiment. Interestingly, we observed that FLAG-tagged opto-RhoA (RhoA-BcLOV4-3xFLAG) exhibited an expression profile similar to that of BcLOV4-mCherry (i.e., cytosolic in its dark state and membrane-localized under blue light, as confirmed by anti-FLAG immunostaining). This observation suggested that the 3xFLAG peptide (GGGS linker followed by DYKDHDG-DYKDHDI-DYKDDDDK) was sufficient to recover BcLOV4's light-inducible membrane binding (**Figure 6.5a**).

To test the generality of this observation, we expressed mCherry-BcLOV4 in HEK cells with and without a C-terminal FLAG tag and imaged cells before and after blue light exposure. Uncapped mCherry-BcLOV4 appeared permanently membrane-localized, while mCherry-BcLOV4-3xFLAG was cytosolic in the dark and bound the membrane in response to blue light stimulation (**Figure 6.5b**). To quantify this phenomenon and assess its statistical significance, we measured the membrane:cytosol

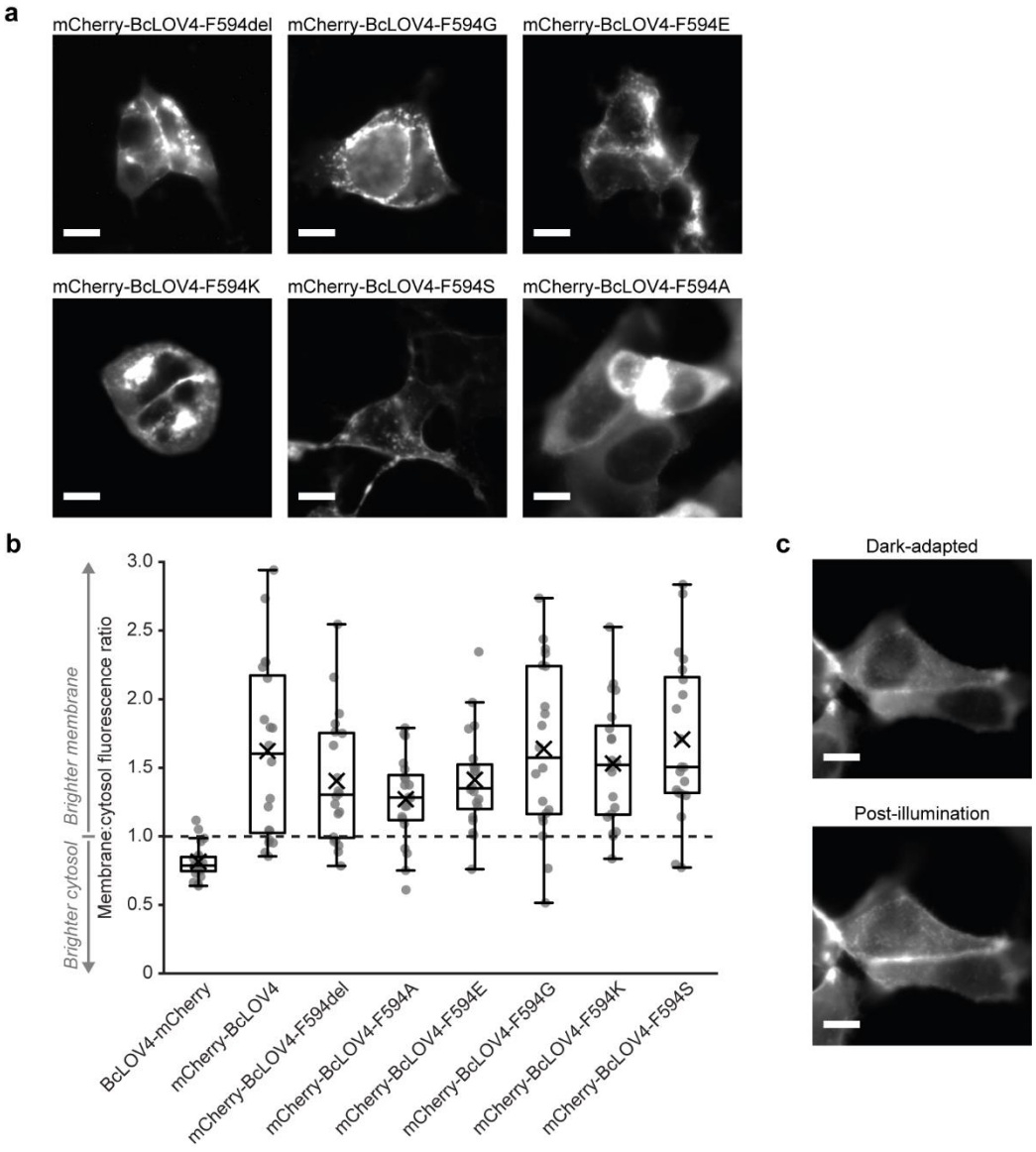

Figure 6.4 BcLOV4 C-terminal mutagenesis

a. Representative images mCherry-BcLOV4 with final F594 residue mutated. **b**. Quantification of dark-state membrane:cytosol protein ratio for C-terminal mutants. N = 20 cells per condition. **c**. Dark-adapted and post-illumination images of mCherry-BcLOV4-F594A. Scale = 10 µm.

fluorescence ratio in each light condition for N = 30 cells per construct and applied a non-parametric Mann-Whitney U test comparing dark- and lit-state cells for each construct (**Figure 6.5c**). For uncapped mCherry-BcLOV4, the ratio was greater than one in both conditions, reflecting the higher protein concentration at the membrane

compared to the cytosol, and no significant difference was observed between dark and lit states (mean ± SEM, dark ratio = 1.62 ± 0.132, lit ratio = 1.66 ± 0.134, p = 0.43). FLAG-capped mCherry-BcLOV4 more closely mirrored the localization pattern observed for BcLOV4-mCherry, with a ratio less than one for dark-state protein and greater than one following blue light stimulation (mean ± SEM, dark ratio = 0.867 ± 0.031, lit ratio = 1.08 ± 0.039, $p < 0.001$).

We also tested the FLAG cap's ability to rescue cytosolic expression in constructs with greater N-terminal bulk and observed light-inducible translocation for 3x-mCherry-BcLOV4-3xFLAG, a construct with ~85 kDa of protein at BcLOV4's N-terminus, while the uncapped version of this construct was permanently membrane-bound. This finding suggested that FLAG capping the C-terminus of BcLOV4 is a valid strategy to make viable the previously disfavored domain arrangements with two protein domains N-terminal to BcLOV4.

6.2.5 Membrane translocation kinetics of FLAG-capped BcLOV4

Membrane association kinetics for mCherry-BcLOV4-3xFLAG were similar to those of BcLOV4-mCherry, with τ_{on} = 1.17 s (95% CI 1.05-1.29 s), demonstrating that FLAG capping has no significant effect on the rapid light-induced membrane translocation of BcLOV4 which makes it suitable for optogenetic tool development (**Figure 6.6a**). Membrane dissociation for this FLAG-capped variant is slower, with τ_{off} = 126.2 s (95% CI = 118.8-133.7 s) (**Figure 6.6b**). This lengthened residence time suggests that adding steric bulk at the termini of BcLOV4 can affect the speed of thermal reversion and release of the membrane by the amphipathic helix.

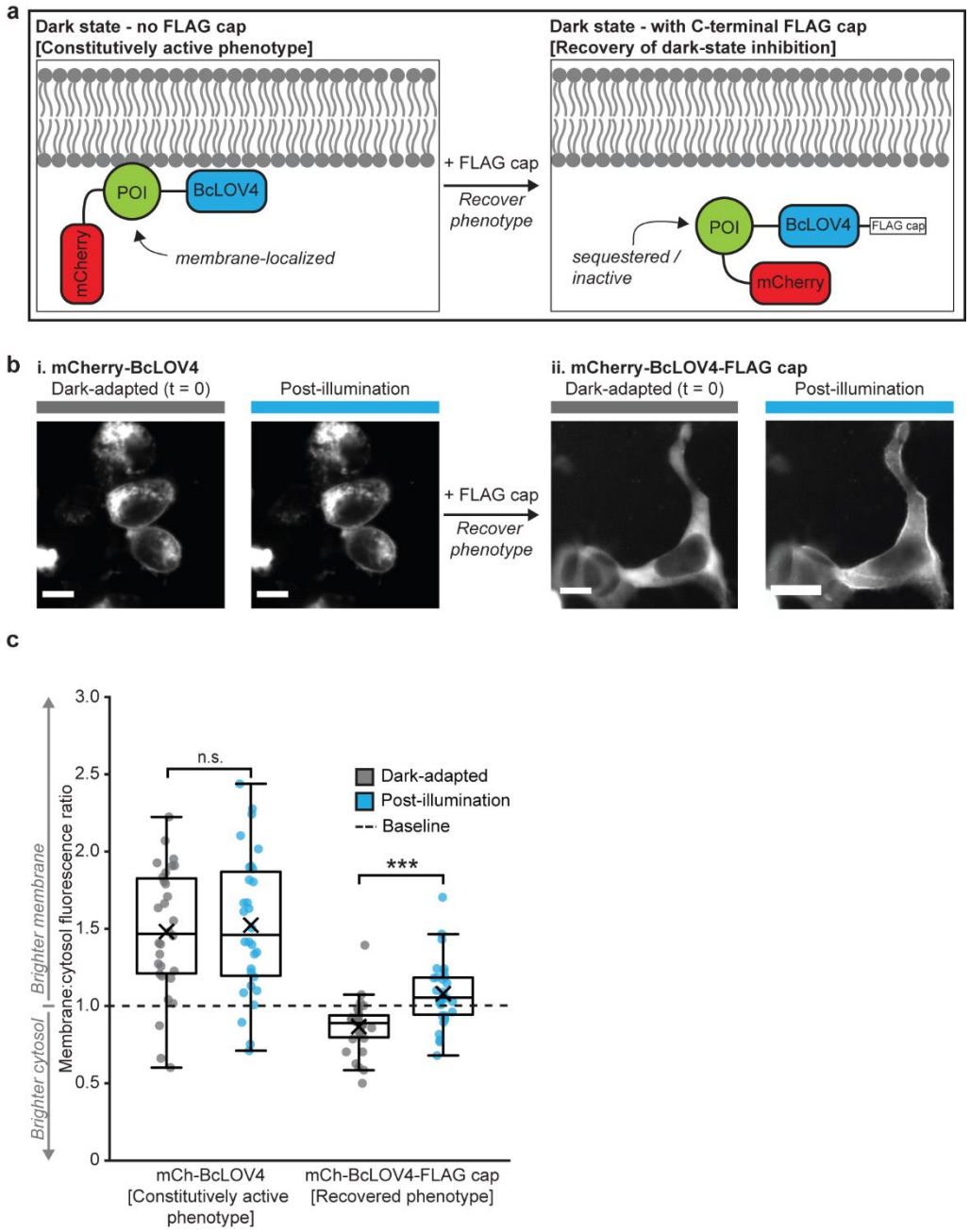

Figure 6.5 FLAG capping rescues constitutively active phenotype

a. Schematic of C-terminal FLAG cap-mediated rescue of dark-state cytosolic expression for previously unviable domain arrangements. **b**. Dark-adapted and post-illumination expression patterns for uncapped vs. 3xFLAG-capped mCherry-BcLOV4. Scale = 10 µm. **c**. Quantification of 3xFLAG rescue of dark-state cytosolic expression via membrane:cytosol protein ratio, measured by mCherry fluorescence. N = 30 cells per condition. Mann-Whitney U test, uncorrected for multiple comparisons. (***) $p < 0.001$, (n.s.) not significant.

6.2.6 Rescue of membrane recruitment and effector function in previously disfavored tool constructs

Following the finding that a 3xFLAG cap on the C-terminus of BcLOV4 was sufficient to rescue the abnormal expression caused by solvent exposure of its C-terminus, we next sought to use the strategy of FLAG-capping to make viable tools from previously disfavored domain arrangements with mCherry and the protein of interest (POI) at the N-terminus of BcLOV4. We screened the expression of POI-mCherry-BcLOV4-3xFLAG and mCherry-POI-BcLOV4-3xFLAG for effectors Rac1, Tiam1, RhoA, ARHGEF11 (RhoGEF), and Intersectin1 (Cdc42-GEF). It should be noted that engineering opto-Cdc42 (see Chapter 4) was only possible when FLAG-capping was included in our screening workflow; the only construct producing robust filopodia in response to blue light without dark-state leakiness was mCherry-Cdc42-BcLOV4-3xFLAG.

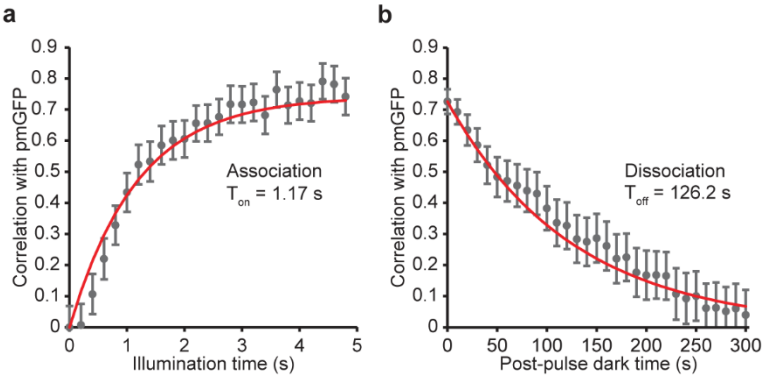

Figure 6.6 Membrane translocation kinetics of mCherry-BcLOV4-3xFLAG in HEK293T cells

Time constants were determined by correlation analysis between a membrane marker (pmGFP) and line section profiles of the mCherry tag. N = 30 cells. **a**. Membrane association: τ_{on} = 1.17 s, 95% CI, 1.05-1.29 s. **b**. Membrane dissociation: τ_{off} = 126.2 s, 95% CI, 118.8-133.7 s.

For each of the effectors we screened, at least one FLAG-tagged construct was capable of initiating pathway signaling following membrane recruitment of the effector.

Figure 6.7 shows the best-performing construct for each effector. mCherry-Rac1-BcLOV4-3xFLAG and Tiam1-mCherry-BcLOV4-3xFLAG both produced lamellipod-like protrusions following DMD stimulation. RhoA-mCherry-BcLOV4-3xFLAG and RhoGEF-mCherry-BcLOV4-3xFLAG induced cell contraction in the stimulated region. Activation of mCherry-Intersectin1-BcLOV4-3xFLAG produced spiky filopodia in response to blue light stimulation. We also observed rescue of dark-state cytosolic expression for disfavored arrangements with Ras pathway effectors iSH and the catalytic domain of SOS (**Figure 6.8**). These results further demonstrate that the addition of FLAG caps to disfavored domain arrangements in our tool screening workflow will expand the possible viable tool constructs and enable the engineering of membrane recruitment tools with structurally diverse effector domains.

6.2.7 Development of a cloning and screening workflow for BcLOV4 tool development

To aid others in creating BcLOV4 fusion tools for optogenetic membrane recruitment, we created a plasmid set and workflow for screening domain arrangements of BcLOV4, mCherry and proteins of interest (**Figure 6.9**). The plasmid set consists of two constructs: BcLOV4-mCherry and mCherry-BcLOV4-3xFLAG. Each plasmid can be digested with three restriction enzymes with different cut sites, resulting in six total backbones for Gibson assembly with the protein of interest. For example, plasmid A contains an EcoRI restriction site before the $(GGGS)_2$ linker separating BcLOV4 from mCherry. Restriction digest followed by phosphatase treatment results in a backbone that can be assembled with $(GGGS)_2$-POI to yield domain arrangement 1, BcLOV4-POI-mCherry. Following cloning, plasmids can be transfected into a cell line of interest and mCherry fluorescence can be visualized to determine which constructs express in the cytosol and translocate to the membrane in response to blue light stimulation. Further

testing of successful constructs can then be performed to measure signaling activation following membrane recruitment. The plasmid set is available from Addgene (plasmids 174511 and 174512).

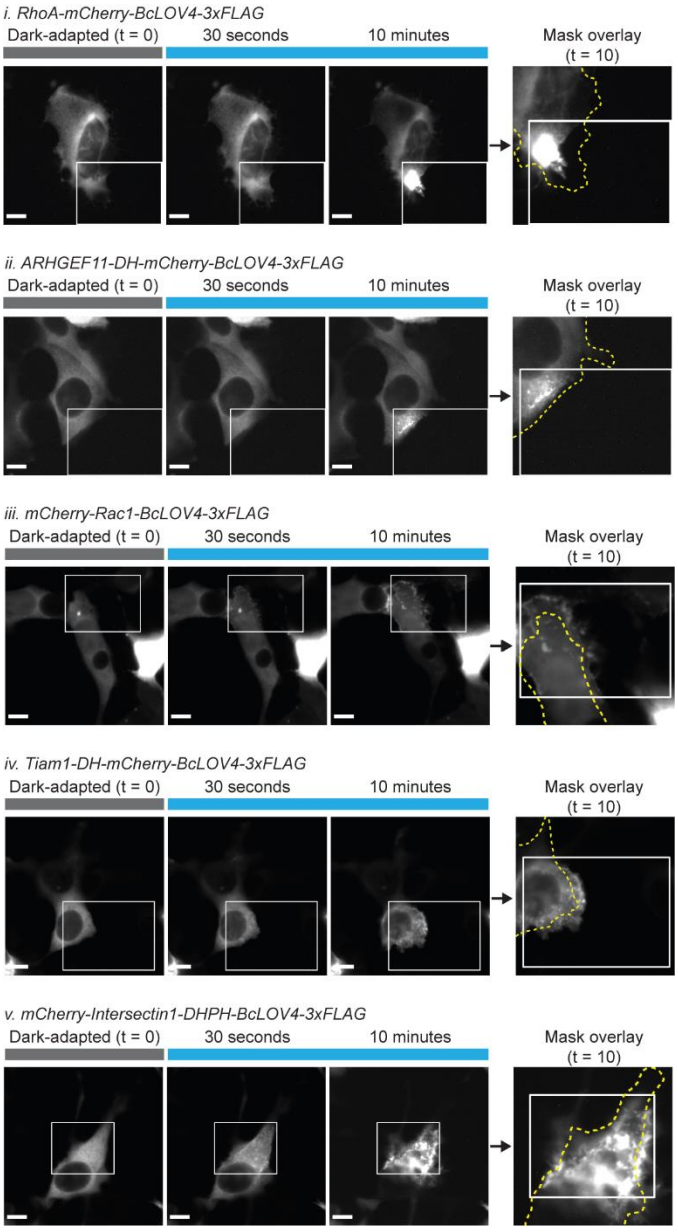

Figure 6.7 Recovered fusions created with previously reported effectors and BcLOV4 C-terminal 3xFLAG tags

mCherry tag was imaged with pulsatile patterned stimulation (1.6% duty ratio). White box = illumination field. Dotted yellow line = cell boundary mask in the dark-adapted state. Scale = 10 µm.

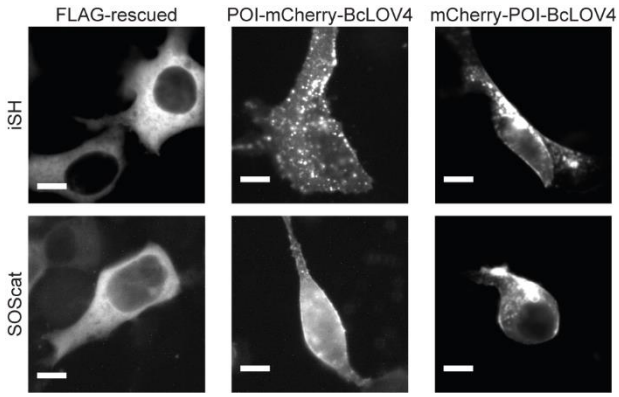

Figure 6.8 Rescue of disfavored Ras pathway effector domain arrangements

Rescued constructs = mCherry-iSH-BcLOV4-3xFLAG and SOScat-mCherry-BcLOV4-3xFLAG. Scale = 10 µm.

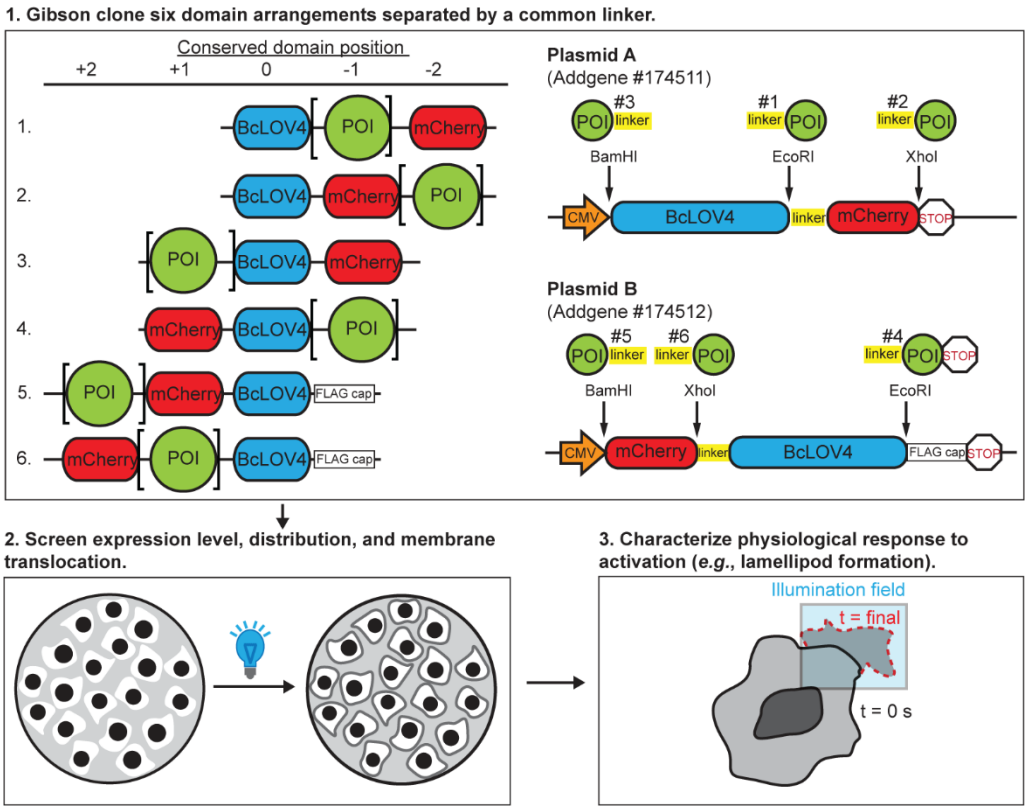

Figure 6.9 Engineering workflow for BcLOV4 optogenetic tools

6.3 Conclusions and future directions

In summary, we created a plasmid set and screening workflow to enable other labs to engineer BcLOV4 optogenetic tools with relative simplicity. As observed in developing GTPase and GEF tools, there is no one-size-fits-all approach to identifying the optimal protein domain arrangement for BcLOV4, the visualization tag, and the protein of interest: RhoA. Cdc42 and Rac1 tools each used different domain arrangements, and GEFs and GTPases from the same pathways did not share orderings. Thus, the ability to screen all possible domain orderings with two plasmids is particularly important to accommodate diverse effector structures. The plasma membrane is a signaling hub for many cellular activities; BcLOV4 has great potential for

single-component optogenetic targeting pathways beyond small GTPases, including Ras-Erk and lipid synthesis pathways.

In developing this tool design workflow, we also uncovered an interesting feature of the BcLOV4 C-terminus: the requirement for a peptide cap to shield its terminal residues from exposure and prevent pre-illumination lipid binding. In the future, an interesting avenue would be to explore whether this C-terminal cap is necessary in other RGS-LOV proteins or whether BcLOV4 is an outlier. The exact role of the C- and N-termini in dark-state inhibition of lipid binding and the potential generality of the uncapped C-terminal phenotype can be further explored when the crystal structure of BcLOV4 is solved at higher resolution. Despite remaining structure-function questions, we have created a tool engineering pipeline and demonstrated the utility of BcLOV4 as a single-component optogenetic tool platform for activation of membrane signaling pathways. Ongoing cryo-EM and mass spectrometry studies may enhance our understanding of BcLOV4 structure-function.

6.4 Materials and methods

6.4.1 Genetic constructs

Fluorescent protein-tagged BcLOV4 constructs, 3xFLAG-tagged constructs, and toolbox plasmids were assembled into the pcDNA3.1 mammalian vector under a CMV promoter by Gibson cloning with HiFi DNA Assembly Master Mix (New England Biolabs, E2621). BcLOV4 and mCherry were amplified from their previously reported mammalian codon-optimized fusion (Addgene plasmid 114595) (69). The DNA sequences of BFP, mNeonGreen, and mKo-kappa were human codon-optimized using the Integrated DNA Technologies (IDT) Codon Optimization Tool and ordered as gBlocks®. GTPase and GEF effectors were amplified from previous domain arrangements discussed in

Chapters 3 and 4. Mutagenesis of BcLOV4's C-terminus was generated by QuikChange site-directed mutagenesis. Briefly, overlapping primers encoding the mutation with melting temperatures ≥ 78°C were designed using Agilent's online primer design tool (https://www.agilent.com/store/primerDesignProgram.jsp). The mutation was introduced over 18 PCR cycles with 8-minute elongation time using the Phusion® high-fidelity DNA polymerase master mix (New England Biolabs, M0531). The template plasmid was digested with DpnI for one hour at 37°C before transformation. All genetic constructs were transformed into competent *E. coli* (New England Biolabs, C2984H). All sequences were verified by Sanger sequencing.

6.4.2 Cell culture and transient transfection

HEK293T (ATCC, CRL-3216) cells were cultured in D10 media composed of Dulbecco's Modified Eagle Medium with Glutamax (Invitrogen, 10566016), supplemented with 10% heat-inactivated fetal bovine serum (FBS) and penicillin-streptomycin at 100 U/mL. Cells were maintained in a 5% CO_2 water-jacketed incubator (Thermo/Forma 3110) at 37°C. Cells were seeded onto poly-D-lysine-treated glass bottom dishes (MatTek, P35GC-1.5-14-C) or into 24-well glass bottom plates (Cellvis, P24-1.5H-N), treated in-house with type I collagen, at 15-20% confluency. Cells were transfected at ~30-40% confluency 24 hours later using the TransIT-293 transfection reagent (Mirus Bio, MIR2700) according to manufacturer instructions and Opti-MEM™ reduced serum media (Thermo Fisher, 3195062). Cells were imaged 24-48 h post-transfection.

6.4.3 Fluorescence microscopy and hardware

Fluorescence microscopy was performed on an automated Leica DMI6000B fluorescence microscope under Leica MetaMorph control, with a sCMOS camera (pco.edge), an LED illuminator (Lumencor Spectra-X), and a 63× oil immersion objective. Excitation illumination was filtered at the LED source (mCherry imaging λ = 575/25 nm; GFP imaging or widefield BcLOV4 stimulation λ = 470/24 nm; miRFP imaging λ = 632/22 nm). Fluorescent proteins were imaged with Chroma filters: mCherry (T585lpxr dichroic, ET630/75 nm emission filter, 0.2–0.5 s exposure), GFP/Alexa Fluor 488 (T495lpxr dichroic, ET 525/50 nm emission filter, 0.2 s exposure). Cells were imaged at room temperature in CO_2-independent media (phenol-free HBSS supplemented with 1% l-glutamine, 1% penicillin-streptomycin, 2% essential amino acids, 1% nonessential amino acids, 2.5% HEPES pH 7.0, and 10% serum). The spatially patterned illuminator was custom-constructed from a digital light processor (DLP, Digital Light Innovations CEL5500), as described in section 3.4.3.

6.4.4 Expression level and membrane:cytosol ratio measurement

HEK293T cells were co-transfected with a GFP membrane marker and mCherry-tagged tool construct in a 1:10 ratio. Cells were imaged at 63× magnification for 3-5 fields of view per construct. mCherry fluorescence was imaged with a 0.5 s exposure time, followed by GFP fluorescence imaging (0.2 s exposure). mCherry fluorescence was the imaged again after 5 seconds of blue light stimulation.

To assess expression level, cells were manually segmented using the pmGFP micrograph to identify cell boundaries, and background-subtracted fluorescence was recorded for N = 25-31 cells per condition. Cell fluorescence was normalized to BcLOV4-mCherry mean fluorescence. To measure membrane:cytosol fluorescence ratio, the

plasma membrane and cytosol were manually segmented using pmGFP localization as a guide. The ratio of mean membrane to cytosol fluorescence was calculated for dark-adapted and post-illumination states for N = 30 cells per condition. Statistical significance was assessed by the two-sided non-parametric Mann-Whitney U test, uncorrected for multiple comparisons.

6.4.5 Anti-His and anti-FLAG immunostaining

Cells were plated in pre-treated 35 mm glass bottom dishes and transfected as described in (5.4.2). 24 hours after transfection, cells were washed once with PBS. Dark-adapted condition plates were placed in an opaque container. Lit-state plates were placed under a strobing blue LED (Mightex, BLS-LCS-0455-03-22, λ = 455 nm, light intensity 15 mW/cm^2) strobing at a 1.6% stimulation duty cycle. After five minutes, media was removed and cells were fixed with 4% paraformaldehyde in PBS at room temperature for 15 minutes, then washed twice with 0.1 M glycine in PBS (hereafter referred to as “PBS-glycine”) for 5 minutes per wash. Cells were blocked in 5% BSA / 1% normal goat serum / 0.4% saponin in PBS (hereafter referred to as “blocking buffer”) at room temperature for 30 minutes. For anti-His immunostaining, cells were incubated with His-Tag Mouse mAb (Cell Signaling Technology, 2366) diluted 1:400 in blocking buffer for 3 hours at room temperature. For anti-FLAG immunostaining, cells were incubated with DYKDDDK Tag Mouse mAb (Cell Signaling Technology, 8146) diluted 1:250 in blocking buffer. Following primary antibody incubation, plates were washed with PBS-glycine three times. Plates were incubated with Anti-Mouse IgG F(ab’)2 Alexa Fluor 488 (Cell Signaling Technology, 440) diluted 1:500 in blocking buffer for 90 minutes at room temperature. Cells were then washed three times in PBS-glycine and imaged plates in PBS.

6.4.6 Membrane localization kinetics

For membrane recruitment quantification, prenylated GFP was co-transfected as a membrane marker with the BcLOV4 fusions as previously described in (3.4.4). Briefly, an mCherry fluorescence image (500 ms exposure) was captured to assess protein expression level and subcellular distribution. Cells were then illuminated with a 5 s-long blue light pulse to stimulate BcLOV4, during which time mCherry fluorescence images were also captured every 200 ms to monitor subcellular localization changes. The GFP membrane marker was imaged immediately after blue light stimulation for correlation analysis. For membrane dissociation via thermal reversion of the photoactivated protein in the dark, mCherry was visualized every 5 seconds for 10-15 minutes in the absence of blue light stimulation. Membrane localization and dissociation were measured by line section analysis and correlation with prenylated GFP in ImageJ and MATLAB as previously described (69).

6.4.7 Microscopy assays

For DMD stimulation assays, mCherry fluorescence was imaged every 15 seconds for 10 minutes. During this time, cells were stimulated for one second per minute (1.6% duty cycle) patterned illumination (25 μm-wide square encompassing ~25% of cell area). The stimulation angle was defined as the angle defined by the polarization axis and the line segment between the cell centroid and the centroid of the stimulated cell area.

CHAPTER SEVEN: Conclusions and future directions

7.1 Conclusions

7.1.1 BcLOV4 as a novel photoreceptor and optogenetic platform

Optogenetic tool engineering to recruit proteins of interest to the membrane has long been an approach to perturb cell physiology and to study the plethora of signaling events at the plasma membrane with spatiotemporal precision. Most existing optogenetic tools for controlling membrane recruitment rely on heterodimerization pairs, which require careful stoichiometric tuning and the use of multiple optical channels for their implementation. Single-chain photoswitching systems can also be associated with high dark-state activity resulting from pathway activation occurring as a result of diffusive contact with the membrane. These issues demonstrated the importance of discovering and characterizing new signaling mechanisms from natural photoreceptors, which may enable the development of new, more broadly applicable optogenetic tool platforms.

Following the 2016 discovery of BcLOV4, a novel fungal photoreceptor which directly binds membrane lipids in its blue light-illuminated state across cell types, we sought to understand the biophysical basis of this light response. We established that the C-terminal amphipathic helix (AH1) is responsible for membrane binding; mutating the acidic amino acids in this helix resulted in a protein that did not bind lipid. Protein characterization showed that the BcLOV4 N-terminal disordered region is not required for protein folding or lipid binding as truncation of residues 1-98 did not change the protein photocycle or in-cell light response. The RGS domain, while apparently non-functional in GPCR signaling in mammalian cells, appears to play a role in dark-state inhibition, as removing this domain resulted in permanently lit-like protein. The C-

terminus following the LOV domain of BcLOV4 also appears to be crucial to chromophore incorporation and protein binding as soluble C-terminal truncations could not be produced. In characterizing in vitro and cellular behavior of CeRGS, we demonstrated that light-induced lipid binding may be general to all RGS-LOV proteins, which is bolstered by multiple sequence alignment data of RGS-LOVs showing conservation of the lipid-binding alpha helix. These findings shed light on this new class of photoreceptor, and we used this knowledge of BcLOV4 structure-function to develop single-component optogenetic tools in the remainder of this work.

7.1.2 Development of a Rho-family optogenetic toolbox

The Rho GTPase pathways are localized to the plasma membrane and underly processes like cell migration and mechanotransduction. The ability to perturb these cascades with single-component optogenetic tools will enable the study of these events with a minimal genetic payload and most other optical channels available for visualizing other cellular structures or proteins. In this work, we created GTPase and GEF tools for the RhoA, Rac1, and Cdc42 pathways. For all tools, we observed robust, spatially confined cytoskeletal rearrangements: RhoA and ARHGEF11 recruitment led to cell contraction, Rac1 and Tiam1 recruitment induced sheet-like lamellipodia formation, and Cdc42 and Intersectin1 recruitment formed spiky filopodial protrusions. Beyond these easily observed changes in cell shape, we also characterized tool activity using pharmacological inhibitors to confirm the mechanism underlying these rearrangements and by measuring change in cell area (RhoA, ARHGEF11, Rac1, Tiam1), change in cell dimensions (RhoA, ARHGEF11), actin polymerization (RhoA, ARHGEF11, Cdc42), and downstream signaling events (RhoA). These tools will benefit the Rho GTPase field in that they can be used to induce robust pathway activation and will allow for comparison

studies within (e.g., GTPase versus GEF) and between (e.g., Cdc42 versus Rac1) signaling pathways without the confounds associated with using optogenetic tools from different platforms.

7.1.3 Recruitment of wildtype GTPase is sufficient for pathway activation

Up to this point, most optogenetic tools for GTPase signaling activation rely on the recruitment of a Rho family GEF to the membrane to catalyze activation of endogenous GTPase. While this approach works, it is inherently limited by the concentration of GTPase at the membrane location to which the tool is recruited. We used the less common method of recruiting the GTPase itself to the membrane—while this approach is technically limited by endogenous GEF concentration to activate the overexpressed GTPase in the tool, the rapidity of GEF turnover suggested that it would result in more robust pathway activation than recruiting the GEF itself.

To our initial surprise, recruitment of the wildtype (i.e., not constitutively active) GTPase was sufficient to induce pronounced cytoskeletal changes, suggesting that mutations to inhibit GDI interaction or lock the GTPase in the active state are not necessary for pathway activation in optogenetic tool fusions. In fact, tool functions worsened when we made these mutations: for the Rac1 and RhoA GTPases, constitutively active mutations resulted in leakier tools with lower contrast ratios for dark versus illuminated cells. This finding suggests that wildtype GTPase tools have lower dark-state activity because pathway activation requires both membrane localization of the tool and interaction with a nearby GEF. In placing GTPase activation under these two layers of control, we achieved tighter control over unwanted dark-state activity without sacrificing activation speed once recruitment occurs. This method allowed us to

create powerful GTPase optogenetic tools and will help guide the future of optogenetic GTPase tool engineering.

7.1.4 Creation of optogenetic tools for signaling pathway termination

Much of the optogenetic tool development in the Rho GTPase field has focused on tools for activating signaling. While the ability to induce pathway activation is important, terminating proteins cannot be ignored for the roles they play in shaping cell signaling and behavior. For example, RhoA signaling termination has been implicated in persistent cell motility (157) and in controlling the timing of neuronal axon elongation (62). We demonstrated that BcLOV4-mediated recruitment of a RhoA GAP domain in cells with elevated basal RhoA signaling resulted in signaling termination measured by a RhoA biosensor. This tool furthers existing termination tool progress, including opto-GAP, which uses using another RhoA GAP in *Drosophila* embryogenesis (96); and opto-RGS, which can be used to terminate GPCR signaling (86). As more non-FRET-based biosensors are developed to enable visualization of active GTPase in conjunction with changes in the cytoskeleton, further GAP tool engineering can occur to control the termination of Rac1 and Cdc42 signaling with spatiotemporal precision.

7.1.5 Elucidation of design principles governing BcLOV4 tool design

In creating BcLOV4-based optogenetic tools, we observed that (1) optimal protein domain arrangements varied from effector to effector, and (2) domain arrangements with BcLOV4 at the C-terminus of the protein were consistently disfavored, resulting in lit-like protein expression patterns. This phenomenon was recapitulated in BcLOV4 constructs in which N-terminal protein bulk was replaced with a small epitope visualization tag, suggesting that the exposed C-terminus of BcLOV4

mediates this dark-state membrane binding. By adding a C-terminal 3xFLAG peptide cap to BcLOV4, we were able to rescue normal dark-state cytosolic expression in these previously disfavored domain arrangements. This simple C-terminal engineering resulted in at least one functional FLAG-tagged construct for each Rho family GTPase or GEF, and, notably, the creation of a Cdc42 tool when all other domain arrangements were not suitable. These design principles, in conjunction with the plasmid set and cloning scheme we reported, will allow others to create their own membrane recruitment tools for signaling pathways of interest.

7.2 Future directions

7.2.1 Solving the BcLOV4 crystal structure

Biophysical and cellular characterization of BcLOV4 have revealed key information about RGS-LOV lipid binding. Notably, the amphipathic helix at the C-terminus of the protein is responsible for binding anionic phospholipids on the inner leaflet of the plasma membrane. While the N-terminus of the protein is expendable in terms of maintaining light-induced membrane binding, the RGS appears to function as a steric occlusion domain, preventing the amphipathic helix from interacting with the membrane when the protein is in its dark state. Efforts toward solving the BcLOV4 protein structure would provide additional information on how the amphipathic helix binds acidic membrane phospholipids and clarify the role of the RGS domain, which to date has not been shown to be functional in terminating GPCR signaling in cells. Structural characterization will also inform future tool engineering with BcLOV4, such as suggesting ways to tune the BcLOV4 lipid binding affinity and specificity for customizable recruitment profiles. It will also provide biophysical data to inform the existing finite element model of BcLOV4 membrane association.

7.2.2 Development of new tools on the BcLOV4 platform

As demonstrated by the wide variety of effectors with which optogenetic membrane recruitment tools have been reported, the plasma membrane contains many biologically interesting and clinically relevant signaling pathways. The workflow we developed to engineer and test BcLOV4 optogenetic tools can be applied to signaling pathways beyond Rho family GTPases, as demonstrated by our collaboration with others to engineer iSH and SOS tools (15). Also of great interest is the creation of additional GAP or dominant negative tools for the Cdc42 and Rac1 signaling pathways. Currently, a challenge of pursuing this research avenue is the lack of non-FRET-based biosensors for these signaling pathways; because signaling termination can be harder to visualize than activation, a biosensor is necessary to quantify changes in GTP-bound GTPase levels following tool activation. For the Cdc42 pathway, we will use Cdc42GAP, a 25 kDa protein previously shown to be localized to the leading edge of filopodia-forming cells (222). Rac1 GAP β2-Chimaerin (30 kDa) has similarly been found at the edge of Rac1-mediated lamellipodia formation (47). Like other chimaerin family proteins, β2-Chimaerin is regulated by membrane-bound receptor tyrosine kinases, particularly the epidermal growth factor receptor (EGFR) (82), further supporting the possibility that its recruitment to the membrane will result in Rac1 GTPase inactivation. The expansion of the BcLOV4 optogenetic pathway will enable others to use blue light to control membrane signaling with a single protein tool.

7.2.3 Using BcLOV4 tools to study signaling pathway integration

An advantage of having tools for the Rho GTPase pathways on the same optogenetic platform is the ability to drastically reduce presence of experimental confounds associated with pooling data from optogenetic tools on different platforms. For example, if a Cry2-GTPase and Phy/PIF-GEF tool are used in an experiment to compare the timescales of GTPase versus GEF activity, a number of differences between the platforms must be accounted for, including normalizing stimulation intensity across two colors of light, determining heterodimer stoichiometric titrations, accounting for the exogenous cofactor requirement of the Phy/PIF system, and comparing expression levels of tools which may use different fluorescent proteins for visualization.

When the BcLOV4 platform is used, only a single plasmid must be transfected, making determining expression conditions easier. Since all tools are activated with the same light wavelength, stimulation paradigms and visualization fluorescent proteins can be shared across conditions. The BcLOV4 Rho GTPase toolbox can thus be used to study questions of signaling integration and inter-pathway comparison. Examples include studying Rho GTPase crosstalk, as the GTPases are known to regulate each other (150, 186), as well as comparing GTPase and GEF recruitment to infer the spatial distribution of GEFs and GAPs in the cell. The BcLOV4 toolbox will make more straightforward the nodal dissection of cell signaling networks.

7.2.4 Using RhoA tools to explore feedback loops in mechanotransduction

Beyond its roles in cell polarity and contraction, RhoA has also been recently identified as a key player in a mechanotransductive feedback loop. As discussed in Chapter 3, RhoA activation leads to an increase in cytoskeletal tension and the maturation of focal adhesions through ROCK and myosin. This increase in tension

drives the nuclear translocation of transcriptional co-activators YAP and TAZ, which upregulate the transcription of RhoA-inactivating GAPs including ARHGAP29 (157). Thus, RhoA activation also includes a mechanism by which over-maturation of the cytoskeleton can be prevented by increasing the presence of RhoA-specific inactivators in the cell. This feedback loop represents an interesting link between the cell's cytoskeletal state and transcriptional activity and is required for cell motility and wound healing.

The optogenetic tools engineered in this thesis will enable the nodal dissection of this feedback loop without experimental confounds due to multiple activation/repression methods using different optogenetic platforms. Having optogenetic tools to control both endogenous RhoA activation (via opto-RhoGEF) and RhoA signaling activation by overexpression of the wildtype GTPase (via opto-RhoA) will allow us to study the effects of local GTPase and GEF concentrations on observed pathway activation. In addition, the creation of a RhoA-terminating optogenetic tools in opto-ARHGAP29 and opto-RhoA-DN enable the comparison of induced vs. endogenous RhoA signaling termination on cell migration.

Since all tools are BcLOV4 protein fusions, assays can be streamlined, using the same stimulatory blue light duty cycle to induce tool activity and similar imaging paradigms to observe tool localization. The advantage of single-component BcLOV4 tools is again apparent: in experiments designed to dissect the RhoA-YAP feedback loop, the ability to conserve optical bandwidth required for tool imaging and maximize the number of optical channels available to visualize RhoA-GTP, YAP, myosin, vinculin, and other pathway components is a significant advantage. The RhoA tools presented in this thesis will expand our ability to characterize this negative feedback loop and, more

generally, to study crucial biological processes like cell migration and wound healing with spatiotemporal precision.

APPENDIX 1: Synthetic cell-like membrane interfaces for probing dynamic protein-lipid interactions

This chapter adapts work from the following publication:

Glantz, S. T.*; Berlew, E. E.*; Chow, B. Y., Synthetic cell-like membrane interfaces for probing dynamic protein-lipid interactions. Methods in enzymology 2019, 622, 249-270.

(*) denotes equal contributions.

A1.1 Introduction

Many key cellular signaling processes in environmental sensing, development, and migration are mediated by dynamic protein-lipid interactions with the plasma membrane, including the recruitment to and undocking from the inner leaflet. The ability to rapidly probe the lipid interactions of these membrane-associated proteins in a highly controlled manner on commoditized instrumentation would facilitate structure-function analyses, inform their signaling mechanism and dynamics, and provide an assay platform for engineering lipid-interacting protein tools.

Protein-lipid overlay (PLO) assays are a common high throughput methodology for screening protein-lipid interactions (53, 114, 184), but these assays test for headgroup interactions without recapitulating a membrane interface and are prone to false positives (171, 271). Another protein-lipid binding assay that can be performed without complex instrumentation is the liposome pulldown (138, 195, 234). Yet, this assay requires the isolation of lipid-bound protein by ultra-centrifugation or solid-support immobilization of protein (148, 276), making it challenging to study proteins that are unstable in aqueous solution and liable to precipitate (as many lipid-interacting proteins

are). Additionally, the assay is low-throughput because results must be resolved in gels. Gold-standard techniques for determining protein affinity are often inaccessible or poorly suited for widescale screening due to cost, such as surface plasmon resonance (SPR) (20, 231), or due to large milliliter-scale protein volumes, such as isothermal titration calorimetry (ITC) (218).

Fluorescence imaging of water-in-oil (w/o) emulsions with lipid-stabilized droplet interfaces offers a complementary platform for screening protein-lipid interactions, determining relative affinities, and monitoring interaction dynamics (69). In this system, the droplet interior emulates the cytosol, while the lipid monolayer-stabilized droplet interface emulates the plasma membrane inner leaflet (**Figure A1.1**). Lipid interfaces are simple to produce as single-emulsions by brief agitation of lipid-containing decane oil (the continuous phase of the emulsion) and a much lower volume of protein-containing aqueous solution (the dispersed phase of the emulsion). Single-emulsions (typically, without lipid stabilization) have long been used prevalently in clonal library preparation in next-generation sequencing (92, 144) and emulsion & digital droplet PCR (188, 221). However, they have also been adapted as synthetic cell-like structures for cell-free in vitro compartmentalization for directed) and for size tuning in exploring the role of cytoplasmic volume in development (74, 75).

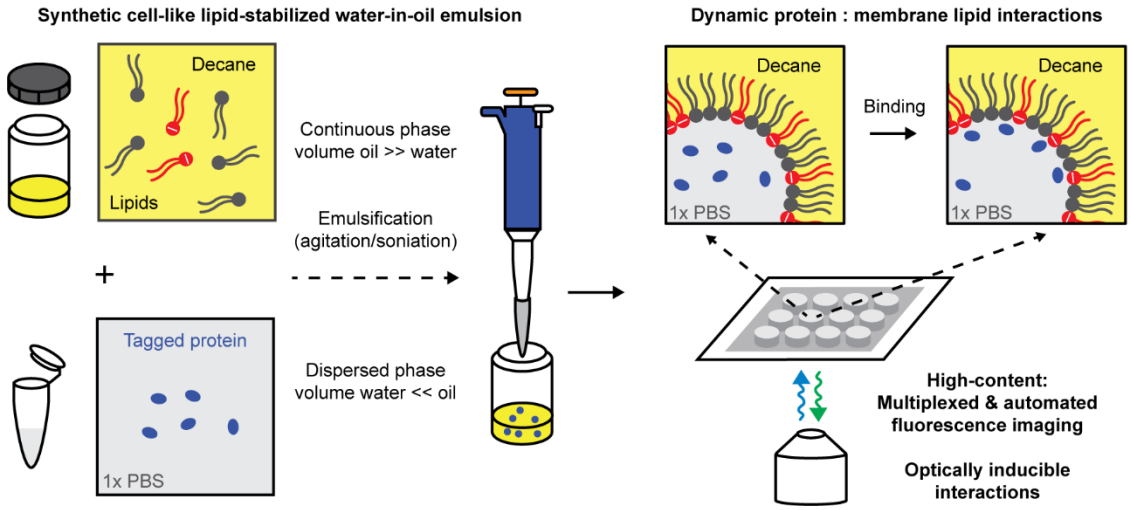

Figure A1.1 Probing dynamic interactions between proteins and membranes in synthetic cell-like lipid-stabilized water-in-oil (w/o) emulsions

Preparation of (10^{-5} m-sized) synthetic cell-like droplets by emulsification, where the dispersed aqueous phase emulates the cell cytosol, and the lipid-stabilized water/oil interface emulates the plasma membrane inner leaflet. Protein : membrane lipid interactions can be screened by automated fluorescence imaging in synthetic cell-like droplets in vitro. Quantitative analysis of spatiotemporal interaction dynamics is facilitated by optical induction with purified recombinant optogenetic tools or photochemical uncaging.

Several aspects of lipid-stabilized single-emulsions make them simple to implement for protein-lipid screening applications and in-depth analyses alike. The composition of the interface is easily tuned by adjusting the lipid mixture in the oil phase prior to emulsification, which only requires pipetting or bath sonication to recapitulate the membrane-like structure. Only a small amount of protein is required per experiment (~1 microliter per assay), which is helpful considering that lipid-interacting proteins are often challenging to solubilize. Once formed, the relative lipid-binding of fluorescently labeled proteins is imaged using an inverted epi-fluorescence microscope, one of the most common instruments found in any biomedical laboratory.

The microscopy-based analysis is amenable to automation and customization in medium-throughput assays in multi-well plate format, and temporally precise induction

using light-responsive proteins (69) or photocaged ligands (30). Recently, we used this platform to establish the relative lipid-binding selectivity and signaling structure-function of BcLOV4, a natural photosensory protein that binds anionic membrane phospholipids through a directly light-regulated electrostatic interaction (69); when expressed in cells, this protein is also useful as a single-component system for optogenetic membrane recruitment of fused proteins. In this report, we show further examples of spatiotemporally resolved and quantitative analyses that can performed using the w/o emulsion platform, such as determining membrane association and undocking/ dissociation kinetics of BcLOV4 and estimating its diffusional sampling distance.

Here, we provide protocols for droplet formation and automated fluorescence imaging and analysis in MATLAB (including code). We also report the production of BcLOV4 protein, which is particularly suitable as a control because it binds a wide range of anionic lipids when optically induced with modest levels of blue light (69). Ultimately, the synthetic cell-like membrane system is useful for (i) screening natural or engineered protein variants to gain structural design insights into lipid-binding function, (ii) testing the specificity of a lipid-binding protein for various lipid compositions, (iii) identifying membrane interactions without the confounding presence of other proteins in cells, and (iv) studying spatiotemporal dynamics of protein-membrane interactions through time-resolved imaging aided by conditional activation by optochemical and optogenetic tools.

Time-resolved and high-content analysis of single cells is one of the most important uses of fluorescence microscopy. As described here, protein-membrane dynamics in synthetic cell-like structures can mirror and/or inform cellular protein-lipid interactions. For example, the post-illumination membrane association kinetics of our BcLOV4 control protein, and its membrane dissociation/undocking kinetics in the dark,

are similar in this in vitro system to the timescales observed in eukaryotic cells (**Figure A1.2**).

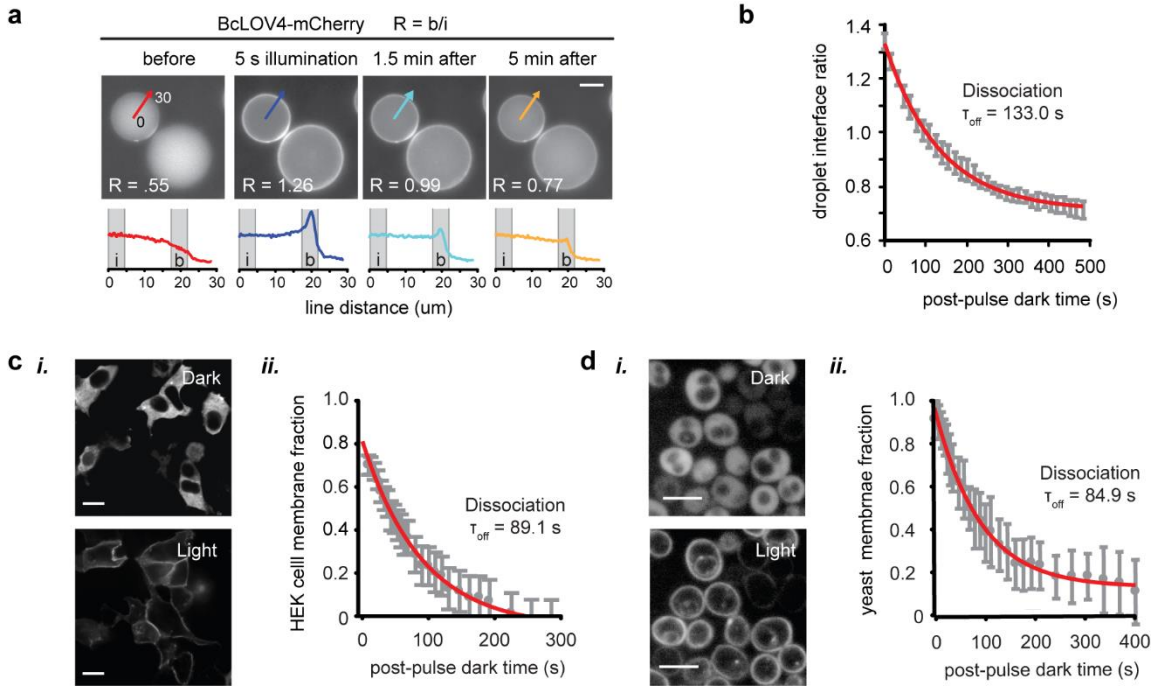

Figure A1.2 Dynamic and photoinducible protein interactions with membrane phospholipids in synthetic cell-like interfaces and eukaryotic cells

The positive control, BcLOV4, is recruited to membrane interfaces through a directly light-regulated electrostatic interaction with anionic phospholipids. Dissociation of photoactivated BcLOV4-mCherry from phospholipid interfaces in the dark is on similar biologically relevant timescales in vitro and in cellulo. **a**. Exemplar fluorescence micrographs of BcLOV4 in droplets show it is in the aqueous phase in the dark and is strongly recruited to the phospholipid-stabilized water/oil interface under blue light, only to revert to the water phase upon termination of illumination. Radial line profiles for time-lapse images taken before, during, and long after illumination may be used to quantitatively assess the ratio (R) of fluorescence signal at the boundary "b" to the interior "i". Scale bar = 20 μm. Blue light pulses: λ = 440/20 nm, 5 s, 15 mW/cm^2. mCherry imaging (λ_{ex} = 550/15 nm, λ_{ex} = 630/75 nm). **b**. Calculating the "R" ratio for droplets over time post-illumination reveals an exponentially decaying fluorescence intensity at the water/oil boundary and measurable dissociation kinetics, τ_{off} = 133s. **c**. HEK cells. [i] Blue light-induced membrane recruitment (scale = 10 μm). [ii] Dissociation in the dark. **d**. S. cerevisiae yeast. [i] Blue light-induced membrane recruitment (scale = 5 μm). [ii] Dissociation in the dark. All panels: 5 sec. blue light pre-illumination at irradiance = 15 mW/cm^2.

More spatiotemporally complex biophysical insights can be inferred in this cell free-system, such as the diffusional sampling distance (137) of membrane-interacting proteins (**Figure A1.3**). In the absence of an anionic membrane target or electrostatic

stabilization, activated BcLOV4 in bulk solution in vitro will form large colloidal aggregates (> 1 µm in size). In large droplets, the two simultaneous processes, of high-affinity membrane binding and the less preferred self-aggregation, result in a dark halo between the droplet interface and an interior core of observable colloids (**Figure A1.3a–c**). The size of this region of depleted protein is indicative of the sampling distance over which the protein can encounter its high-affinity membrane sink, whereas beyond this distance from an anionic membrane (or in the absence of one), the protein self-aggregates (**Figure A1.3d–g**). Photoactivated BcLOV4 has an observed sampling distance of ~12 µm regardless of droplet size, which is larger than the typical eukaryotic cell radius, thus informing why colloidal BcLOV4 photobodies are not formed in the cytosol of cells.

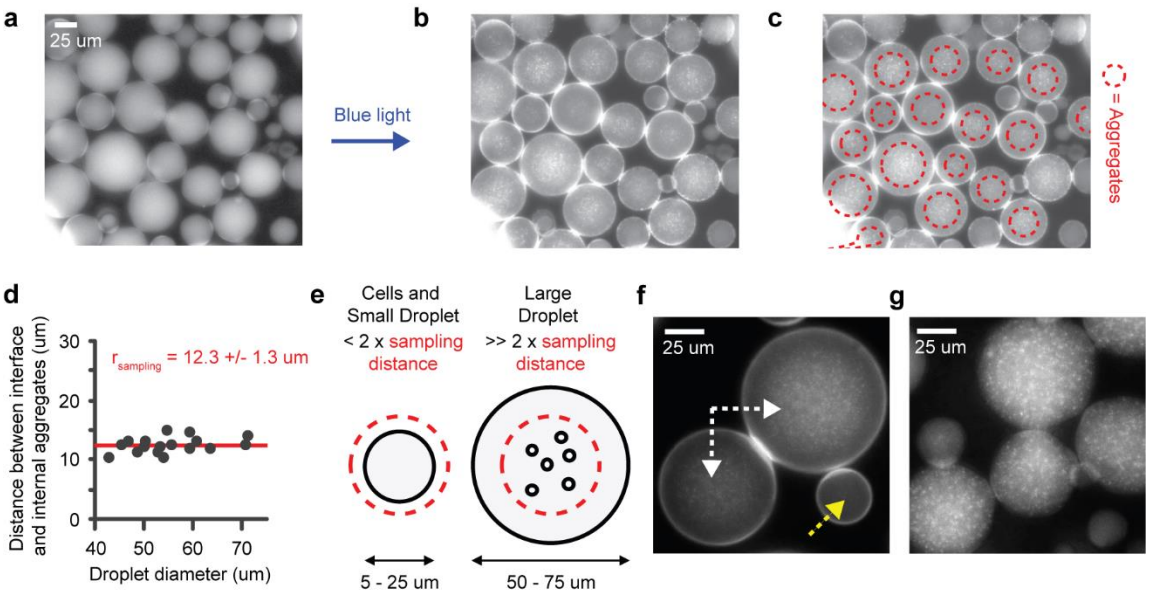

Figure A1.3 Droplet-based high-content analysis of protein diffusional sampling distance

a. Fluorescence micrograph showing BcLOV4-mCherry is uniformly distributed in the dark. **b**. Upon illumination, BcLOV4 binds anionic phospholipid-stabilized interfaces when the membrane target is within the diffusional sampling distance of the protein, but forms colloidal protein aggregates in an electrostatically driven process at large distances from the interface because it is effectively in bulk solution unable to encounter its target. **c**. In large droplets, the distance between the interface and the region of aggregates (highlighted in red) is consistent despite droplet size variation, with **d**. a mean distance of 12.3 ± 1.3 µm as the empirically measured effective diffusional sampling distance. **e**. Scheme of conditions under which BcLOV4 binds anionic membrane interfaces and/or self-aggregates. **f**. Fluorescence micrograph of BcLOV4-mCherry bound nearly exclusively at the membrane interface in a small droplet (yellow arrow) devoid of aggregates, but with clear formation of aggregates in two large droplets (white arrows) as schematized in panel **e**. **g**. BcLOV4-mCherry aggregates form uniformly throughout 100% phosphotidylcholine droplets that lack negatively charged phospholipids at the water/oil interface.

A1.2 Methods development

A1.2.1 Generation of phospholipid-stabilized emulsion droplets

The method reported here for creating synthetic cell-like emulsion droplets (**Figure A1.4**) is adapted from work by others in cell-free signaling (30, 74, 75). We first solubilize the lipids in chloroform to facilitate dispensing, and then the organic solvent is evaporated to generate a lipid film that is subsequently resuspended in decane oil and blended with other lipids to the desired relative composition. Separately, fluorescently labeled protein is prepared in aqueous buffer. Vigorous mixing of the aqueous and decane solutions results in a uniform emulsion, where the aqueous solution is the droplet interior or emulsion dispersed phase when its volume is much lower than the oil volume, which will be the droplet exterior or continuous phase.

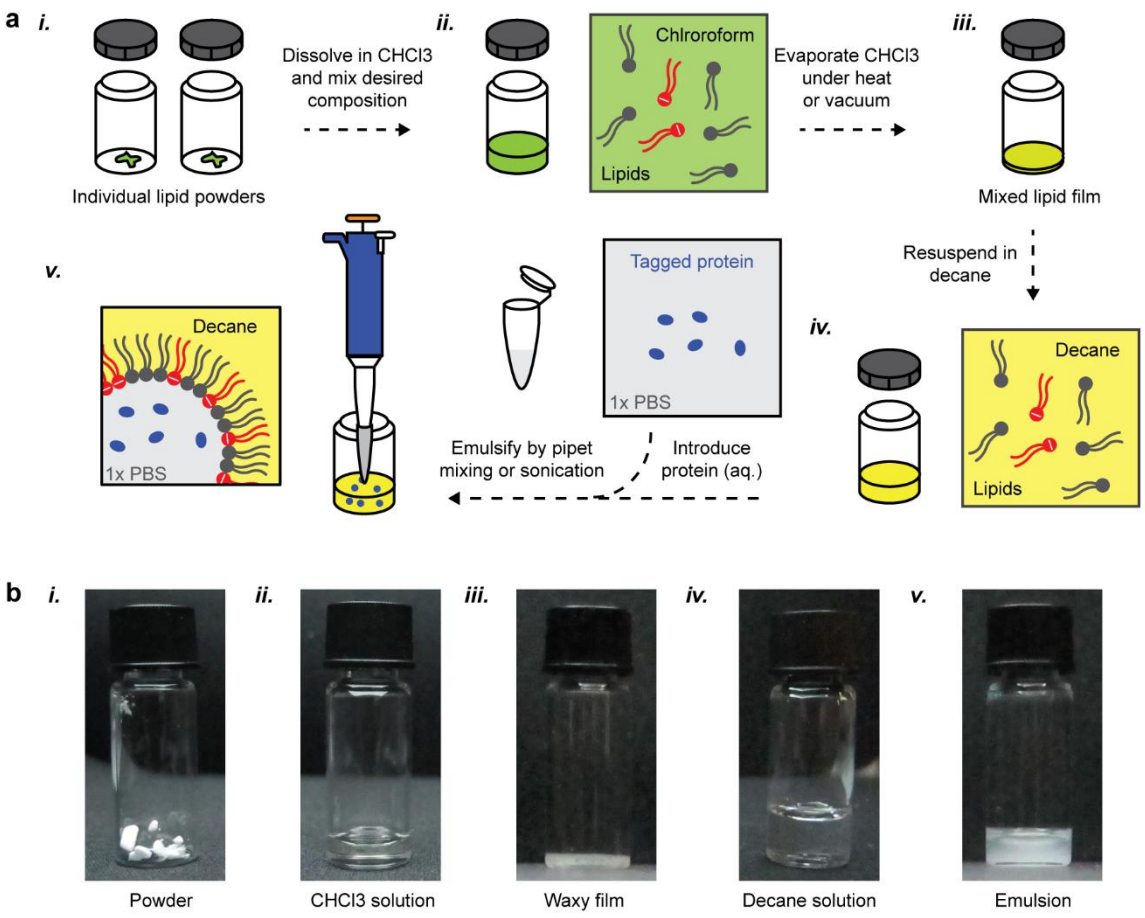

Figure A1.4 Step-by-step preparation of the water-in-oil emulsions

a. Schematic. **b**. Optical images of 2mL glass vials through the process, corresponding to the steps in panel a [i-v]. Note that multiple samples have been pooled for the turbid emulsion in image v. for increased volume for visual clarity.

This protocol describes the generation of phospholipid-stabilized water-in-oil emulsion droplets that have a lipid composition of 80% phosphatidylcholine (PC) and 20% phosphatidylserine (PS), but these lipids may be substituted for alternative lipids. Qualitative interaction screening is possible with phosphatidyl-inositol phosphates (PIPs), based on our results with BcLOV4 and GFP-tagged pleckstrin homology (PH) domains (of design created by others (229)) (**Figure A1.5**). However, we do not recommend quantitative analyses with long-chain PIPs because they distribute non-

uniformly into two populations of droplets, one of high PIP-concentration and one with no PIPs, presumably due to micellar formation in decane to shield the highly hydrophilic headgroups.

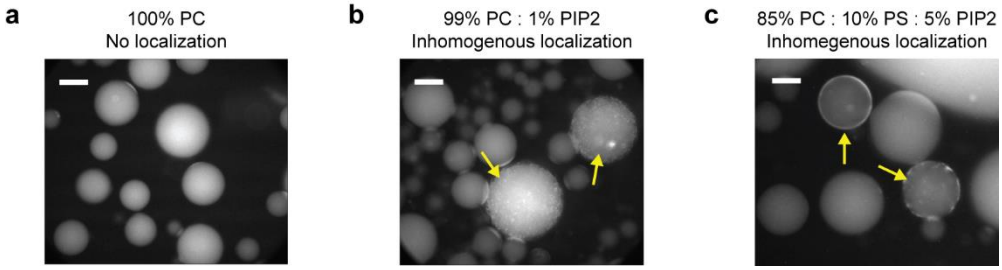

Figure A1. 5 Non-uniform distribution of phosphatidylinositol 4,5-bisphosphate (PIP2) in lipid-stabilized water-in-oil emulsions

Fluorescence micrographs of PIP2 distribution visualized with PLCδ1 pleckstrin homology domain fused to GFP (PLCδ1-GFP). **a**. PLCδ1-GFP in purely PC-stabilized droplets are only found in the droplet interior. **b-c**. Emulsions prepared with PIP2 result show two populations of droplets, one subset with no apparent PIP2, and another subset (yellow arrows) with patches of PIP2 at the interface. Scale bar: (**a-b**) 25 µm, (**c**) 50 µm.

A1.2.1.1 Materials

1. Hamilton 1000 series Gastight glass syringe with removeable needle: 1 mL and 100 µL sizes, with 22-gauge needles (Hamilton, p/n 81365)
2. 2 mL glass vials with Teflon-lined caps (Thomas Scientific 1234R80)
3. Glass Pasteur pipette
4. Phospholipids of choice: e.g. phosphatidylcholine (PC; Avanti Polar Lipids 840051C), phosphatidylserine (PS; Sigma Aldrich P7769), phosphatidyl glycerol (PG; Sigma Aldrich, P8318), and phosphatidic acid (PA; Sigma Aldrich P9511)
5. Chloroform
6. Decane
7. Nitrogen/Argon gas, connected to a low-pressure airbrush or nitrogen spray gun

8. Fluorescently labeled candidate lipid-binding protein of interest (5-10 μM) in 1X phosphate buffered saline (PBS)

9. Vacuum desiccator

10. Chemical fume hood

11. Water bath sonicator

12. Hotplate, preferably with sand or oil bath

A1.2.1.2 Protocol

All work with chloroform and lipids should be performed in glass vials with Teflon-lined caps, and volume transfer should be performed with Hamilton syringes unless otherwise specified. Chloroform should be handled in a working fume hood.

1. Using Hamilton syringes, prepare phospholipid stock solutions in chloroform:
    a. 32.6 mM PC (25 mg PC in 1 mL chloroform)
    b. b. 19 mM PS (15 mg PS in 1 mL chloroform)
2. Direct a stream of dry argon or nitrogen gas at the lipid solutions to evaporate the chloroform solvent. The chloroform should be gently agitated by the gas flow, and should not be splashing violently in the vial. When the organic solvent has been evaporated, a hazy lipid film should be visible at the bottom of the vial. Note that the glass vial will get very cold as the chloroform vaporizes. Throughout the vaporization process, rotating the vial in your gloved hand to warm it will increase the rate of evaporation and generate a more even lipid film on the bottom walls of the vial.
3. Completely dry the film of trace solvent by placing the vials in a vacuum desiccator chamber for 30 minutes at room temperature. Generally, “house vacuum” systems should be sufficient for this purpose. Alternative to steps 2 and

3 above, the vial can be heated in a fume hood in a sand or oil bath, first at 40-50°C to gently evaporate most the solvent, and then completely drying the film in vacuum or heating it above the chloroform boiling point (> 62 °C).

4. Using Hamilton syringes, re-suspend the lipid film in decane. The following concentrations are appropriately soluble for PC and PS.
    a. 32.6 mM PC (25 mg PC in 1 mL decane)
    b. 19 mM PS (15 mg PS in 1 mL decane)
5. Solubilize the lipids in decane by water bath sonication for 2 minutes at room temperature. Then, heat the decane lipid stocks at 50°C for 1-3 hours. The stocks should be uniformly clear with no visible lipid films or clumps. These lipid stocks may be stored at −20°C if not used immediately.
6. Blend phospholipids in decane to generate a desired lipid composition in the oil phase such that the total phospholipid concentration is 20 mM. Store the oil phase at −20°C until ready for use.
7. Prepare the aqueous phase solution of fluorescently labeled protein in 1X PBS (suggested protein concentration of 5-10 μM).

Steps 8-10 can be performed with adjustable non-glass pipettes.

8. Prepare water-in-oil emulsion droplets immediately prior to imaging them, by first transferring 30 μL of the lipid stock in decane to an Eppendorf tube If the lipid stock has been previously frozen, warm the stock to at least room temperature to ensure accurate volume transfer of the viscous solutions in a pipette. Lipid-in-decane solutions can be heated to 37-42°C if needed prior to handling.
9. Pipette 1.3 μL of the protein solution into the 30 μL decane mixture. The water phase should immediately sink to the bottom of the decane as a discrete aqueous phase.

10. Set a pipette to 20 µL volume. Place the pipette tip at the very bottom of the Eppendorf tube to access the aqueous phase and gently pipette up-and-down until the phase separation is noticeably disrupted. Then, pipette up-and-down vigorously (~30 seconds) until a uniformly cloudy suspension is visible (but, avoid foaming). This phospholipid-stabilized water-in-oil emulsion is ready for image analysis.

A1.2.2 Automated fluorescence imaging plates

Standard multi-well microplates for imaging are typically made from plastics like polystyrene that strongly bind phospholipids, leading to droplet instability and rapid accumulation at the microplate wall. However, plates made of acrylic and/or glass do not present such confounds. This section describes the fabrication of custom microwell plates that are defined by holes cut into an acrylic sheet, fused to cover glass as the plate bottom. (**Figure A1.6**)

The 25 µL assay volume in the following section has been optimized for the microwell plate geometry described here in this section, resulting in a monolayer of droplets that are spaced with minimal overlap. However, this combination of microwell plate dimensions and sample volume is not prescribed, and alternative combinations are possible.

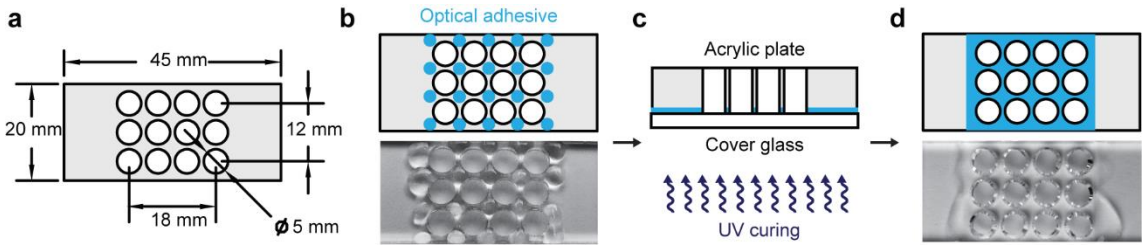

Figure A1.6 Design and assembly of the imaging plate

An acrylic plate is required to avoid lipid interactions with the plastics of standard multiwell plate. **a**. Dimensions of the acrylic cutout from the top down. **b**. Top-down schematic and image of uncured optical adhesive droplet placement (drawn in blue), prior to placement of the coverglass. **c**. Cross-sectional schematic of the imaging plate sandwich and optical adhesive curing process. **d**. Top-down schematic and image of the cured imaging plate. The adhesive seals the crossroads of the grid, but should minimally seep into the circular wells so that imaging is entirely through the coverglass.

A1.2.2.1 Materials

1. Laser cutter (or outsourced to machine shop)
2. ≥ 1/8”-thick clear acrylic
3. Microscope cover glass, 25 x 25 mm, No. 1
4. Norland Optical Adhesive (#81)
5. UV lamp/LED

A1.2.2.2 Protocol

1. Laser-cut plates from > 1/8” clear acrylic, with dimensions described in Figure A1.6a. To keep the piece clean, keep the adhesive paper-backing on when cutting, and cut the piece with the paper facing down on the stage.
2. Remove the paper backing from the acrylic plates.
3. Apply a drop of Norland Optical Adhesive (#81) at each crossroad of the array of holes (dots as shown in Figure A1.6b), using the applicator of the adhesive bottle. The adhesive droplets should be ~ 1 mm-diameter.
4. Cover the holes of the acrylic plate with the glass coverslip (one coverslip per acrylic plate) to form the bottom of the microwells. Ensure that a seal is formed around the circumference of each well, without excess adhesive oozing into the wells.

5. Cure the plates under a UV floodlight, with cover glass facing the light source. The duration will depend on the wavelength and irradiance of the light source; general guidelines and light source-specific protocols for curing are provided by the manufacturer. We use an IntelliRay 400 Shuttered UV Floodlight with Rayven curing chamber for 15 minutes (λ = 365 nm, irradiance = 175 mW/cm^2).
6. Store microwell plates in a clean and covered container to prevent dust accumulation.

A1.2.3 Imaging dynamic membrane recruitment

For imaging analysis, droplets should be stable and not dynamically merge or coalesce into larger droplets. Monolayers of droplets spaced with minimal overlap provide suitably stable imaging conditions for most applications, with enough droplets per field-of-view for error analysis using 20-40x objective lenses. At 20×, 25-75 droplets should be in the field of view, with a mean droplet diameter ~ 20-50 µm.

The protocols below describe assays on an inverted epi-fluorescence microscope, which is suitable for screening and dynamic analyses on the timescale of a few minutes. However, if a confocal microscope is available, confocal microscopy is beneficial when imaging droplets that vary widely in diameter and thus have dissimilar midplanes across a single field-of-view, and also when imaging over extended time periods to account for droplet movement.

A1.2.3.1 Materials

1. Inverted fluorescence microscope, equipped with automation software such as Micromanager or MetaMorph.
2. Additionally, for optogenetic induction with BcLOV4-mCherry, the microscope will require:
    a. Co-aligned and individually controlled LED light sources for BcLOV4 stimulation, (blue, λ ~ 450 nm) and mCherry imaging (yellow/amber, λ ~ 570 nm)
    b. Filter set that permits simultaneous imaging and optogenetic stimulation. For example: λ > 585 nm (long-pass) dichroic mirror, λ = 630 ± 37.5 nm (bandpass) emission filter, with excitation wavelength controlled at the light source
3. Optical power meter
4. Microscope size standard

A1.2.3.2 Protocol

General:

1. Immediately prior to imaging, transfer 25-30 µL of freshly generated emulsion droplets to a new microwell.
2. Focus on the glass bottom of the microwell plate at 20× magnification in brightfield mode, and raise the focal plane until droplets are clearly visible.
3. Use fine focus control to find the droplet top and bottom, and then, set the focus at the droplet midplane prior to fluorescence imaging.

Optical induction of the BcLOV4 control:

4. Determine excitation source settings for BcLOV4 photo-stimulation with 15 mW/cm^2 blue light through a 20× objective lens. Stimulation at this irradiance, which is the in vitro saturation value for BcLOV4, will limit cofactor photobleaching.
    a. Measure the beam power (in W or mW) with an optical power meter. The beam should be smaller than the detector area. If your power meter measures an irradiance (power / area), then multiply the reading by the detector area.
    b. Use a microscope size standard to determine the field-of-view of your objective lens (and approximate beam diameter), and then divide the measured power by this area.
5. Collect four mCherry fluorescence images, each separated by 15 seconds, to capture the “dark-state” images of the blue-light inducible system.
6. If only testing for droplet quality, skip this step and move on to step 7. To capture association dynamics, capture a 5 Hz-framerate movie with simultaneous excitation of BcLOV4 and mCherry.
7. Photo-stimulate BcLOV4 for 5 seconds with 15 mW/cm^2 blue light, and then image the mCherry tag. The protein should be membrane interface-localized. For determining undocking time constants by thermal reversion in the dark, image the droplets every 15 seconds for 5 minutes, without any further blue light stimulation. An exponential fit should yield a time constant of ~ 0.5-2 minutes.

A1.2.4 Image analysis and segmentation

While the distribution of the protein within each droplet can be manually assessed (for example, using tools in ImageJ), such analysis becomes highly rate-

limiting for the medium-to-high throughput assays possible. However, because the droplets are perfectly spherical such that they appear circular when imaged at their midplane, the individual droplets and their respective phase/compartment boundaries are easy to segment computationally. This section describes an automated analysis pipeline (**Figure A1.7**) that finds circles of a given diameter range, and subsequently segments these circles further to distinguish the phospholipid boundary layer from the aqueous interior, and to quantify protein in each compartment. Note that some proteins are beyond a diffusional sampling distance from the membrane-like interface in large droplets (>> 25 μm diameter), and thus, will not find the phospholipid monolayer accessible. Therefore, in this protocol, we have defined an interior “core” region for each droplet that eliminates any protein beyond the sampling distance from the interface. Here, we provide code in MATLAB (available in online supplementary material) for analyzing BcLOV4, but the general approach described in the workflow of **Figure A1.7** and pseudocode in the protocol below should apply to other image analysis programs and proteins of interest.

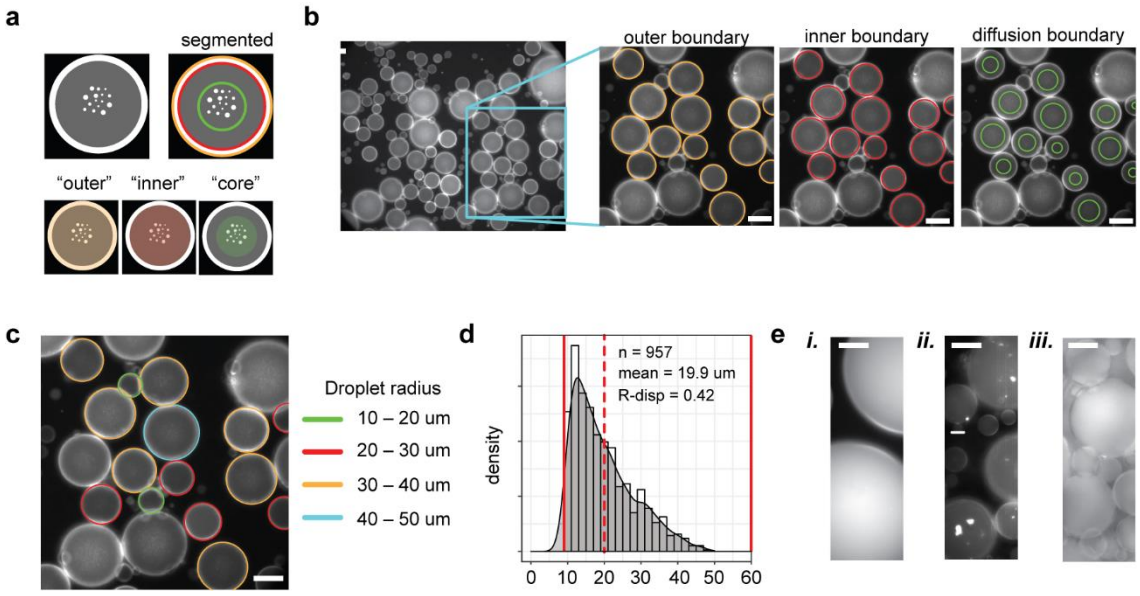

Figure A1.7 Segmentation of the emulsion dispersed phase and droplet interface

a. Schematic of a droplet with robust phospholipid-stabilized water/oil interface recruitment of activated BcLOV4 in the presence of negatively charged phospholipids, and internal aggregation beyond the diffusional sampling length from the droplet exterior. "Outer," "inner" and "core" masks are generated from boundary segmentation as described in the pseudocode. **b**. Example MATLAB analysis of a fluorescence micrograph of phospholipid bound BcLOV4 in 80% PC/ 20% PS droplets in the illuminated state. Automated segmentation identifies the outer boundary (orange), the inner boundary (red) and the interior diffusional sampling length (green). **c**. Droplets vary in radius where **d**. the mean droplet radius is 19.9 µm (red dotted line) and the droplet R-dispersion is 0.42 for 957 droplets identified by MATLAB automated analysis that was set to find droplets ranging from 10 - 60 µm (solid red lines). **e**. Common errors in droplet generation that compromise the segmentation and analysis include: [i] oversized droplets caused by poor emulsification due to insufficient vigor applied when by mixing by pipette. [ii] internal protein aggregates from poor protein stability under the given buffer conditions, [iii] difficult to resolve, overlapping droplets due to overloading of the microwell plate during imaging, [a-e] scale bar = 50 µm.

A1.2.4.1 Materials

1. Image analysis software (MATLAB)

A1.2.4.2 Protocol

1. Input file: Stack of fluorescence micrographs showing the localization of a fluorescently tagged protein in emulsion droplets, with each image corresponding to a different timepoint.

2. Save the input image file as a variable name (in MATLAB, use “imread” function).
3. Identify the outermost boundary for all droplets with a given diameter range (in MATLAB, use “imfindcircles” function) and record each object’s centroid coordinate and radius. This is the outer water/oil (w/o) interface boundary. When finding circles, it is optimal to use a relatively narrow diameter range to improve detection speed and accuracy. Software programs will measure the circle diameter in pixels. Use a micron-scale size reference to convert image pixels to an experiment-relevant size range in microns. For example, at 3.14 pixels/micron, a 20-50 μm droplet diameter range corresponds to a diameter range of 63-157 pixels.
4. For each pair of outermost boundary radius and centroid, generate a virtual inner water/oil (w/o) interface boundary description by subtracting 3 microns in length from the radius.
5. For each pair of outermost boundary radius and centroid, generate a virtual dispersed phase diffusion boundary by subtracting the calculated diffusion length from the radius (for BcLOV4, 12 μm).
6. Generate three masks for each droplet: a mask that extends from the centroid to the (i) outermost boundary (“outer”), (ii) to the inner water/oil interface boundary (“inner”), and (iii) to the diffusion boundary (“core”).
7. For each of the masked regions, calculate the area and sum the fluorescence intensity over all pixels.
8. Quantify the phospholipid boundary protein level as:

$$\text{Normalized boundary intensity} = \frac{\text{Intensity ("outer" - "inner")}}{\text{Area("outer" - "inner")}}$$

9. Quantify the dispersed phase protein level as:

$$\text{Normalized dispersed phase intensity} = \frac{\text{Intensity ("inner" - "core")}}{\text{Area("inner" - "core")}}$$

10. To visualize the segmentation by image processing, draw circles on the image using the identified coordinates. In MATLAB, use “imshow” to display the original image and “viscircles” to display the found objects.

APPENDIX 2: An iLID variant with light-inducible Golgi binding

A2.1 Introduction

In collaboration with the Jared Toettcher lab (Princeton University), we became interested in an iLID truncation which exhibits rapid, reversible, blue light-induced binding to the Golgi apparatus in mammalian cells (**Figure A2.1**). This truncation, hereafter referred to as iLID*, has six N- and C-terminal amino acids removed from the original reported iLID construct (81); the full protein sequence is listed in **Figure A2.2**. Binding to the Golgi apparatus was confirmed by the Toettcher lab by measuring protein co-localization with a fluorescent Golgi apparatus label. Golgi association occurs within 100 msec of blue light stimulation and disappears within 250 msec when the light stimulus is withdrawn. Notably, iLID* binding occurs without the co-expression of an SspB binding partner, which enables wildtype iLID subcellular localization through light-induced heterodimerization. The lack of binding partner requirement suggests that in mammalian cells, iLID* undergoes a blue light-induced conformational change, allowing it to bind a Golgi-associated lipid or protein.

Because different endomembrane organelles have different lipid compositions (111), we hypothesized that iLID*-Golgi association could be the result of a high-affinity interaction with a lipid which is enriched on Golgi membranes. Identifying the protein and lipid interaction occurring in this system is of interest because, to our knowledge, a single protein selectively binding the Golgi in response to light has not been reported. Understanding the protein and lipid structures underlying this light response may suggest new ways to engineer Golgi-targeting optogenetic tools, either by fusing effectors of interest to iLID* or by introducing iLID* moieties to other photoreceptors. To

work toward understanding iLID*-Golgi association, we worked with purified protein and previously described protein-lipid interaction screens (67, 69) to determine whether this interaction could be recapitulated in vitro and identify potential binding partners.

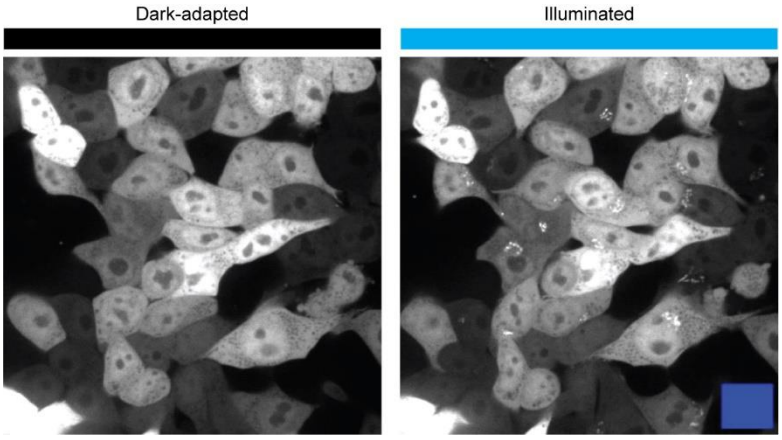

Figure A2.1 An iLID truncation binds the Golgi apparatus in its illuminated state

iLID*-mCherry was expressed in HEK293T cells. Cells were illuminated for 250 msec for the right panel.

```
EFLATTLERI EKNFVITDPR LPDNPIIFAS DSFLQLTEYS REEILGRNCR      50

FLQGPETDRA TVRKIRDAID NQTEVTVQLI NYTKSGKKFW NVFHLQPMRD     100

YKGDVQYFIG VQLDGTERLH GAAEREAVCL IKKTAFQIAE AANDENYE       148
```

Figure A2.2 iLID* protein sequence

Residues removed from the original iLID sequence are shown in red.

A2.2 Results and discussion

A2.2.1 Biophysical characterization of purified protein

To study iLID*-lipid interactions, we initially overexpressed and purified two constructs from *E. coli*: mCherry-iLID* and iLID*-mCherry, with a GGGGA linker

separating the proteins in each construct. Purified protein ran as expected on an SDS-PAGE gel, and flavin binding was confirmed with UV-vis spectroscopy, which showed a triplet peak centered at 447 nm. LOV photocycle was observed by measuring absorbance at 447 nm before and after exposure to blue light (**Figure A2.3**). We proceeded with iLID*-mCherry due to its higher yield and greater drop in A450 following blue light stimulation.

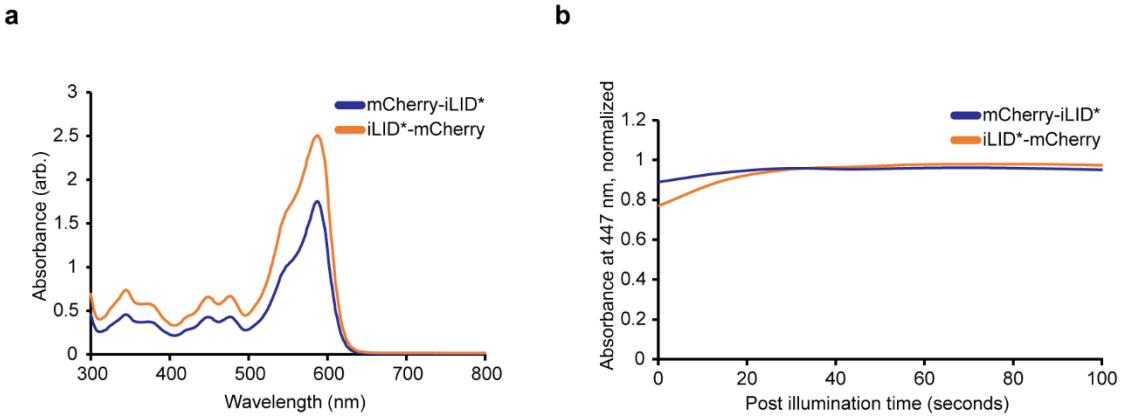

Figure A2.3 Biophysical characterization of iLID truncations

a. UV-vis spectra of purified protein. **b**. Recovery of absorbance at 447 nm following 30 seconds of 15 mW/cm^2 blue light stimulation. Absorbance values are normalized to pre-illumination values.

A2.2.2 Identification of lipid interaction partners

In disentangling the structural basis of iLID*-Golgi association, we considered two main possibilities: (1) that iLID* is binding to a particular lipid headgroup, or (2) that iLID* is associating with the Golgi because of a larger property of the Golgi membrane, like disorder or low curvature radius. Because testing interactions with specific lipids is more straightforward than creating membranes with specific meta-properties, we first used commercially available lipid panel strips to identify any headgroups to which iLID* bound more strongly. In this assay, His_6-tagged purified protein is incubated with strips

spotted with a panel of lipid headgroups; immunostaining is used to obtain colorimetric readout indicating binding. Binding is correlated to spot intensity above the local background reading of the strip. We tested iLID* binding to lipids on three panels: membrane lipids, PIP lipids, and sphingolipids. iLID* did not bind to any of the lipids on the sphingolipid strips. For membrane and PIP lipid strips, we saw enriched signal for several lipids (**Figure A2.4**), demonstrating a preference for lipids with -1 net charge. Interestingly, phosphatidic acid (PA) showed up as a hit on both panels on which it was presented and is known to provide disorder and curvature to Golgi membranes (124, 272).

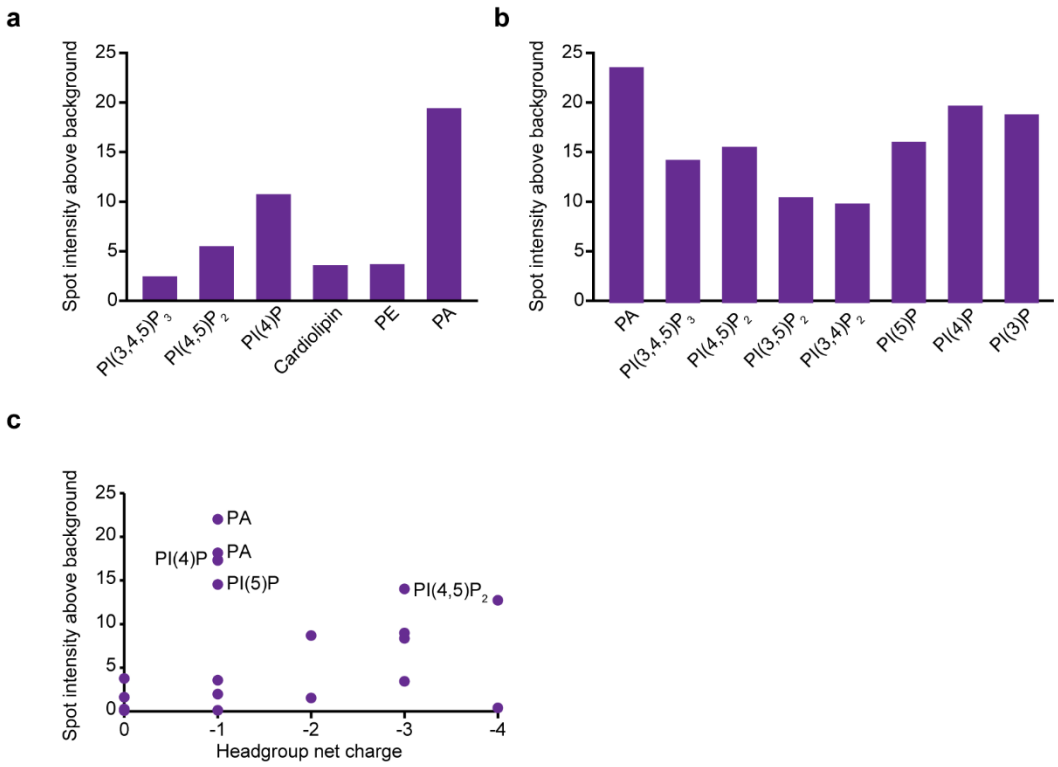

Figure A2.4 Protein-lipid overlay data for iLID*-mCherry

a. Spot intensity for membrane lipid panel for headgroups above background. PE, phosphatidylethanolamine; PA, phosphatidic acid. **b**. Spot intensity for PIP lipid panel for headgroups above background. **c**. Intensity versus headgroup net charge for lipids with intensity above background.

A2.2.3 Demonstration of protein-lipid interaction in water-in-oil emulsions

Since the lipid strip assay involve the presentation of a lipid headgroup in a non-membrane context, we next wanted to demonstrate binding to PA in a more natural context using water-in-oil emulsions (protocells). However, we ran into serious technical issues in attempting to incorporate long- or short-chain PA into the phosphatidylcholine (PC)-containing lipid phase of the protocell mixture. PA appeared to separate within the protocell membrane, indicated by bright protein patches along the membrane even at concentrations as low as 1%, though incorporation appeared to increase as PA concentration was increased to 15%. This non-homogenous lipid phase contrasts with the evenly distributed mixtures of PC and phosphatidyl serine (PS) we observed in BcLOV4 lipid binding characterization.

We next tested whether adding phosphatidylserine to the lipid mixture could be used to help solubilize PA and result in more evenly distributed lipid monolayers. In mixing equimolar amounts of phosphatidylserine and PA with PC solvent; we saw some improved incorporation, especially at the higher end of PS and PA concentrations tested. However, monolayers were still non-uniform, with some protocells showing bright rings at the perimeter from lipid-bound protein and others containing non-membrane-bound protein. Increasing PA concentration to 20% without the use of PS led to well-mixed protocells. iLID*-mCherry bound the lipid phase even in the dark-adapted state and at protein concentrations as low as 0.5 μM (one-tenth the normal protein concentration). Both these findings suggest a high-affinity interaction between iLID* and PA. The protein

also bound phosphatidylserine in the dark state when PS was present at concentrations greater than 15%.

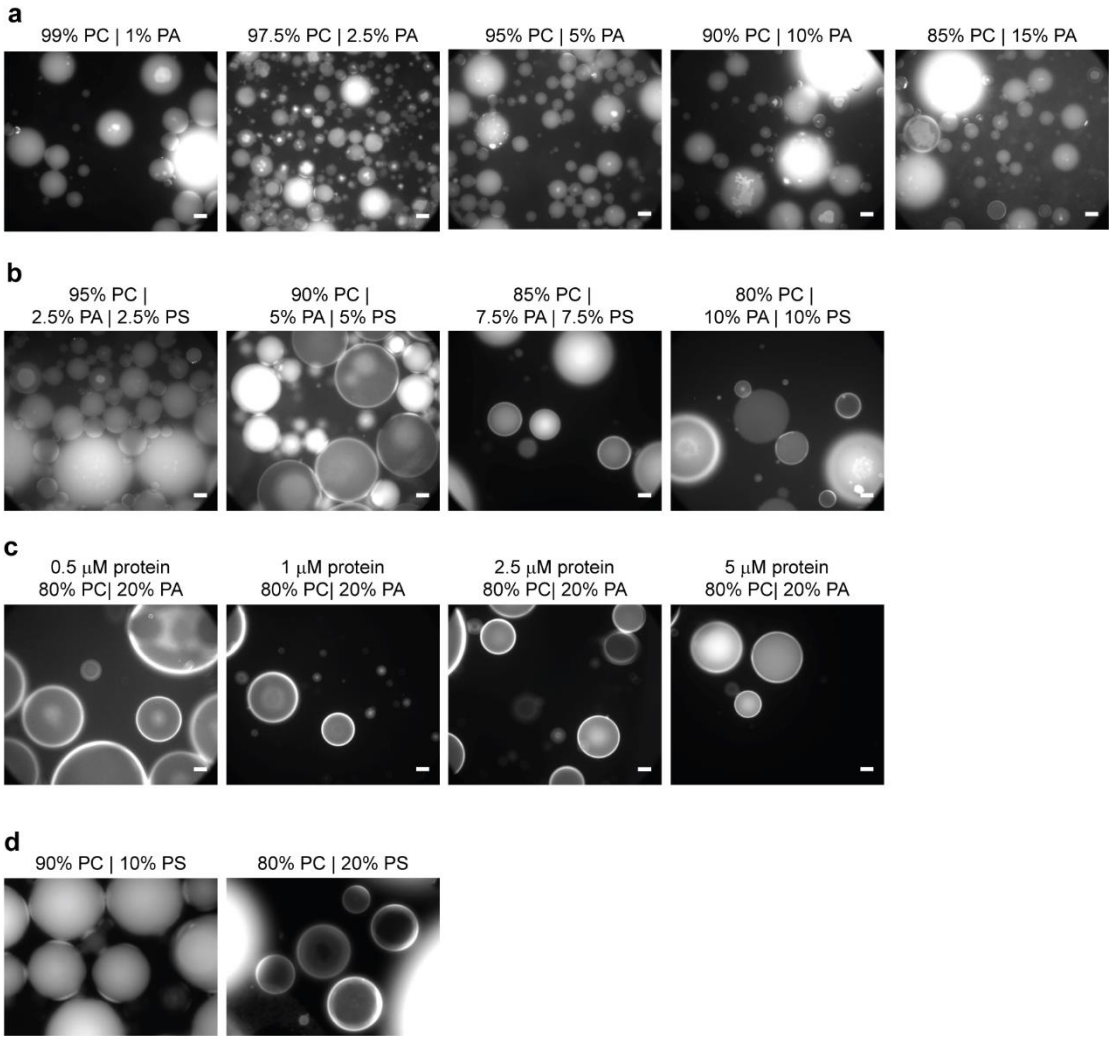

Figure A2.5 Protocells data for iLID*-mCherry

a. Dark-state protocells with increasing PA concentrations and 5 μM protein. **b**. Dark-state protocells with increasing PA and PS concentrations; 5 μM protein. **c**. Dark-state protocells with 20% PA and increasing protein concentrations. **d**. PC- and PS-containing dark-state protocells. (**a-d**) PC, phosphatidylcholine; PA, phosphatidic acid; PS, phosphatidylserine. Scale = 20 μM.

A2.3 Conclusions and future directions

Through these preliminary studies, we found evidence for iLID*-mCherry binding to phosphatidic acid, a component of Golgi membranes. More generally, the protein

exhibits a preference for lipid headgroups with a -1 net charge. Solidifying this interaction as the basis for the light-inducible iLID*-Golgi binding shown in mammalian cells next requires identification of the protein substructures responsible for this interaction through examination of the iLID* crystal structure and screening of blue light response of iLID* mutants of candidate residues. In parallel, iLID* interactions with phosphatidic acid in more realistic liposomal membranes through microscale thermophoresis or surface plasmon resonance can be explored.

From a tool development perspective, iLID* could potentially be used as a mechanism for light-inducible recruitment of signaling proteins to the Golgi. One potential application is in the recruitment of ARHGAP1, a GAP domain which inhibits RhoA signaling at the plasma membrane and Cdc42 signaling at the Golgi(159). In cells, the GTPase Arf1 binds ARHGAP21 and recruits it to the Golgi, where it controls Arp2/3 and filamentous actin. Fusing this GAP domain to iLID* could be a useful strategy for light-inducible termination of Cdc42 Golgi signaling.

A2.4 Methods

A2.4.1 Protein expression and purification

iLID*-mCherry and mCherry-iLID* genes were cloned into a plasmid with a pBAD backbone in frame with an N-terminal His_6 tag. Plasmids were transformed into One Shot TOP10 competent *E. coli* (Thermo Fisher C404010) and plated on LB/ampicillin. A single colony was used to inoculate a 10 mL culture of YT media supplemented with ampicillin and grown at 37 °C with 250 r.p.m. shaking overnight. The following day, the overnight culture was diluted 1:200 into YT media supplemented with ampicillin and grown at 37 °C with 250 r.p.m. shaking until mid-log phase was reached (OD_{600} = 1.0). Protein production was induced with 0.2% arabinose, and cells were grown for 18-22

hours at 18 ºC with 250 r.p.m. shaking in a refrigerated incubator. Cells were then harvested in 250 mL centrifuge bottles by spinning at 3000 x *g* for 20 minutes, and subsequently frozen at -20 ºC for < 2 weeks prior to cell lysis and purification.

Frozen cells were thawed at room temperature for 5-10 minutes and then resuspended in 50 mL lysis buffer (50 mM Tris pH 8.0, 150 mM NaCl, 0.4 mM phenylmethanesulfphonylfluoride (PMSF), 14 µL of β-mercapthoethanol, and a tablet of cOmplete Mini protease inhibitor (Roche)) per liter of harvested cell culture. Re-suspended cells were homogenized with 3 passes through a 21-gauge syringe needle. 10 mL aliquots of lysate were each sonicated 5 times with a duty cycle of 15 seconds ON, 30 seconds OFF with a Fisher Scientific Series 60 Sonic Dismembranator at 100% power (60W). Individual aliquots were pooled and transferred to a 50 mL polycarbonate conical tube and clarified by centrifugation at 25,000 x *g* for 30 minutes at 4 ºC to remove insoluble fractions. The supernatant was decanted and kept at 4 ºC prior to further purification. Flavin mononucleotide was added to the supernatant at a final concentration of 25 mg/mL and incubated at 4 °C for 20 minutes.

Ni-NTA superflow resin (3-4 mL) (Qiagen) was loaded onto a column and equilibrated with resuspension buffer. The supernatant was loaded onto the column followed by three 100 mL washes of resuspension buffer with increasing concentrations of imidazole (10 mM, 20 mM, 30 mM). Protein was eluted in resuspension buffer with 250 mM imidazole and buffer exchanged into 1x PBS using PD-10 desalting columns with Sephadex G-25 resin (GE 17085101). Buffer exchanged material was centrifuged at 4 ºC at 25,000 x *g* for 30 minutes to pellet insoluble protein debris. Buffer exchange was repeated twice more, and the column was re-equilibrated with 1x PBS prior to each usage. Purified protein was stored for < 2 weeks at 4 ºC.

A2.4.2 UV-vis spectroscopy

Absorbance scans were measured on an Ocean optics USB2000+ spectrophotometer with a deuterium/halogen light source. Full spectrum (λ = 250-700 nm range) absorbance scans were measured in quartz cuvettes (Starna Cells 16.100F-Q-10/Z15). Photocycle kinetics were measured by monitoring the absorbance at 447 nm (A447). After baseline measurements were made for 15 seconds at room temperature, the samples were stimulated with blue-light (10 s, λ = 455 nm, 15 mW/cm^2) delivered by a collimated LED (Mightex), and then dark-state recovery was monitored every 0.5 seconds for an additional 2 minutes.

A2.4.3 Protein-lipid overlay assay

Lipid strips were purchased from Echelon Biosciences (Sphingo strips, P-6000; PIP strips, P-6001; Membrane lipid strips, P-6002). Strips were blocked for 1-4 hours in PBS containing 3% BSA without detergent. 0.5 μM of His_6-iLID*-mCherry was then added to PBS / 3% BSA and this solution was incubated with a blocked lipid strip for 1 hour at room temperature. Membranes were washed 4 times with PBS-T (PBS + 0.1% Tween20) and then probed with mouse anti-His primary antibody at 1:2000 dilution (Cell Signaling Technology, 2366) in PBS + 3% BSA for either 1 hour at room temperature or overnight at 4 °C. After an additional 4 washes with PBS-T, membranes were probed with IRDye 680RD Goat (polyclonal) Anti-Mouse IgG (Licor 925-68070) at 1:15000 dilution in PBS-T + 3% BSA for 1 hour at room temperature. Blots were washed an additional 4 times in PBS-T and then in 1x PBS. Blots were imaged on an Odyssey Infrared Imaging System in the λ = 700 nm channel at Intensity 5.

A2.4.4 Protocells assay

Lipids (phosphatidylcholine, P3556; phosphatidic acid, P9511; phosphatidylserine, P7769; all from Millipore-Sigma) were resuspended in chloroform in a glass test tube or round-bottom flask. Chloroform was evaporated under a stream of nitrogen and the remaining lipid film was dissolved into decane (Aldrich D901) at 2.5-25 mg/mL, based on the solubility of each individual phospholipid. To facilitate suspension in decane and to remove excess chloroform, solutions were heated at 50 ºC for 3 hours and sonicated in a water bath for 30 minutes. Lipids were stored in glass vials with Teflon caps (Thomas Scientific 1234R80) at -20 ºC. In experiments, 30 µL of 20 mM lipids (total molarity) was mixed vigorously with 1.28 µL of purified mCherry-tagged protein in PBS (5 µM, unless otherwise specified) by pipetting up and down until a cloudy suspension formed. 20 µL of the water-oil emulsion was transferred to microwells and imaged at 20×.

APPENDIX 3: Toward the characterization of bioinformatically predicted lipase-LOV proteins

A3.1 Introduction

The 2016 bioinformatics study (71) reporting all computationally predicted LOV-effector pairs identified two previously uncharacterized LOV classes: RGS-LOVs, to which BcLOV4 belongs; and lipase-LOVs. Lipase-LOV proteins, if biochemically validated, would represent a new sensor-effector pair and potentially link light inputs to cellular lipid cleavage. One of these lipase-LOVs, from the green algae *Dolichomastix tenuilepis*, was able to be produced recombinantly in *E. coli* at modest yield for investigations into its lipase and LOV protein activities. It should be noted that protein solubility was greatly improved by the inclusion of an N-terminal NusA solubility tag. In addition, four mutations were made to the LOV domain to stabilize flavin binding and blue light photocycle (M352I, S353R, C302V, C304T). We sought to identify what, if any, lipid substrates this predicted lipase cleaves.

Initially, three substrate classes for the *Dolichomastix tenuilepis* lipase (DtLipase) were identified based on functional, structural, and physiological hypotheses. From a functional standpoint, many lipases exhibit broad esterase-like activity (51), so testing DtLipase activity on p-nitrophenyl derivatives with varying chain lengths could be informative. Structurally, alignment of the DtLipase sequence with other lipases showed some homology with PAF-acetylhydrolase-like lipases (7); this type of activity can be tested with a commercially available PAF cleavage endpoint kit (Cayman Chemical). Physiologically, when expressed in Chinese Hamster Ovary cells, DtLipase appears to

localize to a crystalloid endoplasmic reticulum, suggesting it may cleave ester bonds in polysaccharides (158).

Preliminary data showed that DtLipase may exhibit weak cleavage activity on a p-nitrophenyl palmitate substrate (chain length 16), measured by p-nitrophenol absorbance increase at 400 nm over several hours. However, since lipids may self-cleave in solution over time, a non-protein-containing control must be included to determine whether lipase-catalyzed cleavage is occurring. Minimal activity was also observed on phospholipase A2 substrate DBPC, but this assay was conducted without consistent protein concentrations across experimental conditions. Our screening of these substrate classes involved the use of liposomes and lipids in solution to account for the possibility that the lipase has higher activity on lipid interfaces; normalizing the amount of protein across conditions in the same experiment; and the inclusion of non-protein-containing conditions to control for lipid self-cleavage.

A3.2 Results and discussion

A3.2.1 P-nitrophenyl butyrate cleavage assay

We tested the activity of purified DtLipase on liposomes made of p-nitrophenyl butyrate (chain length 4). In this assay, cleavage of the lipid substrate releases p-nitrophenol, which absorbs at 400 nm. Thus, to monitor lipid cleavage, we varied substrate concentration from 5 to 20 μM and incubated with no protein, NusA only, NusA-DtLipase, or the positive control wheat germ lipase. As shown in **Figure A3.1**, wheat germ lipase cleaved all substrate concentrations tested above 5 μM, with p-nitrophenol concentrations increasing at rates of 2-4 μM per minute. NusA and NusA-DtLipase showed similar weak increases of less than 0.5 μM p-nitrophenol per minute, suggesting that no significant cleavage is occurring. This result suggests that if DtLipase

activity is in fact able to cleave p-nitrophenyl butyrate substrates, higher protein concentrations may be required for observable lipase activity.

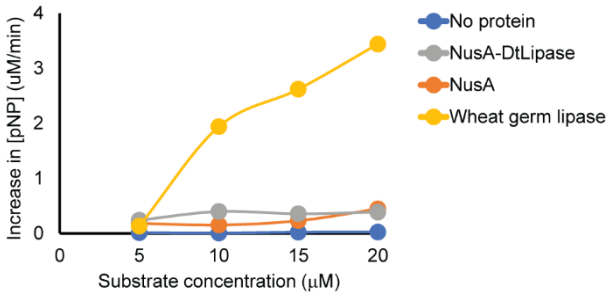

Figure A3.1 DtLipase incubation with p-nitrophenyl butyrate liposomes

Liposomes made of p-nitrophenyl butyrate were incubated with no protein, NusA, NusA-DtLipase, or positive control wheat germ lipase. Lipase-mediated cleavage was monitored by recording the solution's absorbance at 400 nm, which corresponds to the release of p-nitrophenol from the liposome substrate.

A3.2.2 DBPC cleavage assay

We next tested the possibility that DtLipase cleaves a phospholipase A2-type substrate using DBPC. Cleavage is monitored by the release of a fluorescent molecule, which emits at 525 nm. Over a time course of 30 minutes, we observed minimal fluorescence changes from the substrate only. Little difference was observed for DtLipase samples with and without DBPC substrate, suggesting that if DtLipase is exhibiting phospholipase A2-like activity, it is too weak to detect in this assay.

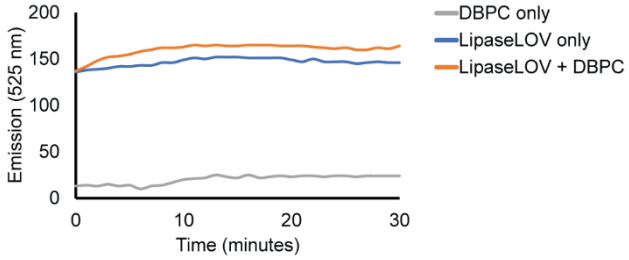

Figure A3.2 DtLipase-LOV incubation with DBPC substrate

DBPC substrate was incubated with or without NusA-DtLipase-LOV. Lipase-mediated cleavage was monitored by recording the solution's fluorescence emission at 525 nm, which corresponds to DBPC cleavage.

A3.3 Conclusions and future directions

In addition to DBPC and p-nitrophenyl butyrate, we also tested DtLipase with a PAF acetylhydrolase activity kit but saw no cleavage with the positive control; thus, that assay would need to be repeated with working standards to assess whether DtLipase is an acetylhydrolase. Together, these results underscore the need to work on DtLipase and lipase-LOV protein expression and purification conditions so that protein can be produced in high enough concentration for meaningful assay results. Another avenue in determining the biochemical validity of lipase-LOV proteins is to investigate the other lipase-LOV proteins identified in the bioinformatics screen, which may be more amenable to bacterial overexpression.

A3.4 Methods

A3.4.1 Protein expression and purification

Bacterial expression plasmids were transformed into BL21(DE3) *E. coli* cells by mixing 10 ng of purified plasmid DNA into 10 µL of chemically competent cells (NEB C2527H), incubating at 4 ºC for 30 minutes, heat-shocking cells in a 42 ºC water bath for 30 seconds, placing heat shocked cells on ice for 2 minutes, and then incubating for 1 hour at 37 ºC in 100 µL S.O.C. media. Transformed cells were grown on Luria Broth (LB) plates with 50 µg/mL kanamycin overnight at 37 ºC, and single colonies were picked and grown overnight to saturation in LB media with 50 µg/mL kanamycin. Cultures for protein production were initiated by diluting saturated overnight cultures 1:200 into fresh LB-kanamycin media in 1-2 L baffled flasks, and subsequently grown at 37 ºC with 250 r.p.m. shaking to a mid-log phase of OD_{600} = 0.5-0.8. Protein production was induced with 0.5 mM isopropyl-beta-D-thiogalactopyranoside (IPTG), and cells were grown for

18-22 hours at 18 ºC with 250 r.p.m. shaking in a refrigerated incubator. Cells were then harvested in 250 mL centrifuge bottles by spinning at 3000 x *g* for 20 minutes, and subsequently frozen at -20 ºC for < 2 weeks prior to cell lysis and purification.

Frozen cells were thawed at room temperature for 5-10 minutes and then resuspended in 50 mL ice-cold lysis buffer (50 mM sodium phosphate, 500 mM NaCl, 0.5% Triton-X-100, pH 6.5) per liter of harvested cell culture. All subsequent steps were carried out on ice or in a 4 ºC cold room. Re-suspended cells were homogenized with 3 passes through a 21-gauge syringe needle. 10 mL aliquots of lysate were each sonicated 5 times with a duty cycle of 15 seconds ON, 30 seconds OFF with a Fisher Scientific Series 60 Sonic Dismembranator at 100% power (60W). Individual aliquots were pooled and transferred to a 50 mL polycarbonate conical tube and clarified by centrifugation at 25,000 x *g* for 30 minutes at 4 ºC to remove insoluble fractions. The supernatant was decanted and kept at 4 ºC prior to further purification.

His_6-tagged proteins were affinity-purified by fast protein liquid chromatogphy (FPLC, AKTA Basic) on Ni-NTA (GE HisTrap FF) columns. All exposed sample-containing FPLC segments were covered with aluminum foil to maintain darkness. After sample loading onto a 5 mL column at 1mL/min, the column was washed with 20 mM imidazole in buffer (50 mM sodium phosphate, 500 mM NaCl, 10% glycerol, pH 6.5) for 15 column volumes, followed by a linear gradient, from 20 to 250 mM imidazole, over 15 column volumes at 5 mL/minute. Proteins were eluted with 500 mL imidazole, and collected in 10 x 2 mL fractions. Samples were pooled based on purity assessed by SDS-PAGE and concentration assessed by absorbance spectroscopy (A280), and then buffer exchanged into 1x PBS using PD-10 desalting columns with Sephadex G-25 resin (GE 17085101). Buffer exchanged material was centrifuged at 4 ºC at 25,000 x *g* for 30 minutes to pellet insoluble protein debris. Buffer exchange was repeated twice more,

and the column was re-equilibrated with 1x PBS prior to each usage. Purified protein was stored for < 2 weeks at 4 ºC.

A3.4.2 P-nitrophenyl butyrate cleavage assay

P-nitrophenylbutyrate (pNPB) was purchased from Millipore-Sigma (P9876). To make 10 mg/mL liposomes, 8.4 µL pNPB was diluted in 1 mL 1X PBS. The mixture was hydrated by heating at 50 °C on a heat block with intermittent vortexing for 30 minutes.The mixture was then sonicated in a water bath sonicator for twominutes and placed on ice. The mixture was then extruded for ten passes with an Avanti Lipid extruder with a 0.05 µm membrane; 5 µL liposomes was used per well of a 96 well plate of this assay. Wheat germ lipase (WGL) positive control was purchased from Millipore-Sigma (L3001) and is listed as containing between 5 and 15 lipase units per mg. For calculations, we assumed a potency of 10 lipase units per mg. WGL (30 mg, 300 units) was dissolved in 500 µL 1X PBS. This solution was then diluted tenfold in DPBS, and 33 µL was used for two units per well in this assay. Protein (either NusA only or NusA-Lipase) was buffer-exchanged into 1x PBS and diluted to a final concentration of 20 µM; 150 µL protein was used per well. Absorbance at 400 nm was measured every 30 seconds for one hour in a Tecan M200 plate reader set to 37 °C with 1 mm amplitude shaking for 1 second between measurements.

A3.4.3 DBPC cleavage assay

Full-length DtLipase-LOV was buffer exchanged into 1x PBS and diluted to 20 µM. DBPC substrate (Echelon Biosciences, L-3000) was dissolved in PBS for a final concentration of 10 µM. Substrate cleavage was measured in a black 96-well plate in a Tecan M200 spectrophotometer, with 200 µL sample volumes. Protein-only condition

used 10 µL protein diluted to 200 µL with PBS. Substrate-only condition used 10 µL substrate diluted to 200 µL with PBS. Protein plus substrate condition used 10 µL of each protein and substrate, diluted to 200 µL with PBS. The plate was exposed to 15 mW/cm^2 blue light for three seconds per minute. Emission was measured at 525 nm using 495 nm excitation and a gain setting of 50.

REFERENCES

1 Abreu-Blanco, M. T., Verboon, J. M. & Parkhurst, S. M. Coordination of Rho family GTPase activities to orchestrate cytoskeleton responses during cell wound repair. *Curr Biol* **24**, 144-155, doi:10.1016/j.cub.2013.11.048 (2014).

2 Adikes, R. C., Hallett, R. A., Saway, B. F., Kuhlman, B. & Slep, K. C. Control of microtubule dynamics using an optogenetic microtubule plus end-F-actin cross-linker. *J Cell Biol* **217**, 779-793, doi:10.1083/jcb.201705190 (2018).

3 Adrian, M., Nijenhuis, W., Hoogstraaten, R. I., Willems, J. & Kapitein, L. C. A Phytochrome-Derived Photoswitch for Intracellular Transport. *ACS Synth Biol* **6**, 1248-1256, doi:10.1021/acssynbio.6b00333 (2017).

4 Alkasalias, T. *et al.* RhoA knockout fibroblasts lose tumor-inhibitory capacity in vitro and promote tumor growth in vivo. *Proc Natl Acad Sci U S A* **114**, E1413-E1421, doi:10.1073/pnas.1621161114 (2017).

5 Ando, R., Mizuno, H. & Miyawaki, A. Regulated fast nucleocytoplasmic shuttling observed by reversible protein highlighting. *Science* **306**, 1370-1373, doi:10.1126/science.1102506 (2004).

6 Andresen, B. T., Rizzo, M. A., Shome, K. & Romero, G. The role of phosphatidic acid in the regulation of the Ras/MEK/Erk signaling cascade. *FEBS Letters* **531**, 65-68, doi:10.1016/s0014-5793(02)03483-x (2002).

7 Arai, H., Koizumi, H., Aoki, J. & Inoue, K. Platelet-activating factor acetylhydrolase (PAF-AH). *J Biochem* **131**, 635-640, doi:10.1093/oxfordjournals.jbchem.a003145 (2002).

8 Aspenstrom, P. BAR Domain Proteins Regulate Rho GTPase Signaling. *Adv Exp Med Biol* **1111**, 33-53, doi:10.1007/5584_2018_259 (2019).

9 Avila-Perez, M., Hellingwerf, K. J. & Kort, R. Blue light activates the sigmaB-dependent stress response of Bacillus subtilis via YtvA. *J Bacteriol* **188**, 6411-6414, doi:10.1128/JB.00716-06 (2006).

10 Bagci, H. *et al.* Mapping the proximity interaction network of the Rho-family GTPases reveals signalling pathways and regulatory mechanisms. *Nat Cell Biol* **22**, 120-134, doi:10.1038/s41556-019-0438-7 (2020).

11 Bement, W. M., Miller, A. L. & von Dassow, G. Rho GTPase activity zones and transient contractile arrays. *Bioessays* **28**, 983-993, doi:10.1002/bies.20477 (2006).

12 Bendezu, F. O. *et al.* Spontaneous Cdc42 polarization independent of GDI-mediated extraction and actin-based trafficking. *PLoS Biol* **13**, e1002097, doi:10.1371/journal.pbio.1002097 (2015).

13 Benedetti, L. *et al.* Optimized Vivid-derived Magnets photodimerizers for subcellular optogenetics in mammalian cells. *Elife* **9**, doi:10.7554/eLife.63230 (2020).

14 Benink, H. A. & Bement, W. M. Concentric zones of active RhoA and Cdc42 around single cell wounds. *J Cell Biol* **168**, 429-439, doi:10.1083/jcb.200411109 (2005).

15 Benman, W. *et al.* Temperature sensing optogenetic probes of cell signaling. (2021).

16 Berlew, E. E. *et al.* Single-Component Optogenetic Tools for Inducible RhoA GTPase Signaling. *Adv Biol (Weinh)*, e2100810, doi:10.1002/adbi.202100810 (2021).
17 Berlew, E. E., Kuznetsov, I. A., Yamada, K., Bugaj, L. J. & Chow, B. Y. Optogenetic Rac1 engineered from membrane lipid-binding RGS-LOV for inducible lamellipodia formation. *Photochem Photobiol Sci*, doi:10.1039/c9pp00434c (2020).
18 Berlew, E. E. *et al.* Designing Single-Component Optogenetic Membrane Recruitment Systems: The Rho-Family GTPase Signaling Toolbox. *ACS Synth Biol* **11**, 515-521, doi:10.1021/acssynbio.1c00604 (2022).
19 Berman, D. M. & Gilman, A. G. Mammalian RGS proteins: barbarians at the gate. *J Biol Chem* **273**, 1269-1272, doi:10.1074/jbc.273.3.1269 (1998).
20 Besenicar, M., Macek, P., Lakey, J. H. & Anderluh, G. Surface plasmon resonance in protein-membrane interactions. *Chem Phys Lipids* **141**, 169-178, doi:10.1016/j.chemphyslip.2006.02.010 (2006).
21 Bolado-Carrancio, A. *et al.* Periodic propagating waves coordinate RhoGTPase network dynamics at the leading and trailing edges during cell migration. *Elife* **9**, doi:10.7554/eLife.58165 (2020).
22 Bordeleau, F. *et al.* Matrix stiffening promotes a tumor vasculature phenotype. *Proc Natl Acad Sci U S A* **114**, 492-497, doi:10.1073/pnas.1613855114 (2017).
23 Bos, J. L., Rehmann, H. & Wittinghofer, A. GEFs and GAPs: critical elements in the control of small G proteins. *Cell* **129**, 865-877, doi:10.1016/j.cell.2007.05.018 (2007).
24 Boulter, E. *et al.* Regulation of Rho GTPase crosstalk, degradation and activity by RhoGDI1. *Nat Cell Biol* **12**, 477-483, doi:10.1038/ncb2049 (2010).
25 Breslin, J. W., Zhang, X. E., Worthylake, R. A. & Souza-Smith, F. M. Involvement of local lamellipodia in endothelial barrier function. *PLoS One* **10**, e0117970, doi:10.1371/journal.pone.0117970 (2015).
26 Brunet, N., Morin, A. & Olofsson, B. RhoGDI-3 regulates RhoG and targets this protein to the Golgi complex through its unique N-terminal domain. *Traffic* **3**, 342-357, doi:10.1034/j.1600-0854.2002.30504.x (2002).
27 Bugaj, L. J., Choksi, A. T., Mesuda, C. K., Kane, R. S. & Schaffer, D. V. Optogenetic protein clustering and signaling activation in mammalian cells. *Nat Methods* **10**, 249-252, doi:10.1038/nmeth.2360 (2013).
28 Bugaj, L. J. *et al.* Cancer mutations and targeted drugs can disrupt dynamic signal encoding by the Ras-Erk pathway. *Science* **361**, doi:10.1126/science.aao3048 (2018).
29 Bugaj, L. J. *et al.* Regulation of endogenous transmembrane receptors through optogenetic Cry2 clustering. *Nat Commun* **6**, 6898, doi:10.1038/ncomms7898 (2015).
30 Caldwell, R. M. *et al.* Optochemical Control of Protein Localization and Activity within Cell-like Compartments. *Biochemistry* **57**, 2590-2596, doi:10.1021/acs.biochem.8b00131 (2018).
31 Calmels, T. P. G. *et al.* Sequence and 3D structural relationships between mammalian Ras- and Rho-specific GTPase-activating proteins (GAPs): the cradle fold. *FEBS Letters* **426**, 205-211, doi:10.1016/s0014-5793(98)00331-7 (1998).

32 Cannon, A. C., Uribe-Alvarez, C. & Chernoff, J. RAC1 as a Therapeutic Target in Malignant Melanoma. *Trends Cancer* **6**, 478-488, doi:10.1016/j.trecan.2020.02.021 (2020).
33 Castellano, F., Montcourrier, P. & Chavrier, P. Membrane recruitment of Rac1 triggers phagocytosis. *Journal of Cell Science* **113**, 2955 (2000).
34 Cavanaugh, K. E., Oakes, P. W. & Gardel, M. L. Optogenetic Control of RhoA to Probe Subcellular Mechanochemical Circuitry. *Curr Protoc Cell Biol* **86**, e102, doi:10.1002/cpcb.102 (2020).
35 Chauhan, B. K., Lou, M., Zheng, Y. & Lang, R. A. Balanced Rac1 and RhoA activities regulate cell shape and drive invagination morphogenesis in epithelia. *Proc Natl Acad Sci U S A* **108**, 18289-18294, doi:10.1073/pnas.1108993108 (2011).
36 Chaves, I. *et al.* The cryptochromes: blue light photoreceptors in plants and animals. *Annu Rev Plant Biol* **62**, 335-364, doi:10.1146/annurev-arplant-042110-103759 (2011).
37 Cheng, L. *et al.* RhoGEF specificity mutants implicate RhoA as a target for Dbs transforming activity. *Mol Cell Biol* **22**, 6895-6905, doi:10.1128/MCB.22.19.6895-6905.2002 (2002).
38 Cherfils, J. & Zeghouf, M. Regulation of small GTPases by GEFs, GAPs, and GDIs. *Physiol Rev* **93**, 269-309, doi:10.1152/physrev.00003.2012 (2013).
39 Cheung, J., Bingman, C. A., Reyngold, M., Hendrickson, W. A. & Waldburger, C. D. Crystal structure of a functional dimer of the PhoQ sensor domain. *J Biol Chem* **283**, 13762-13770, doi:10.1074/jbc.M710592200 (2008).
40 Chou, C. K. *et al.* Dominant-negative Rac1 suppresses Ras-induced apoptosis possibly through activation of NFkappaB in Ha-ras oncogene-transformed NIH/3T3 cells. *Life Sci* **78**, 1823-1829, doi:10.1016/j.lfs.2005.08.039 (2006).
41 Christie, J. M., Saloman, M., Nozue, K., Wada, M. & Briggs, W. R. LOV (light, oxygen, or voltage) domains of the blue-light photoreceptor phototropin (nph1): Binding sites for the chromophore flavin mononucleotide. *Proc Natl Acad Sci USA* **96**, 8779–8783 (1999).
42 Christie, J. M., Swartz, T. E., Bogomolni, R. A. & Briggs, W. R. Phototropin LOV domains exhibit distinct roles in regulating photoreceptor function. *Plant J* **32**, 205-219, doi:10.1046/j.1365-313x.2002.01415.x (2002).
43 Chrzanowska-Wodnicka, M. & Burridge, K. Rho-stimulated contractility drives the formation of stress fibers and focal adhesions. *J Cell Biol* **133**, 1403-1415, doi:10.1083/jcb.133.6.1403 (1996).
44 Clay, M. R. & Halloran, M. C. Rho activation is apically restricted by Arhgap1 in neural crest cells and drives epithelial-to-mesenchymal transition. *Development* **140**, 3198-3209, doi:10.1242/dev.095448 (2013).
45 Crosson, S., Rajagopal, S. & Moffat, K. The LOV domain family: photoresponsive signaling modules coupled to diverse output domains. *Biochemistry* **42**, 2-10, doi:10.1021/bi026978l (2003).
46 Das, S. *et al.* Single-molecule tracking of small GTPase Rac1 uncovers spatial regulation of membrane translocation and mechanism for polarized signaling. *Proceedings of the National Academy of Sciences* **112**, E267, doi:10.1073/pnas.1409667112 (2015).
47 de Beco, S. *et al.* Optogenetic dissection of Rac1 and Cdc42 gradient shaping. *Nature communications* **9**, 4816-4816, doi:10.1038/s41467-018-07286-8 (2018).

48 De, P., Aske, J. C. & Dey, N. RAC1 Takes the Lead in Solid Tumors. *Cells* **8**, doi:10.3390/cells8050382 (2019).
49 Denk-Lobnig, M. & Martin, A. C. Modular regulation of Rho family GTPases in development. *Small GTPases* **10**, 122-129, doi:10.1080/21541248.2017.1294234 (2019).
50 DerMardirossian, C., Schnelzer, A. & Bokoch, G. M. Phosphorylation of RhoGDI by Pak1 mediates dissociation of Rac GTPase. *Mol Cell* **15**, 117-127, doi:10.1016/j.molcel.2004.05.019 (2004).
51 Desnuelle, P. & Savary, P. Specificities of lipases. *Journal of Lipid Research* **4**, 369-384, doi:10.1016/s0022-2275(20)40278-0 (1963).
52 Dowbaj, A. M. *et al.* An optogenetic method for interrogating YAP1 and TAZ nuclear-cytoplasmic shuttling. *bioRxiv*, doi:10.1101/2020.06.08.140228 (2020).
53 Dowler, S. *et al.* Identification of pleckstrin-homology-domain-containing proteins with novel phosphoinositide-binding specificities. *Biochem J* **351**, 19-31, doi:10.1042/0264-6021:3510019 (2000).
54 Drin, G. & Antonny, B. Amphipathic helices and membrane curvature. *FEBS Lett* **584**, 1840-1847, doi:10.1016/j.febslet.2009.10.022 (2010).
55 Dupont, S. *et al.* Role of YAP/TAZ in mechanotransduction. *Nature* **474**, 179-183, doi:10.1038/nature10137 (2011).
56 Dupraz, S. *et al.* RhoA Controls Axon Extension Independent of Specification in the Developing Brain. *Curr Biol* **29**, 3874-3886 e3879, doi:10.1016/j.cub.2019.09.040 (2019).
57 Ellenbroek, S. I. & Collard, J. G. Rho GTPases: functions and association with cancer. *Clin Exp Metastasis* **24**, 657-672, doi:10.1007/s10585-007-9119-1 (2007).
58 Etienne-Manneville, S. & Hall, A. Rho GTPases in cell biology. *Nature* **420**, 629-635, doi:10.1038/nature01148 (2002).
59 Feig, L. A. Tools of the trade: use of dominant-inhibitory mutants of Ras-family GTPases. *Nat Cell Biol* **1**, E25-27, doi:10.1038/10018 (1999).
60 Foley, B. J. *et al.* Characterization of a Vivid Homolog in Botrytis cinerea. *Photochem Photobiol* **94**, 985-993, doi:10.1111/php.12927 (2018).
61 Fu, G. *et al.* Ubiquitous distribution of helmchrome in phototactic swarmers of the stramenopiles. *Protoplasma* **253**, 929-941, doi:10.1007/s00709-015-0857-7 (2016).
62 Fujita, Y. & Yamashita, T. Axon growth inhibition by RhoA/ROCK in the central nervous system. *Front Neurosci* **8**, 338, doi:10.3389/fnins.2014.00338 (2014).
63 Ganguly, A., Thiel, W. & Crane, B. R. Glutamine Amide Flip Elicits Long Distance Allosteric Responses in the LOV Protein Vivid. *J Am Chem Soc* **139**, 2972-2980, doi:10.1021/jacs.6b10701 (2017).
64 Gao, Y., Dickerson, J. B., Guo, F., Zheng, J. & Zheng, Y. Rational design and characterization of a Rac GTPase-specific small molecule inhibitor. *Proceedings of the National Academy of Sciences of the United States of America* **101**, 7618, doi:10.1073/pnas.0307512101 (2004).
65 Garcia-Mata, R., Boulter, E. & Burridge, K. The 'invisible hand': regulation of RHO GTPases by RHOGDIs. *Nat Rev Mol Cell Biol* **12**, 493-504, doi:10.1038/nrm3153 (2011).
66 Ghiaur, G. *et al.* Inhibition of RhoA GTPase activity enhances hematopoietic stem and progenitor cell proliferation and engraftment. *Blood* **108**, 2087-2094, doi:10.1182/blood-2006-02-001560 (2006).

67 Glantz, S. T., Berlew, E. E. & Chow, B. Y. Synthetic cell-like membrane interfaces for probing dynamic protein-lipid interactions. *Methods Enzymol* **622**, 249-270, doi:10.1016/bs.mie.2019.02.015 (2019).
68 Glantz, S. T., Berlew, E. E. & Chow, B. Y. Synthetic cell-like membrane interfaces for probing dynamic protein-lipid interactions. *Methods in enzymology* **622**, 249-270, doi:10.1016/bs.mie.2019.02.015 (2019).
69 Glantz, S. T. *et al.* Directly light-regulated binding of RGS-LOV photoreceptors to anionic membrane phospholipids. *Proc Natl Acad Sci U S A* **115**, E7720-E7727, doi:10.1073/pnas.1802832115 (2018).
70 Glantz, S. T. *et al.* Directly light-regulated binding of RGS-LOV photoreceptors to anionic membrane phospholipids. *Proceedings of the National Academy of Sciences* **115**, E7720-E7727 (2018).
71 Glantz, S. T. *et al.* Functional and topological diversity of LOV domain photoreceptors. *Proc Natl Acad Sci U S A* **113**, E1442-1451, doi:10.1073/pnas.1509428113 (2016).
72 Gleichmann, T., Diensthuber, R. P. & Moglich, A. Charting the signal trajectory in a light-oxygen-voltage photoreceptor by random mutagenesis and covariance analysis. *J Biol Chem* **288**, 29345-29355, doi:10.1074/jbc.M113.506139 (2013).
73 Goedhart, J. & van Unen, J. Molecular perturbation strategies to examine spatiotemporal features of Rho GEF and Rho GTPase activity in living cells. *Small GTPases* **10**, 178-186, doi:10.1080/21541248.2017.1302551 (2019).
74 Good, M. C. Encapsulation of Xenopus Egg and Embryo Extract Spindle Assembly Reactions in Synthetic Cell-Like Compartments with Tunable Size. *Methods Mol Biol* **1413**, 87-108, doi:10.1007/978-1-4939-3542-0_7 (2016).
75 Good, M. C., Vahey, M. D., Skandarajah, A., Fletcher, D. A. & Heald, R. Cytoplasmic volume modulates spindle size during embryogenesis. *Science* **342**, 856-860, doi:10.1126/science.1243147 (2013).
76 Gordon, B. S. *et al.* RhoA modulates signaling through the mechanistic target of rapamycin complex 1 (mTORC1) in mammalian cells. *Cell Signal* **26**, 461-467, doi:10.1016/j.cellsig.2013.11.035 (2014).
77 Govek, E. E., Newey, S. E. & Van Aelst, L. The role of the Rho GTPases in neuronal development. *Genes Dev* **19**, 1-49, doi:10.1101/gad.1256405 (2005).
78 Graziano, B. R. *et al.* A module for Rac temporal signal integration revealed with optogenetics. *The Journal of Cell Biology* **216**, 2515, doi:10.1083/jcb.201604113 (2017).
79 Grecco, H. E., Schmick, M. & Bastiaens, P. I. Signaling from the living plasma membrane. *Cell* **144**, 897-909, doi:10.1016/j.cell.2011.01.029 (2011).
80 Griner, E. M. & Theodorescu, D. The faces and friends of RhoGDI2. *Cancer Metastasis Rev* **31**, 519-528, doi:10.1007/s10555-012-9376-6 (2012).
81 Guntas, G. *et al.* Engineering an improved light-induced dimer (iLID) for controlling the localization and activity of signaling proteins. *Proc Natl Acad Sci U S A* **112**, 112-117, doi:10.1073/pnas.1417910112 (2015).
82 Gutierrez-Uzquiza, A. *et al.* Coordinated activation of the Rac-GAP beta2-chimaerin by an atypical proline-rich domain and diacylglycerol. *Nat Commun* **4**, 1849, doi:10.1038/ncomms2834 (2013).
83 Guvendiren, M. & Burdick, J. A. Stiffening hydrogels to probe short- and long-term cellular responses to dynamic mechanics. *Nat Commun* **3**, 792, doi:10.1038/ncomms1792 (2012).

84 Habuchi, S. *et al.* Reversible single-molecule photoswitching in the GFP-like fluorescent protein Dronpa. *Proc Natl Acad Sci U S A* **102**, 9511-9516, doi:10.1073/pnas.0500489102 (2005).
85 Hallett, R. A., Zimmerman, S. P., Yumerefendi, H., Bear, J. E. & Kuhlman, B. Correlating in Vitro and in Vivo Activities of Light-Inducible Dimers: A Cellular Optogenetics Guide. *ACS Synth Biol* **5**, 53-64, doi:10.1021/acssynbio.5b00119 (2016).
86 Hannanta-Anan, P. & Chow, B. Y. Optogenetic Inhibition of Galphaq Protein Signaling Reduces Calcium Oscillation Stochasticity. *ACS Synth Biol* **7**, 1488-1495, doi:10.1021/acssynbio.8b00065 (2018).
87 Hannanta-Anan, P., Glantz, S. T. & Chow, B. Y. Optically inducible membrane recruitment and signaling systems. *Curr Opin Struct Biol* **57**, 84-92, doi:10.1016/j.sbi.2019.01.017 (2019).
88 Harper, S. M., Christie, J. M. & Gardner, K. H. Disruption of the LOV-Jalpha helix interaction activates phototropin kinase activity. *Biochemistry* **43**, 16184-16192, doi:10.1021/bi048092i (2004).
89 Harper, S. M., Neil, L. C. & Gardner, K. H. Structural basis of a phototropin light switch. *Science* **301**, 1541-1544, doi:10.1126/science.1086810 (2003).
90 Hayer, A. *et al.* Engulfed cadherin fingers are polarized junctional structures between collectively migrating endothelial cells. *Nat Cell Biol* **18**, 1311-1323, doi:10.1038/ncb3438 (2016).
91 He, L. *et al.* Optical control of membrane tethering and interorganellar communication at nanoscales. *Chem Sci* **8**, 5275-5281, doi:10.1039/c7sc01115f (2017).
92 Head, S. R. *et al.* Library construction for next-generation sequencing: overviews and challenges. *Biotechniques* **56**, 61-64, 66, 68, passim, doi:10.2144/000114133 (2014).
93 Hekman, M. *et al.* Reversible membrane interaction of BAD requires two C-terminal lipid binding domains in conjunction with 14-3-3 protein binding. *J Biol Chem* **281**, 17321-17336, doi:10.1074/jbc.M600292200 (2006).
94 Henry, J. T. & Crosson, S. Ligand-binding PAS domains in a genomic, cellular, and structural context. *Annu Rev Microbiol* **65**, 261-286, doi:10.1146/annurev-micro-121809-151631 (2011).
95 Hernandez-Candia, C. N. & Tucker, C. L. Optogenetic Control of Gene Expression Using Cryptochrome 2 and a Light-Activated Degron. *Methods Mol Biol* **2173**, 151-158, doi:10.1007/978-1-0716-0755-8_10 (2020).
96 Herrera-Perez, R. M., Cupo, C., Allan, C., Lin, A. & Kasza, K. E. Using optogenetics to link myosin patterns to contractile cell behaviors during convergent extension. *Biophys J* **120**, 4214-4229, doi:10.1016/j.bpj.2021.06.041 (2021).
97 Herrou, J. & Crosson, S. Function, structure and mechanism of bacterial photosensory LOV proteins. *Nat Rev Microbiol* **9**, 713-723, doi:10.1038/nrmicro2622 (2011).
98 Hollinger, S. & Hepler, J. R. Cellular regulation of RGS proteins: modulators and integrators of G protein signaling. *Pharmacol Rev* **54**, 527-559, doi:10.1124/pr.54.3.527 (2002).
99 Hope, J. M., Liu, A., Calvin, G. J. & Cui, B. Construction of Light-Activated Neurotrophin Receptors Using the Improved Light-Induced Dimerizer (iLID). *J Mol Biol* **432**, 3739-3748, doi:10.1016/j.jmb.2020.04.018 (2020).

100 Hordijk, P. L. *et al.* Inhibition of invasion of epithelial cells by Tiam1-Rac signaling. *Science* **278**, 1464-1466, doi:10.1126/science.278.5342.1464 (1997).
101 Horner, M. *et al.* Phytochrome-Based Extracellular Matrix with Reversibly Tunable Mechanical Properties. *Adv Mater* **31**, e1806727, doi:10.1002/adma.201806727 (2019).
102 Idevall-Hagren, O., Dickson, E. J., Hille, B., Toomre, D. K. & De Camilli, P. Optogenetic control of phosphoinositide metabolism. *Proc Natl Acad Sci U S A* **109**, E2316-2323, doi:10.1073/pnas.1211305109 (2012).
103 Imaizumi, T., Tran, H. G., Swartz, T. E., Briggs, W. R. & Kay, S. A. FKF1 is essential for photoperiodic-specific light signalling in Arabidopsis. *Nature* **426**, 302-306, doi:10.1038/nature02090 (2003).
104 Inaba, H., Miao, Q. & Nakata, T. Optogenetic control of small GTPases reveals RhoA mediates intracellular calcium signaling. *J Biol Chem* **296**, 100290, doi:10.1016/j.jbc.2021.100290 (2021).
105 Inoue, K., Nishihama, R. & Kohchi, T. Evolutionary origin of phytochrome responses and signaling in land plants. *Plant Cell Environ* **40**, 2502-2508, doi:10.1111/pce.12908 (2017).
106 Inoue, T., Heo, W. D., Grimley, J. S., Wandless, T. J. & Meyer, T. An inducible translocation strategy to rapidly activate and inhibit small GTPase signaling pathways. *Nature methods* **2**, 415-418, doi:10.1038/nmeth763 (2005).
107 Inoue, T., Heo, W. D., Grimley, J. S., Wandless, T. J. & Meyer, T. An inducible translocation strategy to rapidly activate and inhibit small GTPase signaling pathways. *Nat Methods* **2**, 415-418, doi:10.1038/nmeth763 (2005).
108 Itoh, M., Tsukita, S., Yamazaki, Y. & Sugimoto, H. Rho GTP exchange factor ARHGEF11 regulates the integrity of epithelial junctions by connecting ZO-1 and RhoA-myosin II signaling. *Proc Natl Acad Sci U S A* **109**, 9905-9910, doi:10.1073/pnas.1115063109 (2012).
109 Itoh, R. E. *et al.* Activation of rac and cdc42 video imaged by fluorescent resonance energy transfer-based single-molecule probes in the membrane of living cells. *Mol Cell Biol* **22**, 6582-6591, doi:10.1128/mcb.22.18.6582-6591.2002 (2002).
110 Izquierdo, E., Quinkler, T. & De Renzis, S. Guided morphogenesis through optogenetic activation of Rho signalling during early Drosophila embryogenesis. *Nat Commun* **9**, 2366, doi:10.1038/s41467-018-04754-z (2018).
111 Jackson, C. L., Walch, L. & Verbavatz, J. M. Lipids and Their Trafficking: An Integral Part of Cellular Organization. *Dev Cell* **39**, 139-153, doi:10.1016/j.devcel.2016.09.030 (2016).
112 Jenny, R. J., Mann, K. G. & Lundblad, R. L. A critical review of the methods for cleavage of fusion proteins with thrombin and factor Xa. *Protein Expression and Purification* **31**, 1-11, doi:10.1016/s1046-5928(03)00168-2 (2003).
113 Kaberniuk, A. A., Shemetov, A. A. & Verkhusha, V. V. A bacterial phytochrome-based optogenetic system controllable with near-infrared light. *Nat Methods* **13**, 591-597, doi:10.1038/nmeth.3864 (2016).
114 Kavran, J. M. *et al.* Specificity and promiscuity in phosphoinositide binding by pleckstrin homology domains. *J Biol Chem* **273**, 30497-30508, doi:10.1074/jbc.273.46.30497 (1998).
115 Kawano, F., Okazaki, R., Yazawa, M. & Sato, M. A photoactivatable Cre-loxP recombination system for optogenetic genome engineering. *Nat Chem Biol* **12**, 1059-1064, doi:10.1038/nchembio.2205 (2016).

116 Kawano, F., Suzuki, H., Furuya, A. & Sato, M. Engineered pairs of distinct photoswitches for optogenetic control of cellular proteins. *Nat Commun* **6**, 6256, doi:10.1038/ncomms7256 (2015).
117 Keely, P. J., Westwick, J. K., Whitehead, I. P., Der, C. J. & Parise, L. V. Cdc42 and Rac1 induce integrin-mediated cell motility and invasiveness through PI(3)K. *Nature* **390**, 632-636, doi:10.1038/37656 (1997).
118 Kegelman, C. D. *et al.* Skeletal cell YAP and TAZ combinatorially promote bone development. *FASEB J* **32**, 2706-2721, doi:10.1096/fj.201700872R (2018).
119 Kendrick, R. E. & Spruit, C. J. Phototransformations of phytochrome. *Photochem Photobiol* **26**, 201-214, doi:10.1111/j.1751-1097.1977.tb07473.x (1977).
120 Kennedy, M. J. *et al.* Rapid blue-light–mediated induction of protein interactions in living cells. *Nat Methods* **7**, 973-977 (2010).
121 Klausen, L. H., Fuhs, T. & Dong, M. Mapping surface charge density of lipid bilayers by quantitative surface conductivity microscopy. *Nat Commun* **7**, 12447, doi:10.1038/ncomms12447 (2016).
122 Klewer, L. & Wu, Y. W. Light-Induced Dimerization Approaches to Control Cellular Processes. *Chemistry* **25**, 12452-12463, doi:10.1002/chem.201900562 (2019).
123 Komatsu, N. *et al.* Development of an optimized backbone of FRET biosensors for kinases and GTPases. *Mol Biol Cell* **22**, 4647-4656, doi:10.1091/mbc.E11-01-0072 (2011).
124 Kooijman, E. E., Chupin, V., de Kruijff, B. & Burger, K. N. Modulation of membrane curvature by phosphatidic acid and lysophosphatidic acid. *Traffic* **4**, 162-174, doi:10.1034/j.1600-0854.2003.00086.x (2003).
125 Kotelevets, L. & Chastre, E. Rac1 Signaling: From Intestinal Homeostasis to Colorectal Cancer Metastasis. *Cancers (Basel)* **12**, doi:10.3390/cancers12030665 (2020).
126 Kotynkova, K., Su, K. C., West, S. C. & Petronczki, M. Plasma Membrane Association but Not Midzone Recruitment of RhoGEF ECT2 Is Essential for Cytokinesis. *Cell Rep* **17**, 2672-2686, doi:10.1016/j.celrep.2016.11.029 (2016).
127 Krauss, U. *et al.* Distribution and phylogeny of light-oxygen-voltage-blue-light-signaling proteins in the three kingdoms of life. *J Bacteriol* **191**, 7234-7242, doi:10.1128/JB.00923-09 (2009).
128 Kraynov, V. S. *et al.* Localized Rac activation dynamics visualized in living cells. *Science* **290**, 333-337, doi:10.1126/science.290.5490.333 (2000).
129 Kukimoto-Niino, M., Ihara, K., Murayama, K. & Shirouzu, M. Structural insights into the small GTPase specificity of the DOCK guanine nucleotide exchange factors. *Curr Opin Struct Biol* **71**, 249-258, doi:10.1016/j.sbi.2021.08.001 (2021).
130 Kuznetsov, I. A., Berlew, E. E., Glantz, S. T., Hannanta-Anan, P. & Chow, B. Y. Single-cell spatiotemporal dynamics of optogenetic membrane recruitment by finite element modeling. *[PLACEHOLDER]* (2021).
131 Lamarche, N. *et al.* Rac and Cdc42 Induce Actin Polymerization and G1 Cell Cycle Progression Independently of p65PAK and the JNK/SAPK MAP Kinase Cascade. *Cell* **87**, 519-529, doi:10.1016/s0092-8674(00)81371-9 (1996).
132 Lamas, I., Merlini, L., Vjestica, A., Vincenzetti, V. & Martin, S. G. Optogenetics reveals Cdc42 local activation by scaffold-mediated positive feedback and Ras GTPase. *PLoS Biol* **18**, e3000600, doi:10.1371/journal.pbio.3000600 (2020).

133 Lamas, I., Weber, N. & Martin, S. G. Activation of Cdc42 GTPase upon CRY2-Induced Cortical Recruitment Is Antagonized by GAPs in Fission Yeast. *Cells* **9**, doi:10.3390/cells9092089 (2020).
134 Lammers, M., Meyer, S., Kuhlmann, D. & Wittinghofer, A. Specificity of interactions between mDia isoforms and Rho proteins. *J Biol Chem* **283**, 35236-35246, doi:10.1074/jbc.M805634200 (2008).
135 Lampi, M. C. & Reinhart-King, C. A. Targeting extracellular matrix stiffness to attenuate disease: From molecular mechanisms to clinical trials. *Sci Transl Med* **10**, doi:10.1126/scitranslmed.aao0475 (2018).
136 Lanning, C. C., Daddona, J. L., Ruiz-Velasco, R., Shafer, S. H. & Williams, C. L. The Rac1 C-terminal Polybasic Region Regulates the Nuclear Localization and Protein Degradation of Rac1. *Journal of Biological Chemistry* **279**, 44197-44210, doi:10.1074/jbc.M404977200 (2004).
137 Lauffenburger, D. A. & Linderman, J. J. *Receptors: models for binding, trafficking, and signaling*. (Oxford University Press on Demand, 1996).
138 Lee, S. H. *et al.* The intermolecular interaction between the PH domain and the C-terminal domain of Arabidopsis dynamin-like 6 determines lipid binding specificity. *J Biol Chem* **277**, 31842-31849, doi:10.1074/jbc.M204770200 (2002).
139 Levskaya, A., Weiner, O. D., Lim, W. A. & Voigt, C. A. Spatiotemporal control of cell signalling using a light-switchable protein interaction. *Nature* **461**, 997-1001, doi:10.1038/nature08446 (2009).
140 Li, Z. *et al.* Structural insights into the YAP and TEAD complex. *Genes Dev* **24**, 235-240, doi:10.1101/gad.1865810 (2010).
141 Lin, K. C., Park, H. W. & Guan, K. L. Regulation of the Hippo Pathway Transcription Factor TEAD. *Trends Biochem Sci* **42**, 862-872, doi:10.1016/j.tibs.2017.09.003 (2017).
142 Liscum, E. & Briggs, W. R. Mutations in the NPH1 locus of Arabidopsis disrupt the perception of phototropic stimuli. *Plant Cell* **7**, 473-485, doi:10.1105/tpc.7.4.473 (1995).
143 Liu, B. *et al.* Signaling mechanisms of plant cryptochromes in Arabidopsis thaliana. *J Plant Res* **129**, 137-148, doi:10.1007/s10265-015-0782-z (2016).
144 Liu, L. *et al.* Comparison of next-generation sequencing systems. *J Biomed Biotechnol* **2012**, 251364, doi:10.1155/2012/251364 (2012).
145 Longenecker, K. *et al.* How RhoGDI binds Rho. *Acta Crystallogr D Biol Crystallogr* **55**, 1503-1515, doi:10.1107/s090744499900801x (1999).
146 Losi, A. & Gartner, W. Old chromophores, new photoactivation paradigms, trendy applications: flavins in blue light-sensing photoreceptors. *Photochem Photobiol* **87**, 491-510, doi:10.1111/j.1751-1097.2011.00913.x (2011).
147 Losi, A., Mandalari, C. & Gartner, W. From Plant Infectivity to Growth Patterns: The Role of Blue-Light Sensing in the Prokaryotic World. *Plants (Basel)* **3**, 70-94, doi:10.3390/plants3010070 (2014).
148 Lu, K. Y. *et al.* Profiling lipid-protein interactions using nonquenched fluorescent liposomal nanovesicles and proteome microarrays. *Mol Cell Proteomics* **11**, 1177-1190, doi:10.1074/mcp.M112.017426 (2012).
149 Ma, G. *et al.* Optogenetic engineering to probe the molecular choreography of STIM1-mediated cell signaling. *Nat Commun* **11**, 1039, doi:10.1038/s41467-020-14841-9 (2020).

150 Mack, N. A. & Georgiou, M. The interdependence of the Rho GTPases and apicobasal cell polarity. *Small GTPases* **5**, 10, doi:10.4161/21541248.2014.973768 (2014).
151 Mahlandt, E. K. *et al.* Visualizing endogenous Rho activity with an improved localization-based, genetically encoded biosensor. *J Cell Sci* **134**, doi:10.1242/jcs.258823 (2021).
152 Maldonado, M. D. M. & Dharmawardhane, S. Targeting Rac and Cdc42 GTPases in Cancer. *Cancer Res* **78**, 3101-3111, doi:10.1158/0008-5472.CAN-18-0619 (2018).
153 Mammoto, A., Takahashi, K., Sasaki, T. & Takai, Y. Stimulation of Rho GDI release by ERM proteins. *Methods in enzymology* **325**, 91-101 (2000).
154 Marei, H. *et al.* Differential Rac1 signalling by guanine nucleotide exchange factors implicates FLII in regulating Rac1-driven cell migration. *Nature Communications* **7**, 10664, doi:10.1038/ncomms10664 (2016).
155 Marei, H. & Malliri, A. GEFs: Dual regulation of Rac1 signaling. *Small GTPases* **8**, 90-99, doi:10.1080/21541248.2016.1202635 (2017).
156 Marjoram, R. J., Lessey, E. C. & Burridge, K. Regulation of RhoA activity by adhesion molecules and mechanotransduction. *Curr Mol Med* **14**, 199-208, doi:10.2174/1566524014666140128104541 (2014).
157 Mason, D. E. *et al.* YAP and TAZ limit cytoskeletal and focal adhesion maturation to enable persistent cell motility. *J Cell Biol* **218**, 1369-1389, doi:10.1083/jcb.201806065 (2019).
158 Melkonian, M., Becker, B. & Becker, D. Scale formation in algae. *J Electron Microsc Tech* **17**, 165-178, doi:10.1002/jemt.1060170205 (1991).
159 Menetrey, J. *et al.* Structural basis for ARF1-mediated recruitment of ARHGAP21 to Golgi membranes. *EMBO J* **26**, 1953-1962, doi:10.1038/sj.emboj.7601634 (2007).
160 Michaelson, D. *et al.* Rac1 accumulates in the nucleus during the G2 phase of the cell cycle and promotes cell division. *J Cell Biol* **181**, 485-496, doi:10.1083/jcb.200801047 (2008).
161 Michaelson, D. *et al.* Rac1 accumulates in the nucleus during the G2 phase of the cell cycle and promotes cell division. *The Journal of cell biology* **181**, 485-496, doi:10.1083/jcb.200801047 (2008).
162 Michaelson, D. *et al.* Differential localization of Rho GTPases in live cells: regulation by hypervariable regions and RhoGDI binding. *J Cell Biol* **152**, 111-126, doi:10.1083/jcb.152.1.111 (2001).
163 Moglich, A., Ayers, R. A. & Moffat, K. Design and signaling mechanism of light-regulated histidine kinases. *J Mol Biol* **385**, 1433-1444, doi:10.1016/j.jmb.2008.12.017 (2009).
164 Moglich, A., Ayers, R. A. & Moffat, K. Structure and signaling mechanism of Per-ARNT-Sim domains. *Structure* **17**, 1282-1294, doi:10.1016/j.str.2009.08.011 (2009).
165 Moglich, A. & Moffat, K. Engineered photoreceptors as novel optogenetic tools. *Photochem Photobiol Sci* **9**, 1286-1300, doi:10.1039/c0pp00167h (2010).
166 Morin, P., Flors, C. & Olson, M. F. Constitutively active RhoA inhibits proliferation by retarding G(1) to S phase cell cycle progression and impairing cytokinesis. *Eur J Cell Biol* **88**, 495-507, doi:10.1016/j.ejcb.2009.04.005 (2009).

167 Motta-Mena, L. B. *et al.* An optogenetic gene expression system with rapid activation and deactivation kinetics. *Nat Chem Biol* **10**, 196-202, doi:10.1038/nchembio.1430 (2014).
168 Mucha, E., Fricke, I., Schaefer, A., Wittinghofer, A. & Berken, A. Rho proteins of plants--functional cycle and regulation of cytoskeletal dynamics. *Eur J Cell Biol* **90**, 934-943, doi:10.1016/j.ejcb.2010.11.009 (2011).
169 Muller, K. *et al.* Synthesis of phycocyanobilin in mammalian cells. *Chem Commun (Camb)* **49**, 8970-8972, doi:10.1039/c3cc45065a (2013).
170 Muller, P. M. *et al.* Systems analysis of RhoGEF and RhoGAP regulatory proteins reveals spatially organized RAC1 signalling from integrin adhesions. *Nat Cell Biol* **22**, 498-511, doi:10.1038/s41556-020-0488-x (2020).
171 Narayan, K. & Lemmon, M. A. Determining selectivity of phosphoinositide-binding domains. *Methods* **39**, 122-133, doi:10.1016/j.ymeth.2006.05.006 (2006).
172 Nardone, G. *et al.* YAP regulates cell mechanics by controlling focal adhesion assembly. *Nat Commun* **8**, 15321, doi:10.1038/ncomms15321 (2017).
173 Nash, A. I., Ko, W. H., Harper, S. M. & Gardner, K. H. A conserved glutamine plays a central role in LOV domain signal transmission and its duration. *Biochemistry* **47**, 13842-13849, doi:10.1021/bi801430e (2008).
174 Natwick, D. E. & Collins, S. R. Optimized iLID membrane anchors for local optogenetic protein recruitment. *bioRxiv*, doi:10.1101/2020.09.05.268508 (2020).
175 Neiditch, M. B. *et al.* Ligand-induced asymmetry in histidine sensor kinase complex regulates quorum sensing. *Cell* **126**, 1095-1108, doi:10.1016/j.cell.2006.07.032 (2006).
176 Nguyen, L. K., Kholodenko, B. N. & von Kriegsheim, A. Rac1 and RhoA: Networks, loops and bistability. *Small GTPases* **9**, 316-321, doi:10.1080/21541248.2016.1224399 (2018).
177 Ni, M., Tepperman, J. M. & Quail, P. H. Binding of phytochrome B to its nuclear signalling partner PIF3 is reversibly induced by light. *Nature* **400**, 781-784, doi:10.1038/23500 (1999).
178 Nihongaki, Y., Kawano, F., Nakajima, T. & Sato, M. Photoactivatable CRISPR-Cas9 for optogenetic genome editing. *Nat Biotechnol* **33**, 755-760, doi:10.1038/nbt.3245 (2015).
179 Niopek, D., Wehler, P., Roensch, J., Eils, R. & Di Ventura, B. Optogenetic control of nuclear protein export. *Nat Commun* **7**, 10624, doi:10.1038/ncomms10624 (2016).
180 O'Neill, P. R., Kalyanaraman, V. & Gautam, N. Subcellular optogenetic activation of Cdc42 controls local and distal signaling to drive immune cell migration. *Mol Biol Cell* **27**, 1442-1450, doi:10.1091/mbc.E15-12-0832 (2016).
181 Oakes, P. W. *et al.* Optogenetic control of RhoA reveals zyxin-mediated elasticity of stress fibres. *Nat Commun* **8**, 15817, doi:10.1038/ncomms15817 (2017).
182 Ohta, Y., Hartwig, J. H. & Stossel, T. P. FilGAP, a Rho- and ROCK-regulated GAP for Rac binds filamin A to control actin remodelling. *Nat Cell Biol* **8**, 803-814, doi:10.1038/ncb1437 (2006).
183 Panagabko, C. *et al.* Ligand specificity in the CRAL-TRIO protein family. *Biochemistry* **42**, 6467-6474, doi:10.1021/bi034086v (2003).
184 Park, D. *et al.* BAI1 is an engulfment receptor for apoptotic cells upstream of the ELMO/Dock180/Rac module. *Nature* **450**, 430-434, doi:10.1038/nature06329 (2007).

185 Pathak, G. P., Strickland, D., Vrana, J. D. & Tucker, C. L. Benchmarking of optical dimerizer systems. *ACS Synth Biol* **3**, 832-838, doi:10.1021/sb500291r (2014).
186 Pertz, O. Spatio-temporal Rho GTPase signaling - where are we now? *J Cell Sci* **123**, 1841-1850, doi:10.1242/jcs.064345 (2010).
187 Pertz, O., Hodgson, L., Klemke, R. L. & Hahn, K. M. Spatiotemporal dynamics of RhoA activity in migrating cells. *Nature* **440**, 1069-1072, doi:10.1038/nature04665 (2006).
188 Pinheiro, L. B. *et al.* Evaluation of a droplet digital polymerase chain reaction format for DNA copy number quantification. *Anal Chem* **84**, 1003-1011, doi:10.1021/ac202578x (2012).
189 Pollard, T. D. Actin and Actin-Binding Proteins. *Cold Spring Harb Perspect Biol* **8**, doi:10.1101/cshperspect.a018226 (2016).
190 Pollard, T. D. Regulation of Actin Filament Assembly by Arp2/3 Complex and Formins. *Annual review of biophysics and biomolecular structure* **36**, 451-477, doi:10.1146/annurev.biophys.35.040405.101936 (2007).
191 Pollitt, A. Y. & Insall, R. H. WASP and SCAR/WAVE proteins: the drivers of actin assembly. *Journal of cell science* **122**, 2575-2578, doi:10.1242/jcs.023879 (2009).
192 Pollitt, A. Y. & Insall, R. H. WASP and SCAR/WAVE proteins: the drivers of actin assembly. *J Cell Sci* **122**, 2575-2578, doi:10.1242/jcs.023879 (2009).
193 Polstein, L. R. & Gersbach, C. A. Light-inducible spatiotemporal control of gene activation by customizable zinc finger transcription factors. *J Am Chem Soc* **134**, 16480-16483, doi:10.1021/ja3065667 (2012).
194 Purvis, J. E. & Lahav, G. Encoding and decoding cellular information through signaling dynamics. *Cell* **152**, 945-956, doi:10.1016/j.cell.2013.02.005 (2013).
195 Pykalainen, A. *et al.* Pinkbar is an epithelial-specific BAR domain protein that generates planar membrane structures. *Nat Struct Mol Biol* **18**, 902-907, doi:10.1038/nsmb.2079 (2011).
196 Quail, P. H. Phytochrome photosensory signalling networks. *Nat Rev Mol Cell Biol* **3**, 85-93, doi:10.1038/nrm728 (2002).
197 Raftopoulou, M. & Hall, A. Cell migration: Rho GTPases lead the way. *Dev Biol* **265**, 23-32, doi:10.1016/j.ydbio.2003.06.003 (2004).
198 Remorino, A. *et al.* Gradients of Rac1 Nanoclusters Support Spatial Patterns of Rac1 Signaling. *Cell Rep* **21**, 1922-1935, doi:10.1016/j.celrep.2017.10.069 (2017).
199 Ren, X. D., Kiosses, W. B. & Schwartz, M. A. Regulation of the small GTP-binding protein Rho by cell adhesion and the cytoskeleton. *EMBO J* **18**, 578-585, doi:10.1093/emboj/18.3.578 (1999).
200 Renicke, C., Schuster, D., Usherenko, S., Essen, L. O. & Taxis, C. A LOV2 domain-based optogenetic tool to control protein degradation and cellular function. *Chem Biol* **20**, 619-626, doi:10.1016/j.chembiol.2013.03.005 (2013).
201 Repina, N. A., Rosenbloom, A., Mukherjee, A., Schaffer, D. V. & Kane, R. S. At Light Speed: Advances in Optogenetic Systems for Regulating Cell Signaling and Behavior. *Annu Rev Chem Biomol Eng* **8**, 13-39, doi:10.1146/annurev-chembioeng-060816-101254 (2017).
202 Ridley, A. J. & Hall, A. The small GTP-binding protein rho regulates the assembly of focal adhesions and actin stress fibers in response to growth factors. *Cell* **70**, 389-399, doi:10.1016/0092-8674(92)90163-7 (1992).

203 Robbe, K., Otto-Bruc, A., Chardin, P. & Antonny, B. Dissociation of GDP dissociation inhibitor and membrane translocation are required for efficient activation of Rac by the Dbl homology-pleckstrin homology region of Tiam. *J Biol Chem* **278**, 4756-4762, doi:10.1074/jbc.M210412200 (2003).
204 Roberts, P. J. *et al.* Rho Family GTPase modification and dependence on CAAX motif-signaled posttranslational modification. *J Biol Chem* **283**, 25150-25163, doi:10.1074/jbc.M800882200 (2008).
205 Rockwell, N. C., Su, Y. S. & Lagarias, J. C. Phytochrome structure and signaling mechanisms. *Annu Rev Plant Biol* **57**, 837-858, doi:10.1146/annurev.arplant.56.032604.144208 (2006).
206 Rohl, C. A., Strauss, C. E. M., Misura, K. M. S. & Baker, D. Protein Structure Prediction Using Rosetta. *Methods Enzymol* **383**, 66-93, doi:https://doi.org/10.1016/S0076-6879(04)83004-0 (2004).
207 Rossman, K. L., Der, C. J. & Sondek, J. GEF means go: turning on RHO GTPases with guanine nucleotide-exchange factors. *Nat Rev Mol Cell Biol* **6**, 167-180, doi:10.1038/nrm1587 (2005).
208 Rost, B. R., Schneider-Warme, F., Schmitz, D. & Hegemann, P. Optogenetic Tools for Subcellular Applications in Neuroscience. *Neuron* **96**, 572-603, doi:10.1016/j.neuron.2017.09.047 (2017).
209 Salomon, M., Christie, J. M., Knieb, E., Lempert, U. & Briggs, W. R. Photochemical and mutational analysis of the FMN-binding domains of the plant blue light receptor, phototropin. *Biochemistry* **39**, 9401-9410, doi:10.1021/bi000585+ (2000).
210 Samadani, A., Mettetal, J. & van Oudenaarden, A. Cellular asymmetry and individuality in directional sensing. *Proc Natl Acad Sci U S A* **103**, 11549-11554, doi:10.1073/pnas.0601909103 (2006).
211 Sato, H. & Feix, J. B. Peptide-membrane interactions and mechanisms of membrane destruction by amphipathic alpha-helical antimicrobial peptides. *Biochim Biophys Acta* **1758**, 1245-1256, doi:10.1016/j.bbamem.2006.02.021 (2006).
212 Sawa, M., Nusinow, D. A., Kay, S. A. & Imaizumi, T. FKF1 and GIGANTEA complex formation is required for day-length measurement in Arabidopsis. *Science* **318**, 261-265, doi:10.1126/science.1146994 (2007).
213 Schaefer, A., Reinhard, N. R. & Hordijk, P. L. Toward understanding RhoGTPase specificity: structure, function and local activation. *Small GTPases* **5**, 6, doi:10.4161/21541248.2014.968004 (2014).
214 Schliwa, M. Action of cytochalasin D on cytoskeletal networks. *J Cell Biol* **92**, 79-91, doi:10.1083/jcb.92.1.79 (1982).
215 Schoenwaelder, S. M. & Burridge, K. Evidence for a calpeptin-sensitive protein-tyrosine phosphatase upstream of the small GTPase Rho. A novel role for the calpain inhibitor calpeptin in the inhibition of protein-tyrosine phosphatases. *J Biol Chem* **274**, 14359-14367, doi:10.1074/jbc.274.20.14359 (1999).
216 Schumacher, J. How light affects the life of Botrytis. *Fungal Genet Biol* **106**, 26-41, doi:10.1016/j.fgb.2017.06.002 (2017).
217 Schumacher, J., Simon, A., Cohrs, K. C., Viaud, M. & Tudzynski, P. The transcription factor BcLTF1 regulates virulence and light responses in the necrotrophic plant pathogen Botrytis cinerea. *PLoS Genet* **10**, e1004040, doi:10.1371/journal.pgen.1004040 (2014).

218 Seelig, J. Thermodynamics of lipid-peptide interactions. *Biochim Biophys Acta* **1666**, 40-50, doi:10.1016/j.bbamem.2004.08.004 (2004).
219 Shang, X. *et al.* Small-molecule inhibitors targeting G-protein-coupled Rho guanine nucleotide exchange factors. *Proc Natl Acad Sci U S A* **110**, 3155-3160, doi:10.1073/pnas.1212324110 (2013).
220 Shang, X. *et al.* Rational design of small molecule inhibitors targeting RhoA subfamily Rho GTPases. *Chem Biol* **19**, 699-710, doi:10.1016/j.chembiol.2012.05.009 (2012).
221 Shao, K. *et al.* Emulsion PCR: a high efficient way of PCR amplification of random DNA libraries in aptamer selection. *PLoS One* **6**, e24910, doi:10.1371/journal.pone.0024910 (2011).
222 Shen, Y. *et al.* Nudel binds Cdc42GAP to modulate Cdc42 activity at the leading edge of migrating cells. *Dev Cell* **14**, 342-353, doi:10.1016/j.devcel.2008.01.001 (2008).
223 Sirokmany, G. *et al.* Sec14 homology domain targets p50RhoGAP to endosomes and provides a link between Rab and Rho GTPases. *J Biol Chem* **281**, 6096-6105, doi:10.1074/jbc.M510619200 (2006).
224 Sit, S.-T. & Manser, E. Rho GTPases and their role in organizing the actin cytoskeleton. *Journal of Cell Science* **124**, 679, doi:10.1242/jcs.064964 (2011).
225 Strickland, D. *et al.* TULIPs: tunable, light-controlled interacting protein tags for cell biology. *Nat Methods* **9**, 379-384, doi:10.1038/nmeth.1904 (2012).
226 Struckhoff, A. P. *et al.* PDZ-RhoGEF is essential for CXCR4-driven breast tumor cell motility through spatial regulation of RhoA. *J Cell Sci* **126**, 4514-4526, doi:10.1242/jcs.132381 (2013).
227 Svitkina, T. The Actin Cytoskeleton and Actin-Based Motility. *Cold Spring Harb Perspect Biol* **10**, doi:10.1101/cshperspect.a018267 (2018).
228 Swartz, T. E. *et al.* Blue-light-activated histidine kinases: two-component sensors in bacteria. *Science* **317**, 1090-1093, doi:10.1126/science.1144306 (2007).
229 Szentpetery, Z., Balla, A., Kim, Y. J., Lemmon, M. A. & Balla, T. Live cell imaging with protein domains capable of recognizing phosphatidylinositol 4,5-bisphosphate; a comparative study. *BMC Cell Biol* **10**, 67, doi:10.1186/1471-2121-10-67 (2009).
230 Takai, Y., Sasaki, T. & Matozaki, T. Small GTP-binding proteins. *Physiol Rev* **81**, 153-208, doi:10.1152/physrev.2001.81.1.153 (2001).
231 Tang, Y., Zeng, X. & Liang, J. Surface Plasmon Resonance: An Introduction to a Surface Spectroscopy Technique. *J Chem Educ* **87**, 742-746, doi:10.1021/ed100186y (2010).
232 Taslimi, A. *et al.* An optimized optogenetic clustering tool for probing protein interaction and function. *Nat Commun* **5**, 4925, doi:10.1038/ncomms5925 (2014).
233 Taslimi, A. *et al.* Optimized second-generation CRY2-CIB dimerizers and photoactivatable Cre recombinase. *Nat Chem Biol* **12**, 425-430, doi:10.1038/nchembio.2063 (2016).
234 Tay, L. W., Wang, Z. & Du, G. Analysis of Phosphatidic Acid Binding and Regulation of PIPKI In Vitro and in Intact Cells. *Methods Enzymol* **583**, 359-374, doi:10.1016/bs.mie.2016.09.043 (2017).
235 Tcherkezian, J. & Lamarche-Vane, N. Current knowledge of the large RhoGAP family of proteins. *Biol Cell* **99**, 67-86, doi:10.1042/BC20060086 (2007).
236 ten Klooster, J. P. & Hordijk, P. L. Targeting and localized signalling by small GTPases. *Biol Cell* **99**, 1-12, doi:10.1042/BC20060071 (2007).

237 Tischer, D. & Weiner, O. D. Illuminating cell signalling with optogenetic tools. *Nat Rev Mol Cell Biol* **15**, 551-558, doi:10.1038/nrm3837 (2014).
238 Toettcher, J. E., Gong, D., Lim, W. A. & Weiner, O. D. Light-based feedback for controlling intracellular signaling dynamics. *Nat Methods* **8**, 837-839, doi:10.1038/nmeth.1700 (2011).
239 Toettcher, J. E., Voigt, C. A., Weiner, O. D. & Lim, W. A. The promise of optogenetics in cell biology: interrogating molecular circuits in space and time. *Nat Methods* **8**, 35-38, doi:10.1038/nmeth.f.326 (2011).
240 Toettcher, J. E., Weiner, O. D. & Lim, W. A. Using optogenetics to interrogate the dynamic control of signal transmission by the Ras/Erk module. *Cell* **155**, 1422-1434, doi:10.1016/j.cell.2013.11.004 (2013).
241 Totsukawa, G. *et al.* Distinct roles of ROCK (Rho-kinase) and MLCK in spatial regulation of MLC phosphorylation for assembly of stress fibers and focal adhesions in 3T3 fibroblasts. *J Cell Biol* **150**, 797-806, doi:10.1083/jcb.150.4.797 (2000).
242 Traut, T. W. Physiological concentrations of purines and pyrimidines. *Mol Cell Biochem* **140**, 1-22, doi:10.1007/BF00928361 (1994).
243 Trojanowski, N. F. & Fang-Yen, C. Simultaneous Optogenetic Stimulation of Individual Pharyngeal Neurons and Monitoring of Feeding Behavior in Intact C. elegans. *C. elegans*` **1327**, 105-119, doi:10.1007/978-1-4939-2842-2_9. (2015).
244 Uda, Y. *et al.* Improvement of Phycocyanobilin Synthesis for Genetically Encoded Phytochrome-Based Optogenetics. *ACS Chem Biol* **15**, 2896-2906, doi:10.1021/acschembio.0c00477 (2020).
245 Ueda, Y. & Sato, M. Cell membrane dynamics induction using optogenetic tools. *Biochem Biophys Res Commun* **506**, 387-393, doi:10.1016/j.bbrc.2017.11.091 (2018).
246 Uehata, M. *et al.* Calcium sensitization of smooth muscle mediated by a Rho-associated protein kinase in hypertension. *Nature* **389**, 990-994, doi:10.1038/40187 (1997).
247 Urano, D. *et al.* Endocytosis of the seven-transmembrane RGS1 protein activates G-protein-coupled signalling in Arabidopsis. *Nat Cell Biol* **14**, 1079-1088, doi:10.1038/ncb2568 (2012).
248 Valon, L. *et al.* Predictive Spatiotemporal Manipulation of Signaling Perturbations Using Optogenetics. *Biophys J* **109**, 1785-1797, doi:10.1016/j.bpj.2015.08.042 (2015).
249 Valon, L., Marin-Llaurado, A., Wyatt, T., Charras, G. & Trepat, X. Optogenetic control of cellular forces and mechanotransduction. *Nat Commun* **8**, 14396, doi:10.1038/ncomms14396 (2017).
250 van Bergeijk, P., Adrian, M., Hoogenraad, C. C. & Kapitein, L. C. Optogenetic control of organelle transport and positioning. *Nature* **518**, 111-114, doi:10.1038/nature14128 (2015).
251 Van Geel, O., Hartsuiker, R. & Gadella, T. W. J. Increasing spatial resolution of photoregulated GTPases through immobilized peripheral membrane proteins. *Small GTPases* **11**, 441-450, doi:10.1080/21541248.2018.1507411 (2020).
252 Van Geel, O., Hartsuiker, R. & Gadella, T. W. J. Increasing spatial resolution of photoregulated GTPases through immobilized peripheral membrane proteins. *Small GTPases*, 1-10, doi:10.1080/21541248.2018.1507411 (2018).

253 Wagner, E. & Glotzer, M. Local RhoA activation induces cytokinetic furrows independent of spindle position and cell cycle stage. *The Journal of Cell Biology* **213**, 641, doi:10.1083/jcb.201603025 (2016).
254 Wagner, E. & Glotzer, M. Local RhoA activation induces cytokinetic furrows independent of spindle position and cell cycle stage. *J Cell Biol* **213**, 641-649, doi:10.1083/jcb.201603025 (2016).
255 Wang, H. *et al.* LOVTRAP: an optogenetic system for photoinduced protein dissociation. *Nat Methods* **13**, 755-758, doi:10.1038/nmeth.3926 (2016).
256 Watson, J. R., Owen, D. & Mott, H. R. Cdc42 in actin dynamics: An ordered pathway governed by complex equilibria and directional effector handover. *Small GTPases* **8**, 237-244, doi:10.1080/21541248.2016.1215657 (2017).
257 Wettschureck, N. & Offermanns, S. Mammalian G proteins and their cell type specific functions. *Physiol Rev* **85**, 1159-1204, doi:10.1152/physrev.00003.2005 (2005).
258 Wittinghofer, A. & Vetter, I. R. Structure-function relationships of the G domain, a canonical switch motif. *Annu Rev Biochem* **80**, 943-971, doi:10.1146/annurev-biochem-062708-134043 (2011).
259 Wong, K., Pertz, O., Hahn, K. & Bourne, H. Neutrophil polarization: spatiotemporal dynamics of RhoA activity support a self-organizing mechanism. *Proc Natl Acad Sci U S A* **103**, 3639-3644, doi:10.1073/pnas.0600092103 (2006).
260 Wu, Y. I. *et al.* A genetically encoded photoactivatable Rac controls the motility of living cells. *Nature* **461**, 104-108 (2009).
261 Wu, Y. I. *et al.* A genetically encoded photoactivatable Rac controls the motility of living cells. *Nature* **461**, 104-108, doi:10.1038/nature08241 (2009).
262 Wu, Y. I., Wang, X., He, L., Montell, D. & Hahn, K. M. Spatiotemporal control of small GTPases with light using the LOV domain. *Methods Enzymol* **497**, 393-407, doi:10.1016/B978-0-12-385075-1.00016-0 (2011).
263 Wu, Y. I., Wang, X., He, L., Montell, D. & Hahn, K. M. Spatiotemporal control of small GTPases with light using the LOV domain. *Methods in enzymology* **497**, 393-407, doi:10.1016/B978-0-12-385075-1.00016-0 (2011).
264 Xin, M. *et al.* Hippo pathway effector Yap promotes cardiac regeneration. *Proc Natl Acad Sci U S A* **110**, 13839-13844, doi:10.1073/pnas.1313192110 (2013).
265 Yamada, T., Ohoka, Y., Kogo, M. & Inagaki, S. Physical and functional interactions of the lysophosphatidic acid receptors with PDZ domain-containing Rho guanine nucleotide exchange factors (RhoGEFs). *J Biol Chem* **280**, 19358-19363, doi:10.1074/jbc.M414561200 (2005).
266 Yang, X. Y. *et al.* p120Ras-GAP binds the DLC1 Rho-GAP tumor suppressor protein and inhibits its RhoA GTPase and growth-suppressing activities. *Oncogene* **28**, 1401-1409, doi:10.1038/onc.2008.498 (2009).
267 Yazawa, M., Sadaghiani, A. M., Hsueh, B. & Dolmetsch, R. E. Induction of protein-protein interactions in live cells using light. *Nat Biotechnol* **27**, 941-945, doi:10.1038/nbt.1569 (2009).
268 Yeung, T. *et al.* Membrane phosphatidylserine regulates surface charge and protein localization. *Science* **319**, 210-213, doi:10.1126/science.1152066 (2008).
269 Yimlamai, D., Fowl, B. H. & Camargo, F. D. Emerging evidence on the role of the Hippo/YAP pathway in liver physiology and cancer. *J Hepatol* **63**, 1491-1501, doi:10.1016/j.jhep.2015.07.008 (2015).

270 Yoshizaki, H. *et al.* Activity of Rho-family GTPases during cell division as visualized with FRET-based probes. *J Cell Biol* **162**, 223-232, doi:10.1083/jcb.200212049 (2003).
271 Yu, J. W. *et al.* Genome-Wide Analysis of Membrane Targeting by S. cerevisiae Pleckstrin Homology Domains. *Molecular Cell* **13**, 677-688, doi:10.1016/s1097-2765(04)00083-8 (2004).
272 Zegarlinska, J., Piascik, M., Sikorski, A. F. & Czogalla, A. Phosphatidic acid - a simple phospholipid with multiple faces. *Acta Biochim Pol* **65**, 163-171, doi:10.18388/abp.2018_2592 (2018).
273 Zhang, H. *et al.* Eight RGS and RGS-like proteins orchestrate growth, differentiation, and pathogenicity of Magnaporthe oryzae. *PLoS Pathog* **7**, e1002450, doi:10.1371/journal.ppat.1002450 (2011).
274 Zhang, K. & Cui, B. Optogenetic control of intracellular signaling pathways. *Trends Biotechnol* **33**, 92-100, doi:10.1016/j.tibtech.2014.11.007 (2015).
275 Zhou, X. X., Chung, H. K., Lam, A. J. & Lin, M. Z. Optical control of protein activity by fluorescent protein domains. *Science* **338**, 810-814, doi:10.1126/science.1226854 (2012).
276 Zhu, H. *et al.* Global analysis of protein activities using proteome chips. *Science* **293**, 2101-2105, doi:10.1126/science.1062191 (2001).
277 Zoltowski, B. D. & Gardner, K. H. Tripping the light fantastic: blue-light photoreceptors as examples of environmentally modulated protein-protein interactions. *Biochemistry* **50**, 4-16, doi:10.1021/bi101665s (2011).
278 Zoltowski, B. D., Vaccaro, B. & Crane, B. R. Mechanism-based tuning of a LOV domain photoreceptor. *Nat Chem Biol* **5**, 827-834, doi:10.1038/nchembio.210 (2009).